Describing temporal variations of the geomagnetic field using a modified virtual observatory scheme: application to Swarm measurements

Diana Saturnino

l'université nantes angers le mans
PÔLE DE RECHERCHE ET D'ENSEIGNEMENT SUPÉRIEUR

UNIVERSITÉ DE NANTES

Thèse de Doctorat

Diana SATURNINO

Mémoire présenté en vue de l'obtention du
grade de Docteur de l'Université de Nantes
sous le label de L'Université Nantes Angers Le Mans

École doctorale : Sciences Pour l'Ingénieur, Géosciences, Architecture

Discipline : Terre Solide et Couches Profondes
Unité de recherche : ***UMR-6112 Laboratoire de Planétologie et Géodynamique***

Soutenue le 30 Novembre 2015

Describing temporal variations of the geomagnetic field using a modified virtual observatory scheme: application to Swarm measurements

Une méthode d'observatoires virtuels pour décrire les variations temporelles du champ géomagnétique et applications aux mesures de la mission Swarm

JURY

Président :	**Antoine MOCQUET**, Professeur, Université de Nantes
Rapporteurs :	**Monika KORTE**, Chercheuse, GFZ Helmhotz Centre Postdam **Mioara MANDEA**, Physicienne (CNAP), CNES
Examinateurs :	**M[a] Alexandra PAIS,** Maître de conférence**,** Universidade de Coimbra **Nicolas GILLET**, Chargé de Recherche, ISTerre Grenoble
Directeur de Thèse :	**Benoit LANGLAIS**, Directeur de recherche, UMR 6112 LPG Nantes
Co-encadrant de Thèse :	**Hagay AMIT**, Chargé de recherche, UMR 6112 LPG Nantes

Aos meus pais. [1]

[1] To my parents.

Acknowledgements

I would like to thank:

- Benoit Langlais for the opportunity given to me to carry out a thesis on the subject of geomagnetism. I increased my knowledge on the subject and grew up as a young researcher and person. Additionally, thanks for all the help dispensed to me when of my arrival as a foreign to Nantes. The time and patience for all bureaucracy was always very helpful.
- Hagay Amit for all the interesting ideas and thought-provoking questions.
- The members of my "Comité de Suivi de Thèse" whose comments, critics and ideas help me to find a way to a valid approach.
- The members of the jury for their time, very interesting questions and discussion about my work.
- All other PhD students who took this trip of three years with me. Thanks for all the time spend together talking about silly things and helping each other from time to time. I loved my gifts! I hope we continue to see each other during the following years; more weekends have to take place.
- Everyone who helped me during these three years with the adaptation to a new country; and also to the ones who reminded me of my country of origin.
- My parents and the rest of my family for all the support. The remembrance of the distance was another lesson to learn.

This thesis work was supported by CNES and Région Pays de la Loire.

The results presented through this thesis rely on:

- data collected at magnetic observatories. The national institutes that support them and INTERMAGNET who promotes high standards of magnetic practice are thanked;
- Swarm L1b data. The access to this data was provided by ESA.

Numerous figures in the manuscript were produced with GMT (Wessel et al., 2013).

Abstract

A description of the temporal variations of the main geomagnetic field (i.e., the secular variation or SV) is crucial to the understanding of core dynamo generation. It is known with high accuracy at observatory locations, which are globally unevenly located, hampering the determination of a global pattern of these variations. Satellites have allowed global surveys of the field and its SV. Their data has been used by global spherical harmonic models using data selection criteria to reduce external contributions. SV small spatial scales may not be well described by these models and can show significant errors compared to ground measurements. This study attempts to extract temporal variation time series from satellite measurements as it is done at observatory locations. We follow a Virtual Observatories (VO) approach, defining a global mesh of VOs at satellite altitude. We apply an Equivalent Source Dipole (ESD) technique. For each VO and a given time interval all measurements are reduced to a unique location, leading to time series similar to those available at the ground. Synthetic data is first used to validate the approach. We then apply our scheme to Swarm mission measurements and locally compare the VO-ESD derived time series to ground observations and to satellite-based model predictions. The approach is able to describe field's time variations at local scales. The global mesh of VO time series is used to derive global spherical harmonic models. For a simple parametrization the model well describes the trend of the magnetic field both at satellite altitude and at the surface. Nevertheless more complex modelling can be made to properly profit of VO-ESD time series.

Keywords: Earth's magnetic field, modelling,inversion data analysis, satellite measurements, Swarm mission, Virtual Observatories, Equivalent Source Dipoles, IGRF model.

Resumé

Le champ magnétique de la Terre est un phénomène complexe qui varie dans le temps et dans l'espace. Sa composante la plus importante, appelée champ principal, trouve sa source dans les courantes électriques issu d'effets de convection dans le noyau externe liquide et conducteur de la Terre. D'autres sources ajoutent des contributions au champ magnétique mesuré autour de la Terre. Le champ principal interagit avec le vent solaire, au sein de la magnétosphère, où des systèmes de courants électriques sont en rotation, comme le ring current ou les ceintures de radiations de Van Allen. Au-dessous de la magnétosphère, dans l'atmosphère de la Terre, se trouve l'ionosphère où des courants sont créés suite à une ionisation par les radiations solaires. Ces courants sont particulièrement importants dans la région équatoriale, avec l'électrojet équatorial. L'ionosphère dans les zones polaires est aussi une zone magnétiquement active où les courants électriques alignés (ou field aligned currents) et électrojets polaires contribuent au champ mesuré. Ces sources sont appelées champs externes (car externes à l'intérieur de la Terre).

Elles induisent des courants électriques dans le manteau supérieur terrestre. De la même façon les océans possèdent aussi des courants induits, liés à la circulation des eaux salées et aux marées. La contribution de la lithosphère provient des roches aimantées dans la croûte, que cette aimantation soit statique et figée (rémanente), ou proportionnelle au champ ambiant (induite). En raison de cette multitude de sources le champ magnétique mesuré en un endroit résulte de la superposition de champs de différentes échelles spatiales et temporelles.

Toutes ces sources existent dans une large gamme d'échelles de temps Dans le domaine qui nous intéresse, ces variations vont de quelques secondes (dues à des oscillations dans les courants ionosphériques), à quelques minutes ou jours (pour des orages magnétiques liés à l'activité solaire), à des siècles ou plus (inversions de polarité du moment dipolaire principal). La connaissance des variations temporelles du champ sur une large gamme d'échelles est donc importante pour mieux en séparer les sources et ainsi mieux comprendre la génération du champ dans le noyau.

La variation séculaire (SV) est communément estimée en calculant la première dérivée temporelle du champ magnétique. On peut l'estimer directement aux observatoires magnétiques grâce aux différences entre les moyennes annuelles (ou mensuelles). Son amplitude est de l'ordre de 10

à 100 nT/an. La SV peut être considérée (en première approximation) comme constante pendant quelques années à quelques décennies, avec des changements brusques et rapides pendant quelques mois, appelés secousses géomagnétiques ou jerks. Ces phénomènes ont une origine interne mais leur dynamique et cause exactes sont débattues (Mandea et al., 2010). La variation séculaire change également dans l'espace. À l'échelle régionale différents observatoires peuvent enregistrer différentes variations temporelles à court terme. La description de ces différents changements du champ magnétique peut aider les études sur la génération du champ du noyau. Ceci souligne la nécessité d'avoir ces mesures de façon homogène et de pouvoir les traiter de manière appropriée.

Des observations avec l'information complète du champ (intensité et direction) sont continuellement acquises à la surface de la Terre depuis 1840 dans les observatoires magnétiques. Le nombre d'observatoires, leur distribution géographique, et la précision des mesures, ont augmenté progressivement vers la distribution d'aujourd'hui, bien que certains anciens observatoires ont été fermés pour une multitude de raisons. La répartition spatiale des observatoires n'est pas parfaite. Elle est inégale sur le globe, avec très peu d'observations dans l'hémisphère sud et sur les océans. Cette distribution spatiale hétérogène limite la résolution et la lisibilité des études de champ géomagnétique, spécialement sur les modèles (Matzka et al., 2010). Néanmoins les mesures des observatoires magnétiques sont essentielles dans la modélisation temporelle du champ. En effet, la précision de la plupart des modèles actuels repose sur des séries temporelles des observatoires magnétiques.

Pour compléter ces mesures, des satellites embarquant des magnétomètres sur une orbite basse (LEO) ont été lancés. Ils ont rendu possible la cartographie du champ géomagnétique à une l'échelle globale. Les mesures sont effectuées avec le même instrument partout et plusieurs fois sur toute la planète, sauf pour une région autour d'axe de rotation (à cause de l'inclinaison des satellites). Les hétérogénéités locales de petites échelles spatiales attribuables au champ de la croûte, qui sont un problème pour les observatoires au sol, contribuent plus faiblement à l'altitude des satellites. Malgré tous les avantages des données satellitaires ils ont aussi des inconvénients. Les variations du champ peuvent être à la fois temporelles et spatiales, en raison des mouvements satellitaires mais aussi de la variation des sources magnétiques. Cela doit être pris en compte lors de l'analyse des données. Les mesures satellitaires doivent être de haute précision, non seulement en ce qui concerne la résolution, mais aussi l'orientation et les valeurs

absolues du champ. De plus les modèles des contributions du champ externe ont besoin d'une bonne distribution des mesures non seulement en longitude et latitude, mais aussi en heure locale (Olsen et al., 2010).

Les mesures satellitaires ne sont pas acquises à une altitude fixe, mais sur une gamme d'altitudes. Cela produit des séries temporelles inégalement réparties en altitude. Même si ceci peut être vu comme un inconvénient, cela peut aider pour bien séparer les sources internes et externes du champ. Enfin le traitement des données satellitaires implique souvent d'abord une sélection de données sur la base des données obtenues par les observatoires au sol, habituellement par l'utilisation d'indices géomagnétiques. Ces indices caractérisent les contributions des sources de l'ionosphère et de la magnétosphère, et mesurent les perturbations de l'activité géomagnétique (Menvielle et al., 2011).

Les missions satellitaires qui mesurent le champ avec une grande précision ont débuté avec POGO-2 en 1965 (Cain, 2007), qui fournissait seulement l'intensité du champ. La mission MAGSAT, qui a volé entre octobre 1979 et juin 1980, a apporté les premières mesures vectorielles à l'échelle globale. Ces données ont rendu possible le calcul de modèles du champ, et ont mis en évidence la domination du champ du noyau jusqu'à au degré et ordre 13 et de la lithosphère au-delà du degré et ordre 15 (Langel and Estes, 1982).

C'est seulement en 1999 que la mission suivante, Ørsted, a été lancée. Ses mesures ont aidé à améliorer les modèles du champ magnétique, pour étudier les phénomènes auroraux et la relation entre les champs externes et encore le couplage de l'énergie du système magnétosphère-ionosphère et vent solaire (Olsen et al., 2000; Neubert et al., 2001; Langlais et al., 2003). Depuis 2005 cependant, seules les données d'Intensité ont qualité suffisant pour être utilisées dans des travaux scientifiques. Le satellite CHAMP, lancé en Juillet 2000, fournissait une meilleure précision des mesures vectorielles que Ørsted (Maus, 2007). Ensemble, ces satellites Ørsted et CHAMP représentent une amélioration sur les caractéristiques de la mission satellite de MAGSAT. Ils ont permis de comparer les changements du champ principal entre les deux époques (1980 et 2000), en particulier dans les échelles spatiales qui ne peuvent pas être atteintes par les observatoires à la surface. Ils ont également permis l'amélioration des modèles de champ lithosphérique (Thébault et al., 2010), de nouvelles observations des sources des champs externes (Stolle et al., 2006), et démontré que le champ magnétique produit par l'océan peut être détecté par des mesures depuis de l'espace (Tyler et al., 2003).

L'accumulation de données d'Ørsted et CHAMP a démontré l'avantage unique de satellites LEO pour la surveillance du champ magnétique de la Terre, et leurs différents plans orbitaux ont montré qu'une constellation de plusieurs satellites faisant des mesures simultanées en différentes régions de la Terre apporteraient de nouvelles possibilités pour la modélisation du champ. La mission Swarm reprend cette idée. Elle a été proposée à l'ESA en 2002, et après de nombreuses années de développement, a été lancée le 22 novembre 2013. Cette mission consiste en une constellation de trois satellites consacrés à l'étude du champ magnétique terrestre et ses interactions avec le système de la Terre (Friis-Christensen et al., 2006). La mission a été conçue pour livrer la première représentation globale des variations du champ magnétique sur des échelles de temps d'une heure à plusieurs années et résoudre le problème de séparation des sources.

La constellation est composé de deux satellite (A et C) volant presque côte à côte à une altitude proche de 470 km, avec une séparation en longitude de $1{,}4^o$ degrés et avec une inclinaison de $87{,}4^o$. Le troisième satellite (B) vole au-dessus, à près de 520 km, sur une orbite quasi polaire (inclinaison 88^o) pour permettre une séparation progressive de l'heure locale par rapport à A et C. Chaque satellite dispose d'un ensemble d'instruments similaires, à la fois pour mesurer le champ magnétique et le champ électrique. L'Absolute Scalar Magnétomèter (ASM) mesure l'intensité du champ à 1 Hz avec une précision de 0,1 nT. Le Vector Field Magnetometer (VFM) fournit des mesures vectorielles à 1 Hz avec une précision de 0,5 nT et est calibré par les mesures de l'ASM. Les mesures du champ magnétique, la navigation, l'accéléromètre, le plasma et les champs électriques sont fournis par l'ESA en tant que données de niveau 1b (Level-1b), qui consistent en sous forme de série temporelle des observations calibrées et formatées, avec par exemple les trois composantes du champ magnétique prises par chaque satellite (Olsen et al., 2013).

Le champ magnétique terrestre peut être décrit mathématiquement comme étant le gradient d'un potentiel scalaire, décrit dans un développement en série d'harmoniques sphériques (SH, Gauss, 1839). Une série de coefficients, dits de Gauss, est ensuite utilisée pour décrire les champs d'origine interne et externe. Les modèles peuvent être basés sur les mesures des observatoires magnétiques et les mesures satellitaires. Habituellement, les données satellitaires sont rigoureusement sélectionnées pour minimiser les contributions variables du champ externe. Toutes les données sont ensuite utilisées pour résoudre le problème inverse qui recherche les sources

responsables pour les observations, à savoir, les coefficients de Gauss. Le champ principal, sa variation séculaire et les contributions de la magnétosphère sont estimés grâce à une inversion en minimisant l'écart entre observations et prédictions par le modèle dans le sens des moindres carrés. En théorie ces contributions sont indépendantes. Ceci est l'approche séquentielle classique.

Une autre approche existe pour modéliser le champ. L'approche compréhensive (comprehensive modelling) utilise les données satellitaires et d'observatoires magnétiques en co-estimatent le champ interne, les champs magnétosphérique et ionosphérique (y compris leurs homologues induits) dans un même (énorme) système d'inversion. Contrairement à l'approche séquentielle, ces modèles incluent le champ ionosphérique dans l'inversion en calculant un champ toroïdal (dans la région de l'ionosphère). Les deux approches peuvent décrire les changements temporels des coefficients principaux du champ interne par une description en utilisant des splines cubiques.

Le champ géomagnétique international de référence (IGRF) décrit le champ principal de la Terre et sa variation séculaire à l'échelle globale. Il est publié tous les cinq ans et comprend une partie prédictive de la variation séculaire pour la prochaine période de 5 ans. Il est calculé jusqu'au degré et ordre 13 pour le champ principal et le degré et l'ordre 8 pour la variation séculaire. Des équipes scientifiques internationales proposent différents modèles candidats sous la forme de coefficients de Gauss qui sont ensuite évalués par le Groupe de travail V-MOD de l'International Association of Geogmagnetism and Aeronomy (IAGA), responsable de l'évaluation et de la production de l'IGRF. La méthode habituelle pour calculer le modèle IGRF final consiste à appliquer un système de pondération à tous les modèles proposés après une comparaison statistique entre les modèles (Thébault et al., 2015a). Les modèles candidats peuvent en effet être relativement différents car ils sont construits avec des choix et des approches scientifiques différentes. Ainsi, le processus d'évaluation n'est pas une tâche simple.

L'IAGA a demandé en 2014 la soumission de modèles candidats avant le 1er octobre pour construire la douzième génération de l'IGRF pour l'époque 2015, ou IGRF-12. Le groupe du LPG Nantes a soumis des modèles candidats, à la fois pour le champ principal en 2015 et la variation séculaire de 2015,0 à 2020,0. Ce travail a abouti à l'élaboration d'un article scientifique (Saturnino et al., 2015), où la construction des modèles présentés est décrite. Ces modèles candidats sont dérivés d'un même modèle parent pour lequel on applique une approche

séquentielle. Le champ principal est extrapolé à époque 2015,0 en utilisant sa variation séculaire associée. Nous avons utilisé les mesures acquises pendant les premiers mois de la mission Swarm entre le lancement et 18/09/2014, et calculé deux modèles différents.

Le premier modèle (V-ASM) est exclusivement basé sur des mesures provenant des satellites Swarm A et C. Il est calculé jusqu'au degré et ordre 25 pour le champ principal, 13 pour la variation séculaire et 2 pour le champ externe. Une sélection de données, basée sur des indices géomagnétiques, a été utilisée pour minimiser les contributions du champ externe. Les mesures aberrantes ont aussi été éliminées dans un second temps. Les mesures d'intensité du champ magnétique sont utilisées pour toutes les latitudes et les mesures vectorielles seulement entre $+/- 50^o$ de latitude magnétique. Un deuxième modèle (Z-ASM) a été calculé en utilisant uniquement la composante verticale (entre $+/- 50^o$ de latitude magnétique) du champ magnétique et l'intensité totale partout. En effet de légères différences existent entre l'intensité mesurée et celle calculée d'après les mesures vectorielles. Ce modèle offre un ajustement aux mesures légèrement meilleur que le premier.

Les deux modèles sont comparés. Les différences entre eux sont petites à l'époque moyenne de leurs mesures et si ils sont tronqués jusqu'au degré de 13. Toutefois, les différences deviennent plus grandes lorsque les modèles sont extrapolés à 2015,0, passant de 0,94 à 3,04 nT (écart quadratique moyen, rms). Cela est probablement une conséquence de l'utilisation d'un intervalle de temps trop court (dix mois) pour construire un modèle robuste de SV. Les deux modèles sont similaires pour le champ principal, ne différant que sur la partie variant dans le temps. Les différences entre les modèles nous ont amenés à choisir le modèle V-ASM comme notre candidat IGRF. Les différences peuvent être liées à la fois à une sélection de données non-optimale au-dessus des zones polaires (où les résidus rms sont plus importants) et à un court intervalle de temps pour construire la SV. Le modèle Z-ASM souligne cependant que cette approche peut être utilisée lorsque seulement l'information directionnelle du champ est partiellement connue.

Les modèles candidats ont été également comparés à la version finale du IGRF-12 (Thébault et al., 2015b). Les différences entre l'IGRF-12 final et le modèle candidat V-ASM sont légèrement inférieures à celles avec le modèle de test Z-ASM, ce qui confirme a posteriori notre choix en ce qui concerne le modèle V-ASM. La version finale du IGRF-12 a été construite en utilisant un système de pondération dans le domaine spatial grâce à une approche itérative re-pondérée des moindres carrés. L'approche calcule un poids pour chaque modèle sur une grille spatiale et

pour les trois composantes du champ magnétique, à la surface de la Terre.

Aujourd'hui, le champ magnétique et sa variation séculaire sont contraints à l'échelle globale par des modèles du champ magnétique. Mais des petites échelles spatiales de la variation séculaire du champ peuvent ne pas être correctement décrites par les modèles. En fait, la prédiction de la variation séculaire par ces modèles satellitaires peut avoir une différence par rapport aux mesures faites en observatoire (au même emplacement). En outre, ces modèles ne décrivent pas bien les variations spatiales des variations rapides de la variation séculaire. En effet des observatoires magnétiques géographiquement proches montrent des petites différences dans leurs variations temporelles du champ. Ces petites différences ne sont pas prédites par les modèles ; elles ne sont pas non plus expliquées par ce que l'on connaît sur le champ externe. Il est donc possible qu'elles soient d'origine interne (noyau). De cela se pose la question scientifique suivante : est-il possible de mieux rendre compte des échelles spatiales régionales de la variation temporelle du champ ? Et de mieux comprendre leur origine ? Telle est la question qui motive ce travail.

L'opportunité d'utiliser les mesures de la mission Swarm, effectuées à des altitudes différentes et par trois satellites, motive un traitement différent des données satellitaires. Nous cherchons à comprendre les échelles spatiales régionales de la variation séculaire, donc un traitement plus local des mesures nous parait prometteur. Nous avons suivi l'approche des observatoires virtuels.

L'approche des observatoires virtuels (VO) a été introduite par Mandea and Olsen (2006) comme une nouvelle façon de traiter les mesures magnétiques satellitaires. L'idée est d'étudier les variations temporelles à court terme du champ principal en extrayant des moyennes mensuelles du champ à l'altitude des satellites, comme on peut le faire au sein des observatoires à la surface de la Terre. La motivation de cette méthode vient du fait que les moyennes mensuelles des observatoires à la surface fournissent un excellent outil pour étudier les changements temporels du champ principal. Cependant, leur répartition inégale limite la détermination des tendances globales de ces changements. Un maillage global d'observatoires virtuels permettrait d'étudier les variations temporelles locales du champ. Pour cela Olsen and Mandea (2007) définissent des volumes cylindriques de données, distribués sur une maille globale et homogène. Puis, dans chaque VO une série temporelle est construite avec toutes les mesures prises dans le volume. Des moyennes mensuelles du champ sont ensuite calculées pour toutes les compo-

santes du champ magnétique. La principale difficulté de cette approche est liée à la nature des mesures satellitaires, car elles sont prises à des altitudes différentes, contrairement aux observatoires terrestres. De plus l'altitude est dépendante du temps, et ceci peut biaiser les résultats. Ainsi, une correction doit être faite pour mettre toutes les mesures à une altitude constante. Pour résoudre ce problème, Mandea et Olsen (2006) utilisent l'hypothèse que les résidus des mesures (après la soustraction d'un modèle du champ principal) peuvent être représentés par un potentiel laplacien. Après avoir calculé les paramètres de ce potentiel dans une inversion, ceux-ci sont utilisés pour estimer un résidu magnétique moyen à une altitude constante. Le résidu moyen représente toutes les mesures pour un moment donné. Cette méthode a besoin d'un modèle du champ principal connu a priori.

Une technique alternative pour ramener les mesures satellitaires vers une altitude constante est proposée dans cette thèse. L'idée est d'utiliser la technique des Source Dipolaires Équivalente (ESD). Cette technique a été introduite afin de réduire des données magnétiques satellitaires collectées à différentes altitudes à une élévation commune sur une petite surface (Mayhew, 1979), ou pour en obtenir des cartes d'anomalies, par exemple, d'anomalies du champ de la croûte à une altitude donnée (Langlais et al., 2004). Cette méthode est basée sur l'expression d'une anomalie magnétique provoquée par un dipôle magnétique. Une maille de dipôles est placée en dessous des observations. Une inversion est faite pour trouver l'aimantation équivalente de chaque source dipolaire, qui ensemble expliquent les observations. Ensuite, le calcul direct se fait pour prédire le champ à une altitude constante grâce aux paramètres des dipôles obtenus.

La technique ESD peut être utilisé avec la méthode des VO pour réduire les observations magnétiques dans un volume de VO et pendant un intervalle de temps donné à une altitude constante. L'idée de l'approche, ci-après dénommé VO-ESD, est la suivante : pour chaque VO une maille de dipôles est placée en dessous, à une profondeur définie, et avec un certain nombre de dipôles. A partir de toutes les mesures satellitaires faites à l'intérieur du VO, pendant une période de temps donnée, l'aimantation équivalente de chacun des dipôles est calculée par une méthode d'inversion itérative de gradient conjugué. Puis, une prédiction est effectuée au centre de l'emplacement du VO, fixé à l'altitude choisie. Cette procédure est effectuée pour chacun des VO, placé sur une maille globale, et pour chaque période de temps (par exemple, un mois). Une série temporelle est ensuite obtenue à chaque emplacement VO. Un modèle global du champ et de sa variation peut alors être construit.

Pour mettre en œuvre cette approche, différents paramètres doivent être précisés : la géométrie, la taille de la maille de dipôle, sa profondeur, l'intervalle de temps utilisé lors de l'inversion, etc. Tous ces paramètres ont été testés au cours d'un processus de validation de l'approche VO-ESD. Cette validation a utilisé des données synthétiques obtenues à l'aide d'un modèle magnétique global de SH du champ principal, le CHAOS-4 (Olsen et al., 2014), tronqué au degré 13. Des prédictions à différentes altitudes du satellite pour les trois composants magnétiques (X, Y, Z) et l'intensité du champ (F) ont été utilisées. Des tests ont été effectués avec une distribution de données régulière en latitude et longitude, sur une distribution aléatoire ou encore sur des orbites synthétiques des trois satellites Swarm.

Les tests initiaux suivent l'idée d'un maillage de dipôles locale, placé en dessous du centre d'un volume cubique de données (1×1×300 km). Le volume contient 400 points, distribués entre 450 et 750 km de altitude. Le maillage de dipôles avait, à ce stade, la même extension en surface que le volume du VO ou moins. Une distribution hexagonale a été utilisée pour la géométrie du maillage de dipôles. Les paramètres testés ont été les suivants : le nombre de dipôles, la profondeur de la maille de dipôles et la distance moyenne entre les dipôles sur le maillage. Les résidus rms obtenus lors de l'inversion avec la technique de l'ESD étaient trop élevés (généralement supérieurs à 5 nT) et erratiques. Il est devenu clair qu'il n'est pas possible d'obtenir des résidus rms suffisamment petits avec un maillage local de dipôles. Pour un champ magnétique complexe comme celui de la Terre, un groupe localisé de sources ne suffit pas à l'expliquer et à le décrire, même pour des mesures à l'échelle locale.

Une approche différente avec un maillage de dipôles sur un hémisphère est ensuite essayée. La maille est placée à la profondeur de l'interface noyau-manteau ($\sim$ 2900 km), mais toujours centré sous la position du VO. Les mêmes mesures synthétiques sont utilisées. Une discrétisation isosahédrique sphérique de la maille de dipôles a été testé mais abandonnée pour une discrétisation hexagonale. Le maillage choisi contient 91 dipôles avec une distance moyenne de 18^o. De l'idée initiale d'un volume cubique de données, une modification est faite et nous choisissons un volume cylindrique pour le VO, avec $1{,}5^o$ de rayon horizontal. Dans cette géométrie toutes les données les plus éloignées sont à la même distance du centre du VO. L'altitude du centre de tous les VO est choisie à 490 km. Les données synthétiques sont distribuées aléatoirement à l'intérieur du cylindre et pour une période de temps de 30 jours. Pour chaque période, les positions des mesures sont donc différentes.

En utilisant la technique des ESD, les mesure synthétiques de chaque période de 30 jours sont prolongées à une altitude moyenne de 490 km et au centre de chaque VO. Les residus rms sont observés et les séries temporelles synthétiques ainsi obtenues à l'attitude choisie sont comparées avec la prédiction par le modèle CHAOS-4, pour la même localisation et instant. Sans variation séculaire initiale ajoutés aux données, les résidus rms sont très proches de zéro (écart inférieur à 0,06 nT). Avec la variation séculaire les résidus sont supérieurs, entre 1 et 1,5 nT. Cette augmentation est due aux variations spatiales et surtout temporelles du champ à travers le volume du VO et pendant la période de 30 jours (et qui ne sont pas modélisées par les ESD). La prédiction au centre du VO est également satisfaisante, étant très proche (inférieur à ± 0.1 nT) de la prédiction au même point et au même instant par le modèle SH utilisé pour les mesures synthétiques. L'ajout de bruit aux données (du bruit blanc de 2, 5 et 10 nT), ne modifie pas de façon significative la capacité de l'approche à prédire le champ magnétique pour un intervalle de temps donné à une altitude constante. L'augmentation des résidus rms suit les valeurs de l'écart type des bruits ajoutés. Les prédictions continuent aussi à être satisfaisantes, avec des différences supérieures à ± 0.1 nT seulement pour le cas du bruit de 10 nT et pour la composante verticale.

Puis l'utilisation des positions des orbites des satellites Swarm (toujours avec des données synthétiques) est testée. Ceci conduit à un changement significatif de la répartition spatiale des données. Plus précisément, des régions sans données existent dans le volume du VO, entre deux orbites des satellites Swarm. Cependant, cela ne change pas de manière significative les résultats de la technique. La technique est toujours capable de prédire les observations avec des résidus rms adéquats et une prédiction moyenne au centre du volume du VO satisfaisante.

Tous ces résultats sont très encourageants, et l'approche VO-EDD est considérée valide. La prochaine étape est l'application à des mesures réelles de la mission Swarm, et la construction de une maille globale et homogène d'observatoires virtuelles et de ses séries temporelles.

Les mesures Swarm utilisées couvrent la période entre novembre 2013 et juin 2015. L'approche est utilisée pour différents intervalles de temps : 27 jours, 30 jours et mensuels (calendaire). Aucune dépendance significative par rapport à la durée n'est trouvée ; pour la suite nous ne considérons plus que l'intervalle de 30 jours. Pour les données Swarm utilisées, cela correspond à 18 périodes consécutives. Dans un premier temps, les prédictions par l'approche VO-ESD sont comparées à des séries temporelles d'observatoires magnétiques à la surface pour toute

l'année 2014. Pour cela des VO ont été construits exactement au-dessus de la localisation de huit observatoires magnétiques. Le centre de tous ces VO est toujours à 490 km d'altitude. Les résidus rms obtenus pour ces huit VO sont du même ordre de grandeur, mais présentent une dépendance avec la latitude (résidus plus élevés à haute latitude). Les séries temporelles VO-ESD obtenues ressemblent de façon significative à celles des observatoires correspondants. Les corrélations entre les séries à la surface et celles à l'altitude du satellite sont significatives, en particulier pour les composantes Y et Z du champ. De plus, tant à la surface qu'à l'altitude satellitaire, les tendances annuelles des séries sont semblables et les VO géographiquement proches présentent des séries temporelles très similaires, exactement comme on l'observe dans les observatoires magnétiques à la surface.

Dans un deuxième temps, l'approche est appliquée à toutes les mesures des satellites Swarm pour un maillage global d'observatoires virtuels. La maille est telle que chaque VO a un volume cylindrique de 3^o de diamètre et les latitudes au centre des VO sont éloignés les unes des autres par $2{,}5^o$, donc les volumes se chevauchent horizontalement. L'altitude de chaque VO a été calculée comme la valeur moyenne de la gamme des altitudes des orbites des satellites Swarm pendant les deux premiers mois de la mission (c'est-à-dire, avant que les satellites n'atteignent leurs altitudes finales). Ainsi, l'altitude de chaque VO dépend de sa latitude centrale : l'altitude diminue du pôle sud vers le pôle nord. Le nombre d'observatoires virtuels est de 6644.

Les séries temporelles du champ magnétique sont ensuite obtenues aux 6644 emplacements pour un total de 18 périodes de 30 jours. Les résidus rms de toutes les inversions révèlent une dépendance à la latitude centrale du VO. Aux latitudes élevées (près des pôles) les composantes horizontales du champ présentent des valeurs élevées de résidus rms, contrairement à la composante verticale qui a de très basses valeurs de résidus rms aux latitudes élevées et de hauts résidus rms à des latitudes proches de l'equateur. Aux latitudes élevées le signal des courants alignés peut être le responsable des valeurs élevées de résidus rms pour les composantes horizontales. Aux basses latitudes, autour de l'équateur magnétique, le signal de la composante verticale du champ est faible (et nul à l'équateur magnétique), donc les contributions des courants électriques autour de l'équateur magnétique peut être relativement importantes pour la composante verticale mesurée. Les contributions externes sur les séries temporelles des prédictions VO-ESD doivent être prises en considération dans la construction d'un modèle global du champ magnétique.

La représentation par des splines cubiques avec une résolution six mois localement et indépendamment pour chaque série de VO fournit une bonne description de l'évolution temporelle de la série temporelle des VO-ESD. Elle est capable de décrire la plupart des changements rapides du champ magnétique observés dans chacun des VO.

Le maillage obtenu des séries temporelles VO-ESD est utilisé pour construire des modèles globaux du champ géomagnétique. Ces modèles ont pour but de tester la capacité de l'approche VO-ESD à dériver des séries temporelles adéquates pour le calcul de modèles globaux du champ principal, avec une amélioration de la variation temporelle du champ à l'échelle locale.

Différents modèles sont calculés, en utilisant différents ensembles de données : un modèle snapshot par période (VO-ESD_1, consistant en 18 modèles), un modèle snapshot de six périodes de temps consécutives (VO-ESD_6, consistant en 13 modèles), un modèle global avec toutes les 18 périodes (VO-ESD_18) et un autre modèle global avec seulement les 16 dernières périodes (VO-ESD_16).

Les modèles snapshot sont calculés uniquement pour le champ principal (degré 30) et pour le champ externe (degré 2). Les modèles de 18 et de 16 périodes sont calculés en tenant compte d'une variation séculaire. La dépendance temporelle des coefficients de Gauss pour le champ interne est considérée comme linéaire pendant tout l'intervalle des données. Le champ interne est toujours calculé jusqu'au degré et ordre 30. Différent degrés maximum pour la variation séculaire et pour champ externe sont testés. De l'intention originale d'obtenir un modèle avec toutes les données (18 périodes) une modification est faite, pour en soustraire les deux premières périodes. En effet, nous constatons que les deux modèles snapshot de 1 période, mais aussi les deux modèles de 6 périodes utilisant ces mesures, présentent des résidus rms plus élevés que les modèles correspondant à d'autres périodes. Leurs spectres sont aussi significativement différents des spectres des autres modèles.

L'expansion de SH pour les sources externes est testée jusqu'au degré et ordre 2, 3, 4 et 5. En l'absence d'une sélection des données (contrairement aux méthodes usuelles), les contributions du champ externe peuvent en effet être considérées plus importantes dans les données, et l'expansion pour le champ externe peut devoir être supérieure à ce qui est fait d'habitude (jusqu'au degré 2). Cependant, aucune différence significative (comme une diminution des résidus rms) n'est observée en augmentant le degré d'expansion du champ externe.

La SV a été calculée pour les degrés 13 et 18 sur les premiers modèles (VO-ESD_18). Toutefois, une comparaison avec le spectre du modèle CHAOS-5 Finlay et al. (2015) montre que l'intervalle de données n'est pas suffisant pour prédire de manière adéquate la variation séculaire au-dessus du degré 10. Ainsi deux modèles avec l'expansion de la variation séculaire jusqu'au degré 10 sont calculés : le modèle VO-ESD_18.30-10-2 et le modèle VO-ESD_16.30-10-2 (les chiffres représentant les degrés maximum pour le champ interne, la variation séculaire et le champ externe).

La soustraction des deux premières périodes améliore de manière significative les résidus rms des modèles. Les différences avec le spectre du champ principal de CHAOS-5 sont également moindres. Cependant, pour la SV le résultat est contraire. La raison peut être le plus faible nombre de données disponibles pour contraindre la variation temporelle du champ principal, ou que l'approximation de une SV linear ne soit pas la plus adéquate.

Nous observons une différence importante pour le degré 5 pour le spectre du champ principal. Le champ prédit par des coefficients g_1^0, h_1^1, g_5^0 et h_5^1 (4 coefficients) explique en grande partie les différences entre nos modèles (VO-ESD_18.30-10-2 et VO -ESD_16.30-10-2) et CHAOS-5 pour l'époque 2014,7. La raison de cette différence pour le degré 5 n'est pas comprise. Cela peut être lié au traitement des données satellitaires avec des observatoires magnétiques virtuels et/ou à une contribution de courants électriques pour le champ externe.

Lorsque l'on analyse les différences entre nos modèles et le modèle CHAOS-5, coefficient par coefficient pour la SV, la principale différence (près de 2 nT/an) réside dans le degré 2. Quatre coefficients ont des différences supérieures à 1 nT/an. L'intervalle temporel (approximativement un an et demi) est peut-être trop court et insuffisant pour décrire correctement la variation séculaire.

En conclusion, l'approche VO-ESD présentée est validée avec des données synthétiques et pour un groupe de paramètres définis. De nos premiers résultats, l'utilisation des deux premiers mois de mesures Swarm ne semble pas adéquate pour une utilisation de l'approche des observatoires virtuels. Son application à des mesures Swarm révèle un comportement similaire entre les séries temporelles VO contiguës comme on le voit à la surface. Les séries temporelles des VO obtenues sont également similaires entre un VO et l'observatoire magnétique correspondant. Les modèles globaux faisant usage de (presque) toute la série temporelle VO-ESD sont comparables à CHAOS-5 jusqu'au degré 14 pour le champ principal. Pour un paramétrage simple, le modèle

est capable de décrire l'évolution du champ magnétique à la fois à l'altitude de satellite et à la surface de la Terre.

Néanmoins des modélisations plus complexes pourront être développées pour tirer pleinement profit des séries temporelles VO-ESD. Par exemple, une représentation par des splines temporelles cubiques peut être appliquée pour décrire la variation temporelle du champ principal à une échelle plus locale, mais aussi globale (même si cette approche ne pourra être utilisée qu'avec un intervalle de temps plus long). La description des champs externes peut aussi être repensée. Une sélection des données peut être faite pour les mesures satellitaires avant l'application de l'approche VO-ESD. Ceci est important, spécialement pour les régions polaires où le champ magnétique a de grandes contributions des courants électriques externes. L'approche VO-ESD pourra montrer des résultats plus intéressants pour une série temporelle plus longue de données satellitaires, avec les mesures Swarm à venir, mais aussi en réexaminant les mesures de Ørsted et de CHAMP. La variation séculaire serait mieux contrainte dans les modèles globaux du champ et des séries temporelles de la variation séculaire pourrait alors être comparée avec celles des observatoires à la surface. Une meilleure contrainte de la variation séculaire à la surface pourra aider les études sur la dynamo terrestre.

Mots clefs: Champ magnétique terrestre, modelisation du champ magnétique, mesures satellitaires, Mission Swarm, observatoires virtuels, sources dipolaires équivalentes.

Contents

Abstract **v**

Resumé **vii**

List of Tables **xxv**

List of Figures **xxvii**

List of Acronyms **xxxix**

List of Symbols **xli**

1 The Earth's magnetic field **1**

1.1 Introduction 1

1.2 History 4

1.3 An abundance of sources 10

1.4 Temporal variations of the field 14

1.5 Measuring the field at the surface 19

1.5.1 Magnetic observatories 20

1.5.2 Geomagnetic indices 24

1.5.3 Other measurements 26

1.6 Measuring the field at satellite altitude 26

1.6.1 Calibration, attitude and errors of satellite measurements 28

1.6.2 A parade of satellites 30

1.6.3 The Swarm Mission 35

2 Models of the Earth's magnetic field **41**

2.1 Spherical harmonic description of the potential field . . . 41

2.2 Representing the temporal variation of the field . . . 45

2.2.1 Main field . . . 45

2.2.2 External fields . . . 47

2.3 The effect of neglecting the external fields . . . 49

2.4 Core and crust contributions . . . 49

2.5 Modelling strategies of the geomagnetic field . . . 51

2.5.1 Sequential approach: CHAOS, GRIMM and others . . . 52

2.5.2 Other modelling approaches using SH . . . 55

2.5.3 Other approaches not using SH . . . 59

2.6 Building a field model: the case of IGRF . . . 61

2.6.1 The 12th-generation IGRF . . . 63

2.6.2 The LPG Nantes candidate models . . . 64

2.6.3 Evaluation of candidate models and the final IGRF-12 . . . 75

2.7 Motivation of this work . . . 78

3 The new VO-ESD approach **81**

3.1 Concept . . . 81

3.1.1 The "virtual observatories" approach . . . 81

3.1.2 The Equivalent Source Dipole technique . . . 83

3.1.3 Definition of the VO-ESD approach . . . 88

3.2 Comparing SV at ground and satellite altitudes . . . 89

3.3 Validation of the VO-ESD approach by application to synthetic data . . . 93

3.3.1 Synthetic data . . . 93

3.3.2 Input parameters . . . 93

3.3.3 Initial tests with a local dipole mesh . . . 96

3.3.3.1 Dipole mesh and VO volume definition . . . 96

3.3.3.2 Results: why it did not work . . . 96

3.3.4 Different approach with a hemispherical dipole mesh . . . 105

3.3.4.1 The new dipole mesh . . . 105

3.3.4.2 The new tests . . . 107
3.3.4.2.1 First automatic iteration selection criterion . . . 109
3.3.4.2.2 Cylindrical volume without noise, without secular variation . . . 110
3.3.4.2.3 Cylindrical volume without noise . . . 110
3.3.4.2.4 Cylindrical volume with noise . . . 111
3.3.4.2.5 Synthetic orbits without noise . . . 114
3.3.4.2.6 Synthetic orbits with noise . . . 116
3.3.4.2.7 Dependence with the number of points . . . 118
3.3.5 Discussion and conclusions of the validation tests . . . 123

4 Application of the VO-ESD approach to Swarm measurements 127

4.1 Data . . . 127
4.1.1 Observatory data . . . 127
4.1.2 Satellite data . . . 128
4.2 Iteration selection criterion . . . 129
4.3 Dependence on time interval . . . 131
4.4 Comparison with ground observatory time series . . . 138
4.4.1 Method . . . 138
4.4.2 Inversion results . . . 138
4.4.3 Statistical analysis . . . 145
4.4.4 Discussion . . . 151
4.5 A global mesh of virtual observatories . . . 152
4.5.1 Method . . . 152
4.5.2 Results . . . 154
4.6 Comparison with an SH model . . . 157
4.6.1 Method . . . 157
4.6.2 Comparison . . . 158
4.7 Discussion and conclusions of the application of the VO-ESD approach . . . 166

5 Global models using VO-ESD **169**

5.1 Parametrization and terminology of the models 169

5.2 Results 173

5.2.1 Statistics, spectra and comparison with an SH model 173

5.2.2 Fit to observatory monthly means 188

5.3 Discussion and conclusions 192

6 General conclusions and perspectives **195**

A Inverse problem **201**

B Appendix **205**

B.1 IGRF-12 205

B.2 Electrical conductivity of the Earth's mantle 226

C VO-ESD_1 and VO-ESD_6 models residuals **237**

Bibliography **245**

List of Tables

1.1 Satellite missions of relevance for main geomagnetic field studies. 31

2.1 Evolution of the IGRF, with each generation interval of validity and related references. 61

3.1 Intervals of values of the dipole mesh parameters. 96

3.2 Rms residuals between synthetic data and predictions of the selected iteration solution for each magnetic component and the field intensity over a 30-day period and for different VO volumes examples. See text for details. 122

3.3 Rms residuals between synthetic data and predictions of the selected iteration solution for each magnetic component and the field intensity over a 30-day period and for different examples of the number of points in the VO data volume. See text for details. 122

4.1 Ground magnetic observatories location and the correlation coefficient between their time series and the respective virtual observatory. 145

4.2 Linear secular variation (first time derivative for 1-year time interval, in $nT.yr^{-1}$) for the considered ground observatories monthly means time series (OMM) and respective VO-ESD predicted (VO) time series, and both at the ground (CH) and at satellite altitude (CHS) given by the CHAOS-5 model. 146

4.3 Location and reason of selection for the VOs compared in Sections 4.5 and 4.6. . 159

5.1 Model terminology, with associated parameters, number of vector ($<55^o$ absolute magnetic latitude) and scalar ($>55^o$) measurements, and associated rms residuals. 170

5.2 Linear secular variation (first time derivative, in nT.yr^{-1}) for the considered ground observatories monthly means time series (O(all)) and given by model VO-ESD_16.30-10-2 (M16) for the period 2013.9-2015.4; by CHAOS-5 model (CH) and for the observatory montly means (O(12)) for the year 2014 (cf. Table 4.2). 189

5.3 Core radius estimates (in km) given by the two expressions proposed by Langlais et al. (2014) and the VO-ESD_16.30-10-2, CHAOS-5 and IGRF-12 field models. 194

List of Figures

1.1 Predictions given by the IGRF-12 model (see Thébault et al. (2015b) on B.1) for the (a) field intensity (F) as of January 2015, (b) difference between January 2015 and January 2014 of the field intensity (dF/dt), (c) radial field (B_r) as of January 2015, (d) difference between January 2015 and January 2014 of the radial field (dB_r/dt) at the Earth's surface, (e) radial field (B_r) as of January 2015 and (f) the difference between January 2015 and January 2014 of the radial field (dB_r/dt) at the CMB. 3

1.2 Components of the geomagnetic field in a local Cartesian coordinate system, seen from northeast. An explanation of the variables is given in the text. From Olsen et al. (2007). 6

1.3 Reconstructed series of direct measurements of declination in Paris and London from the mid-16th century to 2000 (see Alexandrescu et al., 1997). Adapted from Courtillot and Le Mouël (2007). 8

1.4 Scheme of the Earth's magnetic field various sources. See the text for abbreviations. From Olsen and Stolle (2012). 11

1.5 The magnetic field strength of the internal field as a function of horizontal wavelength λ_n (*top axis*) and SH degree n (*bottom axis*), at (satellite altitude) 350 km, given by the field models CHAOS-4 (Olsen et al., 2014) for $n \leq 90$, MF7 (Maus, 2010b) for $90 < n \leq 133$, and NGDC-720 (Maus, 2010a) for $n > 133$. The grey curve is for the core field and the green one for the time change in one year. Amplitudes and spatial scales for various external fields are indicated by orange areas. The scale at the top is, for a satellite at 8 km s^{-1}, the time period τ that would correspond to the presented spatial scales. See the text for abbreviations and sections 2.1 and 2.4. From Olsen and Stolle (2012). 13

1.6 (*Top*) Dst and Ap geomagnetic indices, for the first months of 1989. (*Bottom*) Daily means of the X component relative to a mean level (X_0, the mean of the year 1989) as measured at the magnetic observatory of Chambon-la-Forêt (France), showing the magnetic storm of March 1989. 16

1.7 (*Left*) Monthly means and (*right*) first time derivative of monthly means (following eq. 1.8) for the three magnetic components as measured at the magnetic observatory of Chambon-la-Forêt (France) between 1960 and 2013. 17

1.8 First time derivative of the Y component of the magnetic field (following eq. 1.8) as measured at different ground magnetic observatories in Europe: CLF (France), DOU and MAB (Belgium), FUR and NGK (Germany), HAD, ESK and LER (UK), and BEL (Poland), for a ten years period. 18

1.9 Locations of ground-based magnetic observatories which are members of INTERMAGNET as of June 2015. 22

1.10 (*Left*) The path of a satellite at inclination i in orbit around the Earth. From Olsen et al. (2010). (*Right*) Ground track of 24h of the CHAMP satellite orbit on August 16, 2010 (*gray curves*). Highlighted is one orbit when the satellite starts close to the geographic North pole and flies southward during local nightime conditions (*blue*). After approximately 45 min, it reaches its closest approach to the geographic South pole and moves northward on the dayside (*red*). Dark yellow dots indicate the locations of ground-based magnetic observatories. Locations of the magnetic poles in 2010 are shown by the purple squares. Adapted from Olsen and Stolle (2012). 28

1.11 Ørsted (a), CHAMP (b) and Swarm (c) satellites. Credits: DRSI (now DTU Space); Astrium; ESA. 33

1.12 Orbit characteristics for Ørsted (*left*) and CHAMP (*right*) satellites in dependence of time. *Top:* mean altitude. *Bottom:* local time of ascending (*red*) and descending (*blue*) node. From Olsen et al. (2010). 34

1.13 A Swarm satellite and its instruments. Credit: ESA. 36

1.14 Swarm's ASM sensor (*left*) and optical bench (*right*). Credit: ESA. 38

1.15 Daily mean altitude of the three Swarm satellites from November 2013 to June 2015. 39

2.1 Schematic of a cubic B-spline basic functions, $M_l(t)$, $l = 1, ..., 10$, used to represent the time change of each Gauss coefficient. There are six interior knots and four exterior knots at each endpoint. From Olsen et al. (2006b). 46

2.2 (a) Spatial power spectrum of the geomagnetic field (in nT^2) for different models, at the Earth's surface. Figure from Olsen et al. (2007). (b) Spatial power spectrum of first time derivative (secular variation, solid curves, in $(nT.yr^{-1})^2$) and second time derivative (secular acceleration, dashed curves in $(nT.yr^{-1})^2$) of the geomagnetic field for various magnetic field models, at the Earth's surface. Figure from Olsen and Stolle (2012). 51

2.3 Histograms of the number of measurements from all geomagnetic times (*top panel*) and geomagnetic quiet-times (*bottom panel*) used to derive the CM5 model as a function of time. Note that both plots have the same scale and legend. A vector measurement counts as 3 measurements. This figure illustrates the great reduction of available data when strict data selection is applied. Figure from Sabaka et al. (2015). 57

2.4 First time derivative of the Y component of the magnetic field as measured (*in black*) at four european observatories: CLF (France), MAB (Belgium), FUR (Germany) and BEL (Poland), and the respective prediction by a global geomagnetic field model (*in blue*, Finlay et al. (2015)), for a time period of ten years. Note different SV scales although all intervals are of 30 nT. See the text for an explanation of the purpose of the grey dotted lines. 79

3.1 Example of the construction of a grid of virtual observatories by Olsen and Mandea (2007). Represented at each grid point (*black dots*) are the time series of the dZ/dt at 400 km altitude, for the time interval 2001–2005. Also shown are satellite data (*blue*), predicted values by the CHAOS model (*red*) and predicted values of the VO derived model (*green*), both for internal part only. 84

3.2 Geometry for one dipole point and one observation point in a spherical coordinate system (see text for details). Adapted from Dyment and Arkani-Hamed (1998). 85

3.3 Time series of the X, Y and Z magnetic components at the CLF observatory (*black*) and Swarm measurements within a cylinder centred at the CLF location (*blue*). 90

3.4 Time series of the magnetic field (*left*) and the first time derivative (*right*) for the X, Y and Z magnetic components at the CLF observatory (*black line*) and at satellite altitude (490 km, *blue dotted line*), as given by the CHAOS-4 model. Note that for the SV, the range scale for each magnetic component is the same both at the surface and at satellite altitude. 91

3.5 Magnitude of the horizontal vector gradient of SV for the X, Y and Z magnetic components (i.e., $\frac{\partial}{\partial t}|\bigtriangledown_h X|$, $\frac{\partial}{\partial t}|\bigtriangledown_h Y|$ and $\frac{\partial}{\partial t}|\bigtriangledown_h Z|$, at *top*, *middle* and *bottom*, respectively), at the Earth's surface and at epoch 2002.0, as given by the CHAOS-4 model truncated at SH degree 13. 92

3.6 Scheme of the VO-ESD approach application. The parameters needed to be defined are shown, as well as the mean altitude (*red line*) of the satellite measurements (*black lines*) and the centre of the VO volume (*red point*). 95

3.7 Synthetic data VO volume of $1^o \times 1^o \times$ 300 km, centred at 39.5^{o}N 8.5^{o}E. As an example, the horizontal east-west magnetic field component is plotted. 97

3.8 Example of four hexagonal dipole meshes with $d = 0.100^o$, and four different number of dipoles, $M = 7$, 37, 61 and 91. 97

3.9 Example of four hexagonal dipole meshes with $M = 19$ and four different mean distance between dipoles, $d = 0.050^o$, 0.100^o, 0.125^o and 0.150^o. 98

3.10 Example of the obtained rms residuals between synthetic data and predictions of each iteration by each magnetic component and the field intensity, (*left*) for all inversion iterations and (*right*) for a zoom around the last iterations, for the case of a dipole mesh with $M = 19$, $d = 0.125^o$ and placed at a depth of 4370 km. 99

3.11 As in Fig. 3.10, for a dipole mesh with $M = 37$, $d = 0.150^o$ and placed at a depth of 3670 km. 99

3.12 As in Fig. 3.10, for a dipole mesh with $M = 7$, $d = 0.150^o$ and placed at a depth of 3320 km. 100

3.13 As in Fig. 3.10, for a dipole mesh with $M = 61$, $d = 0.075^o$ and placed at a depth of 3070 km. 100

3.14 Rms residuals as a function of the number of dipoles for all cases tested. Note that the values for each case correspond to the last iteration solution. 101

3.15 Rms residuals as a function of the mean distance between dipoles within a dipole mesh, for all cases tested. Note that the values for each case correspond to the last iteration solution. 101

3.16 Rms residuals as a function of the number of dipoles (M) for four different dipole mesh cases: (*top left*) $d = 0.050^o$ and depth of 3070 km, (*top right*) $d = 0.075^o$ and depth of 3070 km, (*bottom left*) $d = 0.150^o$ and depth of 3070 km, and (*bottom right*) $d = 0.050^o$ and depth of 6320 km. 102

3.17 Rms residuals as a function of the depth at which the dipole mesh is placed. Three plots are zooms of the first one, focusing on different intervals of depth. . 103

3.18 Rms residuals as a function of the mean distance (d) between dipoles within the dipole mesh, for four different dipole mesh cases: (*top left*) $M = 7$ and depth of 6070 km, (*top right*) $M = 19$ and depth of 6270 km, (*bottom left*) $M = 37$ and depth of 4070 km, and (*bottom right*) $M = 61$ and depth of 3070 km. 104

3.19 (*Left*) Half of an icosahedral dipole mesh centred at the location of the ground magnetic observatory of Chambon-la-Forêt, France (CLF) for a latitudinal extend of 90^o (*top*) and 60^o (*bottom*). (*Right*) Rms residuals between synthetic data and predictions for each iteration for the field intensity over a 30-day period for a cubic grid of 500 points and for the two dipole meshes on the left. 106

3.20 Example of an hexagonal dipole mesh, with $M = 91$ and $d = 18^o$, centred at the location of the ground magnetic observatory of Chambon-la-Forêt, France (CLF). 107

3.21 Rms residuals between synthetic data and predictions of each iteration for each magnetic component and the field intensity, (*left*) for all inversion iterations and (*right*) for a zoom around the last iterations, over a 30-day period for a cubic data volume of 500 points centred at the location of the ground magnetic observatory of Chambon-la-Forêt, France (CLF). 108

3.22 Example of a 800 points VO volume cylinder centred at the location of the ground magnetic observatory of Chambon-la-Forêt, France (CLF), spanning a 30-day time period. 109

3.23 Rms residuals between synthetic data and predictions of each iteration for each magnetic component and the field intensity over a 30-day period and a cylindrical 800 points VO volume **without SV** and centred at CLF. The selected iteration solution is highlighted with a violet vertical dotted line. 110

3.24 Rms residuals between synthetic data and predictions of each iteration for each magnetic component and the field intensity over a 30-day period and for a cylindrical 800 points VO volume centred at CLF **without noise** added; (*left*) for all inversion iterations and (*right*) for a zoom around the selected iteration solution. The selected iteration solution is highlighted with a violet vertical dotted line. . 111

3.25 Predictions by the ESD technique (*red*) for the three magnetic components at the centre of the VO for each 30-day period and a cylindrical 800 points VO volume centred at CLF **without noise** added. Also showed are the predictions by a SH model at the middle of the time period (*blue*). The residuals between the model and the ESD predictions are also shown (*green*), with its axis on the right. 112

3.26 Rms residuals between synthetic data and predictions for iterations around the selected one, for each magnetic component and the field intensity over a 30-day period and a cylindrical 800 points VO volume centred at CLF. Presented are the cases (*top*) with **2 nT** white noise, (*middle*) **5 nT** white noise, and (*bottom*) **10 nT** white noise. The selected iteration solutions are highlighted with a violet vertical dotted line. 113

3.27 Predictions by the ESD technique (*red*) for the three magnetic components at the centre of the VO for each 30-day period and a cylindrical 800 points VO of synthetic data with 2 nT white noise added. Also showed are the predictions by an SH model at the middle of the time period (*blue*). The residuals between the model and the ESD predictions are also shown (*green*), with its axis on the right. 114

3.28 As in Fig. 3.27, for 5 nT white noise. 115

3.29 As in Fig. 3.27, for 10 nT white noise. 116

3.30 (*Top and middle*) Examples of Swarm orbits within a cylindrical VO volume for two different time periods of 1-month. (*Bottom*) Evolution of the altitude of Swarm orbits for the same VO cylindrical volume represented on top. The VO central position altitude (r_{vo} = 490 km) is outlined as a blue line and the satellite names are marked. 117

3.31 Rms residuals between synthetic data and predictions for (*left*) all inversion iterations and (*right*) for a zoom around the selected iteration solution, for each magnetic component and the field intensity for the case of **synthetic Swarm orbits without noise** within a VO volume centred at CLF. The selected iteration solution is highlighted with a violet vertical dotted line. 118

3.32 Predictions by the ESD technique (*red*) for the three magnetic components at the centre of the VO for each 30-day period and for the case of **synthetic Swarm orbits without noise** within a VO volume centred at CLF. Also shown are the predictions by an SH model at the middle of the time period (*blue*). The residuals between the model and the ESD predictions are also shown (*green*), with its axis on the right. Note the change of the right side axis interval for the Z component. 119

3.33 Same as Fig. 3.31, for a case with (*left*) **5 nT** and (*right*) **10 nT** noise added. . 119

3.34 As in Fig. 3.32, for a case with **5 nT** noise added. Note the change of the right side axis interval for the Z component. 120

3.35 As in Fig. 3.32, for a case with **10 nT** noise added. Note the change of the right side axis interval for the Z component. 121

3.36 Same as Fig. 3.24, for a case with 500 points. 121

4.1 Location of the eight ground magnetic observatories whose time series were used for comparison on this study. 128

4.2 Rms residuals between synthetic data and predictions as a function of the inversion solution iteration, around the final selected one. This example corresponds to the application of the VO-ESD approach to a VO centred at $\vartheta_{vo} = 21.25^o$, $\phi_{vo} = 54.67^o$ and for eighteen time periods with duration of 30 days. 130

4.3 Rms residuals between synthetic data and predictions per iteration (a zoom around the selected iteration), for the three magnetic components and the field intensity, for four different case examples of the time interval, T: (*top left*) case 1, (*top right*) case 2, (*bottom left*) case 3, (*bottom right*) case 4. These examples correspond to a period around 2014.5. See text for details. 132

4.4 Rms residuals between synthetic data and the prediction given by the selected iteration solution for the field intensity, as a function of time, for the four case examples for T. 132

4.5 Predictions by the VO-ESD approach (*red*) for the three magnetic components at the centre of the VO, and the predictions by an SH model at the mean time of the time period (*blue*) for different values of T: (*left*) case 1 and (*right*) case 2. For each magnetic component (each line) the y-axis are the same. 134

4.6 As in Fig. 4.5, for cases 3 (*left*) and 4 (*right*). 135

4.7 Differences between the predictions by an SH model and the VO-ESD approach at each mean time (predictions showed in Fig. 4.5), for different values of T: (*left*) case 1 and (*right*) case 2. 136

4.8 As in Fig. 4.7, for cases 3 (*left*) and 4 (*right*). 137

4.9 Rms residuals between all Swarm measurements and the ESD technique given by the selected iteration solution for the three magnetic components and field intensity, for the eight considered ground magnetic observatory locations at satellite altitude. 139

4.10 Residuals between Swarm measurements and the ESD technique for the three magnetic components and field intensity, at three VO, as a function of time. . . 140

4.11 Time series of the three magnetic components at LER and ESK ground magnetic observatory (*grey circles*) and corresponding VO given by the VO-ESD approach (*blue pluses*). Note that the difference between maximum and minimum in the y-axis is the same both at the ground and satellite altitude, for each magnetic component. 141

4.12 As in Fig. 4.11, for HAD and CLF ground observatories. 142

4.13 As in Fig. 4.11, for DOU and FUR ground observatories. 143

4.14 As in Fig. 4.11, for CZT and DRV ground observatories. 144

4.15 As in Figs. 4.11 to 4.14 but with the addition of linear fits to the time series, representing the computed linear secular variation, for LER and ESK ground observatories. 147

4.16 As in Fig. 4.15, for HAD and CLF ground observatories. 148

4.17 As in Fig. 4.15, for DOU and FUR ground observatories. 149

4.18 As in Fig. 4.15, for CZT and DRV ground observatories. 150

4.19 (*Top*) Global mesh of virtual observatories. (*Bottom*) Polar view of the northern hemisphere, with $30^o \leq \vartheta_{vo} \leq 90^o$. 153

4.20 Altitude for all VOs as a function of the latitude of the VO centre. 154

4.21 Rms residuals between Swarm mesurements and the ESD predictions given by the selected iteration solution for all 18 periods and all VOs as a function of the VO latitude. 156

4.22 VO-ESD predictions (*blue pluses*) with a cubic B-spline description (*blue lines*), and the CHAOS-5 predictions (*black dots*), for two VO located at: (*top*) $\vartheta_{vo} = -33.75^o$, $\phi_{vo} = 88.50^o$ and (*bottom*) $\vartheta_{vo} = 46.25^o$, $\phi_{vo} = 1.80^o$. 160

4.23 As in Fig. 4.22, for two nearby VO located at: (*top*) $\vartheta_{vo} = 6.25^o$, $\phi_{vo} = 6.25^o$ and (*bottom*) $\vartheta_{vo} = 6.25^o$, $\phi_{vo} = 8.75^o$. 161

4.24 As in Fig. 4.22, for two VO located at: (*top*) $\vartheta_{vo} = -73.75^o$, $\phi_{vo} = 136.10^o$ and (*bottom*) $\vartheta_{vo} = 88.75^o$, $\phi_{vo} = 225.00^o$. 162

4.25 As in Fig. 4.22, for two VO located at: (*top*) $\vartheta_{vo} = -31.25^o$, $\phi_{vo} = 332.42^o$ and (*bottom*) $\vartheta_{vo} = 31.25^o$, $\phi_{vo} = 123.39^o$. 163

4.26 As in Fig. 4.22, for two VO located at: (*top*) $\vartheta_{vo} = -36.25^o$, $\phi_{vo} = 26.15^o$ and (*bottom*) $\vartheta_{vo} = 8.75^o$, $\phi_{vo} = 66.71^o$, ... 164

4.27 As in Fig. 4.22, for two VO located at: (*top*) $\vartheta_{vo} = 6.25^o$, $\phi_{vo} = 66.25^o$ and (*bottom*) $\vartheta_{vo} = 1.25^o$, $\phi_{vo} = 66.25^o$. 165

5.1 Distribution of vector (*red*) and scalar (*blue*) measurements for three periods (2013.956, 2014.203 and 2015.369) of the VO-ESD time series, used as input data to the different models. 172

5.2 Magnetic energy spectra of the geomagnetic field at the Earth's surface, for all eighteen 1-period snapshot models, VO-ESD_1.TX, and for the CHAOS-5 model (for $n \leq 20$ and epoch 2014.70). 172

5.3 Magnetic energy spectra of the geomagnetic field at the Earth's surface, for all thirteen 6-period models, VO-ESD_6.TX, and for the CHAOS-5 model (for $n \leq 20$ and epoch 2014.70). 173

5.4 Magnetic energy spectra of the geomagnetic field at the Earth's surface, for the different computed models using 16 or 18 periods, and the CHAOS-5 model (for $n \leq 20$) at epoch 2014.70. Also shown are the differences between CHAOS-5 and the other models (for $n \leq 20$). Note that some curves do superimpose. . . . 174

5.5 Magnetic energy spectra of the first time derivative (secular variation) of the geomagnetic field at the Earth's surface, for the different computed models using 16 or 18 periods, and the CHAOS-5 model (for $n \leq 20$), at epoch 2014.7. Also shown are the differences between CHAOS-5 and the other models (for $n \leq 18$). Note that some curves do superimpose, like the differences for models VO-ESD_16, and the differences for models VO-ESD_18. 175

5.6 Residuals between the VO-ESD time series used as input data and the models (*top*) VO-ESD_1.T02 (epoch 2014.041) and (*bottom*) VO-ESD_1.T10 (epoch 2014.707). From (*top left*) to (*bottom right*), X, Y, Z, and F, respectively. . . . 176

5.7 Residuals between the VO-ESD time series used as input data and the models (*top*) VO-ESD_6.T01 (mean epoch 2014.16) and (*bottom*) VO-ESD_6.T10 (mean epoch 2014.92). Each value corresponds to the mean of the residuals during the six periods over a $5^o \times 2.5^o$ surface for vector and $10^o \times 2.5^o$ surface for scalar components. From (*top left*) to (*bottom right*), X, Y, Z, and F, respectively. . . 177

5.8 Residuals between the VO-ESD time series used as input data and the models (*top*) VO-ESD_18.30-18-3 and (*bottom*) VO-ESD_18.30-10-2 at epoch 2014.707. From (*top left*) to (*bottom right*), X, Y, Z, and F, respectively. 178

5.9 As in Fig. 5.8, for models (*top*) VO-ESD_16.30-10-2, (*middle*) VO-ESD_16.30-10-3 and (*bottom*) VO-ESD_16.30-10-5. 181

5.10 Absolute difference of Gauss coefficients between some computed models and the CHAOS-5 model for (*top*) $n \leq 20$ and (*bottom*) $n \leq 7$ at epoch 2014.70. Note that the green and brown curves are superimposed. 182

5.11 Absolute difference of Gauss coefficients between some computed models and the CHAOS-5 model for (*top*) $n \leq 10$ and (*bottom*) $n \leq 7$ at epoch 2014.70. Note that the red, green and brown curves are superimposed. 183

5.12 Difference at Earth's mean radius between CHAOS-5 and VO-ESD_16.30-10-2 models at epoch 2014.70 and truncated for $n \leq 20$. From (*top left*) to (*bottom right*), X, Y, Z, and F, respectively. 184

5.13 Same as Fig. 5.12 between CHAOS-5 and VO-ESD_16.30-10-5. 184

5.14 Same as Fig. 5.12 between CHAOS-5 and VO-ESD_18.30-10-2. 185

5.15 Magnetic field given by the differences of the g_1^0, h_1^1, g_5^0 and h_5^1 coefficients between CHAOS-5 and VO-ESD_16.30-10-2 at epoch 2014.70. From (*top left*) to (*bottom right*), X, Y, Z, and F, respectively. 185

5.16 Difference between models VO-ESD_6.T01 and VO-ESD_6.T13 at their mean time, corresponding to the variation of the field during one year. From (*top left*) to (*bottom right*), X, Y, Z, and F, respectively. 186

5.17 Diffference between models VO-ESD_6.T03 and VO-ESD_6.T09 at their mean time, corresponding to the difference during six periods of 30 days (approximately six months). From (*top left*) to (*bottom right*), X, Y, Z, and F, respectively. . . 186

5.18 Secular variation given by model VO-ESD_16.30-10-2 at epoch 2014.66, which corresponds to the epoch of the difference of Fig. 5.16. From (*top left*) to (*bottom right*), X, Y, Z, and F, respectively. 187

5.19 Vertical component (Z) of the (*left*) main field and (*right*) secular variation at the CMB as given by the VO-ESD_16.30-10-2 model at epoch 2014.70 and truncated at $n = 13$. From (*top left*) to (*bottom right*), X, Y, Z, and F, respectively. . . . 187

5.20 Observatory monthly means (*black dots and left axis*) and model CHAOS-5 (*black line and right axis*) and VO-ESD_16.30-10-2 (*green line and right axis*) at ground observatory locations (Table 5.2). Left and right axis have both the same scale range for each component and observatory. 190

C.1 Residuals between the VO-ESD time series used as input data and corresponding 1-period VO-ESD_1 model. For each model and from (*top left*) to (*bottom right*), X, Y, Z, and F, respectively. 238

C.2 Residuals between the VO-ESD time series used as input data and the VO-ESD_6 models. Each value corresponds to the mean of the residuals during the six periods over a $5^o \times 2.5^o$ surface for vector and $10^o \times 2.5^o$ surface for scalar components. For each model and from (*top left*) to (*bottom right*), X, Y, Z, and F, respectively. 241

List of Acronyms

ACC	Accelerometer
ASM	Absolute Scalar Magnetometer
BGS	British Geological Survey
C^3FM	Continous Covariant Constrained endpoints Field Model
CHAMP	Challenging Mini-Satellite Payload
CHAOS	CHAMP, Ørsted and SAC-C model of the Earth's magnetic field
CHUs	Camera Head Units
cgs	centimetre-–gram-–second system of units
CM	comprehensive modelling
CMB	Core Mantle Boundary
CNES	Centre National d'Études Spatiales
CRF	STR Common Reference Frame
CSC	Compact Spherical Coil (vector magnetometer)
DGRF	Definitive Geomagnetic Reference Field model
ESA	European Space Agency
ESD	Equivalent Source Dipoles technique
ESRIN	European Space Research Institute or Centre for Earth Observation of ESA
FAC	field aligned currents
GIN	Geomagnetic Information Node
GRIMM	GFZ REference Internal Magnetic Model
GFZ	Helmholtz-Centre Potsdam - German Research Centre for Geosciences
IAGA	International Association of Geomagnetism and Aeronomy
IGRF	International Geomagnetic Reference Field model
INTERMAGNET	INTErnational Real-time MAGnetic NETwork
IPGP	Institute de Physique du Globe de Paris
IRLS	Iteratively Reweighted Least-Squares
ISGI	International Service of Geomagnetic Indices
IUGG	International Union of Geodesy and Geophysics
IZMIRAN	Institute of Terrestrial Magnetism, the Ionosphere and Radio Propagation

LEO	low Earth orbit satellite
LP	Langmuir Probe
LPGN	Laboratoire de Planétologie et Géodynamique
MAGSAT	MAGnetic Field SATellite
MEME	Model of the Earth's Magnetic Environment
MF	main field
NASA	National Aeronautics and Space Administration
OGO	Orbiting Geophysical Observatories
OIFM	Ørsted initial field model
OVH	Overhauser Magnetometer
PEJ	polar electrojet
POMME	POtsdam Magnetic Model of the Earth
QD	Quasi-dipole coordinates
RC	Ring Current magnetic index
RMS	root mean square
SA	secular acceleration
SAA	Sout Atlantic Anomaly
SAC-C	Satellite de Aplicaciones Cientifico-C
SCARF	Satellite Constellation Application and Research Facility
SH	spherical harmonics
SI	International system of physical units
SIM	Star Imager
STR	Star TRacker
SV	secular variation
S/C	spacecraft related
TII	Thermal Ion Imager
VFM	Vector Field Magnetometer
VMD	Vector Magnetic Disturbance index
VO	Virtual Observatories
VO-ESD	VO and ESD combined approach
WDC	World Data Centre for geomagnetism

List of Symbols

Symbol	Unit	Denotation
t	s	time
τ	s	arbitrary time period
μ_0	N/A^2	permeability of vacuum
ϵ_0	F/m	permittivity of vacuum
$\mathbf{J}$	A/m^2	current density vector
$\mathbf{E}$	V/m	electrical field vector
$\mathbf{B}$	nT	magnetic induction vector
$\mathbf{m}$	Am^2	magnetic moment vector
r, R	km	arbitrary radius (from the centre of the Earth)
a	km	Earth's mean radius (6371.2 km)
θ	degree (^{o})	co-latitude
ϑ	degree (^{o})	latitude
ϕ	degree (^{o})	longitude
ϑ_{vo}	degree (^{o})	VO centre location latitude
ϕ_{vo}	degree (^{o})	VO centre location longitude
r	km	radius
r_{vo}	km	VO centre location radius
r_C	degree (^{o})	VO cylinder radius
σ_C	nT	residuals rms for a magnetic component C
ΔC	nT	residual for a magnetic component C
n	nT	degree of spherical harmonic representation
m	nT	order of spherical harmonic representation
λ_n	km	spatial wavelength for degree n
g_n^m, h_n^m	nT	Gauss SH coeficients of degree n and order m
$R_n(r)$	nT^2	Mauersberger-Lowes spectrum for SH degree n and at radius r

Symbol	Unit	Denotation
C		arbitrary magnetic component
X	nT	magnetic component pointing north (south-north)
Y	nT	magnetic component pointing east (west-east)
Z	nT	vertical magnetic component
I	degree (^{o})	inclination
D	degree (^{o})	declination
H	nT	horizontal magnetic component
F	nT	field intensity
B_r	nT	magnetic radial component (in spherical coordinates)
B_θ	nT	magnetic azimuthal component (in spherical coordinates)
B_ϕ	nT	magnetic polar component (in spherical coordinates)
d	degree (^{o})	mean distance between dipole within a dipole grid
Dst	nT	geomagnetic index (of the magnetospheric ring-current strenght)
Kp		global geomagnetic activity index
Υ		cost funtion
$\mathbf{r}$		radial direction vector
T		time interval of a VO volume data
N_m		maximum degree in an SH expansion
N		number of points within a VO volume
M		number of dipoles within a dipole grid
SD		standard deviation
$\mathbf{C}$		vector of measurements
$\delta\mathbf{c}$		column vector of residuals
$\mathbf{A}$		matrix of partial derivatives
$\mathbf{W}$		matrix of weights
$\mathbf{p}$		vector of parameters

Chapter 1

The Earth's magnetic field

1.1 Introduction

The Earth's magnetic field or geomagnetic field is neither an homogeneous nor a steady phenomenon. It varies in space and time, partly due to the interaction with solar wind but more importantly by its own generation processes. The geomagnetic field $\mathbf{B}$ is a vector (with direction and magnitude), with tesla as unit (1 T = 1 V s^{-1} m^{-2}) and can be approximated by a dipole whose axis is tilted about 10^o (9.7^o at epoch 2015.0 (Thébault et al., 2015b)) with respect to the spin axis of the Earth. The magnetic field points down toward the Earth's interior in most of the northern hemisphere and away from it in most of the southern hemisphere. The field is induced by electrical currents in the molten, electrically conducting Earth's outer core. These currents are maintained by fluid flow that is driven by thermal and compositional convection in the core. Above the core-mantle boundary (CMB) the magnitude of $\mathbf{B}$ decreases with $1/r^3$, where r is the radial distance. Other electrical current systems in the Earth's environment add contributions to the measured magnetic field. The field which has its source within the outer core is termed main field as it is by far the largest in magnitude (cf. Section 1.3). Figure 1.1 presents the main magnetic field at the Earth's surface as of January 2015, given by the IGRF-12 model (see Section 2.6). The morphology of the main field at Earth's surface is characterized by the inclined axial dipole. But important spatial features show up which an

inclined dipole cannot account for. Some of those features (Fig. 1.1) are the contrast between the relatively weak ($\sim$ 61,000 nT) northern maximum and the stronger ($\sim$ 66 700 nT) southern part, and the very weak ($\sim$ 22,300 nT) minimum localized in South Atlantic and known as South Atlantic Anomaly (SAA). This anomaly is thought to be linked to reversed flux patches on the CMB (Tarduno et al., 2015). The low intensity region of SAA represents a region with enhanced external currents activity at lower altitudes, which is a problem to low-orbit satellites or commercial flights (Heirtzler, 2002).

Figure 1.1 also shows a map of the change on the intensity field and the radial field during one year (at the Earth's surface). The radial field has increased in the Atlantic area and decreasing in the southeast Asian area, with absolute changes of up to 120 nT.yr^{-1}. The larger changes in the field intensity occur in North America, where the field decreases by 120 nT.yr^{-1}, and over the Indian Ocean, where it increases by 105 nT.yr^{-1}. One interesting fact is the relatively weak change throughout the Pacific and that an important increase occurs in the vicinity of the SAA, which has been slightly increasing in size and moving westward (Olson and Amit, 2006).

The geomagnetic field, being a very complex phenomenon with a multitude of sources, makes arduous the complete understanding of its physical processes. The study of the outer core's physical processes is hampered by its location and the impossibility of direct measurements. Thus the magnetic field measurements made at the Earth's surface, or at satellite altitude, are the main tools to sudy it. Furthermore, the main magnetic field at the core-mantle boundary lives in spatial scales smaller than the ones found at the surface (Fig. 1.1), because small-scales are attenuated in an insulating medium (Merrill et al., 1998). Knowing with detail the temporal variations of the main field at small scales is important to better constrain dynamo studies.

Numerical models of the geodynamo have been developed (Glatzmaier and Roberts, 1995; Christensen et al., 2010; Christensen and Wicht, 2007). They intend to mimic the magnetic field generation and maintenance and from that unveil the physical processes responsible for it. The inverse problem of solving for the flow at the core-mantle boundary from time series of secular variation is also employed to infer the physical behaviour of the core magnetic field (Holme,

2007). The knowledge of the temporal variation of the magnetic field at all scales, temporal and spatial is very important in order to infer adequately the core flow.

The outline of the manuscript is as follows. First, important notions on geomagnetism are given. Second, the existing modelling approaches of the Earth's magnetic field are present. From this, one part of the work developed during this thesis is addressed. It corresponds to the submission of geomagnetic field candidate models for the twelfth generation of the IGRF.

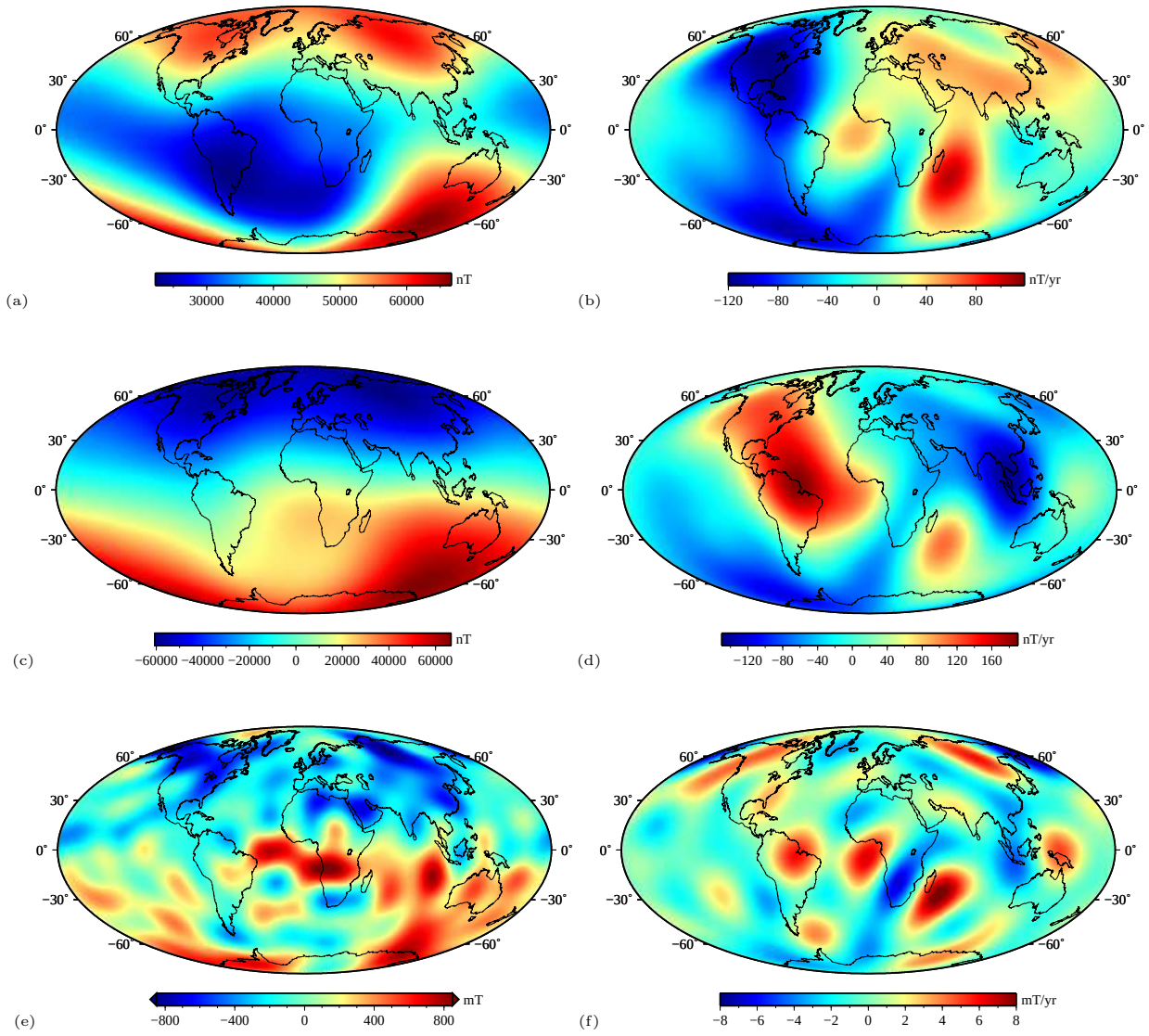

Figure 1.1: Predictions given by the IGRF-12 model (see Thébault et al. (2015b) on B.1) for the (a) field intensity (F) as of January 2015, (b) difference between January 2015 and January 2014 of the field intensity (dF/dt), (c) radial field (B_r) as of January 2015, (d) difference between January 2015 and January 2014 of the radial field (dB_r/dt) at the Earth's surface, (e) radial field (B_r) as of January 2015 and (f) the difference between January 2015 and January 2014 of the radial field (dB_r/dt) at the CMB.

The resulting scientific paper is presented. Third, the theory and validation using synthetic data of the modelling approach developed during this thesis are presented. Finally, the results from the first applications of the developed technique to Swarm data are presented, followed by some conclusions and a list of open questions worthy an immense future work.

1.2 History

The knowledge of the existence of magnetic forces in stones, through their tendency to attract iron, has been known for long, having first been noted in China. The attractive force of natural magnets (lodestone or loadstone) is referred in a number of Greek manuscripts, were the magnets are referred to mostly as the rock of Magnesia (the name of a place either in Macedonia, Crete or Asia Minor). The names magnetism as well as magnetite (Fe_3O_4) were derived from the Greek word. The earliest observational description is attributed to the Greek philosopher Thales of Miletus (624-546 BC), latter transcribed by Aristoteles in his *De Anima* (On the soul), about two centuries later. The fact that magnets have the property to align in the north-south direction was discovered in ancient China. It may have been a Chinese scholar around the year 1000 who first placed a lodestone on a "boat" floating in water and observed that wherever and whenever one performed the experiment, the boat always rotated to face south (however some claims place this discovery as 1000 years earlier, Mitchell (1932)). The compass as an instrument was then first developed by the Chinese. From Alexandeer Neckman (1157-1217), a monk at St. Albans (England) we know that by the year 1187, magnetic needles were being mounted on pivots, free to rotate at will toward any horizontal direction, as modern compass (Mitchell, 1932). European navigators (like Vasco da Gama or Fernão de Magalhães) were able to voyage thanks to this instrument.

In 1269 Pierre Pélerin de Maricourt wrote a letter (*Epistola Petri Peregrini de Maricourt ad Sygerum de Foucacourt militem: De Magnete*, only printed as late as 1558) where he explained various properties of the magnets based on experiments. From all the properties described the most important are: the finding of the two magnetic poles, the determination of the polarity of

the poles and the forces between them, and that a magnetic pole cannot be isolated. The first European navigators assumed that the compass would always point exactly to the geographical north, which is not true. This discrepancy now well-known and referred as *declination* was generally recognized by the middle of the fifteenth century. In 1581, Robert Norman, a London instrument maker, reported in his publication *The Newe Attractive* the fact that the true direction of the field was not horizontal and that a compass needle would point downward, or dip. By his repeated experiments he found out that the dip angle, now known as *inclination*, was $71^o50'$ in London (Kono, 2007).

An introduction to the magnetic components may be done now. The Earth's magnetic field measured at a given point at the surface is traditionally described by its components on a "right-hand" local topocentric reference coordinate system. Figure 1.2 illustrates the nomenclature for a location on the northern hemisphere, where the total field points into the Earth. The field is resolved in horizontal (H) and vertical (Z) components with Z pointing downward along the local vertical. The horizontal component is resolved in the X component pointing to geographic north and in the Y component pointing to geographic east. Then the declination is given by

$$D = \tan^{-1}\left(\frac{Y}{X}\right), \tag{1.1}$$

and the inclination by

$$I = \tan^{-1}\left(\frac{Z}{H}\right), \tag{1.2}$$

where the horizontal intensity (H) is just

$$H = \sqrt{X^2 + Y^2}. \tag{1.3}$$

The total intensity of the field, denoted F, is obviously

$$F = \sqrt{X^2 + Y^2 + Z^2}. \tag{1.4}$$

The horizontal components X and Y can be obtained by

$$X = H\cos(D) \tag{1.5}$$

$$Y = H\sin(D). \tag{1.6}$$

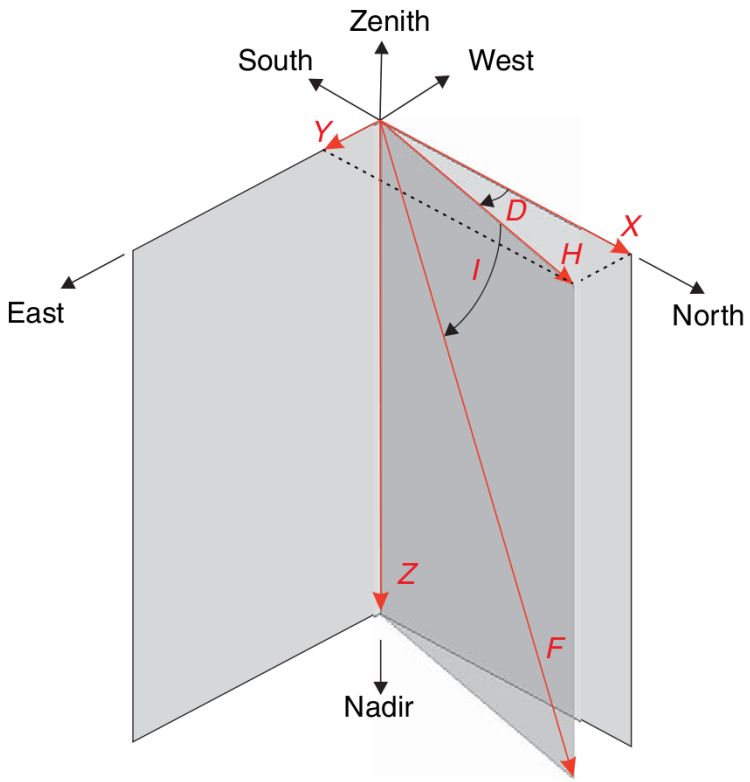

Figure 1.2: Components of the geomagnetic field in a local Cartesian coordinate system, seen from northeast. An explanation of the variables is given in the text. From Olsen et al. (2007).

In 1600 William Gilbert (1540-1603), chief physician to Queen Elizabeth I and president of the Royal College of Physicians published *De Magnete*, a book widely regarded as the first scientific text (being entirely free from appeals to heavenly causes, common of that epoch) and that had a profound influence in Europe. Gilbert founded the science of electricity by the description of his experiments in *De Magnete*. His most important contributions are as follows: magnets and iron are the same (considered different kinds of matter at the time); the similarity of the spherical magnet and the Earth, from which his famous conclusion arose "The Earth is a great magnet"; and that inclination is determined by the magnetic latitude. Many of the findings of Pierre Pélerin de Maricourt are usually attributed to William Gilbert, as some

points/findings in *De Magnete* are also described in *Epistola*. However, Gilbert did not refer to Pélerin in his descriptions. That added to the popularity of Gilbert may have caused the neglect of Pélerin's contribution. Nevertheless, some Gilbert's conclusions are different from Pélerin's: the latter found a correspondence between the spherical magnet and the celestial globe; Gilbert, on the other hand, concluded that it is the same as the Earth, or the Earth is a spherical magnet (Kono, 2007).

Some years after (between 1602 and 1604) Guillaume Le Nautonier publishes *Mecometrie de l'eymant*, work that after being cited by some authors in the following years, disappears from the historic works until been recognized by Mandea and Mayaud (2004). In it Le Nautonier introduces an equivalent notion of the magnetic dipole (later defined by Gauss as the main source of the geomagnetic field) whose axis is not the same as the one of the Earth's rotation. This thesis is contrary to Gilbert's, for who geographical and magnetic rotation axes were the same. While Gilbert points out the idea of magnetised regions at the Earth's surface as the sources of the declination irregularities stating that declination is a local phenomenon, Le Nautonier follows the idea that declination is a global phenomenon. From this assumption he derives in the *Mecometrie de l'eymant*, a technique to calculate the longitude from the knowledge of the latitude and declination. He publishes tables of declination per degree of latitude and longitude. However, he ignored that the magnetic field is far more complex than a dipolar field and his tables were latter proved to be wrong.

In 1624, Edmund Gunter (1581-1626), professor of astronomy at Gresham College, collected observation that strongly pointed to a temporal variation of the declination. Henry Gellibrand (1597-1636), Grunter's successor at Gresham, completed the study and published the discovery of secular variation (temporal changes in the main field) in 1635. The fact that the Earth's magnetic field changes in time had important consequences to navigation and orientation, bringing new scientific questions. Soon, effort was put into magnetic data collection in order to observe the nature and source of changes of the magnetic phenomena. Historical series of D and I have been recently gathered (see Fig. 1.3) and illustrate the variability of the magnetic field over decadal timescales (Courtillot and Le Mouël, 2007).

George Graham, a London clock maker, observed short-term variations on the declination. Anders Celsius and Olof Hjorter, after performing experiments in Uppsala (Sweden) in 1740-47, confirmed Graham's results and found out that the activity of the northern lights was accompanied by a large change in declination. Magnetic storms and solar quiet-day variations were discovered.

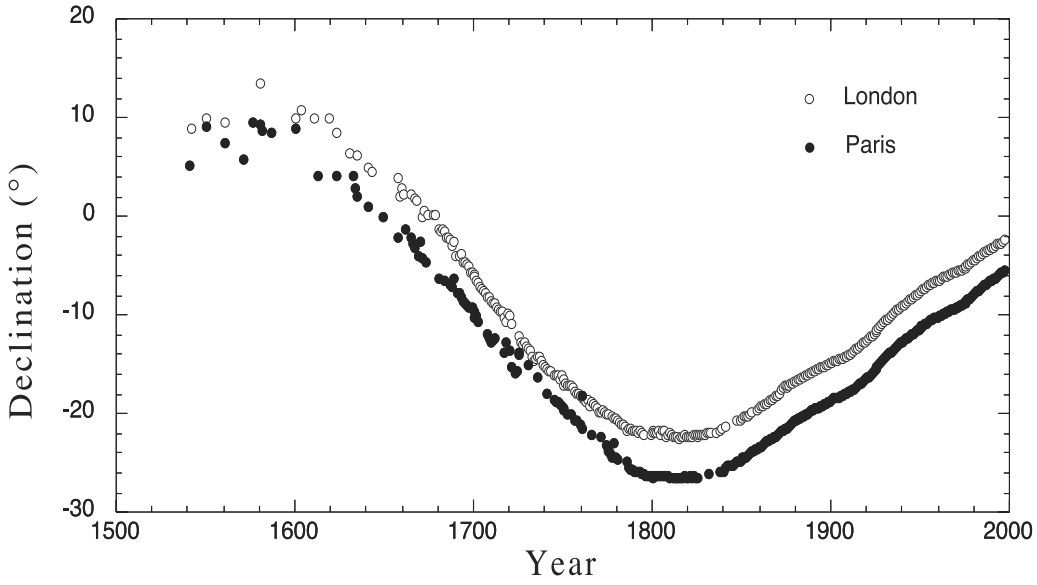

Figure 1.3: Reconstructed series of direct measurements of declination in Paris and London from the mid-16th century to 2000 (see Alexandrescu et al., 1997). Adapted from Courtillot and Le Mouël (2007).

At the end of the 17th century Edmund Halley (1656-1742) organized an expedition devoted to the determination of the declination in various parts of the Atlantic. From his measurements he publishes in 1701 (*General Chart of the Variation of the Compass*) the first isogonic map (map with lines of equal declination) of the Atlantic, which become a classic. By 1683, Halley produced a model for the field temporal and spatial variations in terms of dipoles moving generally westward deep within the Earth. He considered an Earth with two concentric shells, possibly separated by a fluid, each magnetised but with offset dipolar axis. A relative rotation between the two spheres would originate a westward drift of some parts of the observed magnetic field (cf. Section 1.4). The westward drift of small-scale features of the geomagnetic field is an important proxy for the fluid motions in the outer core (cf. Section 1.3).

Karl Friedrich Gauss (1777-1855), a German mathematician and geomagnetist, obtained a modern description of the main geomagnetic field. He completed the idea of the magnetic field as a vector by defining and determining its strength for the first time in 1832. This permitted the calibration of measurements in all magnetic observatories, which led Gauss and colleagues to establish a worldwide system of magnetic observatories, some of which have been running continuously till today. It was he who proposed the use of spherical harmonics to describe the potential field (see Section 2.1) and deduced from its application that the main source of the measured magnetic field is within the solid Earth, not outside, with the dipole ($n = 1$) being the dominant term. Although today the SI unit for magnetic induction is the tesla (T, named after the Serbian American electrical engineer Nikola Tesla, 1856-1943), the cgs unit is named after Gauss, where 1 tesla = 10^4 gauss. The tesla is an inconvenient size for geomagnetism, usually the field intensity being referred in nanotesla (1 nT = 10^{-9}T) or microtesla (1 μT = 10^{-6}T).

In the 20th century, the study of magnetised rocks in different points on the globe led to the discovery that, more than wander of its position in time, the magnetic field's dipole reversed its polarity hundreds of times during the Earth's geological history. Today there is no doubt that most rocks containing magnetic minerals (igneous or sedimentary) can record information on the magnetic field at the time of their formation. By 1963, it was conclusively demonstrated that the field was reversed all over the globe during a number of well-defined epochs going back as 4 million years (Cox et al., 1963). It was also found that a record of the field's reversals is present on the seafloor rocks, which allowed an accurate chronology for the main field over the last 160 million years and had major implications to plate tectonic theory (Gee and Kent, 2007). From the analysis of polarity timescales, it was concluded that the reversal process is irregular and occurs without memory of the past (events occur independently from each other). The polarity timescale is a source of information about the nature of the geomagnetic field, as it provides a long record of the geomagnetic field behaviour. The dynamo polarity changes could represent the changes in the dynamo process (Kono, 2007).

The possibility to measure the geomagnetic field with high precision using satellites (since the sixties, see Section 1.6) brought new insights into the nature of the field's different contributions. It allowed unveiling the spatial and temporal variations of the crustal field (magnetised rocks),

the ionospheric and magnetospheric currents, the oceanic driven electric currents which also contribute to the measured magnetic field, or the Earth-Sun environment. The studies on core dynamics and mantle conductivity were also improved by satelite data as well as the fast development of higher quality magnetic field models (see Section 2.5).

1.3 An abundance of sources

The sources of the Earth's magnetic field differ in nature and location. The fields they produce also widely differ in magnitude and spatio-temporal behaviour. A voyage through those sources follows. Figure 1.4 presents a scheme of the various sources of the geomagnetic field and their separation into internal and external sources.

Surrounding the Earth, up to 10 or 20 Earth radii, is the region termed *magnetosphere*. Within the magnetosphere the solar wind does not blow and the magnetic field is mostly the one of a dipole, ranging from 10 nT to 60 μT. The boundary between this region and the solar wind, the *magnetopause*, is highly complex with a continuously shock wave being form (due to the high speed of the solar wind). The magnetosphere can be divided in different regions, like the *van Allen radiation belts* (named after the American space scientist responsible for the instrument that discover them, James Alfred van Allen, 1914-2006) where protons and electrons move spirally along magnetic lines and reflect back and forth from the high intensity field in the poles. The equatorial circulation of the system consists in the *ring current*, which generates part of the magnetic field measured at the surface (Baumjohann and Nakamura, 2007).

Between 50 km and 600 km or more above the Earth's surface lies the *ionosphere*, so named due to the presence of high densities of charged particles. The ionosphere itself is divided into layers: D, E and F. The differences between them are the different concentrations of specific particles and electrons (Baumjohann and Nakamura, 2007).

The sun's ultraviolet light ionizes the atoms of the upper atmosphere, thus the dayside hemisphere of the ionosphere is much more conducting than the nightside hemisphere. Strong electrical currents then drive in the sun side hemisphere, on a dynamo solar driven process.

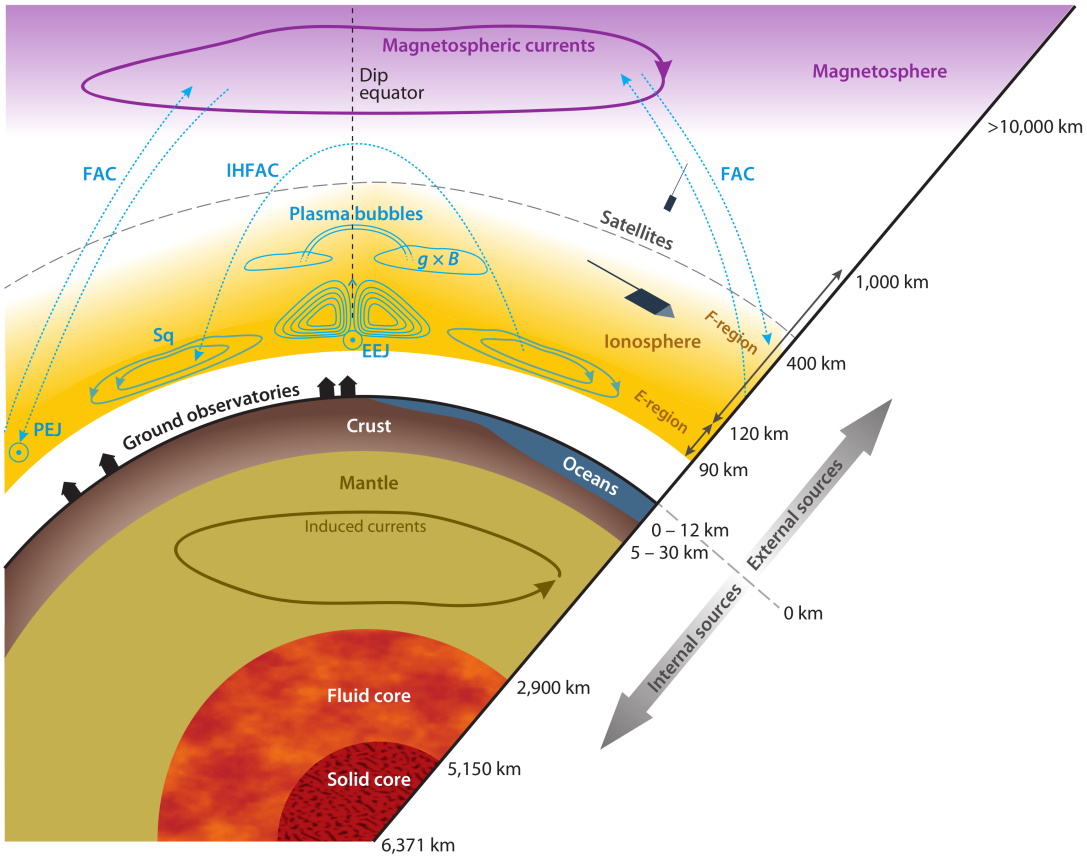

Figure 1.4: Scheme of the Earth's magnetic field various sources. See the text for abbreviations. From Olsen and Stolle (2012).

These currents generate a magnetic field up to 80 nT in intensity. As the currents pass following the sun once a day the measured magnetic field suffers a variation. These daily variations are called *quiet-solar variations* or Sq and depend mainly on local time. When deriving models of the internal field (see Section 2.5) one usually selects only nightside data to minimize the field contributions from the ionospheric region. During periods of higher solar perturbations, denoted magnetically disturbed, an additional variation is felt in the field and the daily variation is enhanced or even obscured by the more energetic magnetic activity. Other electrical sources contribute to the measured magnetic field. As the geomagnetic field is strictly horizontal at the dip equator (inclination equal to zero), there is an enhancement of the conductivity in the ionospheric dynamo region called *Equatorial electrojet* (EEJ), flowing along the dayside dip equator (Baumjohann and Nakamura, 2007).

Furthermore, complicated current systems flow in the Polar Regions. They are particular strong during times of enhanced solar perturbations but always present (Olsen and Stolle,

2012). The *auroral* or *polar electrojets* (PEJ) are horizontal electrical currents flowing in the E-region auroral belts ($\pm$ 65^o-70^o magnetic latitude). They vary widely in amplitude, from 100 nT during quiet periods to several thousand nT during major magnetic storms. The polar ionosphere is also dominated by the *field aligned currents* (FAC), electrical currents flowing along the field lines of the ambient magnetic field and that connect the ionosphere with the magnetosphere (Baumjohann and Nakamura, 2007). The FAC that connect one hemisphere to another are called *interhemispheric field aligned currents* (IHFAC). They were proposed by van Sabben (1966) and unambiguously detected by Olsen (1997) using satellite data.

Other currents exist in the ionosphere, like the plasma bubbles (see, e.g. Kelley, 2009), the meridional current system in the low latitude F-region (see e.g., Heelis, 2004) and others. Contributions in the ionospheric F-region are important even during local night time, when the ones from Sq and EEJ are absent. In fact, ionospheric and magnetospheric fields, which are referred as the external field, can be present even during night and/or magnetic quiet time, thus making it very difficult to separate their contribution with data selection (Olsen and Stolle, 2012).

On small spatial scales (say, less than 500 km) we find the one source that is not electrical: the lithospheric or crustal field due to magnetised rocks within the solid Earth. These rocks have been magnetised in the past (permanent magnetisation), but also bear an additional magnetisation proportional to the present ambient magnetic field (induced magnetisation). Clearly, such rocks can only be found in regions of the solid Earth, where the temperature is less than the Curie temperature of the minerals ultimately carrying the permanent magnetisation. This restricts magnetised rocks to lie in the uppermost layers of the Earth (Olsen et al., 2007). The crustal field's magnitude is weak on average, but it can vary substantially as a function of location, from fractions to thousands of nT. An example of a huge anomaly is the one called Bangui magnetic anomaly (centred in Bangui, Central African Republic, Africa), covering an area of 250 km and reaching an amplitude of 500 nT (Girdler et al., 1992). The spatial variability of the crustal field results in a spatial spectrum with fairly comparable contributions from all length scales at the Earth's surface (cf. Section 2.4).

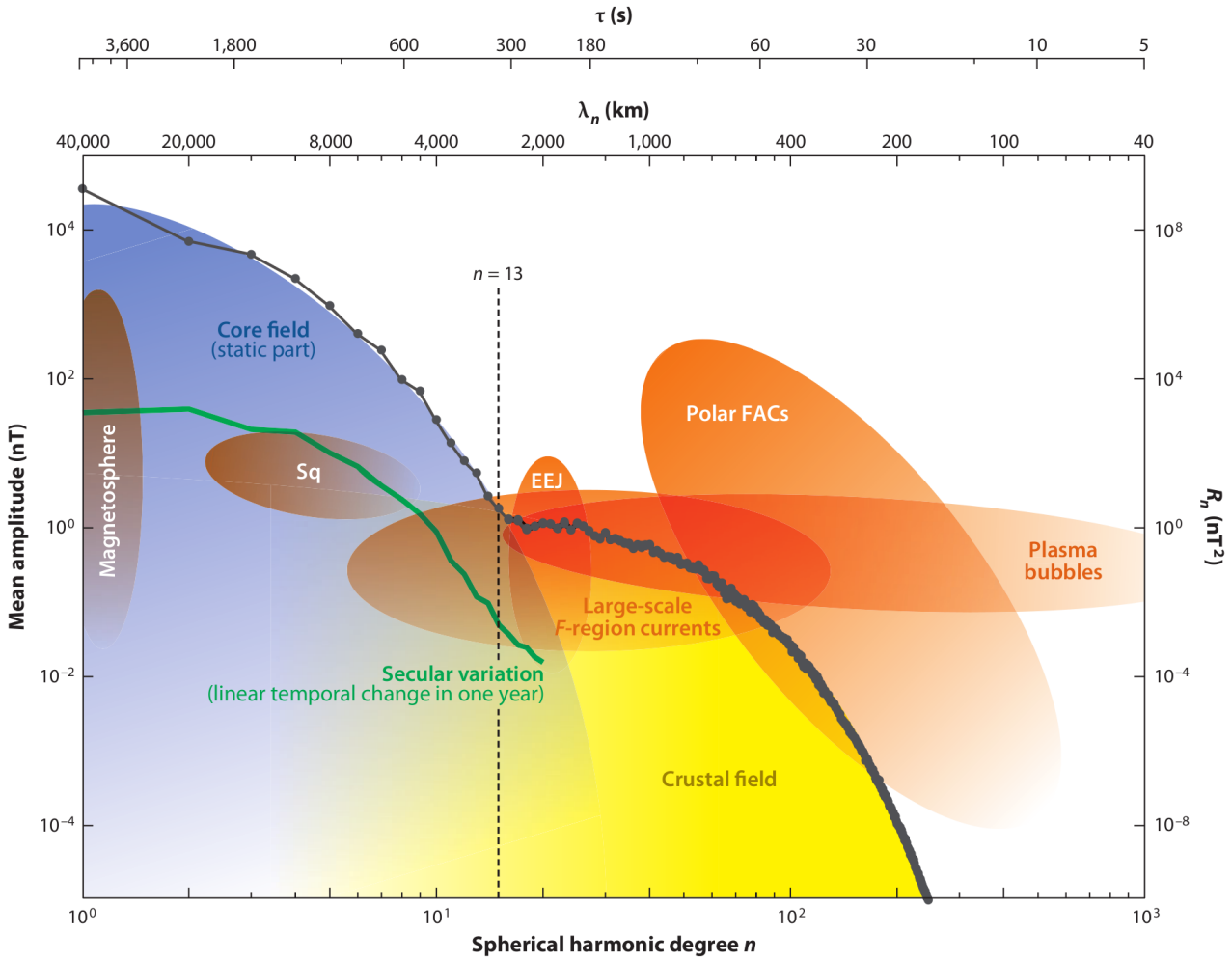

Figure 1.5: The magnetic field strength of the internal field as a function of horizontal wavelength λ_n (*top axis*) and SH degree n (*bottom axis*), at (satellite altitude) 350 km, given by the field models CHAOS-4 (Olsen et al., 2014) for $n \leq 90$, MF7 (Maus, 2010b) for $90 < n \leq 133$, and NGDC-720 (Maus, 2010a) for $n > 133$. The grey curve is for the core field and the green one for the time change in one year. Amplitudes and spatial scales for various external fields are indicated by orange areas. The scale at the top is, for a satellite at 8 km s^{-1}, the time period τ that would correspond to the presented spatial scales. See the text for abbreviations and sections 2.1 and 2.4. From Olsen and Stolle (2012).

By far the strongest field, of the order of 30,000 nT around the equator and 60,000 nT near the poles, is the one produced in the fluid outer core through a self-sustaining dynamo process, named the main field or core field. This field changes widely in time. As it changes in secular timescales its first derivative is historically referred as the secular variation (SV). Mainly dipolar, the main field also has significant multipolar terms. The magnetic contributions of the multipolar terms correspond to smaller spatial scales (and therefore higher degree spherical harmonics, see Sections 2.1 and 2.4). These contributions fall off faster with distance, leaving

the dipole dominant at the surface. The sum of the main with the crustal field is referred as the internal field, with the main field dominating at large scales and the crustal at scales on the order of less than 2000 km at the Earth's surface (cf. Section 2.4).

There are also electrical currents in the crust and mantle of the Earth. The electrical conductivity of rocks reacts with the main and external fields, resulting in the so-called induced currents, which produce the induced fields. The currents induced by the main field are hardly observed. By the other hand, externally induced currents can be observed and can reach magnitudes of a fraction of the external inducing fields. The oceans also provide with similar induced currents linked to the salt and tidal flows within the main field. Their contribution is small, of about a few nT at the Earth's surface (Olsen et al., 2007).

As a result of this abundance of sources, the measured magnetic field is then a superposition of fields of different spatial and temporal scales. The separation of all these sources is difficult and challenging. A large number of measurements taken at different times and locations is needed to properly separate the different geomagnetic field contributions and construct adequate geomagnetic field models.

1.4 Temporal variations of the field

The different timescales of the field are related to the different associated physical processes (Fig. 1.5). The smallest timescale is related with the daily, strong and rapidly varying magnetic field associated with the magnetic vector of the sun. This timescale of 10^{-15} s is much too short for ordinary interests in the main field studies. However, the sunspot cycle of 11-years causes a modulation of the magnetic field through the occurrence of magnetic storms on that time scale (Backus et al., 1996).

Around 1 Hz, sporadical oscillations of the magnetic field with an amplitude of a few nT occur. These are called *whistlers* and result from a lightning stroke located on the other side of the Earth close to the magnetic field line that passes through the observer; the lightning sets off

a wave that propagates through the ionosphere along a magnetic field line and disperses as it moves, so that high frequencies arrive first (Storey, 1953).

At periods of 1 to 300 s there are quasi-periodic global variations called *micropulsations*, that can last for several hours. Their amplitude could be up to a few nT. They are excitations by the solar wind of the resonances of the magnetosphere (Baumjohann and Nakamura, 2007).

Magnetic storms are fluctuations in the magnetic field, with periods of minutes to days. They are caused by complex interactions between intense fluxes of particles from the sun (during periods of high sunspot activity) travelling with the solar wind and the magnetosphere (Baumjohann and Nakamura, 2007). The magnetic storms are known for they specific register in magnetograms of the X component: after an initial and short (a few minutes) elevation, there is a sudden drop to a level below the mean value for the site, then a long (a few days) recovery phase brings the field to its normal level (see Fig. 1.6). As mentioned in the previous section the magnetic field varies with a daily period due to the magnetospheric currents.

All the referred variations are external in origin. These temporal variations can be used to provide information on the electrical properties of the Earth's crust and mantle, by the study of externally induced currents (Olsen, 1999; Kuvshinov and Olsen, 2006; Civet et al., 2015) (see Appendix B.2). On the other hand, the temporal variations of the main field can help to understand the physical processes within the core.

Time fluctuations in the source of the field itself (secular variation), cause variations on the yearly (or monthly) means of the magnetic field recorded at geomagnetic observatories (see Section 1.5.1) at a rate of a 10 to 100 nT per year (see Fig. 1.7). As a first approximation, the SV can be described as a set of linear changes over some years to some decades, with occurrences of abrupt changes for periods of some months, called *geomagnetic jerks*. This phenomenon was first recognized by Courtillot et al. (1978) by the observation of a quite sudden change (impulse) in the slope of the secular variation around the year 1970. Further studies and analyses placed the jerk in 1969. This has come to be known as the 1969's geomagnetic jerk, and it can be well seen in Fig. 1.7 on the first time derivative of the Y component. A jerk is characterized by a V-shaped curve of the secular variation, or equivalently as a step-like secular acceleration

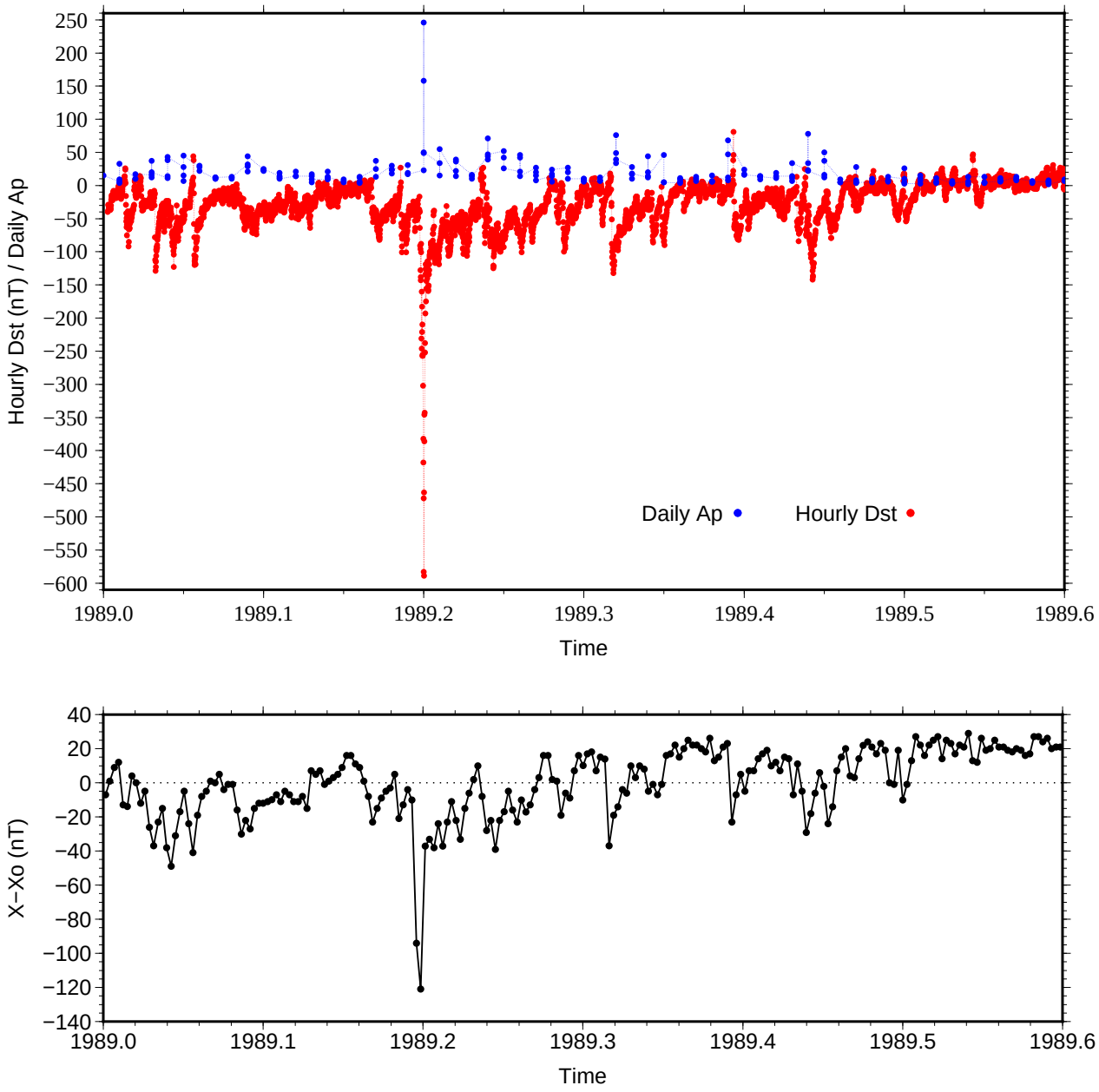

Figure 1.6: (*Top*) Dst and Ap geomagnetic indices, for the first months of 1989. (*Bottom*) Daily means of the X component relative to a mean level (X_0, the mean of the year 1989) as measured at the magnetic observatory of Chambon-la-Forêt (France), showing the magnetic storm of March 1989.

(i.e., the magnetic field's second time derivative) (Mandea et al., 2010). Initially, the origin of jerks was unclear, whether internal or external. The first studies pointed out an internal origin (Malin and Hodder, 1982), however the fact that some jerks are not observed on a global scale put some difficulties to this approach. Subsequent studies (Alexandrescu et al., 1995; Le Huy et al., 1998; Bloxham et al., 2002; Pinheiro and Jackson, 2008) established jerks as a

large-scale secular variation phenomenon, leading to a consensus on its internal origin. But, the reasons for the irregular occurrence in time and space or the dynamical origin of jerks are still under debate (Mandea et al., 2010).

The secular variation changes in space too. At regional scales, different magnetic observatories register different short-term temporal variations of the field. This can be seen in Fig. 1.8. Even if the general trend of the secular variation is similar, there are differences between nearby observatories, e.g., during 2002 in the BEL observatory (Poland) the field changed less than 2.5 nT.yr^{-1}, whereas in the FUR observatory (east Germany) it changed by approximately 20 nT.yr^{-1}.

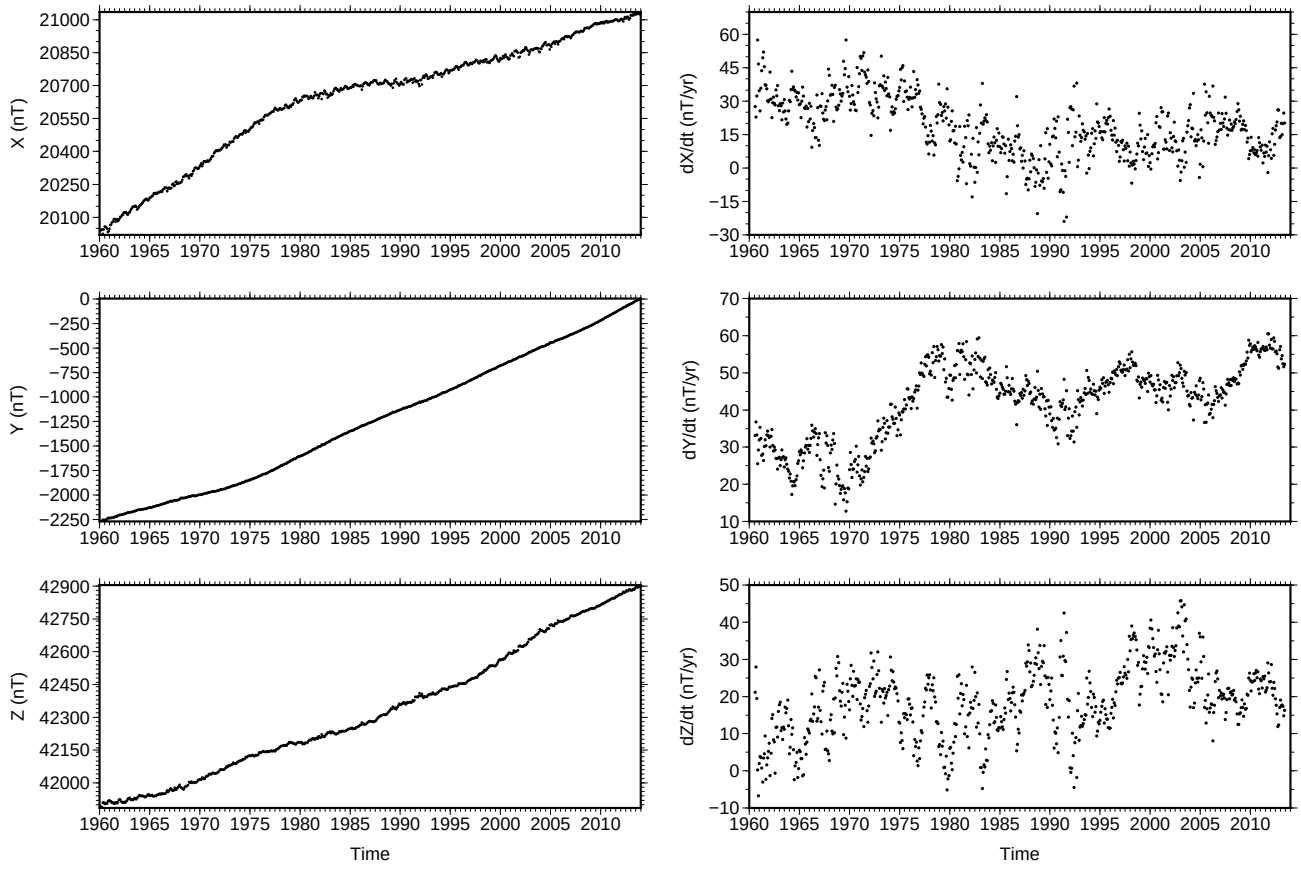

Figure 1.7: (*Left*) Monthly means and (*right*) first time derivative of monthly means (following eq. 1.8) for the three magnetic components as measured at the magnetic observatory of Chambon-la-Forêt (France) between 1960 and 2013.

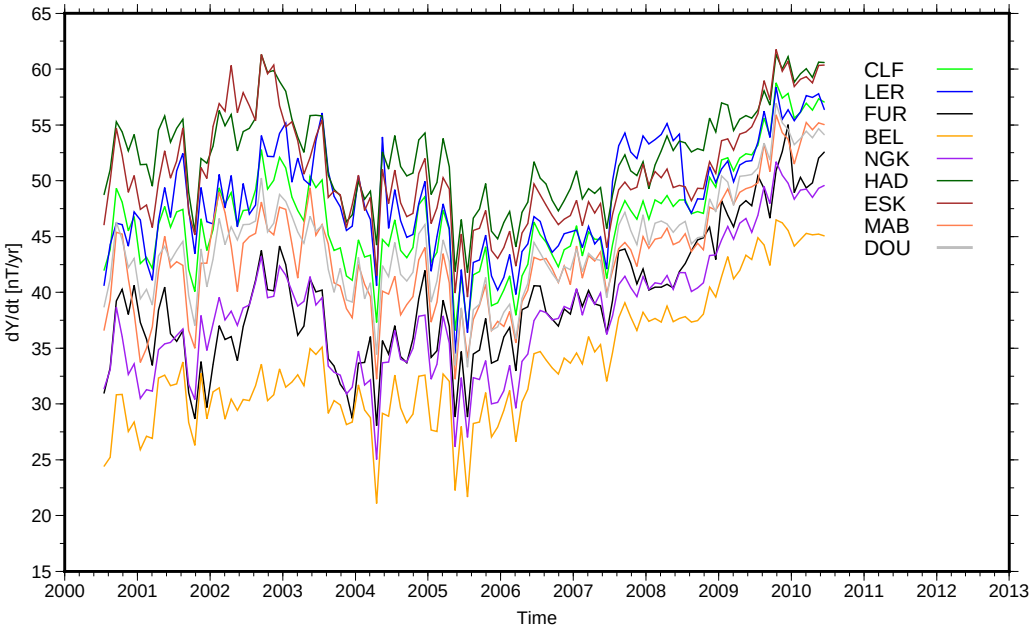

Figure 1.8: First time derivative of the Y component of the magnetic field (following eq. 1.8) as measured at different ground magnetic observatories in Europe: CLF (France), DOU and MAB (Belgium), FUR and NGK (Germany), HAD, ESK and LER (UK), and BEL (Poland), for a ten years period.

Another manifestation of the secular variation is that the local declination and inclination can change about 30^o or more during a time of 100 years or so (Fig. 1.3). These changes have amplitudes at the Earth's surface of the same size as the nondipole field, tens of nT. There is a tendency of the dipole to drift to the west (Amit and Olson, 2008). Non-dipole features have also been observed to drift westward, in what is known as *westward drift*. This phenomena was first noticed by Halley, who estimated a time period of 700 years to a drift of 360^o, i.e. $0.51^o.\text{yr}^{-1}$. However, this westward drift is not globally homogeneous. The actual timescale is about $0.15^o.\text{yr}^{-1}$ (Finlay and Jackson, 2003). Another question is if large features can cross the Pacific Ocean, a place where the secular variation is smaller in amplitude than in the Atlantic Ocean (Hulot et al., 2002). There are still many questions related to this drift of the main magnetic field, mostly for its physical source. Aubert et al. (2013) proposed that the westward drift is driven by gravitational locking of the mantle to the inner core.

The intensity of the dipole part of the geomagnetic field is currently rapidly decreasing. The

dipole moment vector (in A.m^2), is given by

$$\mathbf{m} = \frac{4\pi a^3}{\mu_0}\left(g_1^1\hat{\mathbf{x}} + h_1^1\hat{\mathbf{y}} + g_1^0\hat{\mathbf{z}}\right) \tag{1.7}$$

where a is the Earth's mean radius (6371.2 km), μ_0 is the permeability of vacuum, $\hat{\mathbf{x}}, \hat{\mathbf{y}}, \hat{\mathbf{z}}$ are Cartesian unit vectors with origin at the Earth's centre, and g_1^0 and (g_1^1, h_1^1) are respectively the axial and equatorial dipole Gauss coefficients (see Section 2.1). The strength of the dipole moment has been decreasing over the past 160 years by nearly 9% and by about 30% over the past 2,000 years according to historical and archeomagnetic measurements (the latter from remanent magnetisation measurements of pottery and other archeomagnetic materials) (Jackson et al., 2000; Olson and Amit, 2006; Korte et al., 2005, 2011).

The most dramatic variations of the dipole are polarity reversals. Paleomagnetic measurements of magnetised rocks and lavas point to timescales between 2,000 and 10,000 years for the transition of the dipole from one polarity to another (Kono, 2007). Not only has the dipole moment strength varied, but also the geomagnetic pole and the magnetic dip pole locations. Geomagnetic poles are the antipodal points of intersection between the tilted axis of a central inclined magnetic dipole and the sphere of $r = a$. The magnetic dip poles are defined as the points on the Earth's surface where the magnetic field inclination is vertical. These magnetic dip poles have been changing, both in the northern and southern hemispheres, in a not erratic way, constantly moving northward since 1900 (see e.g., Thébault et al. (2015b)) on Appendix B.1). The geomagnetic poles latitude has been recently (since 1965) changing poleward, after beeing nearly constant for more than a century, whereas its longitude has been changing westward since 1920 (Amit and Olson, 2008).

1.5 Measuring the field at the surface

There are many different kinds of geomagnetic field measurements, including those at the magnetic observatories at the surface of the Earth, aeromagnetic surveys at very low altitude or satellite measurements made higher above. Each type of measure is made with its own

purpose. It is through the combination of all different measurements that the knowledge of the magnetic field sources can be better achieved. Following is a description of the usage of ground magnetic observatories and other type of magnetic measurements at or close to the surface of the Earth.

1.5.1 Magnetic observatories

In 1834 Carl Gauss and Wilhelm Weber (1804–1891, a German physicist) established the Göttigen Magnetic Union (Magnetische Verein), with the objective of the establishment of an observatory network at sites around the world where the observation of the magnetic field would be made with regularity. The original set of observations provided the data for Gauss' first spherical harmonic analysis of the geomagnetic field (see section 2.1). Therefore it is only since 1840 that complete information of the field (direction and intensity) is continually measured at the Earth's surface. Many scientists participated in the idea of establishing a global network of magnetic observatories, such as Alexander von Humboldt (1769–1859, a Prussian geographer, naturalist, and explorer), who can be considered as a major driving force of this idea, by organizing observational voyages to distant locations and who especially attracted Gauss to magnetic problems, or Edward Sabine (1788–1883, an Irish soldier and natural scientist) who established a magnetic observatory in Canada and made a connection between the magnetic field variations and the sunspot cycle. The number of magnetic observatories gradually grew and their distribution increased toward the distribution of today (see Fig. 1.9), although some former observatories have closed for a multitude of reasons. For history of the grow of the magnetic observatories see Chapman and Bartels (1940).

The distribution of the observatories is mainly determined by the location of habitable land and local availability of expertise, funds, data transmission in infrastructures and energy supply. As a result ground-based magnetic observatories have an uneven spatial distribution on the globe and are sparse in the southern hemisphere and oceanic regions. The heterogeneous spatial distribution of the observatories limits the resolution and reability of field models, therefore it concerns the scientific community. Some projects aimed to place magnetic observatories at

sea. International collaboration programs exist with the purpose of installing observatories in new regions that are often economically fragile, by providing the instruments and the adequate technical assistance (Alexandrescu et al., 1994; Langel et al., 1995; Mochizuki et al., 1997; Turner et al., 2007; Korte et al., 2009).

Observatories are run worldwide by different institutes, whose interests range from geology, mapping, seismology, meteorology to solar-terrestrial physics and astronomy. These institutes have established strong networks of magnetic observatories. IAGA (International Association of Geomagnetism and Aeronomy) regularly organizes Workshops on Geomagnetic Observatory Instruments, Data Acquisition and Processing. To establish an international precision system of the magnetic observations (as each observatory had its own measure precision), the INTERMAGNET (INTErnational Real-time MAGnetic observatory NETwork)[1] was created (Fig. 1.9). This network groups all observatories who follow a strict precision criteria and are capable of delivering their measurements on near real-time. All data is grouped within five GIN (Geomagnetic Information Node): Edinburgh (UK), Golden (USA), Kyoto (Japan), Ottawa (Canada) and Paris (France). Minute and hourly magnetic measurements can be obtained from the site[2] of the WDC (World Data Centre for geomagnetism) of Edinburgh. The WDC are part of the ICSU (International Council for Science) World Data Centre System and ensure the long-term availability of the geomagnetic data for research and educational purposes. Although data checks have been made to previous data and feedback is provided by users, the WDC is ultimately a depository. So, the quality of the data varies and the data should be used carefully.

Important products derived from the continuous monitoring of the observatories are the so-called daily, monthly or annual means representing the daily, monthly or annual averaged values of the geomagnetic components (Reay et al., 2011). The current definition of annual mean is a mean over all data, however there was in the past some variability in exactly what was reported as an annual mean. Occasionally data reported to only the five quietest days of every month (the five days where the magnetic solar activity was smallest) (Jackson and

[1] `www.intermagnet.org`
[2] `http://www.wdc.bgs.ac.uk/catalog/master.html`

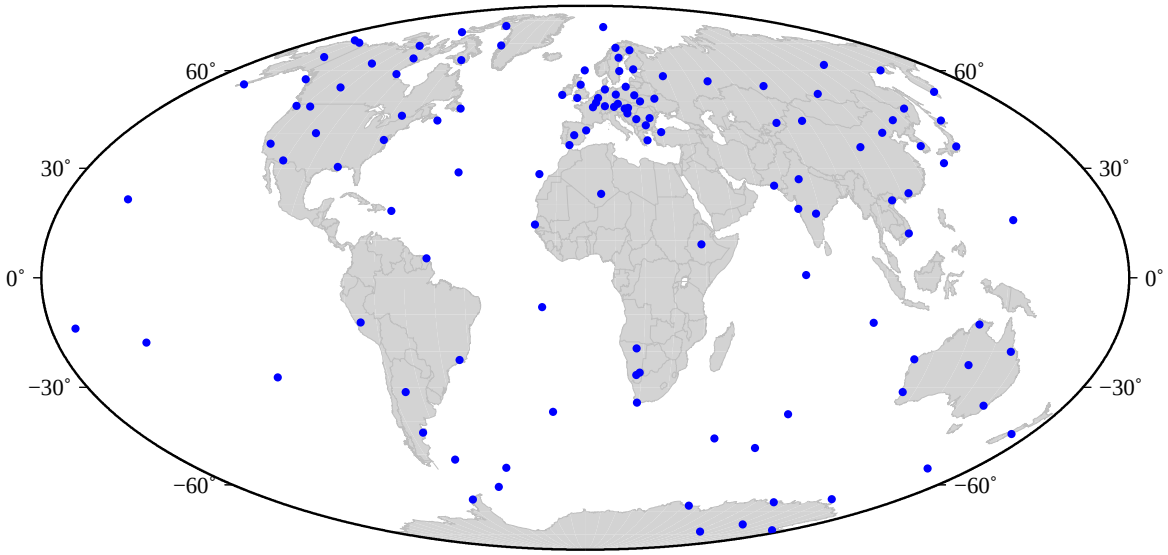

Figure 1.9: Locations of ground-based magnetic observatories which are members of INTERMAGNET as of June 2015.

Finlay, 2007). So, compromises are required in treating historical data.

The INTERMAGNET observatories deliver one-minute values of the three components of the geomagnetic field (X, Y and Z). The vector magnetometer used in the magnetic measurements, usually drift in time due to several factors like temperature variations or ageing of the electronics. Thus a periodic recalibration should be provided. Sometimes a correction is also needed for the tilt of the pillar on which the magnetometer is mounted. For the periodic recalibration, absolute measurements are performed on a regular basis (usually once in a week). These measurements should be made by a trained observer using a single-axis fluxgate magnetometer mounted onto a non-magnetic theodolite and a scalar magnetometer (see e.g., Jankowski and Sucksdorff, 1996). The absolute measurements define a baseline used to calculate a calibration curve. INTERMAGNET observatories deliver two types of data: preliminary data, available in quasi-real time (less than 72 hours); and a definitive data, which is produced some months later at the end of the civil year and accounts for baseline variations. The preliminary data may have no baseline corrections applied, making then only adequate to studies of rapid variations, mostly of external origin.

Observatory data reveal the field's changes on a wide range of time scales, from seconds to

centuries. This is important to the understanding of the physical processes within and outside the Earth. Observatory measurements are critical in time-dependent field modelling (Matzka et al., 2010). Indeed, the accuracy of many of the modern field models relies on observatory time series. The processing of satellite data often initially involves a data selection on the basis of the data obtained by ground observatories, usually by the use of geomagnetic indices (see below). Furthermore, observatory data can be also used in the derivation and validation of satellite derived products like the L2 products derived from Swarm measurements (see Section 1.6.3 and Ridley and Macmillan (2014)).

There is however a limitation with observatory magnetic data. Each observatory is subject to a quasi-constant field associated with the magnetised crust in the region it is located. This is called observatory bias. If observatory data is mixed with other magnetic data (survey, satellite), this bias must be accounted for, otherwise it will alter the solution for the main field because each observatory records its own bias. To solve this, some approaches have been developed. The first, introduced by Langel et al. (1982) is to solve for the observatory biases (three per observatory, in the X, Y and Z directions) as unknowns at the same time as solving for the magnetic field. This technique is still used today, for e.g., in the comprehensive series of models (see Section 2.5). A second one is to subtract the bias from the observatory data (see e.g., Bloxham and Jackson, 1992). One way to do it is to subtract a computed value of crustal biases for each component at each observatory. Other way is to work with the rate of change (first time derivative) of the field given by the observatory (e.g., the C^{3}FM model, see Section 2.5). To compute the first time derivative of a magnetic component one proceeds as follows. For example, for monthly means of the eastward component (Y):

$$\left.\frac{dY}{dt}\right|_{t_i} = Y(t_i + 6) - Y(t_i - 6), \tag{1.8}$$

where t_i denotes a particular month. On the same way, one can compute the first time derivative from annual means, as

$$\left.\frac{dY}{dt}\right|_{t_i+1/2} = Y(t_i) - Y(t_i - 1), \tag{1.9}$$

where t_i is here in years. This calculation approach is known as n step filter (Box and Jenkins,

1976). It eliminates the crustal biases because its signals should be the same for both dates t_i, $t_i - n$ and therefore cancel. Furthermore, the amplitude of even irregular annual and semi-annual variations are filtered out (Wardinski and Lesur, 2012). To compute the crustal biases a comparison is made between the mean value of the field of the observatory and the value given by a previous model based only on quiet time high quality satellite data (Langlais and Mandea, 2000). The different approaches do not have a noticeable difference on their results (Jackson and Finlay, 2007).

Recently the scientific community dedicated to global field modelling demanded for baseline corrected observatory magnetic data released on a shorter time scale (Peltier and Chulliat, 2010). The one year delay of definitive data contrasts with the rapidly available calibrated data from satellite missions, as Ørsted, CHAMP and the recent Swarm mission (see Section 1.6.3). To address this need a new data product, the quasi-definitive, was recently proposed and developed by INTERMAGNET and its distribution started some time before the launch of the Swarm mission. This data will enhance the calculation of Level 2 products (field models of the various field sources) of the Swarm mission (Friis-Christensen et al., 2006), and also improve the quality of quick-look versions of geomagnetic indices such as the Dst (Macmillan and Olsen, 2013). The quasi-definitive data are intended to be within the 5 nT of the final definitive data and are required to be submitted within 3 months of collection. This initiative started in 2011 and by April 2013 47 observatories were submitting quasi-definitive data (Macmillan and Olsen, 2013).

1.5.2 Geomagnetic indices

Ground based magnetic observatories observations are also used to the derivation of geomagnetic indices. Geomagnetic indices characterize the contributions from the ionospheric and magnetospheric field sources, i.e., they are a measure of the disturbances of geomagnetic activity, which is a signature of the response of the magnetosphere and ionosphere to solar wind forcing. For a detailed description of the various indices see for e.g., Mayaud (1980); Menvielle et al. (2011). IAGA officially supports, through the International Service of Geomagnetic In-

dices, ISGI[3], a number of indices. They are today a fundamental parameter in solar terrestrial studies and also on the satellite data selection and external field parametrizations in magnetic field models. Two indices typically used in geomagnetic field models are the Kp and the Dst (cf. Fig. 1.6).

Kp is an index of global geomagnetic activity computed every 3 h UT. It aims at describing the irregular disturbances of the geomagnetic field caused by solar particle radiation within the 3 h interval. Kp is currently derived from 13 subauroral magnetic observatories. After subtract the regular daily variation (defined a priori as the mean daily variation of the 5 quietest days of each month), the difference between the highest and the lowest values during the 3 h interval for the most disturbed horizontal magnetic component is computed. Then, the difference is converted to a K value, i.e., it takes values between 0 (quietest) and 9 (most disturbed) on a quasi-logarithmic scale. The local value (of each observatory) is converted to a standardized value, given in a scale of thirds (0^0, 0^+, 1^-, 1^0, 1^+,..., 8^+, 9^-, 9^0). Hence, Kp is the planetary mean of the 13 observatory values. For geomagnetic modelling the data selection criteria is often Kp$\leq 2^0$, which corresponds (depending of the solar activity of the year) to about 50 % of the data. The daily mean of the eight Kp values is denoted Ap.

Dst is a measure of the magnetospheric ring-current strength. It is determined on a hourly basis from the H component of the four low-latitude observatories Honolulu (Hawai,USA), San Juan (Puerto Rico), Kakioka (Japan) and Hermanus (South Africa). For each observatory a baseline is computed from annual mean values of H, calculated from the five quietest day of each month. This baseline, computed at the end of each calendar year is subtracted from the value of H, as well as the regular daily variation. This method is subjective as it depends on the chosen baseline, which changes with time (Langel and Estes, 1985). This makes the data selection based on Dst questionable. Instead the use of the first time derivative (less influenced by baseline instabilities) has been recently used. A common data selection criterion is $|dDst/dt| \leq 2$ nT.h^{-1}. The Dst index does not only contain the magnetic signal of the magnetospheric ring current but also contributions due to the induction in the Earth's interior. Thus it contains both external and induced contributions, that can be separated by models of

[3] `http://isgi.unistra.fr/index.php`. All indices can be found from here.

electrical conductivity of the Earth's mantle (Olsen et al., 2005b).

1.5.3 Other measurements

If one is interested in magnetic maps on a regional scale the actual magnetic observatories distribution is not sufficient. A regional map of the magnetic field is important in terms of position and navigation. The necessary spatial resolution for these maps cannot be obtained by global geomagnetic models predictions, whose spatial scales are longer. This is the reason of the existence, in some countries, of a repeat station network. It consists on a more or less homogeneously mesh of locations where magnetic observations are made every three to five years. The measurements obtained like this are usually used to regional modelling (Kotzé et al., 2007) but can also be added to a dataset for a global geomagnetic model (Langlais and Mandea, 2000).

There are other types of magnetic measurements, commonly made with a specific purpose, like the geologic map of a region or a mining prospection. Examples are the aeromagnetic and marine surveys (see e.g., Vogt and Avery, 1974), and stratospheric balloons (Achache et al., 1991). These measurements have spatial scales smaller than the satellite ones and thus they can be coupled with the latter to improve crustal field modelling (see e.g., Maus et al., 2009).

1.6 Measuring the field at satellite altitude

The possibility to use low Earth orbit (LEO) satellites to map the geomagnetic field opened a new world of options to geomagnetic modelling. The advantages of satellite based magnetic measurements are as follows.

- A satellite can sample the magnetic field nearly all over the Earth. An exception is the polar cap areas where the satellite orbit inclination is different from 90^o (an orbit inclination is measured as the angle at which the satellite crosses the equator while passing from the Southern Hemisphere to the Northern Hemisphere (Fig. 1.10)).

- All measurements are taken with the same instrument.
- The field decreases with the cube of the radial distance. A measurement taken at a given altitude (for e.g. 400 km) corresponds to a spatial average over an area (at the Earth's surface) of the same scale. Local heterogeneities of smaller scales, like the crustal contributions, do not contribute to the measurements.
- The number of measurements delivered is by far higher than at ground observatories.

Important disadvantages are as follows.

- A satellite mission is costly.
- A LEO satellite moves at approximately 7.8 km.s^{-1}. As a consequence an observed magnetic field variation can be due to both a temporal or spatial change. This has to be taken into account during the analysis of the data.
- If a satellite visits a certain longitude every day, it will not provide a dense longitudinal coverage. Still, external field contribution models need a good distribution of measurements not only in longitude and latitude but also in local time (Olsen et al., 2010).
- As the satellite moves through an electrical plasma (present at satellite altitudes), electrical currents are present, therefore the mathematical representation of the field as a gradient of a Laplacian potential is not sufficient to describe all the constributions to the measurements.
- The necessary measurements should be of high accuracy, not only regarding resolution but also orientation and absolute values.

The satellite measurements are acquired not at one fixed altitude but over a range of altitudes. This produces uneven distributed in altitude time series, which can be seen as a disadvantadge. However it is mainly an advantadge as it allows for the separation of internal and external sources of the field.

The necessity of high accuracy measurements makes the instruments calibration and the knowledge of the satellite's attitude essential. This is described below, followed by a description of

the important satellite missions for geomagnetic field studies, with focus on the latest: the Swarm mission.

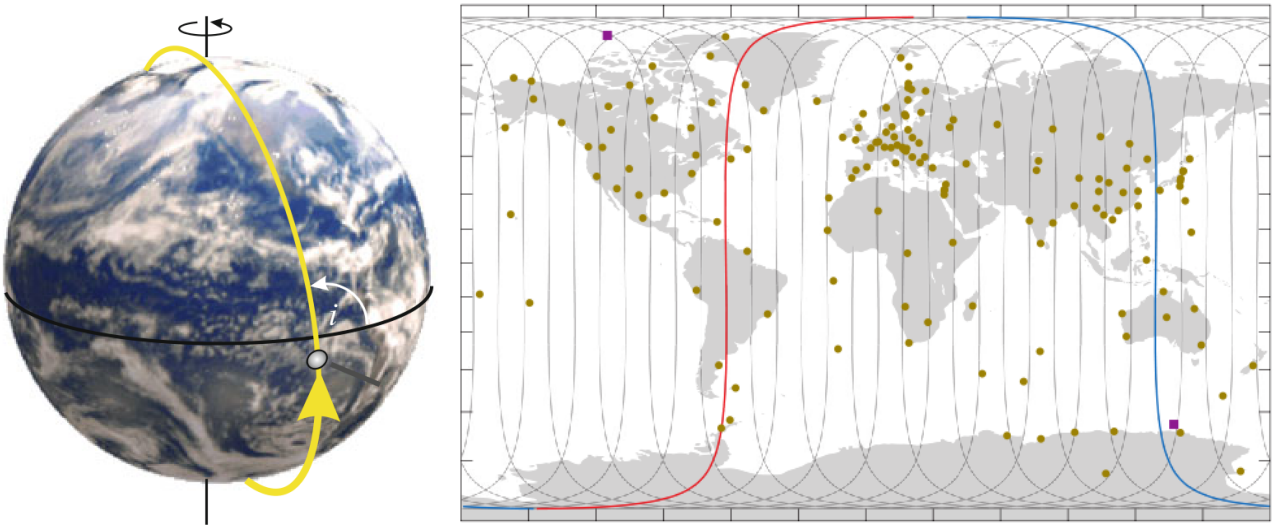

Figure 1.10: (*Left*) The path of a satellite at inclination i in orbit around the Earth. From Olsen et al. (2010). (*Right*) Ground track of 24h of the CHAMP satellite orbit on August 16, 2010 (*gray curves*). Highlighted is one orbit when the satellite starts close to the geographic North pole and flies southward during local nightime conditions (*blue*). After approximately 45 min, it reaches its closest approach to the geographic South pole and moves northward on the dayside (*red*). Dark yellow dots indicate the locations of ground-based magnetic observatories. Locations of the magnetic poles in 2010 are shown by the purple squares. Adapted from Olsen and Stolle (2012).

1.6.1 Calibration, attitude and errors of satellite measurements

Calibration and attitude of magnetometers are essential in the acquisition of high accuracy magnetic measurements necessary to obtain reliable magnetic field models (both for the internal and external fields). Satellites carry an absolute magnetometer, usually an Overhauser magnetometer (OVH), a vector or tri-axial fluxgate magnetometer (VFM), and a Star Imager (SIM), which is a high-accuracy attitude determination instrument, with the inertial stellar coordinates as reference. Usually the VFM and the SIM are mounted together and afar from the OVH. The recent high-accuracy missions have placed the absolute magnetometer at the end of a long boom, in a way that the absolute magnetic field measured by it is assumed unaffected by spacecraft fields.

The vector magnetometer is not an absolute instrument so it must be calibrated. The calibration consists on the conversion of raw vector readings into scaled magnetic field measurements (in nT) in the orthogonal coordinate system of the attitude sensor. This is done by comparing the output of the VFM with the measured magnetic field intensity given by the OVH, for each satellite. The VFM is calibrated before launch, but an in-flight estimation of calibration parameters is needed routinely.

In addition, the relative rotation between the attitude sensor reference system (the star alignment) and the magnetometer coordinate system has to be determined with an accuracy of a few arc seconds. The estimation of the three Euler angles which describe the rotation is called alignment of the magnetometer. However performing the calibration with scalar data alone does not allow calculating the rotation between the attitude sensor reference system and the magnetometer coordinate system. To obtain this an independent model of the Earth's magnetic field is used to compare the measurements of the magnetic field vector with the attitude, which is a limiting factor for the alignment. The Euler angles needed for the alignment may not be static, due to thermomechanical instabilities of the magnetometer/star-imager system, as it happened with the CHAMP satellite (see Section 1.6.2). To overcome this problem, the data is sorted into bins of a defined time (for e.g. 10 days) and within each bin the Euler angles are treated as static. For more information on the calibration of satellite measurements see e.g., Olsen et al. (2003). A number of magnetic field models incorporate the alignment in their inversion scheme, to avoid the inconsistency of deriving a field model from vector data obtained using an already existing and different magnetic field model (see e.g., Olsen et al. (2006b); Sabaka et al. (2013, 2015)).

Today, satellite measurements are required to be of high accuracy. This implies that any disturbance or error in the data will be of most importance and that the intrinsic error of a satellite instrument must be known. The sources of error in magnetic measurements are numerous, connected with the instrument relation with its environment (problems related with Sun heat, see Section 1.6.3), an instrument deficiency, satellite maneuvers or change/update of the satellite' software, due to the calibration of the measurements, errors in the attitude position of the satellite (a usual source of error, see Section 1.6.2), and others. Thus a magnetic

satellite mission involves a continuous monitoring of the obtained data and instruments during its lifetime than can be from a couple of months to more than a decade.

1.6.2 A parade of satellites

The first satellite measurements of the Earth's magnetic field were taken by satellites Sputnik 3 (in 1958, Dolginov et al. (1962)), Cosmos 26 and Cosmos 49 (in 1964), but not with a good quality. Table 1.1 details the most relevant satellite missions to the Earth's main magnetic field. The first global high-precision mapping of Earth's magnetic field was possible by the launch of the POGO-2 satellite in 1965. POGO-2 was part of the OGO (Orbiting Geophysical Observatories) satellite series, which consisted in a series of 6 different satellites launched between 1964 and 1969 by NASA. OGO's purpose was to conduct diversified geophysical experiments to obtain a better understanding of the Earth as a planet and to develop and operate a standardized observatory-type satellite. The polar orbit (POGO) mission, within the OGO programme consisted on three satellites, POGO-2, -4 and -6, which flew at sufficiently low altitude (between 400 to 1500 km) to be fitting to study the Earth's magnetic field (Cain, 2007). POGO satellites were equipped with optically pumped rubidium vapor absolute magnetometers and measured only the magnetic field intensity. The intrinsic error of the measurements is believed to be lower than 1 nT, but the uncertainty in the position location brings this error to about 7 nT. Despite the fact that they provided only intensity data, POGO satellites opened the way to scientific developments, like the first IGRF (see Section 2.6) model. Their data is important in constraining the main magnetic field evolution during the 1965–1971 time period. They also led to the first global magnetic anomaly map (Regan et al., 1975) of the lithospheric field, and the first observations of external currents from space, like the equatorial electrojet (Cain and Sweeney, 1973). POGO data remains important as it can be used with data collected at different epochs to the study of the main and the nearly static lithospheric fields.

The MAGSAT mission, which flew between October 1979 and June 1980, brought the first globally distributed measurements of the geomagnetic field vector. This mission operated at an altitude of 325-550 km in a near-polar dawn-dusk orbit of inclination 97^o. It sampled the

ambient field with a scalar (cesium) magnetometer and a triaxial fluxgate magnetometer, at 16 Hz with a resolution of ± 0.5 nT. The attitude was measured by two star-trackers and its errors limited the accuracy of vector data to about 4 nT rms (Purucker, 2007). MAGSAT was the first mission to provide magnetic vector measurements, allowing overcoming the Backus effect, difficulty in the POGO data. The Backus effect (Backus, 1970; Alberto et al., 2004) resides in the non-uniqueness of the determination of the magnetic field from using intensity measurements only, even if it is assumed the availability of those measurements at all locations (for the same altitude), except in very specific situations. This effect translates into several errors in the recovered model, especially in the neighborhood of the magnetic equator. The availability of vector data made possible to compute the first high degree and order models of the internal field, which pointed out the domination of the core field up to degree and order 13, and the lithospheric one beyond degree and order 15 (see Section 2.4). Magnetic lithospheric anomaly maps were improved, but also the knowledge on the magnetospheric and ionospheric currents (Langel and Estes, 1985; Olsen, 1997).

Table 1.1: Satellite missions of relevance for main geomagnetic field studies.

Satellite	Dates	Inclination (^{o})	Altitude (km)	Remarks
POGO-2	Oct. 1965 – Sept. 1967	87	410 - 1510	Scalar only
POGO-4	July 1967 – Jan. 1969	86	410 - 910	Scalar only
POGO-6	June 1969 – June 1971	82	400 - 1100	Scalar only
MAGSAT	Nov. 1979 – May 1980	97	325 - 550	Scalar and vector
Ørsted	Feb. 1999 –	96.5	650 - 850	Scalar and vector
CHAMP	July 2000 – Sept. 2010	87	260 - 450	Scalar and vector
SAC-C	Nov. 2000– Dec. 2004	97	698 - 705	Scalar only
Swarm	Nov. 2013 –	88/87	530/450	Scalar and vector

After Magasat, some initiatives worked as follow-on missions, but it was only with the launch of Ørsted, in February 1999, than the next high-precision mapping of the Earth's magnetic field was possible. Ørsted is a Danish mission with international contributions, named in honor of the Danish scientist Hans Christian Ørsted (1777-1851) who discovered electromagnetism in 1820. This mission became the model for following missions like CHAMP and Swarm, marking the beginning of the International Decade of Geopotential Field Research (promoted by IAGA in 1997 with the goal to secure uninterrupted geomagnetic field satellite survey measurements

spanning a decade (Kerridge, 2007)). The mission objectives were to perform highly accurate and sensitive measurements of the geomagnetic field and global monitoring of the high energy charged particles in the Earth's environment. Ørsted contains an 8 m long boom, deployed shortly after launch, carrying the magnetic field instruments (Fig. 1.11), consisting in a (scalar) proton Overhauser magnetometer, a CSC (Compact Spherical Coil) fluxgate vector magnetometer, and a Star Imager. The satellite weights $\sim$ 60 kg, measures 34 $\times$ 45 $\times$ 72 cm and its orbit has an inclination of 96.5^o, a period of 100.0 min, a perigee at 650 km, and an apogee at 860 km. The orbit plane is slowly drifting i.e., the local time of the equator crossing decreases by 0.91 min.day^{-1} (Fig. 1.12), which corresponds to a scanning of all local times within 790 days (2.2 years). Initially nominal lifetime of the mission was 14 months, but the satellite is still healthy and provides high-precision scalar magnetic data (quality vector data stopped atthe end of 2004). The absolute magnetometer samples the field at 1 Hz with an accuracy better than 0.5 nT and is mounted at the bottom of the boom. The vector magnetometer, mounted at a 6 m distance from the body of the satellite samples the field at 100 Hz (polar latitudes) or 25 Hz (other latitudes) with a resolution better than 0.1 nT, and is calibrated using the field from the absolute magnetometer. Due to attitude errors the accuracy of the vector components is limited to 2–8 nT (4 nT rms), depending on the component. Ørsted data have been helping to improve magnetic field models, to study auroral phenomena and the relationship between external fields and the energy coupling of solar wind magnetosphere-ionosphere system (Ultré-Guérard et al., 1998; Olsen et al., 2000; Neubert et al., 2001). Since 2004 however, only intensity data is available.

Two additional satellites were launched a few months after Ørsted: CHAMP (Challenging Mini-Satellite Payload) on July 2000 and SAC-C (Satellite de Aplicaciones Cientifico-C, the third satellite of the Argentinean space program), in November 2000. The three satellites carried practically the same instrumentation and provided data for more than one decade. Measurements (intensity only) from SAC-C are available until 2004. This satellite has a circular sun-synchronous orbit at an altitude of about 700 km and local time of 10:30/22:30. CHAMP (Maus, 2007) was a more successful satellite (Figs. 1.10 and 1.11). It was a German mission of an almost circular, near-polar orbit (87.3^o) with an initial altitude of 454 km, which

decreased until its atmospheric entry on September 2010. The satellite advanced 1 h in local time each 11 days and covering all local times within 130 days (Fig. 1.12). The accuracy of the scalar measurements was similar to that of Ørsted but it was better for the vector components, finer than 0.2 nT, when the attitude of the satellite was measured by the two star imager (> 60 % of the time) (Kuvshinov and Olsen, 2005; Maus et al., 2007).

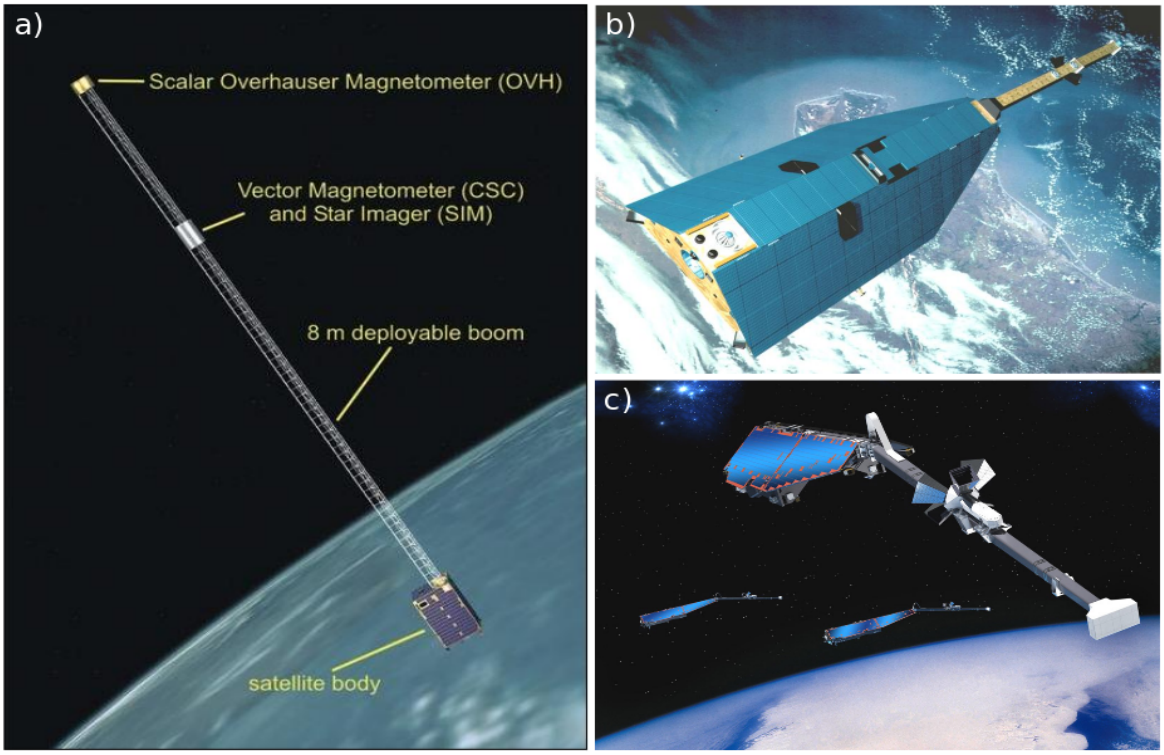

Figure 1.11: Ørsted (a), CHAMP (b) and Swarm (c) satellites. Credits: DRSI (now DTU Space); Astrium; ESA.

Ørsted and CHAMP satellites represented an improvement on the satellite mission characteristics from the original MAGSAT concept. Both satellites were designed to perform better quality measurements and to have orbits that avoided the MAGSAT limitation of the dawn-dusk orbit, which is not optimal to the study and description of the time variations of external fields. In particular Ørsted and CHAMP made possible night-time measurements, which have much weaker ionospheric signal. Other aspect is the longer (than MAGSAT's) lifetime of the satellite especially in the case of Ørsted that continues to deliver intensity data. This is possible because of the higher launch altitude of the satellites. The disadvantage is that Ørsted is much

less sensitive to short wavelengths of the internal field than MAGSAT.

Ørsted was the first vector mission to be launched nearly twenty years after MAGSAT, allowing to compare the changes in the main field between the two epochs, particularly in the medium spatial scales that cannot be monitored from ground based observatories, renewing the interest on the core flows and other mechanisms responsible for these changes. Ørsted also permitted the construction of high degree secular variation models (Olsen, 2002; Gillet et al., 2010), or the improvement of the knowledge on the lithospheric and externally induced fields (Purucker et al., 2002; Neubert and Christiansen, 2003).

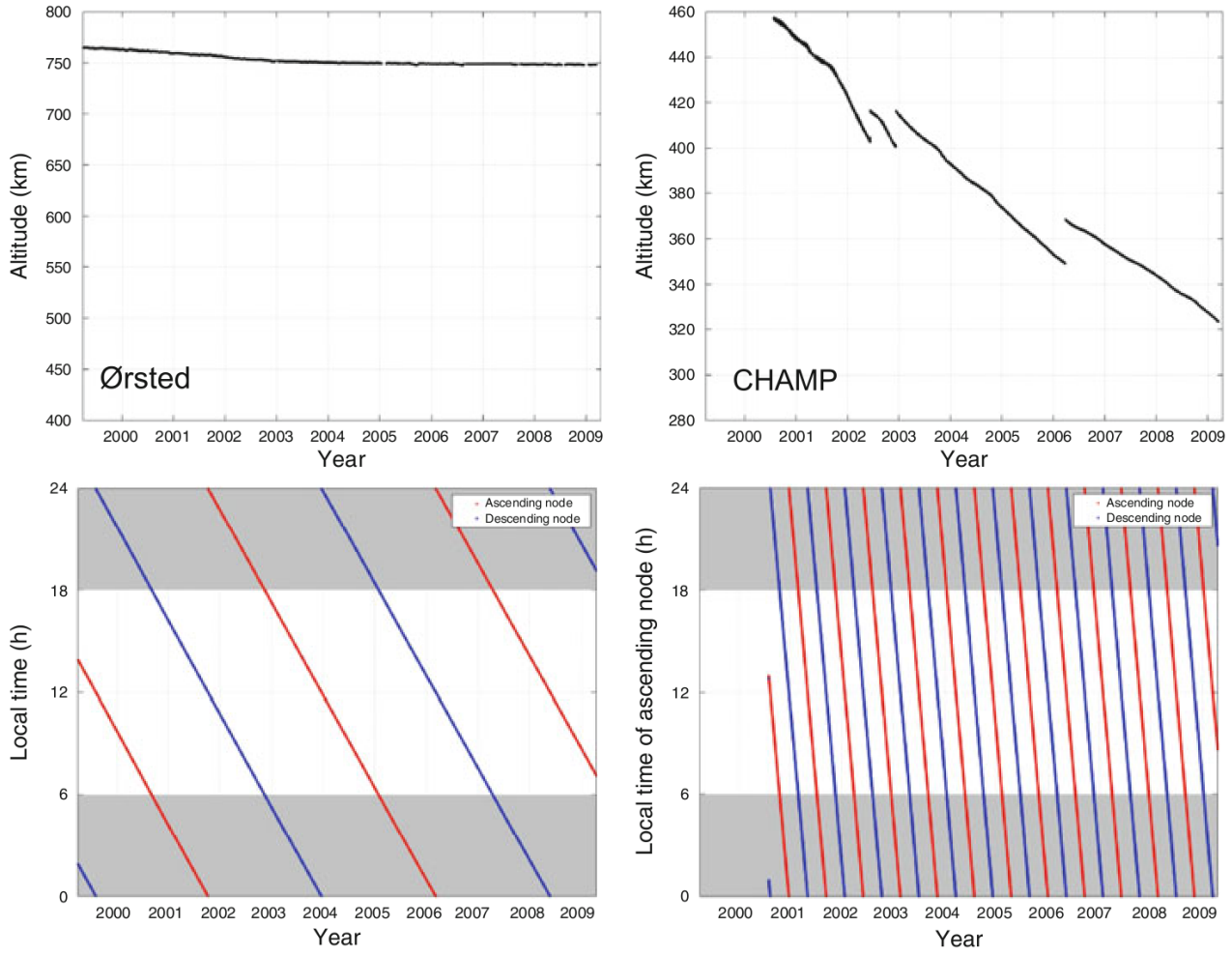

Figure 1.12: Orbit characteristics for Ørsted (*left*) and CHAMP (*right*) satellites in dependence of time. *Top:* mean altitude. *Bottom:* local time of ascending (*red*) and descending (*blue*) node. From Olsen et al. (2010).

The lower orbit of CHAMP permitted an improvement of the lithospheric field models (Maus et al., 2002; Thébault et al., 2010). CHAMP also allowed new observations of the ionospheric

F-region and other external field sources (Lühr et al., 2002; Stolle et al., 2006), and the demonstration that ocean produced magnetic field contribute and can be detected in the magnetic field measured from space (Tyler et al., 2003). The accumulation of data from Ørsted and CHAMP demonstrated the unique advantage of LEO satellites for continuously monitoring the Earth's magnetic field. Ørsted and CHAMP orbited in very different orbital planes leading to the comprehensive modelling approach (e.g., Sabaka et al., 2004), and showing that a constellation of several satellites making simultaneous measurements over different regions of the Earth would open a new world of possibilities to the magnetic field exploration.

1.6.3 The Swarm Mission

On 22 November 2013 the European Space Agency (ESA) successfully launched the Swarm three-satellite mission devoted to the study of the geomagnetic field and its interactions with the Earth's system (Friis-Christensen et al., 2006). The objective of the Swarm mission is to deliver the best survey of the geomagnetic field and its temporal variation, simultaneously obtaining a space-time characterization of both the internal field sources in the Earth and the ionospheric-magnetospheric current systems. The main research objectives of the mission are:

- studies of core dynamics, geodynamo processes, and core-mantle interaction;
- mapping of the lithospheric magnetisation and its geological interpretation;
- determination of the 3-D electrical conductivity of the mantle;
- investigation of electric currents flowing in the magnetosphere and ionosphere.

In addition, two secondary research objectives were defined:

- identification of ocean circulation by its magnetic signature;
- quantification of magnetic forcing of the upper atmosphere.

A constellation consisting in several satellites opens new possibilities for exploring the geomagnetic field from space. The mission was designed to derive the first global representation of the geomagnetic field variations on times scales from an hour to several years and address the

problem of source separation. Detailed description of the mission objectives and goals can be found in Friis-Christensen et al. (2006).

Swarm's three satellites are identical, having a trapezoidal shape with a long boom (Fig. 1.13), and were launched together on a single rocket. That rocket was the Rockot launcher, which is a converted SS-19 intercontinental ballistic missile, and was launched from the Plesetsk Cosmodrome in northern Russia. The development of Swarm was carried out by ESA's European Space Research and Technology Centre ESTEC, in the Netherlands. Intensive testing was done pre-flight, also in southern Spain at the German-Spanish Calar Alto Astronomical Observatory. The mission is operated by ESA's European Space Operations Centre ESOC, in Germany, via the primary ground station in Kiruna, Sweden. The launch and early orbit phase lasted three days during which the booms were deployed and all satellites units were switched on. A commissioning phase to ensure all instruments were working accurately lasted three months. During this phase complementary ground stations in Norway, Antarctica and Australia were used to increase daily contact with the satellites. The scientific data is managed in ESA's Centre for Earth Observation, ESRIN, in Italy, with processing and archiving in the UK.

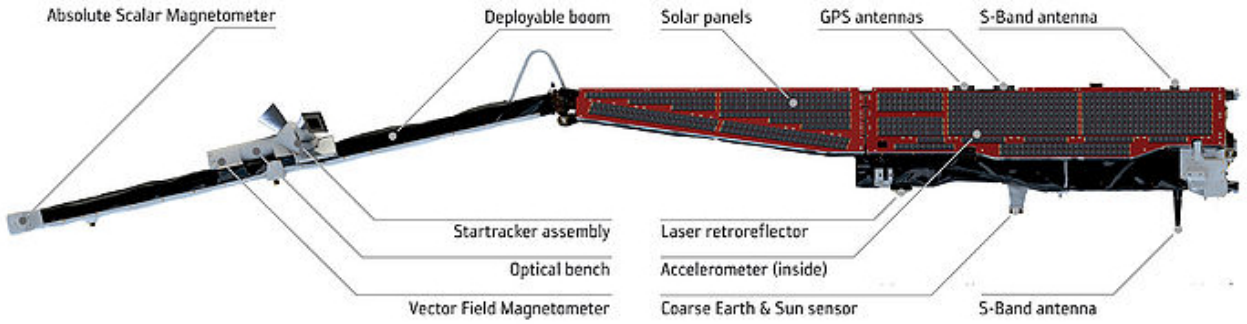

Figure 1.13: A Swarm satellite and its instruments. Credit: ESA.

The three-spacecraft constellation consists of two satellites (A and C) flying almost side-by-side at an altitude close to 470 km, longitude separation of 1.4^o and inclination of 87.4^o. The third satellite (B) flies above (see Fig. 1.15), close to 520 km on a more polar orbit (inclination of 88^o) to allow for a progressive local time separation with respect to A and C, of about an hour on November 2014. Initially it was to Swarm C to be placed on the higher orbit, but a problem

detected early in the first weeks of the mission on Swarm C redundant scalar magnetometer obliged ESA to place a completely functional satellite in the higher orbit (Swarm B was the chosen one) and leave Swarm C in tandem with Swarm A.

Each satellite is about 9.1 m long (including a 4 m deployable boom) and only 1.5 m wide, in order to reduce the effect of air drag and needed propellant to stay at the correct altitude. The boom is at the back of the satellite, as the front surface is needed to collect and measure the speed and direction of incident ions. The satellite has no moving parts, ensuring that no vibrations could influence the accelerometer, placed at the centre of the satellite. The Absolute Scalar Magnetometer (ASM) is located at the end of the boom (see Fig. 1.13), far away from any magnetic disturbance that the electrical units on the body may cause. Mounted halfway along the boom there is the optical bench holding the Vector Field Magnetometer (VFM) and the three Star TRackers (STR).

The ASM measures the magnetic field intensity at 1 Hz with an accuracy of 0.15 nT rms, and as an absolute instrument it is not subject to changes of its parameters over time. It was designed by CEA-Leti (Laboratoire d'Électronique, de Technologie et d'Instrumentation, France) in partnership with CNES (Centre National d'Études Spatiales, France). This instrument is the first ever spaceborne magnetometer to use a common sensor to simultaneously deliver independent absolute scalar and experimental vector readings of the magnetic field with no impact on the magnetometer's scalar performance, using a so-called vector mode (Léger et al., 2015).

The VFM measures the magnetic field vector at the tip of the optical bench on the boom. The instrument is a 3-axis CSC. It is an analog instrument and as such subject to temporal changes due to radiation and aging effects of the electronics. These effects are estimated on a daily basis by comparison between the VFM with the ASM outputs (see Section 1.6.1). The VFM provides 1 Hz vector measurements with an accuracy of 0.5 nT.

The STR is comprised of three Camera Head Units (CHUs) mounted on the innermost end of the optical bench, and provides the attitude of the satellite with respect to an inertial stars reference system. All three CHUs provide simultaneously at 1 Hz rate the attitude of the

satellite. However one head is regularly blinded by the Sun leaving the attitudes of just two heads. The provided attitudes are then combined into one attitude, the attitude of the STR Common Reference Frame (CRF), and then interpolated to obtain CRF and S/C (spacecraft) attitudes at different required time instants.

Each satellite also contains an electrical field instrument that determines the ions density, the ions drift velocity and the electric field at the spacecraft front panel. The instrument has two components: the Langmuir Probe (LP) and the Thermal Ion Imager (TII). Additionally, each satellite has a GPS receiver for precise orbit determination and an accelerometer (ACC) for observing non-gravitational forces.

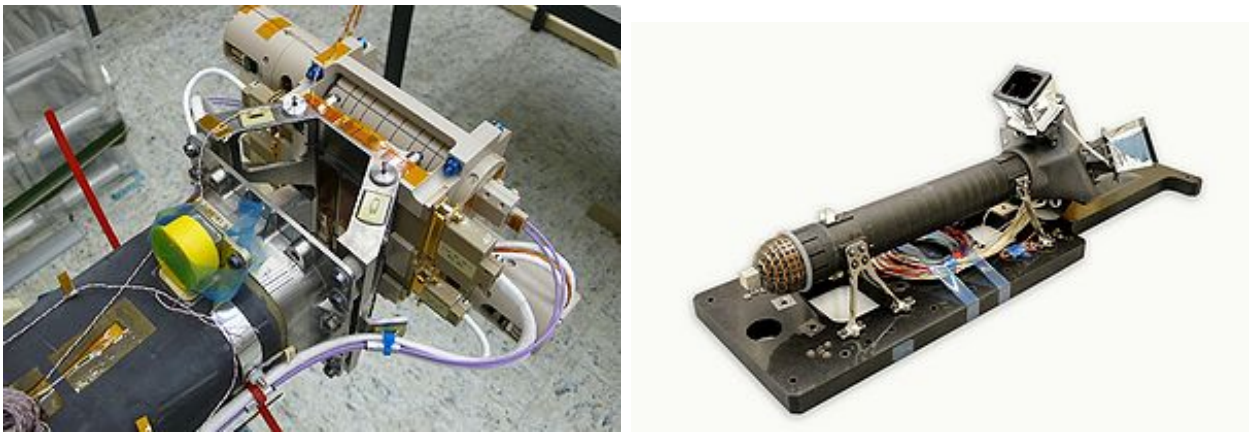

Figure 1.14: Swarm's ASM sensor (*left*) and optical bench (*right*). Credit: ESA.

Magnetic field, navigation, accelerometer, plasma and electric field measurements are provided by ESA as Level-1b data, which consists in calibrated and formatted time series of the observations for e.g., the (three components) magnetic field measurements taken by each one of the three satellites (Olsen et al., 2013). Level-1b data and higher-level Swarm products are distributed by ESRIN. Higher-level (Level-2) products are derived by SCARF (Satellite Constellation Application and Research Facility), which was designed by ESA to derive commonly scientific models and quantities and make them available to the scientific community at large. These advanced products are determined from Level-1b products and auxiliary (non-Swarm) data, like ground observatory measurements. SCARF is composed by six European partners: DTU (Denmark), TU Delft (Netherlands), BGS (Great Britain), ETH (Switzerland), GFZ

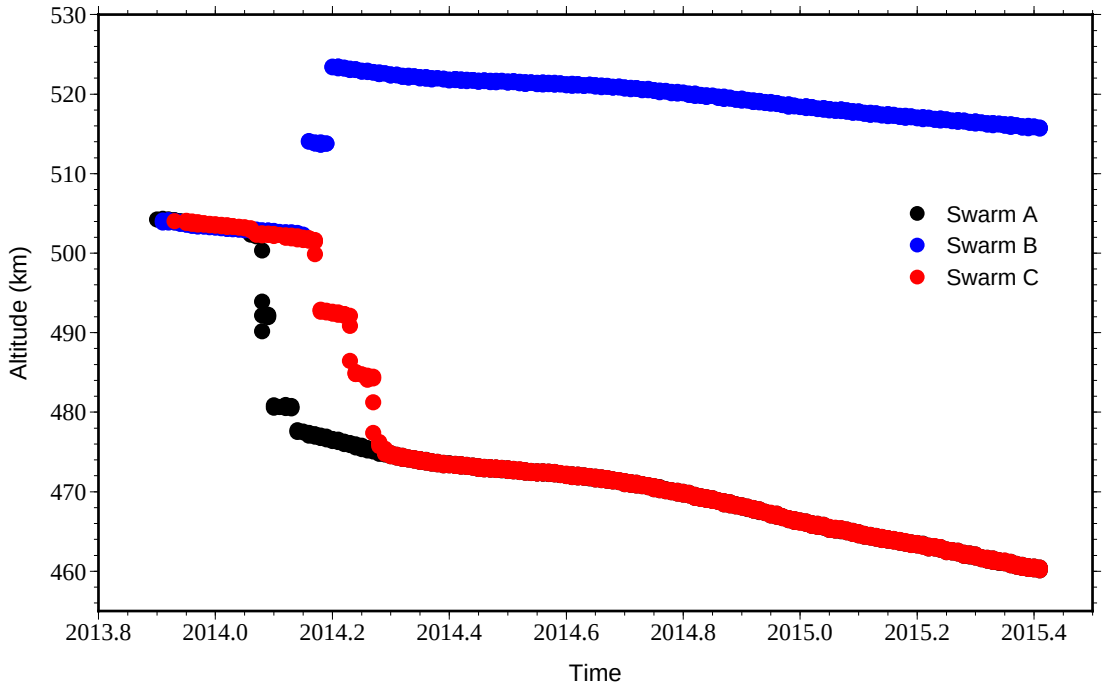

Figure 1.15: Daily mean altitude of the three Swarm satellites from November 2013 to June 2015.

(Germany) and IPGP (France); with contributions from CUP (Czech Republic), NOAA and GFSC/NASA (USA). SCARF team implemented algorithms to derive models of the geomagnetic field describing sources in the core, ionosphere, lithosphere and magnetosphere, models of the electrical conductivity of the Earth's mantle and time series of thermospheric wind and density at Swarm satellite positions (Olsen et al., 2013). The Level-1b data is provided individually for each one of the three satellites on a daily basis, in files containing calibrated and corrected measurements given in physical, SI units in geo-localised reference frames.

Since an early phase of the mission an unexpected disturbance of varying strength and direction was detected on all three satellite's measurements. These vector disturbances are believed to be correlated with the Sun incident angle, with respect to the spacecraft. A model of the disturbances was proposed by V. Lesur (GFZ, Potsdam) (Tøffner-Clausen, 2015; Lesur et al., 2015)). The model uses a spherical harmonic description for the Sun incident angles. The magnetic vector disturbance, denoted $\mathbf{dB}_{Sun}$ is modelled as:

$$\mathbf{dB}_{Sun} = \sum_{n=1}^{N_m} \sum_{m=0}^{n} \left(g_n^m \cos(m\alpha) + h_n^m \sin(m\alpha)\right) P_n^m(\cos\beta), \tag{1.10}$$

where α and β are the Sun incident angles with respect to the spacecraft $+\mathbf{x}_{S/C}$ and $-\mathbf{y}_{S/C}$ axis, respectively. The last term corresponds to the associated Legendre functions (see Section 2.1 and eq. 2.12) and n and m are the degree and order of the Gauss coefficients g and h. In the model, N_m is the maximum degree of the coefficients and it is set to 25. The parameters g_n^m and h_n^m are estimated by a iteratively re-weighted least-squares fit of the calibrated and corrected scalar measurements of the ASM and VFM (intensity, the modulus of the vector components of the VFM). For each satellite specific parameters are calculated, as the disturbances are different from one satellite to another. A co-estimation of small corrections of pre-flight calibration parameters is done.

On November 5th 2014 the ASM instrument on Swarm C stopped providing data. Due to the lack of intensity data the calibration process of the VFM instrument of Swarm C had to be reconsidered. The calibration and characterization of the disturbance in the VFM of Swarm C has been done since using ASM measurements of the parent satellite Swarm A, by:

$$F_{A\to C} = F_A(t_A) - F_{model}(t_A, \mathbf{r}_A) + F_{model}(t_C, \mathbf{r}_C), \tag{1.11}$$

where $F_A(t_A)$ are the ASM measurements on Swarm A; t_A, $\mathbf{r}_A$, t_C and $\mathbf{r}_C$ are times and positions of Swarm A and C respectively chosen such that $|t_A - t_C| < 50$ seconds and $\mathbf{r}_A$ and $\mathbf{r}_C$ are at the same geographical latitude. F_{model} is a main field model of the Earth's core (SIFM+, Olsen et al. (2015)) and crust (CHAOS-4b, Olsen et al. (2014)) up to degree and order 85 for the static part and 13 to the secular variation.

The calibration is performed on a daily basis and then the magnetic vector disturbance $\mathbf{dB}_{Sun}$ is applied to the data. This new version of corrected data was released under the baseline 04. A Swarm product baseline depends on its level, processed version and relative calibration and characterization on the data base. The corrected data was firstly released in May 2015. However the model for the vector disturbances (as on June 2015) is not capable to correct the data from periods of specific spacecraft manoeuvres (Tøffner-Clausen, 2015).

Chapter 2

Models of the Earth's magnetic field

This chapter presents the classical mathematical description of the geomagnetic main field used in modelling. Special attention is given to the IGRF model and its recent 12th generation, in which I, LPG Nantes and CNES colleagues submitted candidate models. A general description of some recent geomagnetic models is also given. Finally the motivations for this thesis work are presented.

2.1 Spherical harmonic description of the potential field

The classical theory for geomagnetism is defined by the equations of electrodynamics. For detailed information on the mathematical description of geomagnetism see e.g., Backus et al. (1996); Langel (1987). From Maxwell's equations (in SI units):

$$\nabla \times \mathbf{B} = \mu_0(\mathbf{J} + \epsilon_0 \partial_t \mathbf{E}) \tag{2.1}$$

$$\nabla \cdot \mathbf{B} = 0, \tag{2.2}$$

where $\mu_0 = 4\pi \cdot 10^{-7}$ H/m is the permeability of vacuum, $\epsilon_0 = 8.85 \cdot 10^{-12}$ F/m the permittivity of vacuum, $\mathbf{J}$ (A/m^2) the electrical current density, $\mathbf{E}$ (V/m) the electrical field, t the time (in seconds) and $\mathbf{B}$ (T) the magnetic field (magnetic induction, in nT). The term $\mu_0\epsilon_0\partial_t\mathbf{E}$

on Eq. 2.1 is only important for cases when time scales are smaller than the velocity needed by light to cross a feature with a typical length in the system. Hence, this term can be neglected for a global-scale magnetic field as the Earth's (Davidson, 2001). The term $\mu_0\mathbf{J}$ can also be neglected because the conductivity of the atmosphere, between the surface of the Earth and the ionosphere is small ($\sigma \approx 10^{-13}$ S/m) compared to the conductivity of the core ($\sigma \approx 0.75 \times 10^6$ S/m (Poirier, 2000)) resulting in a negligible current density $\mathbf{J}$. Thus it follows that above the CMB and bellow the ionosphere the magnetic field can be taken as curl-free:

$$\nabla \times \mathbf{B} = 0, \tag{2.3}$$

and $\mathbf{B}$ can be represented as the gradient of a scalar potential, V:

$$\mathbf{B} = -\nabla V. \tag{2.4}$$

Since, from Eq. 2.2, the divergence of $\mathbf{B}$ is zero, V must obey Laplace's equation:

$$\nabla^2 V = 0. \tag{2.5}$$

In spherical coordinates Eq. 2.5 is written as

$$\frac{1}{r}\frac{\partial^2 (rV)}{\partial r^2} + \frac{1}{r^2 \sin\theta}\frac{\partial}{\partial \theta}\left(\sin\theta \frac{\partial V}{\partial \theta}\right) + \frac{1}{r^2 \sin^2\theta}\frac{\partial^2 V}{\partial \phi^2} = 0, \tag{2.6}$$

where (r, θ, ϕ) are radius, co-latitude and longitude spherical coordinates.

The previous approximations are valid if we consider that there are no sources in the atmosphere. However, it is known that currents flow within the ionosphere as well as into and out of the ionosphere along magnetic field lines. So, some models take into account these currents using a toroidal field desciption (e.g., Lesur et al., 2008; Sabaka et al., 2015).

The decomposition of a magnetic field $\mathbf{B}$ on a sphere with radius $r = R$ (Langel, 1987; Olsen et al., 2007) can be written as:

$$\mathbf{B}(R, \theta, \phi) = \mathbf{B}_i(R, \theta, \phi) + \mathbf{B}_e(R, \theta, \phi) + \mathbf{B}_{tor}(R, \theta, \phi) \tag{2.7}$$

where $\mathbf{B}_i$ and $\mathbf{B}_e$ are the potential fields produced on the sphere by all sources below and above the observation altitude $r = R$, respectively, and $\mathbf{B}_{tor}$ is the toroidal field produced by the local poloidal currents on the sphere $r = R$. $\mathbf{B}_i$ and $\mathbf{B}_e$ are represented by potentials for $r \geq R$ and $r \leq R$, respectively, with $\mathbf{B}_i = -\nabla V_i$ and $\mathbf{B}_e = -\nabla V_e$. At the surface of the Earth, where $r = a$, Gauss wrote (Gauss, 1839; Taylor, 1841) these potentials as a series expansion in spherical harmonic (SH) functions:

$$V_i(r,\theta,\phi) = a\sum_{n=1}^{\infty}\left(\frac{a}{r}\right)^{n+1}\sum_{m=0}^{n}\left(g_n^m Y_n^{m,c}(\theta,\phi) + h_n^m Y_n^{m,s}(\theta,\phi)\right) \tag{2.8}$$

$$V_e(r,\theta,\phi) = a\sum_{n=1}^{\infty}\left(\frac{r}{a}\right)^{n}\sum_{m=0}^{n}\left(q_n^m Y_n^{m,c}(\theta,\phi) + s_n^m Y_n^{m,s}(\theta,\phi)\right), \tag{2.9}$$

where (g_n^m,h_n^m) and (q_n^m,s_n^m) are the Gauss coefficients describing the field below and above $r = a$, respectively, n and m are the degree and order of the Gauss coefficients and $Y_n^{m,c}$ and $Y_n^{m,s}$ are the Schmidt quasi-normalised real surface spherical harmonics (Langel, 1987), given by

$$Y_n^{m,c}(\theta,\phi) = \cos(m\phi)P_n^m(\theta) \tag{2.10}$$

$$Y_n^{m,s}(\theta,\phi) = \sin(m\phi)P_n^m(\theta), \tag{2.11}$$

with the associated Legendre functions in the quasi-normalized form:

$$P_n^m(\theta) = \begin{cases} P_{n,m}(\cos\theta), & m = 0, \\ \left[2\frac{(n-m)!}{(n+m)!}\right]^{1/2} P_{n,m}(\cos\theta), & m > 0, \end{cases} \tag{2.12}$$

where

$$P_{n,m}(\cos\theta) = (1-\cos^2\theta)^{\frac{m}{2}}\frac{\partial^m}{\partial\cos^m\theta}\left(\frac{1}{n!2^n}\frac{d^n}{d\cos^n\theta}(\cos^2\theta - 1)^n\right). \tag{2.13}$$

In Eq. 2.8 and 2.9, terms in $(a/r)^{n+1}$ go to zero as r goes to infinity and so describe fields from sources inside the sphere $r = a$. In Eq. 2.8 and 2.9 terms in $(r/a)^n$ go to zero as r goes to zero and so describe fields from sources outside the sphere $r = a$. The term for $n = 0$ corresponds to a magnetic monopole and violates Eq. 2.2, being normally omitted from the analysis. The multiplier a is added so that the spherical harmonic coefficients have the same dimensions as

B. The additional toroidal field (recall Eq. 2.7) is defined by

$$\mathbf{B}_{tor}(r,\theta,\phi) = \sum_{n=1}^{\infty}\sum_{m=0}^{n}\left(\varsigma_n^{m,c}(r)\mathbf{\Gamma}_n^{m,c}(\theta,\phi) + \varsigma_n^{m,s}(r)\mathbf{\Gamma}_n^{m,s}(\theta,\phi)\right), \tag{2.14}$$

with

$$\mathbf{\Gamma}_n^{m,(c,s)}(\theta,\phi) = \nabla \times Y_n^{m,(c,s)}(\theta,\phi)\mathbf{r}, \tag{2.15}$$

where $\mathbf{r}$ is the radial vector direction. When $R = a$, Eq. 2.7 reduces to the sum of the two potential fields $\mathbf{B}_i$ and $\mathbf{B}_e$, since the (practically) neutral atmosphere at that location has no local currents. Then the Gauss coefficients (g_n^m, h_n^m) and (q_n^m, s_n^m) describe the field of internal and external origin, respectively. When R corresponds to a sphere between 400 km and 1000 km, the F-region where the satellites usually revolve, local currents appear and $\mathbf{B}_{tor}$ is non-zero. Then the Gauss coefficients (g_n^m, h_n^m) will represent the internal field, the externally induced fields within the Earth, and the potential field produced by all ionospheric sources below $r = R$ (being the E-region where the main source is located at ∼110 km). The coefficients (q_n^m, s_n^m) will then describe the magnetospheric sources located above $r = R$ (Olsen et al., 2007).
From a potential, the magnetic field components are given by (in spherical coordinates):

$$Br = -\frac{\partial V}{\partial r}, \quad B_\theta = \frac{\partial V}{r\partial\theta}, \quad B_\phi = -\frac{1}{r\sin\theta}\frac{\partial V}{r\partial\phi}. \tag{2.16}$$

The transformation to the local Cartesian coordinates system (see Section 1.2) is simply given by

$$X = -B_\theta, \quad Y = B_\phi, \quad Z = -B_r. \tag{2.17}$$

2.2 Representing the temporal variation of the field

2.2.1 Main field

The magnetic field time variation was firstly modelled by expanding the Gauss coefficients in a Taylor series in time about some epoch, T_0. The set of coefficients to invert $p = (g_n^m, h_n^m, q_n^m, s_n^m)$ is expanded as

$$p(t) = p_{T_0} + \dot{p}_{T_0} \cdot (t - T_0) + \frac{\ddot{p}_{T_0} \cdot (t - T_0)^2}{2!} + ..., \tag{2.18}$$

where T_0 denotes the epoch at which the model is being derived (Langel, 1987). Then, $\mathbf{p}$ includes p_{T_0} and all derivatives in the solution of the inverse problem (see Appendix A).

A representation such as this is only adequate locally in time, i.e., over short time spans (a few years) and becomes inaccurate when applied outside the span of data used to infer the derivatives. The degradation in accuracy is greater with higher time derivatives as one departs from the time span of the data (Langel, 1987). For a model spanning over a long time periods (say, longer than 5 years), a large number of terms will be required in Eq. 2.18, which brings numerical instabilities and lack of flexibility to the parametrization (Jackson and Finlay, 2007). Since the temporal change is highly nonlinear with time, a more complex description is necessary.

Other methods of expressing the time dependency were introduced after the mid-1980. Gradually the methods converged toward the use of cubic B-splines as temporal basis functions following the example of Bloxham and Jackson (1992), heavily influenced by Langel et al. (1986).

The spline representation takes the form (e.g. for g_n^m):

$$g_n^m(t) = \sum_{l=1}^{L} g_{n,l}^m \cdot M_l(t), \tag{2.19}$$

where $M_l(t)$ is a basis of B-splines functions (De Boor, 2001) depending on time and L is the number of basis functions. To fit a set of data over the interval range (t_a, t_b), it is necessary to specify the desired knots $(t_i, i = 1, ..., k)$ and to introduce additional knots,

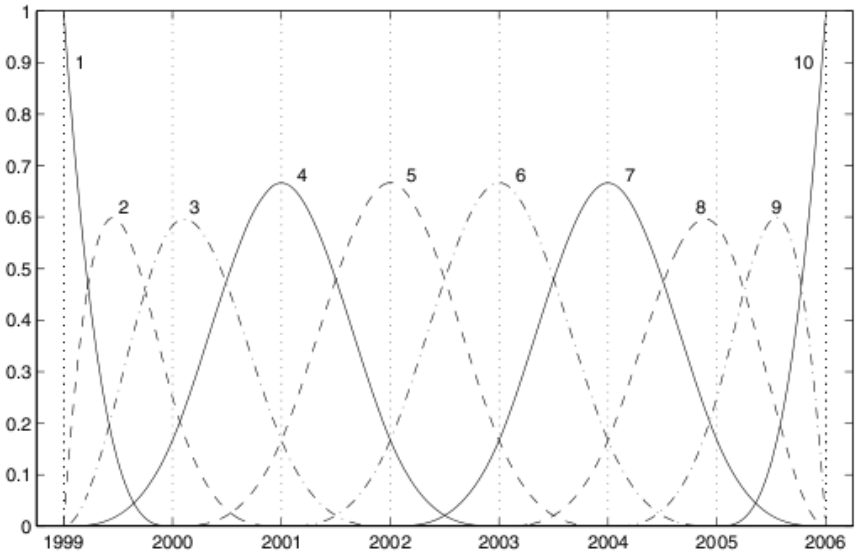

Figure 2.1: Schematic of a cubic B-spline basic functions, $M_l(t)$, $l = 1, ..., 10$, used to represent the time change of each Gauss coefficient. There are six interior knots and four exterior knots at each endpoint. From Olsen et al. (2006b).

whose number depends on spline order. For a cubic B-spline four extra knots are necessary: $t_{-3}, t_{-2}, t_{-1}, t_0, t_{k+1}, t_{k+2}, t_{k+3}$ and t_{k+4} such that

$$t_{-3} \leq t_{-2} \leq t_{-1} \leq t_0 \leq t_a, \quad t_b \leq t_{k+1} \leq t_{k+2} \leq t_{k+3} \leq t_{k+4}. \tag{2.20}$$

Generally, one uses $t_{-3} = t_{-2} = t_{-1} = t_0 = t_a$ and $t_{k+1} = t_{k+2} = t_{k+3} = t_{k+4} = t_b$. A basis function $M_{l=i}(t)$ is non-zero only over the range $t_{i-4} < t < t_i$, and zero everywhere, with negative first and second derivatives at $t = t_{i-4}$ and $t = t_i$. If two or more knots are chosen at the same t, the continuity of the spline is reduced at the point (Langel, 1987). Fig. 2.1 shows an example with $L = 10$.

As the B-spline basis is a "local" basis, meaning that the basis functions are zero outside a small range, it requires less computational memory than other methods. Also, the B-splines provide a flexible basis for smoothly varying descriptions of data.

Many models apply the idea of regularization in time, by typically minimizing a combination of temporal and spatial norms measuring the field complexity on the core-mantle boundary (CMB). The relative weights of the spatial and temporal norms are scaled by the so-called dumping parameters (λ). These are chosen depending of what is desired, for example, that the

data will be fitted within their estimated errors or that no unnecessary temporal oscillations will be introduced, and that the complexity of the model at the CMB will be compatible with accurate observations or single epoch models (Olsen et al., 2007).

2.2.2 External fields

Before satellite measurements were available, the modelling of the external contributions (from the magnetosphere, magnetotail and ring currents) was very difficult. These contributions are of the order of 10 to 40 nT in satellite measurements during magnetically quiet periods (Baumjohann and Nakamura, 2007). An important aspect to note is that the determination of external field Gauss coefficients (like q_1^0) must have into account that the external sources vary both with local and universal time.

Not accounting for the local time variation Langel and Estes (1985) determined using MAGSAT data, for epoch 1980.0, the external coefficients depending on the Dst index:

$$q_1^0 = 18.4 - 0.63\ Dst \tag{2.21}$$

$$q_1^1 = -1.1 - 0.06\ Dst \tag{2.22}$$

$$s_1^1 = -3.3 + 0.17\ Dst \tag{2.23}$$

They also calculated the contribution of external field induced currents within the Earth to the internal potential e.g., g_1^0. The idea is that g_1^0 can be expressed as a constant for the core field plus an induced internal field proportional to q_1^0 (at epoch 1980.0):

$$g_1^0 = -29991.6 + 0.270\ q_1^0, \tag{2.24}$$

still, the corresponding induced contributions to g_1^1 and h_1^1 are taken as negligible (Langel, 1987). The local time dependence was more difficult to map with Magsat data, since the data were only acquired at dawn and dusk local times. But for the POGO data the same authors

found an expression for q_1^0:

$$q_1^0 = a + b\ Dst, \tag{2.25}$$

where the coefficients a and b depend on the local time t, in degrees. However the results using POGO data are based on scalar field measurements only, being consequently in some way uncertain. Note also the different epochs of the two spacecraft, POGO (1965-1971) and MAGSAT (1980). This is important as the average intensity of the ring current and the Dst baseline definition can both change between the two epochs. The Dst index is an indicator of the large scale relative change of the magnetospheric fields (ring current mostly) but it is relative, not absolute, and its value completely depends upon the quiet time level used as the baseline definition (Olsen et al., 2005b). This way of modelling the external fields' time dependence has been widely used even if sometimes with a few differences. The usual procedure is to add to the potential equation of the external field (Eq. 2.9) an additional term with the time dependence of q_1^0.

Recent models represent the time variation of magnetospheric sources with a linear dependence of Dst(t) (similar to Eq. 2.21) modulated by seasonal and diurnal oscillations (Sabaka et al., 2002; Sabaka et al., 2004). In these models the ionospheric and magnetospheric sources are parametrized by toroidal and potential fields depending on a great number of parameters. Other models use a decomposition of the Dst(t) time series into external and induced parts, using an 1D model of the electrical conductivity of the mantle (Olsen et al., 2005b; Olsen et al., 2009) in the form

$$Dst(t) = E_{Dst}(t) + I_{Dst}(t). \tag{2.26}$$

Other technique consists in parametrize the magnetosphere and associated induced fields by solving for time-varying degree-1 coefficients ($n = 1$, $m = 0$) in Eq. 2.9 into bins of some hours (from 1 to 12 hours) length, where the field is treated as static. The idea behind is that a separating the external time variations into small bin sizes would help in the determination of high-degree secular variation (Olsen et al., 2009).

As a way to improve the time variability of the external sources in a model, Olsen et al. (2014) derived a new geomagnetic index, called RC, which describes the strenght of the magnetospheric ring current even during quiet conditions, when the baseline of Dst is less stable.

Other approaches exist like describe the temporal variations of the external Gauss coefficients by B-splines, with knots separated by a small time interval for e.g., 3 months (Lesur et al., 2010); or the adoption of other geomagnetic indices like the VMD (Thomson and Lesur, 2007), designed to monitor rapid variations in both the strength and direction of the large-scale external fields.

2.3 The effect of neglecting the external fields

A number of main field and secular variation models neglect the external fields contribution. In fact these contributions are small (see for e.g., Eq. 2.21) when compared to the main field. However, the temporal variability of the external field is significant in magnitude, often 5-10 $\mathrm{nT.yr^{-1}}$, compared to the magnitude of the secular variation of the main field (~ 25 $\mathrm{nT.yr^{-1}}$). Neglecting the external sources will thus be in principle more important for models of secular variation than for main field models. Additionally, not modelling the external sources may introduce spurious effects to the internal contribution. Although the spherical harmonic external field should be, in theory, orthogonal to the internal one, the usual data distribution does not allow this orthogonality (Langel, 1987).

2.4 Core and crust contributions

It is generally agreed that at the Earth's surface ($r = a$) the magnetic field is dominated by the main (core) field for degrees $n \leq 13$ and by the lithospheric field for degrees $n > 15$ (Lowes, 1974; Langel and Estes, 1982). This arises from the interpretation of the "spatial power spectrum" of the geomagnetic field. This spectrum was introduced by Mauersberger (1956) and popularized by Lowes (1966, 1974) (thus called the Mauersberger-Lowes spectrum) and is a quantity that represents the power of the magnetic field for a given spherical harmonic degree n, of spatial

wavelength $\lambda_n = 2\pi r/(n+1)$ (where $\lambda_{n=13} \sim 3000$ km):

$$R_n(a) = (n+1)\sum_{m=0}^{n}\left[(g_n^m)^2 + (h_n^m)^2\right]. \tag{2.27}$$

For the field which originates from the core, Eq. 2.27 can be downward continued:

$$R_n(r) = R_n(a)\left(\frac{a}{r}\right)^{2n+4}. \tag{2.28}$$

The spatial wavelength λ_n expression clearly points out that higher degree (higher n) correspond to smaller spatial scales. Figure 2.2a displays the Mauersberger-Lowes (Eq. 2.28) spectrum predicted by the internal field models CHAOS (Olsen et al., 2006b) and CM4 (Sabaka et al., 2004), and by a crustal field model MF5 (Maus et al., 2007). This figure shows the dominance of the dipole ($n = 1$) component in the internal field, and that the spectrum has two almost linear branches, with a transition from descending to ascending around degree 14. Both internal and crustal fields could comparably contribute to degree 14. It is considered that the internal field could only be recovered with some precision for $n \leq 13$.

Satellite data helped to improve the magnetic field modelling by providing more and globally distributed data. This improvement can be seen from the spatial energy spectra of the first time derivative of the geomagnetic field (calculated from the first time derivative of the Gauss coefficients, $\dot{g}_n^m$, $\dot{h}_n^m$) of various models as displayed on Fig. 2.2b. A model using the first months of MAGSAT data (Langel and Estes, 1985) displays a "flat" behaviour indicative of noise, for degrees $n > 6$. The addition of more data allowed to decrease the noise level by ~ 40 nT.yr^{-1} (Langel et al., 1988b). A major improvement was possible by Ørsted observations and the secular variation is resolved up to $n = 11$ (OSV model, Olsen (2002)). With the inclusion of more satellite data, thanks to CHAMP, models using a combination of data resolve the secular variation up to $n = 13$ (POMME-2 and GRIMM-2 models, (Maus et al., 2005b; Lesur et al., 2010)) and up to degree $n = 15$ with a noise level as low as 0.02 (nT.yr^{-1})^2 (CHAOS-4 model, Olsen et al. (2014)). However, these models represent a mean secular variation averaged over several years, because they were determined using temporal regularization, which for the

higher degrees should be different from an instantaneous secular variation (Olsen and Stolle, 2012).

It is also possible to resolve the secular acceleration (SA), as can be seen in the spectra on the same figure (Fig. 2.2b). The SA spectra are quite different, showing that the different temporal regularizations of the models influence how they resolve the second time derivative of the field. The main field small scales ($n > 13$) cannot be inferred due to the crustal contribution (Fig. 2.2a). Despite that, as the crustal field is time independent (on the timescales here considered), the main field time changes can be in principle inferred for smaller scales ($n \geq 15$) than the main field itself.

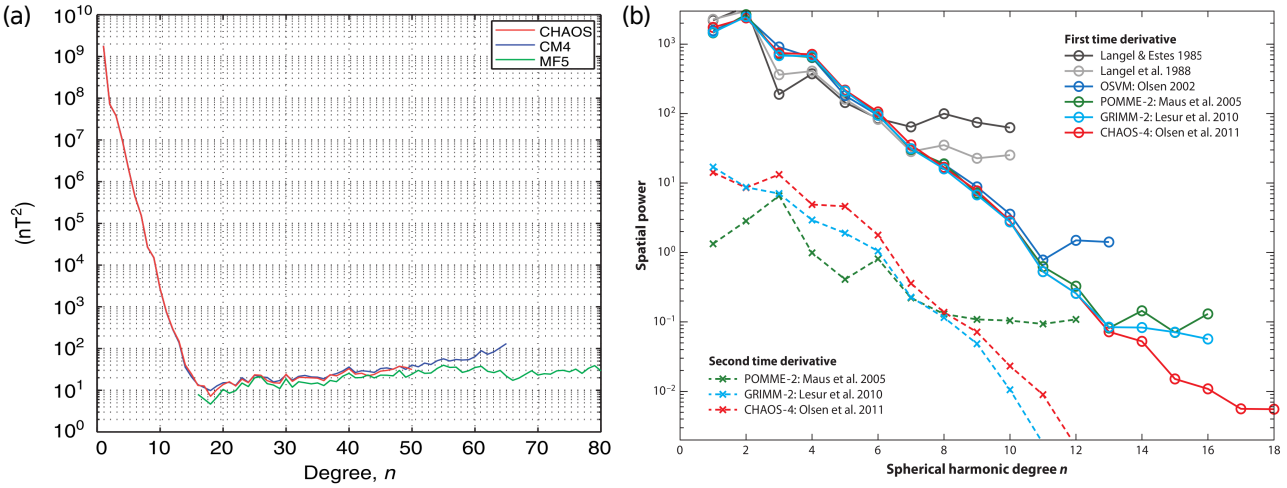

Figure 2.2: (a) Spatial power spectrum of the geomagnetic field (in nT^2) for different models, at the Earth's surface. Figure from Olsen et al. (2007). (b) Spatial power spectrum of first time derivative (secular variation, solid curves, in $(nT.yr^{-1})^2$) and second time derivative (secular acceleration, dashed curves in $(nT.yr^{-1})^2$) of the geomagnetic field for various magnetic field models, at the Earth's surface. Figure from Olsen and Stolle (2012).

2.5 Modelling strategies of the geomagnetic field

Spherical harmonics is the usual representation in global models of the main geomagnetic field. The first models attempted to describe the internal field by application of Eq. 2.8 (sequential approach). The signals from other sources (external, induced) were treated as noise. To model other fields and/or exclude non-main field signals from the measurements some procedures are

taken like performing data selection, use a simple (or complex) parametrization of the external fields, apply damping and/or add error covariance matrices in the inversion scheme. These procedures can be used together or in different combinations. The models can then be very different due to the different choices of selection and parametrization.

2.5.1 Sequential approach: CHAOS, GRIMM and others

Nowadays geomagnetic field models take advantage of the recent satellite data which increases their complexity and accuracy. Ørsted Initial Field Model (OIFM) was one of the first satellite-based models (Olsen et al., 2000), and it was computed as a snapshot of the main field at epoch 2000.0, using only a few weeks of Ørsted data. It employed data selection using geomagnetic indices (see Section 1.5.2), selecting only night time data and used only intensity data for magnetic latitudes greater than 50^o to minimize the signals from the FACs (cf. Section 1.3). The main field for OIFM was computed up to SH degree 19. The magnetospheric field sources were parametrized by a potential field with static part (up to degree 2), a time varying part of external origin and also an induced field (both of degree 1) whose temporal variation depends on the Dst index. The OIFM took also into account correlated attitude errors of the data using covariance matrices.

The succeeding models were designed in a similar way, using more data (longer time periods and/or less strict data selection) and solving also for the secular variation (Olsen, 2002; Langlais et al., 2003; Lesur et al., 2005). An IRLS scheme with Huber weights has been used as an improved statistical way to deal with data errors (Constable, 1988). The large-scale magnetospheric contributions are now also modelled with annual and semi-annual periodicity in their zonal terms, and the rapidly changing part was parametrized not using Dst but the new $\tilde{RC}$ index, also estimated from ground observatories (Olsen, 2002).

As more satellite data was made available a more complex way to model the time variations was needed. Taylor expansions around a specific epoch or cubic B-splines were used (see Section 2.2). Recent models use the Taylor expansion up to the quadratic term, like the POMME model series (Maus et al., 2005, 2006). This model uses exclusively satellite data (CHAMP and

Ørsted). The POMME magnetic field model uses damping in its inverse scheme to control the first and second time derivatives. The data selection is strict, not only using geomagnetic indices but also a selection based on ionospheric plasma instabilities (Stolle et al., 2006). Corrections for magnetospheric currents using a criteria based on the state of the interplanetary field (IMF)[1], oceanic tidal signals (Kuvshinov and Olsen, 2005), and gravity-driven ionospheric currents in the F-layer (Maus and Lühr, 2006) were also implemented. These corrections led to a more accurate estimation of the field, especially for the secular variation. The POMME model is today in its 7th version[2], spanning up to SH degree 133. Some changes in the parametrization of the external currents have been made during the derivation of the last versions. But the idea is always to subtract external contributions to the main field by using indices like the solar flux index F10.7 (which is a measure of the noise level generated by the sun at the wavelength of 10.7 cm at the Earth's orbit i.e., an indicator of solar activity[3]).

The CHAOS series of models (Olsen et al., 2006b) aim at describing core field changes with high spatial resolution of the first time derivative and high temporal resolution of the rapid field changes, using a multi-year continuous time series of satellite and observatory data (10 to 20 years). The model consists of SH expansion coefficients describing the magnetic field vector in an "Earth-Centered Earth-Fixed" (ECEF)[4] coordinate system and sets of Euler angles needed to rotate the satellite vector readings from the magnetometer frame to the star imager frame. (Olsen et al., 2014). It uses the B-spline approach to model the temporal variation. Usually the time-dependence of the low degree coefficients ($n \leq 20$) are described by B-splines (cubic in CHAOS, but of order 6 in CHAOS-4, Olsen et al. (2014)), while the higher coefficients are static. Damping is also used to control second and sometimes third time derivatives of the radial component of the field (B_r). The external sources (mainly magnetospheric) and their induced counterparts are parametrized with an expansion of the near magnetospheric sources (ring current) in the Solar Magnetic (SM)[5] coordinate system (up to $n = 2$) and of remote

[1]More information can be found in `http://omniweb.gsfc.nasa.gov/html/ow_data.html`.

[2]`http://www.geomag.org/models/pomme7.html`

[3]More information can be found in `http://omniweb.gsfc.nasa.gov/html/ow_data.html`.

[4]Earth-Centered Earth-Fixed. Conventional terrestrial system. The Z-axis is aligned with the mean rotation axis and points north. The X-axis intersects the sphere of the Earth at 0° latitude (Equator) and 0° longitude (Greenwich).

[5]Solar Magnetic coordinates: in this system, the Z-axis is chosen parallel to the north magnetic pole and the

magnetospheric sources (e.g., magnetopause currents) in the Geocentric Solar Magnetospheric (GSM)[6] coordinates (up to $n = 2$, but restricted to order $m = 0$). The SM coefficients of $n = 1$ depend explicitly on time, with an expansion of external and induced parts of the index RC (Olsen et al., 2014). This translates into a modification of Eq. 2.25 in the form

$$q_1^0 = \hat{q}_1^0 \left[\epsilon(t) + \iota(t) \left(\frac{a}{r} \right)^3 \right] + \Delta q_1^0(t), \tag{2.29}$$

where $\epsilon(t)$ and $\iota(t)$ are the time-dependent magnetospheric ring-current and its Earth-induced counterpart field contributions as estimated by the RC index, respectively, $\hat{q}_1^0$ is a static regression value, and $\Delta q_1^0(t)$ is a baseline correction computed in bins of 5 days. In addition, the CHAOS model series co-estimate the Euler angles describing the rotation between the vector magnetometer frame and the star imager frame (cf. Section 1.6.1). The latest model of this series, CHAOS-5 (Finlay et al., 2015), took advantage of the recent Swarm measurements and served as a parent model for the DTU Space IGRF-12 candidate models (see Section 2.6.1).

The GRIMM models (Lesur et al., 2008) aim at describing both the core and the lithospheric fields. The model is built from satellite (only CHAMP) and observatory hourly means (less than 10 years) and parametrizes large-scale external contributions and their induced counterpart. Data selection is different from the one made by CHAOS, as it used different indices to minimize external contributions and also uses vector data at polar latitudes (contrary to CHAOS). Time variations are described by order 6 B-splines for the internal field and order 2 for the external field. A quadratic smoothing semi-norm is applied as a regularization process. The core and lithospheric fields are modelled sequentially for GRIMM-2 (Lesur et al., 2010). The second generation is also oriented towards core field studies. The data selection is strict but it is also built such that the SV remains accurately described (Lesur et al., 2011).
Both CHAOS and GRIMM models showed that the second time derivative (secular acceleration) of the core field has a high temporal variability (cf. Fig. 2.2b).

Y-axis perpendicular to the Earth-Sun line towards dusk. The X-axis does not point directly at the Sun. The SM system rotates with both a yearly and daily period with respect to inertial coordinates.

[6]Geocentric Solar Magnetospheric system: the X-axis are from the Earth to the Sun. The Y-axis is defined to be perpendicular to the Earth's magnetic dipole so that the X-Z plane contains the dipole axis. The positive Z-axis is chosen to be in the same sense as the northern magnetic pole.

Technically, all referred models are similar. The main differences are in the way time dependences are dealt with, either for the internal field or external and induced fields. Differences between these main field models usually do not exceed 13 to 16 nT at any place on the Earth's surface up to degree 13. For the SV models the comparison is difficult. Usually above degree 12 all SV estimates are averages over the full range of data ($\sim$ 10 years of satellite data). Spatial regularization is always needed to avoid excessive power in small wavelengths on the CMB. The accuracy of such models SV for degree 1 is also lower than one could expect as it is difficult to separate contributions from the large magnetospheric field on small time periods of data. For higher time derivatives (like SA) such models are still less accurate (Lesur et al., 2011), even if some agreement is found up to degree 8.

2.5.2 Other modelling approaches using SH

A new approach arose, known as comprehensive modelling (CM), aiming at making the best of observatory and satellite data and co-estimate models of the internal, magnetospheric and ionospheric (including their induced counterparts) in the same (huge) inversion scheme. The previously mentioned sequential models did not model the ionospheric field as its sources are located between the ground-based observatories and the satellite observations. The CM approach, on the other hand, models the ionospheric field as well. The idea is to separate the sources originated:

- below the Earth's surface;
- by the potential field produced by the ionospheric currents flying in the E-region (110 km altitude);
- by the toroidal field locally produced in the ionospheric F-region (up to 1000 km altitude), at altitude $r = R$;
- and the potential field produced by all sources above $r = R$.

Futhermore, the first comprehensive models (Sabaka and Baldwin, 1993; Sabaka et al., 2002) used not only satellite data but also a longer time series of ground magnetic measurements

(beginning in 1960), in a compromise between good data and a better temporal constraint of the magnetic field.

A number of practical limitations exist, thus an elaborated approach is needed. The uneven spatial distribution of ground observatories is a limitation. Another limitation is the time needed by satellites to complete a good coverage of the globe, as during this time (a few days for a single satellite, but depending on the satellite orbit) the ionospheric and magnetospheric fields could significantly change (today with Swarm this limitation should be less problematic). An important limitation is that there are toroidal currents between the E-region and the satellite orbit (e.g., Stolle et al., 2006). Another limitation is that the field originated below the Earth's surface is the sum of the core and lithospheric fields and also the externally-induced currents. These models rely on geomagnetic indices to select data at quiet-times. The external fast changing field (magnetospheric field, mainly dipolar) is parametrized by the Dst index. Other external fields are parametrized by known sun-related temporal periodicities. The crustal field is taken as static and the temporal changes of the core field are taken as having longer timescales than the external field. A B-spline expansion is used for the description of the internal lowest degrees temporal variations. The F-region toroidal currents are the limiting issue of these models and together with non-modelled field sources are dealt as noise (Olsen et al., 2007).

The latest version of the CM series is the CM5 (Sabaka et al., 2015). It is derived from over 12 years of satellite data (CHAMP, Ørsted and SAC-C) and observatory data, using the Swarm Level-2 Comprehensive Inversion (CI) algorithm (Sabaka et al., 2013). The CM5 includes a new treatment for attitude error in satellite vector measurements, a 3-D conductivity model of the ionospheric induction and a new weighting scheme. A strict data selection is employed Fig. 2.3), selecting only nightside and quiet-time data. The model successfully extracts the oceanic M_2 tidal magnetic field, improved the lithospheric field recovery over the older CM4 model (Sabaka et al., 2004), and the 3-D induction modelling captures anomalous solar-quiet departures in coastal observatory daily records. Its description of lithospheric, ionospheric and oceanic M_2 tidal fields is considered satisfactory to serve as validation tool for the Level-2 Swarm products.

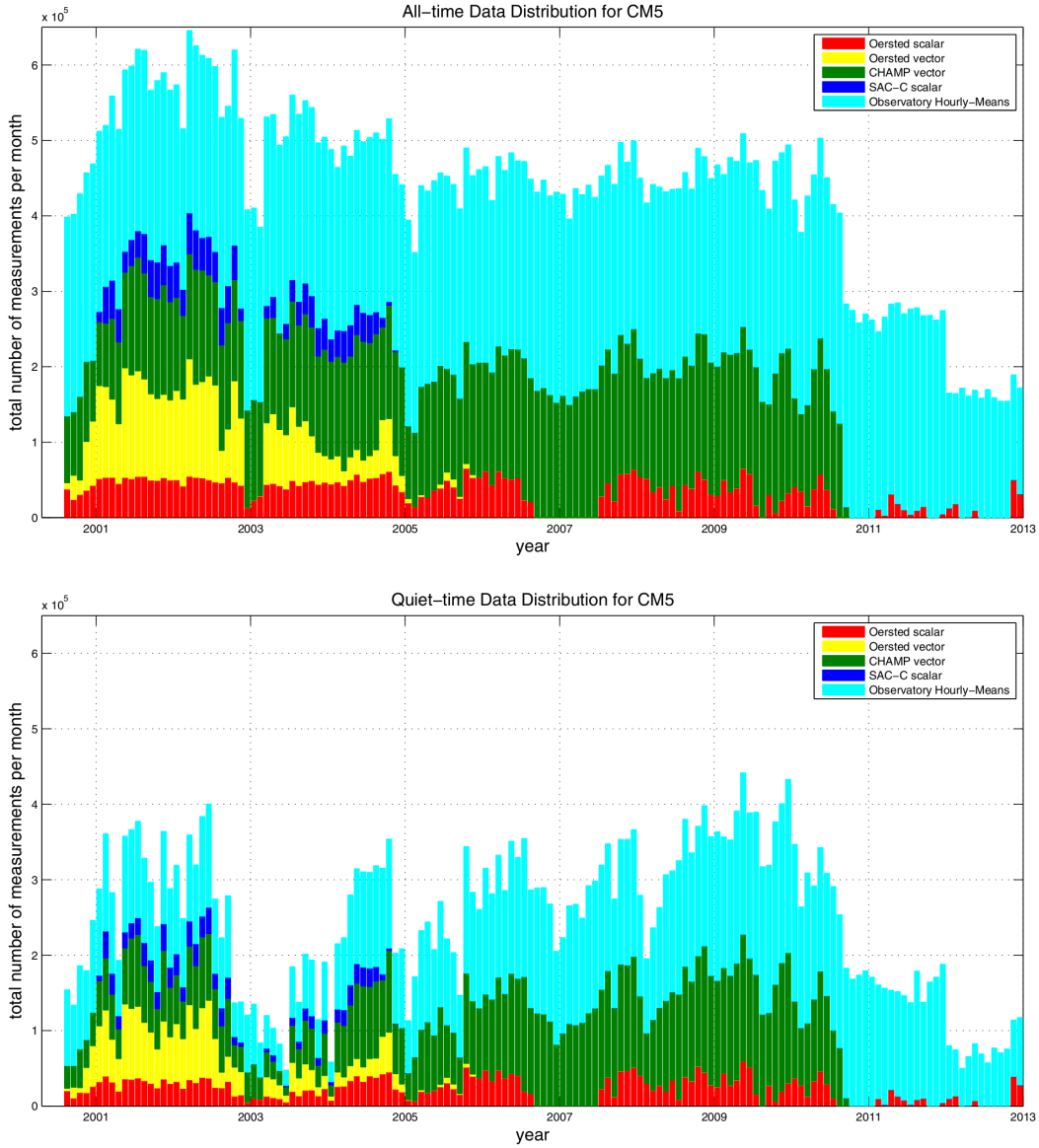

Figure 2.3: Histograms of the number of measurements from all geomagnetic times (*top panel*) and geomagnetic quiet-times (*bottom panel*) used to derive the CM5 model as a function of time. Note that both plots have the same scale and legend. A vector measurement counts as 3 measurements. This figure illustrates the great reduction of available data when strict data selection is applied. Figure from Sabaka et al. (2015).

Other models attempt to incorporate physical constraints. An example is the model derived by Wardinski and Holme (2006) termed C^{3}FM (Continuous Covariant Constrained endpoints Field Model). The model temporal variation is described by B-splines and it is derived from observatory and repeat station monthly and annual means, between 1980 and 2000. The model does not use absolute field values but estimates of the secular variation (following Eq. 1.8).

The authors search models that would be smooth at the CMB and that also fit the data at the Earth's surface, so their model is derived in a way to be as close as possible to a priori field models derived from satellite data (Cain et al., 1989; Olsen, 2002). In 2012 an extended version of C^3FM was derived (Wardinski and Lesur, 2012), using a new method which satisfies the frozen-flux constraint (the frozen-flux idea is that at the CMB the diffusion of the magnetic field can be neglected, see for e.g., Roberts and Scott (1965)). No parametrization is done to describe the external and crustal fields.

Other such model is the one by Jackson (2003), which uses a few months of satellite data from MAGSAT (epoch 1980) and Ørsted (epoch 2000) to compute two snapshot of the magnetic field at the CMB. The model does not account for external or crustal fields. It is directly computed at the CMB in equally spaced nodes by a series of constraints, such as the total fluxes outgoing (resp. ingoing) on the CMB in 1980 and 2000 are equal (i. e., frozen-flux). The model is then expressed in the form of Gauss coefficients. This so-called maximum entropy approach looks for as many high-degree Gauss coefficients as tolerated by the data in order to sharpen the small-scale features, otherwise distorted by a simply truncated model or smoothed by a model using high regularization. But this approach might also sharpen features that are not sharp.

Gillet et al. (2013) proposed the stochastic approach. This approach complements the information given by observations with some a priori information on the time evolution of the geomagnetic field, through time covariance functions. The time series of spherical harmonic coefficients are seen as realizations of a continuous and differentiable stochastic process, mainly relying on two properties of magnetic observatory records: time spectra and existence of geomagnetic jerks. The a priori information allows to use the model errors, estimated from the posterior covariance matrix, in data assimilation algorithms used to re-analyse or forecast the core dynamo dynamics (see below). The latest of such models, termed COV-OBS.x1 (Gillet et al., 2015), covers observatory data since 1840, and it is constrained at recent epochs by first differences of observatory annual means and satellite data, including from Swarm (until epoch 2014.6). It estimates internal and external fields, even if the latter are handled in a simple way (single coefficient for the axial dipole in geomagnetic dipole coordinates) compared with models using exclusively recent observations (Gillet et al., 2015), due to the compromise with a long

time-span of measurements. The internal field is expanded up to $n = 14$ and all coefficients are projected onto order 4 cubic B-splines, with a 2-year knot separation. An a priori covariance matrix on the model coefficients is used instead of the commonly regularization procedures (second and third time derivatives penalization and damping on spatial norms). Candidate models for IGRF-12 were derived from an ensemble of COV-OBS.x1 SV and MF coefficients realizations, with associated errors (Gillet et al., 2013).

Approaches aiming at forecast the magnetic field and based on variational geomagnetic data assimilation emerged recently (Fournier et al., 2007; Liu et al., 2007; Canet et al., 2009). The IPGP parent model for IGRF-12 candidate models was derived from this method (Fournier et al., 2015). An initial model is constructed (by the sequential approach referred above) and then fed to a geodynamo inversion as an initial condition. This initial condition is added to the initial numerical condition of the geodynamo model, built by a run of the model unconstrained by data. Then, the geodynamo inversion runs are used to forecast the secular variation for the next 5 years. The field is then computed by a deterministic integration (Fournier et al., 2015). For a detailed description of data assimilation applied to geomagnetism see for e.g., Fournier et al. (2010). Other methods to forecast the geomagnetic field have been implemented, see e.g., Whaler and Beggan (2015).

2.5.3 Other approaches not using SH

Global representations of the magnetic field not using SH exist, and have been used. Some methods are based on either dipole or monopole equivalent sources distributed over a surface (Mayhew and Estes, 1983; Langel, 1987; O'Brien and Parker, 1994). An equivalent source dipole technique was used during this thesis, and is described in the next chapter. These methods using equivalent sources have been mostly applied in the context of geomagnetic crustal field modelling. They have also been used to describe the remanent magnetic field of Mars (Langlais et al., 2004), or to model the magnetic field of Mercury (Oliveira et al., 2015).

One of the disadvantages of the spherical harmonics representation is its difficulty to address poor and/or uneven geographical distribution of data. If a region has a high concentration of

measures and the field is complex, high-degree spherical harmonic may be required to describe very well the field on that region, but for another region less represented by data, it will generate "ringing effects", i.e., excessive power at the truncation degrees corresponding to small length scales (Olsen et al., 2007). Strategies were developed to avoid this ringing, such as the so-called harmonic splines (Shure et al., 1982). Those splines are linear combinations of harmonics, and the model is maximally smoothed according to some objective criteria and yet consistent with the data. A detailed description can be found in Langel (1987).

Lesur (2006) proposed another method, derived from a set of functions represented in terms of SH of a given maximum degree L and centred at specific latitudes and longitudes. The number of such functions and their position centres are chosen to model any potential field up to $n = L$. The functions can be transformed to the classical SH representation. This technique is adequate to either regional or global geomagnetic field models.

Wavelets are also a strategy proposed to deal with uneven data distribution and/or very localised sources needed to be accounted for (as ionospheric sources with satellite data). Wavelets are local, with only small-scale wavelets where needed, making it possible to use a model with few parameters. Global geomagnetic field modelling using wavelets was introduced by Holschneider et al. (2003) and Chambodut et al. (2005). It was also used to modelling small-scale crustal field (Mayer and Maier, 2006).

An alternative approach consists in combining regional field representations by putting together a large coverage of regional models, with adjusted resolutions. One of the techniques that could be used is the so-called spherical cap harmonic analysis (SCHA) first introduced by Haines (1985). Thébault et al. (2006) modified the approach and called it Revised SCHA (R-SCHA).

A revision of these and other methods to model the geomagnetic field both on global and regional scales can be found in Langel (1987) or Schott and Thébault (2011). The availability of high quality satellite and observatory data sets combined with new advanced techniques will continue to allow in the future the advance of geomagnetic field models.

2.6 Building a field model: the case of IGRF

The International Geomagnetic Reference Field (IGRF) is a series of models describing the Earth's large-scale main field and its secular variation, between epochs 1900 A.D. and the present. It is the International Association of Geomagnetism and Aeronomy (IAGA, a member of the International Union of Geodesy and Geophysics, IUGG) that since 1965 (Zmuda, 1971) organizes the production of the models. It results from an international effort of a number of scientific groups to produce the most accurate model of the main geomagnetic field at a given epoch. The scientific groups combine magnetic field modelers and the institutes involved in collecting and disseminating magnetic field data from magnetic observatories, ground surveys, and low Earth orbiting (LEO) satellites. The IGRF is widely used in studies on the crustal magnetic anomalies, magnetospheric field contributions and in space weather. It is used as a source of orientation information by commercial organizations and/or individuals.

Table 2.1: Evolution of the IGRF, with each generation interval of validity and related references. Adapted from Thébault et al. (2015b) and Barton (1997).

Name	Valid for	Definitive for	Reference
IGRF-12	1900.0-2020.0	1945.0-2010.0	Thébault et al. (2015b)
IGRF-11	1900.0-2015.0	1945.0-2005.0	Finlay et al. (2010)
IGRF-10	1900.0-2010.0	1945.0-2000.0	Maus et al. (2005)
IGRF-9	1900.0-2005.0	1945.0-2000.0	Macmillan et al. (2003)
IGRF-8	1900.0-2005.0	1945.0-1990.0	Mandea and Macmillan (2000)
IGRF-7	1900.0-2000.0	1945.0-1990.0	Barton (1997)
IGRF-6	1945.0-1995.0	1945.0-1985.0	Langel (1992)
IGRF-5	1945.0-1990.0	1945.0-1980.0	Langel et al. (1988a)
IGRF-4	1945.0-1990.0	1965.0-1980.0	Barraclough (1987)
IGRF-3	1965.0-1985.0	1965.0-1975.0	Peddie (1982)
IGRF-2*	1955.0-1980.0	—	IAGA (1975)
IGRF-1	1955.0-1975.0	—	Zmuda (1971)

*Same as IGRF-1 (IGRF 1965) extended to 1975.0.

The first IGRF model was adopted in 1968 for epoch 1965.0, and named IGRF 1965. Zmuda (1971) described its purpose as being "to form an agreed basis for the main field calculations and to unify results in studies". The model was based on the results of a dozen or so research groups

around the world. It was supposed to be valid from 1955 to 1972, and it was truncated to degree $N = 10$ in both main field and secular variation terms. This first version was then updated six times (Barton, 1997). Table 2.1 provides a summary of the history of IGRF generations. As time progressed more accurate models were adopted and the Definitive Geomagnetic Reference Field (DGRF) models were introduced in 1981 to provide more accurate models for past epochs. They are named *definitive* because any further improvement of these retrospectively determined models is unlikely (Thébault et al., 2015b) i.e., the data sets employed cannot be improved significantly. At the present only the models from 1945 onward are considered definitive, as the data previous to 1945 can still be revised or completed.

The IGRF-designated models are eventually replaced by definitive models. At the moment the IGRF consists into a series of models at 5-year intervals. It has to be regularly revised with newly acquired data to be able to continuously follow the temporal and spatial changes of the geomagnetic main field. The period between revisions is however sufficiently short to preserve its utility as a reference model in applications requiring a fixed reference standard (Thébault et al., 2015b).

Each IGRF generation consists now on a set of three components: 1) the DGRF, the definite model from 1945 A.D. to the epoch of the latter IGRF generation; 2) the IGRF, that is not definitive and that could be replaced by the respective DGRF in the next generation; 3) the predictive secular variation, provided to predict the time variation of the large scale geomagnetic field for the 5 years following the latter IGRF generation. Every time a new IGRF is computed all the data available covering the desirable period, especially the last five years is taken into account. Then candidate models in the form of Gauss coefficients (g_n^m,h_n^m) for the main field and ($\dot{g}_n^m$,h_n^m) for the secular variation are produced by the various independent scientific teams, usually applying simple classical techniques (Olsen et al., 2007).

Since the 9th generation of IGRF (Macmillan et al., 2003) Gauss coefficients are computed up to SH degree and order 13 for the field, and up to SH degree and order 8 for the secular variation. All coefficients are rounded at 0.1 nT or 0.1 nT.yr^{-1}, respectively. The maximum truncation degree N = 13 is defined so as not to include the crustal magnetic field contributions

that dominate at higher degrees (Langel and Estes, 1982).

The candidate models are then assessed by the IAGA Working Group V-MOD (for e.g., Lowes et al., 2000; Maus et al., 2005a; Finlay et al., 2010; Thébault et al., 2015a) and a weighting scheme is derived to calculated from them the final IGRF model. The IGRF/DGRF series advantage is their simplicity and the fact they can predict the field for the following (five) years. However, the usual employed simple modelling is limited in its temporal and spatial parametrization, thus caution should be taken. One must be aware of their limitations. Maus et al. (2005a) note that IGRF for 2005.0 "is estimated to have a formal root mean square error over the Earth's surface of only 5 nT, though it is likely that the actual error is somewhat larger than this", while "the corresponding errors of the adopted secular variation model for 2005.0–2010.0 is estimated at 20 $nT.yr^{-1}$ (Olsen et al., 2007). This means that the error on the predicted field can be more than 100 nT at the surface of the Earth. To note that the IGRF predictions are only valuable for the large scale temporal variations of the main field and do not take into account the crustal sources that can reach several 100 nT" (Cohen et al., 1997).

2.6.1 The 12th-generation IGRF

The most recent IGRF is the 12th generation, named IGRF-12. In May 2014 the IAGA task force responsible for IGRF-12 (from the Division V Working Group V-MOD) requested candidate field models to be submitted by 1st October 2014. The requested models were:

- internal (main) field model for 2015.0 to SH degree and order 13 (IGRF-2015.0);
- internal (main) field model for 2010.0 to SH degree and order 13 (DGRF-2010.0);
- predicted average secular variation model for 2015.0-2020.0 to SH degree and order 8 (SV-2015.0-2020.0).

A number of scientific teams submitted their respective candidate models. The community of geomagnetic field modellers benefitted from by the timing of the call. It arrived some months after the launch of ESA's Swarm satellite constellation on November 2013 (see Section 1.6.3). All candidate models took advantage of this new set of data, despite the time interval restriction

of just ten months. While some candidate models relied only on Swarm measurements, others added them to their set of observatory and other satellite mission data. The number of institutions participating in IGRF-12 was larger than for any previous generation. That was possible due to the availability of ground and satellite magnetic data provided by different institutions and the cooperation between scientists. For information on the complete list of participants, please see the article on the final IGRF-12 by Thébault et al. (2015b), which is reproduced on Appendix B.1. The Laboratoire de Planétologie et Géodynamique de Nantes (LPG Nantes) submitted a main field and secular variation candidate models for the 12th generation of the IGRF. In the following section the description of these candidate models is presented.

2.6.2 The LPG Nantes candidate models

This section corresponds to the manuscript submitted to and published in Earth, Planets and Space by myself, B. Langlais, F. Civet, E. Thébault and M. Mandea. It presents the derivation of the magnetic field and secular variation candidate models submitted by the LPGN team to the 12th generation of the IGRF (Saturnino et al., 2015).

Saturnino *et al. Earth, Planets and Space* (2015) 67:96
DOI 10.1186/s40623-015-0262-7

Earth, Planets and Space
a SpringerOpen Journal

LETTER Open Access

Main field and secular variation candidate models for the 12th IGRF generation after 10 months of Swarm measurements

Diana Saturnino[1*], Benoit Langlais[1], François Civet[1], Erwan Thébault[1] and Mioara Mandea[2]

Abstract

We describe the main field and secular variation candidate models for the 12th generation of the International Geomagnetic Reference Field model. These two models are derived from the same parent model, in which the main field is extrapolated to epoch 2015.0 using its associated secular variation. The parent model is exclusively based on measurements acquired by the European Space Agency Swarm mission between its launch on 11/22/2013 and 09/18/2014. It is computed up to spherical harmonic degree and order 25 for the main field, 13 for the secular variation, and 2 for the external field. A selection on local time rather than on true illumination of the spacecraft was chosen in order to keep more measurements. Data selection based on geomagnetic indices was used to minimize the external field contributions. Measurements were screened and outliers were carefully removed. The model uses magnetic field intensity measurements at all latitudes and magnetic field vector measurements equatorward of 50° absolute quasi-dipole magnetic latitude. A second model using only the vertical component of the measured magnetic field and the total intensity was computed. This companion model offers a slightly better fit to the measurements. These two models are compared and discussed.We discuss in particular the quality of the model which does not use the full vector measurements and underline that this approach may be used when only partial directional information is known. The candidate models and their associated companion models are retrospectively compared to the adopted IGRF which allows us to criticize our own choices.

Keywords: Magnetic field; Main field; Secular variation; Modeling; IGRF; Time extrapolation

Findings

Introduction

The International Geomagnetic Reference Field (IGRF) is a time series of Main Field (MF) Spherical Harmonic (SH) Gauss coefficients aiming to describe the large-scale Earth's magnetic field of internal origin, also known as the main field. It is published every 5 years and includes a predictive Secular Variation (SV) part for the next 5-year period. IGRF models result from a collective and international effort, in order to derive the most accurate model of the main geomagnetic field at a given epoch.

Since the ninth generation of IGRF (Macmillan et al. 2003) Gauss coefficients are computed up to SH degree and order 13 for the static part and up to SH degree and order 8 for the secular variation part. All coefficients are rounded at 0.1 nT or 0.1 nT.yr^{-1}, respectively.

The latest 12th generation of the IGRF model comes almost 1 year after the successful launch of the ESA three-satellite Swarm mission on 22 November 2013. A full presentation of the mission and of some of its expected outputs can be found in Olsen et al. (2013), Chulliat et al. (2013), and Thébault et al. (2013). After an initial stage where all three satellites flew around 495 km, two satellites fly almost side-by-side at a nominal altitude close to 465 km, while the third one flies some 50 km higher. All three are on near polar orbits. Each satellite carries two magnetic field instruments on a boom. The first one is the Vector Fluxgate Magnetometer (VFM) and is co-mounted on an optical bench with the Star TRacker (STR) with three Camera Head Units (CHUs) to determine the attitude of the spacecraft. This is necessary to transform the vector readings into geocentric B_X, B_Y, and B_Z magnetic

*Correspondence: diana.saturnino@univ-nantes.fr
[1] Laboratoire de Planétologie et Géodynamique de Nantes, UMR 6112 CNRS, Université de Nantes, Nantes, France
Full list of author information is available at the end of the article

field components (horizontal northward, horizontal eastward, and vertical downward, respectively). The second one is the Absolute Scalar Magnetometer (ASM) and aims at providing very accurate 1 Hz absolute scalar measurements F for both scientific and VFM calibration purposes.

Our candidate model exclusively relies on the measurements made by the low-altitude Swarm A and C spacecrafts. In the following, we describe the data selection scheme. Because some discrepancies were observed between the scalar magnitude as computed from the VFM measurements and the ASM direct measurements, two datasets were built. In the first dataset, all VFM and ASM measurements were considered. In the second one, we disregarded the horizontal magnetic field components of the VFM measurements. These two datasets are used to derive two models, which are denoted V-ASM and Z-ASM, respectively. In the third section, we briefly describe the model parametrization, and compare and discuss the two models in "Comparison of V-ASM and Z-ASM models" section, justifying our decision to present the V-ASM model as our IGRF-12 candidate model. Finally, we retrospectively compare our models to the adopted IGRF-12 model, which allows us to underline the shortcomings of the chosen approach.

Data selection

Our models are based on Swarm A and C satellite measurements. This facilitates the identification of outliers as these satellites fly side-by-side. Whenever appropriate, the priority is given to versions RPRO301, OPER302, and OPER301 of the processed measurements. The following flags (Tøffner-Clausen 2013), although provisional, are used:

- `flags_B`: 0 or 1 (VFM is nominal or ASM is turned off);
- `flags_F`: 0 or 1 (ASM is nominal or running in vector mode);
- `flags_q`: between 0 and 6, or between 16 and 22 (at least two CHUs nominal);
- `flags_Platform`: 0 or 1 (nominal telemetry or thrusters not activated).

We then select measurements according to several parameters to reduce the importance of external fields. The Dst and Kp indices are used, as well as a local time selection:

- $-5 \leq \mathrm{Dst} \leq 5$ nT for the considered time;
- $|\ \mathrm{dDst/dt}\ | \leq 3\ \mathrm{nT.h^{-1}}$;
- $0^0 \leq \mathrm{Kp} \leq 1^+$;
- $\mathrm{Kp} \leq 2^-$ for the previous and following 3-h time intervals;
- local time between 20:00 and 4:00.

This latter selection criterion is preferred over a more strict one based on the illumination of the spacecraft. This would result in large gaps over polar areas during the summer of each hemisphere (Lesur et al. 2010). VFM and ASM measurements are used within $\pm$ 50° quasi-dipole magnetic latitude, while only scalar measurements by the ASM are considered in the polar areas. Known differences exist between intensity F measurements by the ASM and intensity B computed from VFM measurements, with a root mean square (rms) difference of the order of 1 nT. At the time of deriving the model, no official and definitive strategy has been defined, so we do not take these differences into account and do not scale VFM intensity to match ASM measurements. Instead, we overcome this problem by building two datasets. Both use intensity measurements, but while the first one is completed by full vector measurements, in the second one, we consider only the vertical component of the measurements. This means that the second dataset and associated model depend more moderately on these calibration issues.

In a preliminary stage, we also check data for possible outliers, by looking for possible large discrepancies between observations and predictions by a first version of our model. We chose to eliminate all data acquired on the days when such large discrepencies were observed (year–day of year): 2013352 (VFM), 2014084 (ASM and VFM), 2014085 (ASM and VFM), 2014098 (ASM and VFM), 2014099 (ASM and VFM), 2014181 (ASM), 2014182 (ASM), 2014185 (ASM), 2014188 (ASM). Only Swarm C measurements were eliminated in this step. We however note that this selection came only after data selection with respect to flags and indices. In the last stage of our approach, we further reject measurements associated with large residuals, exceeding 15 nT for B_Z, 25 nT for B_X or B_Y for the VFM, and 35 nT for the ASM (these arbitrary values are about five times the final rms difference). This corresponds to remove about 1 % of ASM measurements and 0.2 % of the VFM triplets.

Finally, data are decimated along tracks. Only one measurement every 15 days is kept, corresponding to a spacing of about 100 km along orbit. Data distribution is homogenized, keeping a maximum of three data points per $6 \times 6°$ bins per 15-day intervals. The resulting geographic and time data distributions are shown in Figs. 1 and 2, respectively. The local time drift of the spacecraft results in no vector triplets during two periods, at the beginning of the northern spring and at the end of the southern winter. During these two periods, the only data fulfilling our selection criteria are ASM measurements very close to the pole, i.e., where fast local time variations occur. This means that these measurements may be on the day side and above

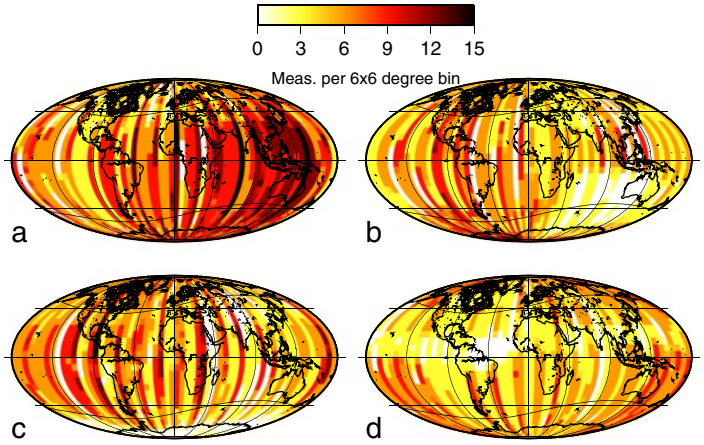

Fig. 1 Number of measurements per 6 × 6° bin, centered on the winter solstice (**a**), spring equinox (**b**), summer solstice (**c**), and autumn equinox (**d**)

the sun horizon, this is especially true for the measurements above the northern hemisphere in June and July.

Model parametrization and statistics

While IGRF MF and SV models are published up to SH degree and order 13 and 8, respectively, we computed parent models to higher degree to avoid possible aliasing (e.g., Whaler 1986). The static part of the internal field, described by g_n^m, h_n^m Gauss coefficients of degree n and order m, is computed up to SH degree 25 and the secular variation up to 13. Given the short time interval covered by the data (10 months), we assume a constant secular variation and do not consider secular acceleration. The external magnetic field is described by q_n^m, s_n^m Gauss coefficients. It is computed up to SH degree 2. A linear dependence with respect to the Dst index for the first degree is also considered with $\tilde{q}_n^m$ and $\tilde{s}_n^m$, with internal induced counterpart represented by Q_1. Internal and external magnetic potentials at spherical

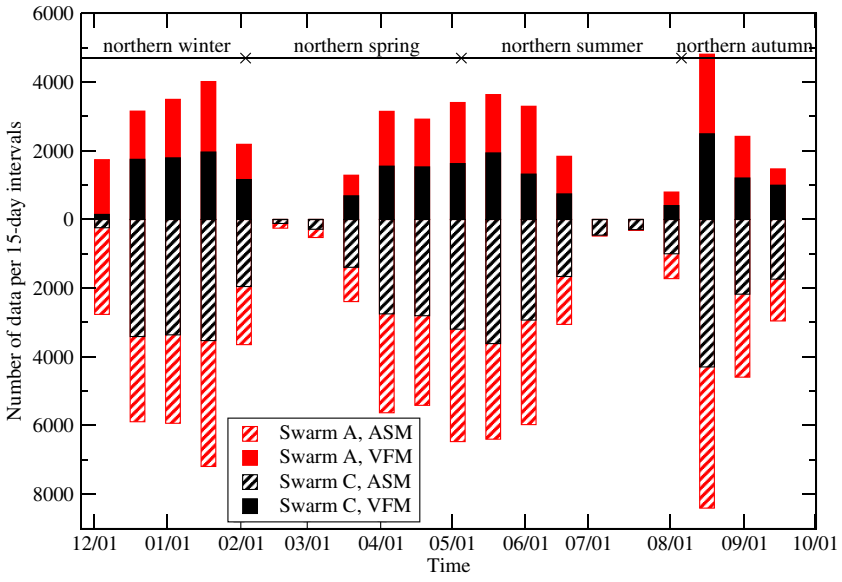

Fig. 2 Time distribution for Swarm A and Swarm C ASM and VFM measurements, per 15-day intervals. Seasons are indicated for comparison with Fig. 1

coordinates (r, θ, ϕ) are written as (e.g., Langlais et al. 2003):

$$V_{\text{int}}(r,\theta,\phi,t) = a\sum_{n=1}^{25}\left(\frac{a}{r}\right)^{n+1}\sum_{m=0}^{n}\left(g_n^m(t)\cos(m\phi) + h_n^m(t)\sin(m\phi)\right)P_n^m(\cos(\theta)) \quad (1)$$

$$\begin{aligned} V_{\text{ext}}(r,\theta,\phi,t) = {} & a\sum_{n=1}^{2}\left(\frac{r}{a}\right)^{n}\sum_{m=0}^{n}\left(q_n^m\cos(m\phi) + s_n^m\sin(m\phi)\right)P_n^m(\cos(\theta)) \\ & + Dst\sum_{n=1}^{1}\left[\left(\frac{r}{a}\right)^{n} + Q_1\left(\frac{a}{r}\right)^{n+1}\right] \\ & \times\sum_{m=0}^{n}\left(\tilde{q_n^m}\cos(m\phi) + \tilde{s_n^m}\sin(m\phi)\right)P_n^m(\cos(\theta)) \end{aligned} \quad (2)$$

where a is the Earth's reference radius (6371.2 km) and Q_1 is set to 0.27 (Langel and Estes 1985). The inverse problem is linearized and solved using a least square method (Cain et al. 1989). The choice of the initial model has no effect on the final result as long as it is close enough to the actual field, such as a model at a different epoch (e.g., Langlais et al. 2003). Convergence was reached after two iterations.

There are 881 coefficients to solve, using 38,437 Swarm A ASM scalar measurements, 22,320 Swarm A VFM vector triplets, 40,609 Swarm C ASM scalar measurements, and 21,292 Swarm C VFM vector triplets. The mean epoch of measurements is 2014.3. To overcome the denser data distribution close to the poles, we used a $1/\sin\theta$ weighting scheme (with θ being the colatitude). In the first model, we observed that the misfit for Swarm C was slightly larger than for Swarm A. Because both satellites essentially measure the same magnetic field, they should be associated with similar errors. We therefore chose to give more importance to the latter, with a 9/8 ratio, and weighted the data accordingly.

We give in Table 1 the statistics of the derived model, denoted V-ASM. As mentioned, the misfit associated with Swarm C measurements is slightly worse than that associated with the Swarm A measurements, with a 9/8 ratio (corresponding to the different weights allocated to both satellites). This is particularly true for the B_Y component, for which both the rms and the mean differences are 14 and 100 % larger, respectively. This fact, combined to the slight differences between the ASM scalar reading of the magnetic field intensity and the one computed from the VFM measurements, led us to explore an alternative modeling strategy.

It is not possible to model the Earth's magnetic field using only scalar measurements without any prior because of the so-called Backus effect. This effect comes from the non-uniqueness of the inverse problem and is characterized by focused large errors perpendicular to the measured field. This occurs mostly in the equatorial region, and it results in large differences in the vertical component. This effect was discovered and described when no spacecraft vector magnetic field measurements were available (e.g., Backus 1970; Hurwitz and Knapp 1974; Lowes 1975; Stern and Bredekamp 1975). Different strategies have been proposed to alleviate it. Hurwitz and Knapp (1974) were probably the first to include vector data in the equatorial region, to better constrain the position of the magnetic equator and resolve the sectoral harmonics. These additional data can be provided by the magnetic observatories, which have however a poor geographic distribution. Additional information can also be obtained from a triaxial magnetometer on board a satellite, which requires an accurate determination of the satellite attitude (Holme 2000; Holme and Bloxham 1995). Indeed, (Khokhlov et al. 1997, 1999) showed that it is possible to eliminate the Backus effect if the position of the geomagnetic equator (where $B_Z = 0$) is known. This position can be directly estimated by a time extrapolation from a previous or later epoch model (Ultré-Guérard et al. 1998a,b) or indirectly from measurements of the equatorial electrojet (Holme et al. 2005).

An approach similar to that of Ultré-Guérard et al. (1998a) was already employed in the context of IGRF modeling, but this was to test the quality of the candidate models rather than to propose a new model (Mandea and Langlais 2000). Here, we combine direct measurements of the position of the geomagnetic equator (i.e., vertical field measurements) to scalar measurements. The new model will not depend on the possibly more perturbed

Table 1 Root mean square and mean differences (in nT) for the two parent models and for Swarm A and C. The *B* misfit corresponds to intensity rms difference computed from the VFM dataset. *F* misfits are sorted with respect to the magnetic absolute latitude 50°

		Root mean square difference						Mean difference					
Model	Sat.	B_X	B_Y	B_Z	B	$F_{\leq 50}$	$F_{>50}$	B_X	B_Y	B_Z	B	$F_{\leq 50}$	$F_{>50}$
V-ASM	A	4.10	3.94	2.71	3.05	3.07	8.93	0.12	0.72	0.16	−0.09	0.01	−0.46
V-ASM	C	4.19	4.49	3.10	3.03	3.11	9.31	0.32	1.41	−0.07	0.19	0.18	−0.26
Z-ASM	A	4.38	4.14	2.51	3.04	3.05	8.91	0.58	0.74	0.23	−0.03	0.04	−0.14
Z-ASM	C	4.46	4.72	2.88	3.02	3.09	9.29	0.80	1.49	−0.04	−0.33	0.01	0.20

Table 2 Root mean square differences at the surface of the Earth (in nT) between the candidate models for different truncation degrees and different epochs. In the last row, only the SV is considered (in nT.yr^{-1})

Model 1	Model 2	Epoch	Degree	B_X	B_Y	B_Z	B
V-ASM	Z-ASM	2014.3	25	1.39	1.81	1.90	1.48
V-ASM	Z-ASM	2014.3	13	0.72	0.68	1.13	0.94
V-ASM	Z-ASM	2015.0	25	2.71	2.34	3.67	3.26
V-ASM	Z-ASM	2015.0	13	2.46	1.62	3.36	3.04
IGRF-12	V-ASM	2015.0	13	6.40	5.50	9.22	9.30
IGRF-12	Z-ASM	2015.0	13	6.77	5.87	9.77	9.90
V-ASM	Z-ASM	2015.0	8 (SV)	2.64	1.65	3.59	2.98

horizontal components (Table 1), and mismatch between B and F (below 50° absolute magnetic latitude) should not introduce any intrinsic error. This latter point is however debatable, as even the intensity of the measured vertical field depends on the measured F ASM value through the calibration process.

We give in Table 1 the statistics of this second model, denoted Z-ASM, derived using the second dataset. The rms difference for the B_Z component is improved, with a decrease of about 7 % for both satellites with respect to the V-ASM model. The misfit for F and B also display a slight decrease with respect to the V-ASM model. On the contrary, the rms differences for horizontal components and for both satellites are degraded, in a similar proportion than for the B_Z improvement. The mean deviation for B_X difference changes significantly from the V-ASM to the Z-ASM model, with an increase of 0.5 nT for both Swarm A and C datasets. A similar change is also observed for F in polar areas.

Comparison of V-ASM and Z-ASM models

We now compare our two models at the Earth's reference radius. We present in Table 2 rms differences between the models, for two different epochs (the mean epoch at 2014.3 and the reference epoch at 2015.0) and for the full expansion (i.e., $N^{\max} = 25$) or that truncated to SH degree and order 13 (corresponding to the IGRF candidate model). Our two models are very similar at their mean time, with differences of the order of 1.5 to 2 nT, for the full spherical harmonic expansion. These differences increase by a factor of 2 (except for B_Y) when both models are extrapolated to epoch 2015.0 (third row of Table 2) and decrease slightly when the models are truncated to degree 13 for the main field (fourth row).

The geographic distribution of the differences between V-ASM and Z-ASM truncated models is presented in Figs. 3 and 4 at their mean epoch and at 2015.0, respectively. These differences are dominated by both small scales (longitudinal B_Y and B_Z differences) and an almost dipolar pattern (East-West for B_Y and North-South for B_Z). This is confirmed when examining the differences coefficient by coefficient. We show in Fig. 5 these differences up to SH degree 13. The largest difference is 0.48 nT (for g_1^1), and it exceeds 0.1 nT for only 16 coefficients. Beyond SH degree 13, noticeable differences, between 0.1 and 0.2 nT, are only found for degree 15, 16,

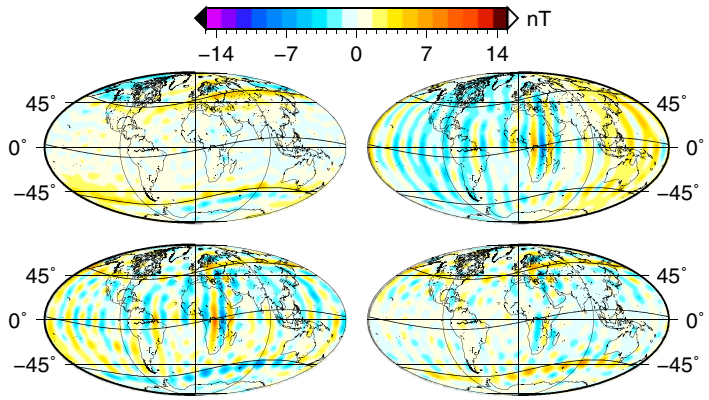

Fig. 3 Difference at Earth's mean radius between V-ASM and Z-ASM models at epoch 2014.3 and for the full expansion. From *top left* to *bottom right*, B_X, B_Y, B_Z, and B, respectively. Thin lines indicate magnetic equator and 50° magnetic quasi-dipole latitudes

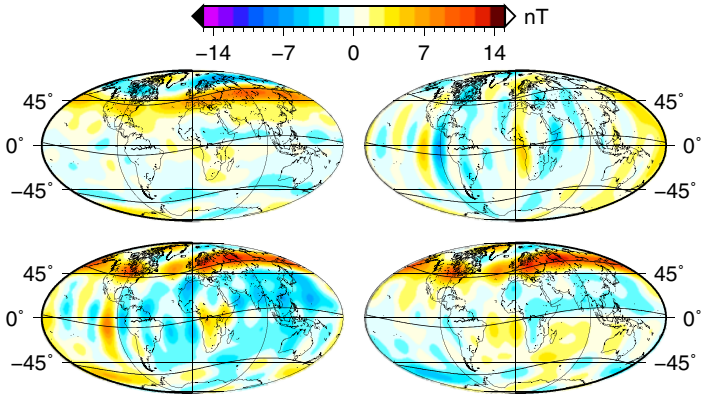

Fig. 4 Same as Fig. 3 between V-ASM and Z-ASM models at epoch 2015.0 and truncated to $n = 13$

and 17 sectoral coefficients (not shown). Together with those of the inclined dipole, they explain the geographic differences seen in Fig. 3. There are also some differences which coincide with the ±50° magnetic latitude data separation into scalar only and scalar plus vector measurements. These differences are moderate at the mean epoch of measurements, but they increase when the model is extrapolated to 2015.0, as seen in Fig. 4. Above northern Europe, the two models differ by more than 10 nT, except for B_Y. The difference is less important in the southern hemisphere.

When comparing the two SV models truncated at degree 8 (Fig. 6 and Table 2), we obtain differences with similar geographical patterns and comparable intensity values as for the MF model comparison. The coefficient comparison is shown in Fig. 7. The largest difference is 1.47 nT.yr^{-1} for g_2^0. The 11 coefficients with largest differences explain almost 90 % of total difference (2.54 versus 2.98 nT.yr^{-1} rms differences for the full model for B, with a correlation coefficient of 0.8 between the full model and that based on these 11 coefficients only).

We finally compare the spectra of the different models, which are presented in Fig. 8 at epoch 2015.0. Both V-ASM and Z-ASM MF models are very similar, and their differences do not exceed 4 nT^2 per degree. The differences between the two SV models are slightly larger, up to 8 nT^2.yr^{-2} per degree. Both V-ASM and Z-ASM models display larger energy in their secular variation spectra

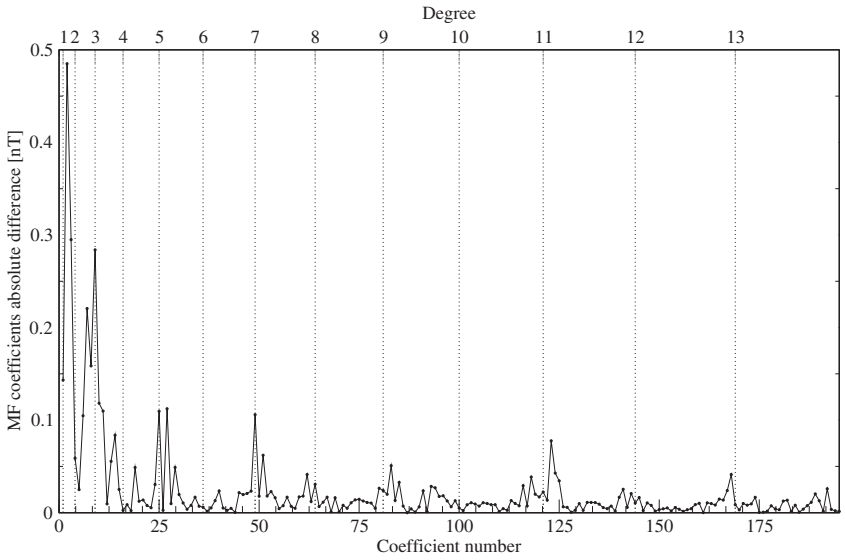

Fig. 5 Absolute difference of Gauss coefficients between V-ASM and Z-ASM models up to 13 at epoch 2015.0

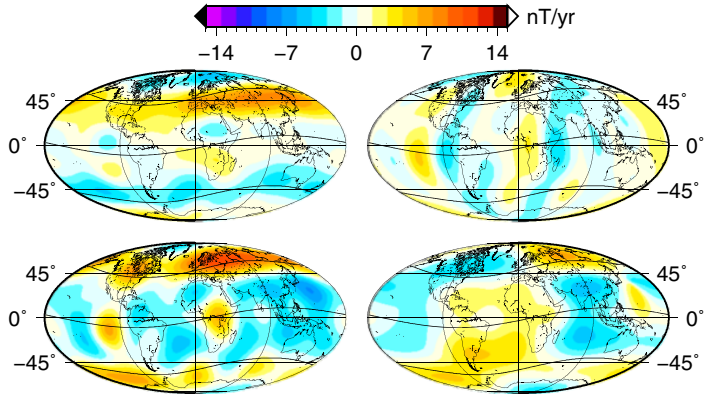

Fig. 6 Same as Fig. 3 between V-ASM and Z-ASM secular variation models at epoch 2015.0 and truncated to $n = 8$

for degree 10 and 12 terms, with the Z-ASM model being 50 % more energetic than the V-ASM model for these two terms. Although these SV coefficients are not directly included in the SV candidate model for IGRF, these may affect our MF candidate model when it is extrapolated to epoch 2015.0, and this is the reason why we eventually decided to present truncated versions of the V-ASM (MF and SV) model for IGRF candidate models. We nonetheless observe that the spectrum of our candidate model is probably too energetic for its SV part at SH degrees 7 and 8. It is likely that the SV is not constrained enough when using less than 1 year of measurements (e.g., Barraclough 1985; Langlais et al. 2003).

Comparison with the IGRF-12 model

We now compare our candidate and our test models (which are truncated and extrapolated versions of the V-ASM and Z-ASM parent models, respectively) to the adopted 12th IGRF generation. This a posteriori comparison is only possible because IGRF was adopted between the time at which we computed our candidate models and the time at which this study is written (Thébault et al. 2015b). Note that IGRF models depend, among others, on our candidate models.

Statistics are given in Table 2. We also show geographic differences between IGRF and our candidate models in Fig. 9 and compare the different spectra in Fig. 8. A more

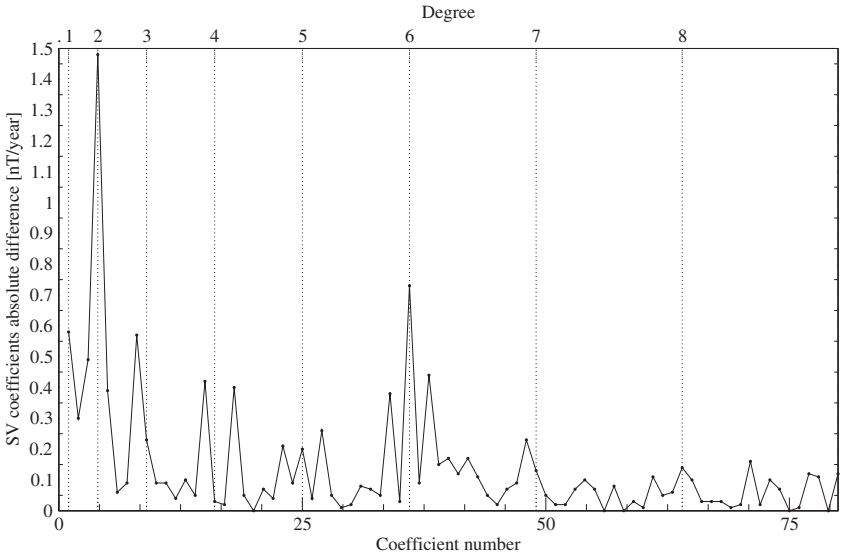

Fig. 7 Absolute difference of Gauss coefficients between V-ASM and Z-ASM SV models up to degree 8 at epoch 2015.0

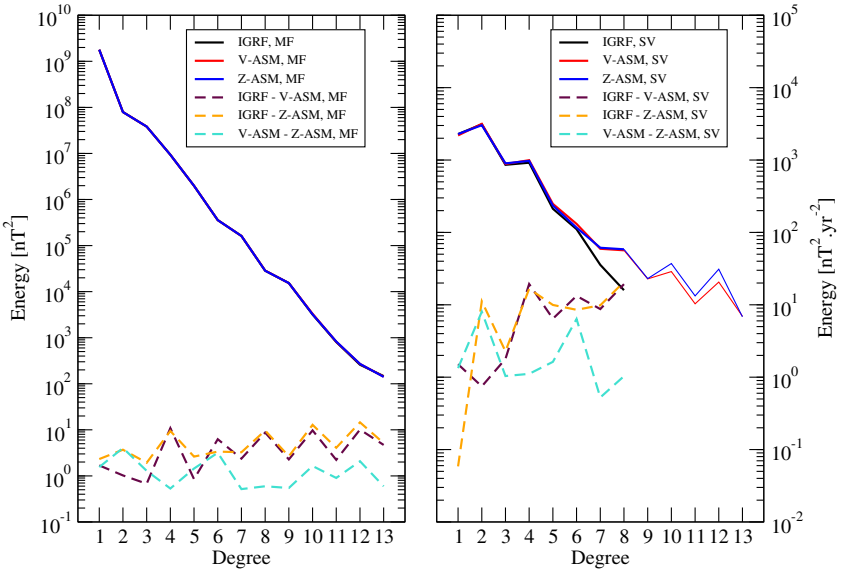

Fig. 8 Magnetic energy spectra of V-ASM, Z-ASM, and adopted IGRF models, for the main field (*left panel*) and the secular variation (*right panel*). Also shown are the spectra of the differences between models. For the SV, models are shown up to degree 13, although terms for $n > 8$ are not considered for IGRF. Note that on the *left panel*, *red*, *black*, and *blue curves* are superimposed

complete comparison between the adopted IGRF and all other candidate models can be found in Thébault et al. (2015a). Rms differences between IGRF and our candidate model range between 6 and 10 nT for the main field depending on the field component. This is almost three times that between our two parent models. A close look at the geographic distribution of the residuals reveals that most of the differences are located poleward of 50° absolute magnetic latitude. In the equatorial region, differences range between ± 9.5 nT but may exceed ± 40 nT in polar areas. Globally, differences tend to be aligned with magnetic latitudes, this may be related to noise that correlates with magnetic latitudes such as the noise due to the ionosphere and magnetosphere. The considered time interval of 10 months is also probably too short to reliably constrain the secular variation up to degree and order 8. Nonetheless, differences between IGRF and our V-ASM-derived candidate model are slightly lower than those with our Z-ASM-derived test model, which supports our preferred choice regarding the V-ASM model.

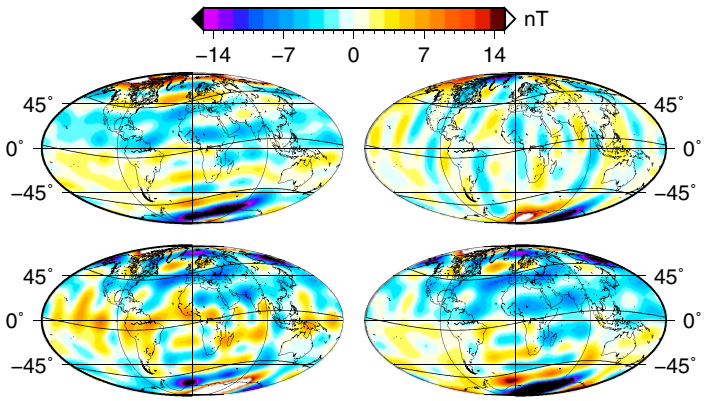

Fig. 9 Same as Fig. 3 between IGRF and V-ASM main field models at epoch 2015.0 and truncated to $n = 13$

Concluding remarks

We present two candidate models for IGRF-12 for the main field at epoch 2015.0 and for the secular variation between 2015 and 2020. We choose to compute parent models with a simple parametrization and without adding regularization or temporal splines. Only Swarm A and C measurements, acquired during the first 10 months of the mission, are considered, with external activity indices selection and outliers removal. We compare two different modeling strategies, one using full vector measurements and one using only vertical component measurements, both in addition to intensity measurements. We show that the differences between these models are small when they are compared at the mean epoch of measurements for $n \leq 13$. However, they become larger when the models are extrapolated to 2015.0, increasing from 0.94 to 3.04 nT. This is very likely a consequence of using a too short time interval to construct our SV model.

The two models are relatively similar for the static part, and only the time-varying part is different. The analysis of this difference lead us to chose the V-ASM parent model of our MF and SV candidates for IGRF. We believe that this difference is related both to a non-optimal data selection above polar areas (where the misfit is very large) and to a too short time interval to constrain the secular variation. We however want to underline that using the vertical magnetic field in complement to globally distributed scalar measurements to reduce the Backus effect is promising, and that such approach may be explored in the future if required.

Competing interests

The authors declare that they have no competing interests.

Authors' contributions

All authors contributed to the manuscript. DS and BL initiated the work. FC and ET made initial data selection and tests. All authors participated to the construction of the candidate models. All authors read and approved the final manuscript.

Acknowledgements

The authors acknowledge ESA for provided access to the Swarm L1b data. DS and FC are supported by CNES and Région Pays de la Loire. This work was partly funded by the Centre National des Études Spatiales (CNES) within the context of the "Travaux préparatoires et exploitation de la mission Swarm" project. We also thank two anonymous reviewers for their detailed comments.

Author details

[1] Laboratoire de Planétologie et Géodynamique de Nantes, UMR 6112 CNRS, Université de Nantes, Nantes, France. [2] Centre National d'Études Spatiales, Paris, France.

Received: 12 February 2015 Accepted: 3 June 2015
Published online: 20 June 2015

References

Backus G (1970) Non-uniqueness of the external geomagnetic field determined by surface intensity measurements. J Geophys Res 75:6337–6341. doi:10.1029/JA075i031p06339

Barraclough DR (1985) A comparison of satellite and observatory estimates of geomagnetic secular variation. J Geophys Res 90:2523–2526. doi:10.1029/JB090iB03p02523

Cain JC, Wang Z, Kluth C, Schmitz DR (1989) Derivation of a geomagnetic model to $n = 63$. Geophys Jour 97:431–441. doi:10.1111/j.1365-246X.1989.tb00513.x

Chulliat A, Vigneron P, Thébault E, Sirol O, Hulot G (2013) Swarm SCARF dedicated ionospheric field inversion chain. Earth Planets Space 65. doi:10.5047/eps.2013.08.00

Holme R (2000) Modeling of attitude error in vector magnetic data: application to Ørsted data. Earth Planets Space 52:1187–1197. doi:10.1186/BF03352351

Holme R, Bloxham J (1995) Alleviation of the Backus effect in geomagnetic field modelling. Geophys Res Lett 22. doi:10.1029/95GL01431

Holme R, James MA, Lühr H (2005) Magnetic field modelling from scalar-only data: resolving the Backus effect with the equatorial electrojet. Earth Planets Space 57. doi:10.1186/BF03351905

Hurwitz L, Knapp DG (1974) Inherent vector discrepancies in geomagnetic main field models based on scalar F. J Geophys Res. 79:3009–3013. doi:10.1029/JB079i020p03009

Khokhlov, A, Hulot G, Le Mouel J-L (1997) On the Backus effect-I. Geophys J Int 130. doi:10.1111/j.1365-246X.1997.tb01864.x

Khokhlov A, Hulot G, Le Mouel J-L (1999) On the Backus effect-II. Geophys J Int 137. doi:10.1046/j.1365-246X.1999.00843.x

Langel RA, Estes RH (1985) The near-Earth magnetic field at 1980 determined from MAGSAT data. J Geophys Res. 90:2495–2509. doi:10.1029/JB090iB03p02495

Langlais B, Mandea M, Ultré-Guérard P (2003) High-resolution magnetic field modeling: application to MAGSAT and Ørsted data. Phys Earth Planet Int 135:77–91. doi:10.1016/S0031-9201(02)00207-8

Lesur V, Wardinski I, Hamoudi M, Rother M (2010) The second generation of the GFZ Reference Internal Magnetic Model: GRIMM-2. Earth Planets Space 62. doi:10.5047/eps.2010.07.007

Lowes FJ (1975) Vector errors in spherical harmonic analysis of scalar data. Geophys J R Astr Soc 42:637–651. doi:10.1111/j.1365-246X.1975.tb05884.x

Macmillan S, Maus S, Bondar T, Chambodut A, Golovkov V, Holme R, Langlais B, Lesur V, Lowes F, Lühr H, Mai W, Mandea M, Olsen N, Rother M, Sabaka T, Thomson A, Wardinski I (2003) The 9th-generation International Geomagnetic Reference Field. Phys Earth Planet Int 140:253–254. doi:10.1111/j.1365-246X.2003.02102.x

Mandea M, Langlais B (2000) Use of Ørsted scalar data in evaluating the pre-Ørsted main field candidate models for the IGRF 2000. Earth Planets Space 52:1167–1170. doi:10.1186/BF03352347

Olsen N, Friis-Christensen E, Alken P, Beggan CD, Chulliat A, Doornbos E, da Encarnacao JT, Hamilton B, Hulot G, van den IJssel J, Kuvshinov A, Lesur V, Luehr H, Macmillan S, Maus S, Noja M, Olsen PEH, Park J, Plank G, Puethe C, Rauberg J, Ritter P, Rother M, Sabaka TJ, Schachtschneider R, Sirol O, Stolle C, Thébault E, Thomson AWP, Toffner-Clausen L, Velimsky J, Vigneron P, Visser PN (2013) The Swarm Satellite Constellation Application and Research Facility (SCARF) and Swarm data products. Earth Planets Space 65. doi:10.5047/eps.2013.07.00

Stern DP, Bredekamp JH (1975) Error enhancement in geomagnetic models derived from scalar data. J Geophys Res 80:1776–1782. doi:10.1029/JA080i013p01776

Thébault E, Finlay CC, Alken P, Beggan C, Canet E, Chulliat A, Langlais B, Lesur V, Lowes FJ, Manoj C, Rother M, Schachtschneider R (2015a) Evaluation of candidate geomagnetic field models for IGRF-12. Earth Planets Space. Under revision

Thébault E, Finlay CC, Beggan C, Alken P, Aubert J, Barrois O, Bertrand F, Bondar T, Boness A, Brocco L, Canet E, Chambodut A, Chulliat A, Coïsson P, Civet F, Du A, Fournier A, Fratter I, Gillet N, Hamilton B, Hamoudi M, Hulot G, Jager T, Korte M, Kuang W, Lalanne X, Langlais B, Léger J-M, Lesur V, Lowes FJ, Macmillan S, Mandea M, Manoj C, Maus S, Olsen N, Petrov V, Rother M, Sabaka TJ, Saturnino D, Schachtschneider R, Sirol O, Tangborn A, Taylor V, Thomson A, Tøffner-Clausen L, Vigneron P, Wardinski I, Zvereva T (2015b) International Geomagnetic Reference Field: the twelfth generation. Earth Planets Space. doi:10.1186/s40623-015-0228-9

Thébault E, Vigneron P, Maus S, Chulliat A, Sirol O, Hulot G (2013) Swarm SCARF dedicated lithospheric field inversion chain. Earth Planets Space 65. doi:10.5047/eps.2013.07.00

Tøffner-Clausen L (2013) Swarm level 1b product definition. Technical Report SW-RS-DSC-SY-0007, Issue 5.15. National Space Institute, Technical

University of Denmark [Available at https://earth.esa.int/documents/10174/1514862/Swarm_L1b_Product_Definition.]
Ultré-Guérard P, Hamoudi M, Hulot G (1998a) Reducing the Backus effect given some knowledge of the dip-equator. Geophys Res Lett 25. doi:10.1029/98GL02211
Ultré-Guérard P, Jault D, Alexandrescu M, Achache J (1998b) Improving geomagnetic field models for the period 1980–1999 using Ørsted data. Earth Planets Space 50:635–640
Whaler KA (1986) Geomagnetic evidence for fluid upwelling at the core-mantle boundary. Geophys J R Astr Soc 86:563–588. doi:10.1111/j.1365-246X.1986.tb03844.x

2.6.3 Evaluation of candidate models and the final IGRF-12

In December 2014 the IAGA Division V Working Group V-MOD issued the revision and evaluation of the 12th generation of IGRF. All candidate models were evaluated and compared to all others and to a mean model. For a detailed description of the evaluation process see Thébault et al. (2015a). Seven candidate MF models for the DGRF epoch 2010.0 and ten candidate MF models for the IGRF epoch 2015.0 were submitted. In addition, nine SV models were submitted for the predictive part covering epochs 2015.0–2020.0. The teams who submitted candidate models were formed by scientists from the following organizations: BGS, DTU Space, ISTerre, IZMIRAN, NGDC–NOAA, GFZ, USTHB/EOST, NASA–GSFC, IPGP, CEA/CNES, LPG Nantes, CNES, ETH Zurich, and GFZ. All candidate models were derived from parent models. Detailed description on most of the parent models can be found in the correspondent papers (Alken et al., 2015; Finlay et al., 2015; Lesur et al., 2015; Hamilton et al., 2015; Fournier et al., 2015; Gillet et al., 2015; Sabaka et al., 2015; Saturnino et al., 2015).

In order to derive the final IGRF-12 model all candidate models had to be analysed. The comparisons between all models were made using the following criteria:

- Difference between a model's Gauss coefficients with another's. This analysis is done coefficient by coefficient.
- Difference between one model and a "mean" model estimated from a defined number of candidate models. To the calculation of the "mean" model different weights can be allocated to each model, which results in a "weighted mean" model.
- SH power spectrum (see Eq. 2.28) per SH degree is computed for each candidate model and for the difference between two candidate models. Comparisons are taken at the mean surface of the Earth, $r = a$, which corresponds to the surface where the IGRF is often employed by users. Then, the power spectrum of the differences is summed from degree 1 to the degree of truncation ($N = 13$ for the IGRF 2015.0), which provides the mean square vector field at altitude r. Taking the square root it yields the root mean square (RMS) vector field difference between two models. One can also compute the mean value

of RMS difference between one model and a "mean" model build with all other models.

- Computation of the azimuthal power spectrum between a pair of models. This corresponds to reorganize the square of the coefficients as a function of the azimuthal ration m/n, which varies from 0 for purely zonal terms to 1 for sectoral terms (Sabaka et al., 2004). This ratio is defined positive for g_n^m and negative for h_n^m coefficients.
- Difference between two models coefficients, normalized by the geomagnetic power spectrum, denoted sensitivity matrix, and expressed in percentage for each degree and order. This enables to see the resemblance or mismatch between two different candidate models.
- SH correlation per degree between two models. Two models may have systematic differences in amplitude (thus, a large RMS) but still be linearly correlated (Langel and Hinze, 1998).
- Visual comparison between candidate models predictions on the physical space.

From the analysis of the results obtained with the above criteria, decision on how to construct DGRF-2010, IGRF-2015, and SV-2015-2020 had to be taken. In later generations of the IGRF model fixed weights were assigned to each candidate model based on the information collected from the above described criteria (Finlay et al., 2010). Usually, a group of models having a smaller variance than the others was identified and a simplification was to give this group unit weight and most of the others zero weight.

In the case of the IGRF-12, the evaluation results showed that some models agreed better among themselves than others. However investigating if whether any model is flawless and worthy to be omitted from the final model is no trivial task. In fact self-consistency between some models is no indication that they are "more" correct but that they were constructed with similar scientific choices. Most differences between models can be assigned to the different choices in the data selection, the removal and/or correction of specific sources to the measured field, the analytical method employed or the hypothesis of the physics of the Earth's core taken into account. Rejecting candidate models who present such differences could lead to a biased solution estimated from candidate models only relying on similar approaches (Thébault et al., 2015a). Hence the idea of a rejection of any model was put aside. For simplicity a common

global error distribution was assumed for the model population, which follows a normal law in its central region but has a long tail, due to a small amount of rather different models. A Huber weighting scheme in spatial domain through an iteratively reweighted least-squares (IRLS) approach was devised. The approach calculates a weight, for each model and on a grid of locations in space (and for three component of the magnetic field) at the surface $r = a$. This analysis was carried out for each one of the models DGRF-2010, IGRF-2015, and SV-2015-2020. It allowed to include all candidate models but the most dissimilar aspects of certain models were down weighted. The inclusion of all different model philosophies encourages new modelling improvements and keeps the IGRF project attractive to modellers. The resulting robust weighting scheme correlates well with the spatial differences between a candidate model and the arithmetic mean model. Spatial features common to all models received equal weight. Their regions show where the IGRF-12 is better constrained in space by all candidate models. However, the Huber weighting scheme does not allow treating each coefficient independently (even when certain coefficients of a candidate model seem wrong or not adequate) and as it is a purely statistical scheme, there is little control to the weights assigned numerically.

The resulting IGRF-12 coefficients are available to the public on the IAGA Division V Working Group V-MOD webpage[7], or print (Thébault et al., 2015b). The rounding error of IGRF-2015 (and SV-2015-2020) is about 1.5 nT (or nT.yr^{-1}) for a precision of 0.1 nT (or nT.yr^{-1}) on each Gauss coefficient.

[7] `http://www.ngdc.noaa.gov/IAGA/vmod/igrf.html`

2.7 Motivation of this work

If one looks at the predictions of typical satellite-derived global geomagnetic model (e.g., CHAOS-5) for some observatories in Europe (Fig. 2.4), thus at a regional spatial scale, one can see that the model:

- describes the general trend of the secular variation at all observatories;
- does not capture the short-term oscillations at the different observatories. For example (see vertical grey dotted lines), if in MAB the SA is not significant during 2002 (the second time derivative is approximately constant), in FUR the SA is more significant for the same time period. However, the model curves for both observatories have the same behaviour. At the end of 2009, similarly, the model does not differentiate the faster SA in FUR (compared with MAB).

Then, at this regional spatial scale, the different short-term oscillations are not fully described by the model and also all observatories have their temporal variation smoothly described with nearly the "same" curve. The spatial resolution of the temporal variation is limited. This is intentional, as regularization is applied during the estimation of the model, by minimizing the field's second and third time derivatives at the core surface (Finlay et al., 2015), on the assumption that these short-term variations are external in origin. However, these short-term variations may also be of internal (core) origin.

A good description of the main field and its temporal variation is important to the knowledge of the flow motions at the CMB and the coupling mechanism between core and mantle. For example, the study of geomagnetic jerks provides information on the electrical conductivity of the mantle that reflects the chemical and physical properties of the Earth's interior or the core-mantle coupling. A common way to study jerks is to use ground based magnetic observatory time series which describe the secular variation at a local spatial scale. However, the uneven distribution of these observatories does not allow such study at a global scale, i.e., using time series all over the globe. The virtual observatories approach (Mandea and Olsen, 2006) tries to respond to this issue.

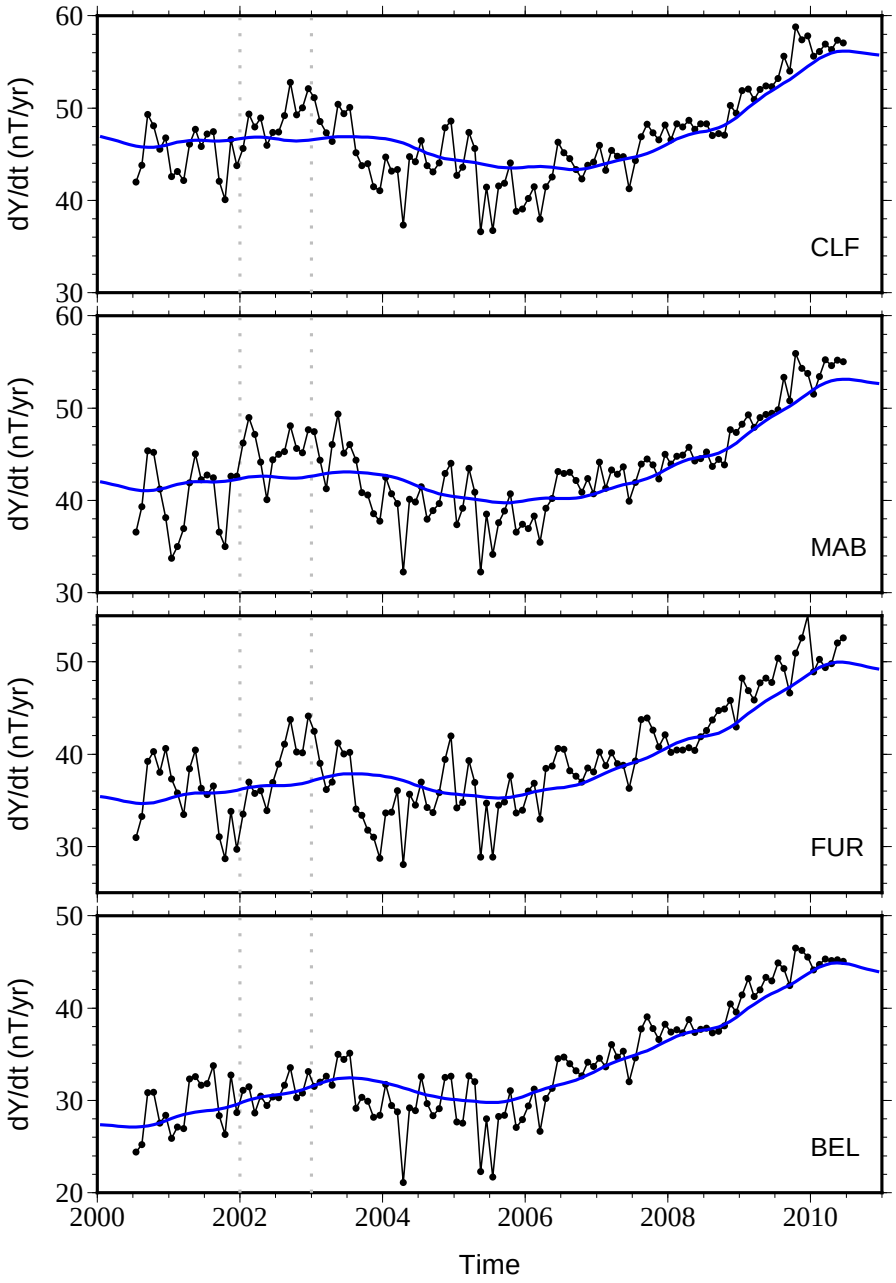

Figure 2.4: First time derivative of the Y component of the magnetic field as measured (*in black*) at four european observatories: CLF (France), MAB (Belgium), FUR (Germany) and BEL (Poland), and the respective prediction by a global geomagnetic field model (*in blue*, Finlay et al. (2015)), for a time period of ten years. Note different SV scales although all intervals are of 30 nT. See the text for an explanation of the purpose of the grey dotted lines.

The prospects of new Swarm mission measurements at the time of the beginning of this work motivated us to develop a new virtual observatories scheme. The scientific question which drove this work was: is it possible to better reconstruct the local spatial scales of the secular variation?

The concern was placed on the description of the temporal changes of the magnetic field at local scales and to develop a numerical technique to obtain a more detailed extraction of those changes using satellite data. The attention was placed only on the description of the observed magnetic field, and not on results from numerical dynamos. During the development of the new approach several assumptions were made as well as complications were overcome.

Chapter 3

The new VO-ESD approach

In this chapter the modelling approach developed during this thesis is presented. The motivation was the search of a better reconstruction of the regional spatial scales of the secular variation. First, the theory of this new approach is given, followed by the description of the parameters and strategies considered to obtain its validation. Since the approach follows the virtual observatories (VO) philosophy and makes use of the equivalent source dipoles (ESD) technique it his termed VO-ESD approach.

3.1 Concept

3.1.1 The "virtual observatories" approach

The virtual observatories approach was first introduced by Mandea and Olsen (2006) as a new way to process magnetic satellite measurements. The purpose was to study the short-term temporal variation of the field, by extracting magnetic field monthly mean values at satellite altitude, as it would be done at ground observatories. This leads into a global distributed grid of virtual observatories (VO, see Fig. 3.1). At each VO, a time series of the field changes is constructed from the extracted monthly means. From the comparison between VO time series and the corresponding ground observatory time series, Mandea and Olsen (2006) found a good

agreement at time scales of months to years.

The motivation for this method arose from the fact that observatory monthly means provide an excellent opportunity to study the main field's temporal changes. However, the ground observatories spatial distribution on the globe is very uneven, hampering the determination of secular variation global patterns spatial resolution. Satellite measurements have a global distribution allowing the construction of global geomagnetic models using spherical harmonics. But these models continue to be somehow indirect: a model prediction at one location is based on the analysis of all the globally distributed data rather than only on the data in the vicinity of the location (Mandea and Olsen, 2006). Another situation would be a perfectly global distribution of observatory locations to study the spatial patterns of the field temporal changes. When constructing field models from ground observatory data the geomagnetic activity of external origin is filtered out as the commonly calculated monthly means average out diurnal signals. Furthermore, all local times are considered in the calculations. In contrast, satellite derived field models commonly apply a strict data selection, comprised of quiet local night-times and geomagnetically quiet days (by means of geomagnetic indices). Thus, these two modelling strategies are largely different in their data selection criteria. However, the features of a model should be independent from the data selection to be considered as robust (Olsen and Mandea, 2007).

Olsen and Mandea (2007) constructed a global field model from VO-derived monthly means for the time period 2001–2005, and used it to investigate the 2003 geomagnetic jerk, the first to occur during the geomagnetic high quality satellite era. They found that the 2003 jerk was not worldwide in occurrence.

The main difficulty in constructing a virtual observatory from satellite measurements is the very nature of those measurements, i.e., they are taken at different altitudes, and those altitudes are time dependent. If this altitude change is not properly accounted for, it will produce false signals of the temporal changes of the magnetic field. Mandea and Olsen (2006) defined a virtual observatory as a cylindrical volume with a 400 km radius made of all available CHAMP measurements within the volume. Then a correction was made to bring all data to a constant

400 km altitude. This correction is based on the assumption that the measurements residuals (after subtracting a main field model) can be represented by a Laplacian potential field, defined by 8 parameters. Those parameters are estimated by an iterative weighted least square process and the mean magnetic residual at the centre of each VO ($r_{vo} = a$+400 km,ϑ_{vo},ϕ_{vo}) for a period of one month is computed. Then the main magnetic field at that location is finally added. This procedure is repeated for each month at each VO location. This procedure needs an a priori main geomagnetic field model.

Beggan et al. (2009) used the VO approach to directly invert secular variation time series to calculate flow models at the CMB. Examining the residuals of the obtained flow models they found temporally and spatially varying biases and patterns in the vector components. They suggested that external field effects are not completely removed from the obtained VO secular variation data, creating unrealistic secular acceleration. So, the assumption that short-term external effects are zero over a period of a month may not be true (Beggan et al., 2009).

3.1.2 The Equivalent Source Dipole technique

The Equivalent Source Dipole (ESD) technique was introduced by Mayhew (1979) for the representation of satellite magnetic field data at a regional scale. It has been widely used to reduce satellite magnetic data collected at different altitudes to a common elevation over a small area in order to, for example, derive crustal anomaly maps at a given altitude or at the surface (Langlais et al., 2004). This method is based on the expression of a magnetic anomaly caused by a magnetic dipole. Considering the magnetic moment $\mathbf{M}$ of a dipole located at (r_d, θ_d, ϕ_d), and that there are no sources between the dipole and the observation location (r, θ, ϕ), the observed magnetic potential is expressed as (Dyment and Arkani-Hamed, 1998)

$$V = -\mathbf{M} \cdot \nabla \frac{1}{l}. \tag{3.1}$$

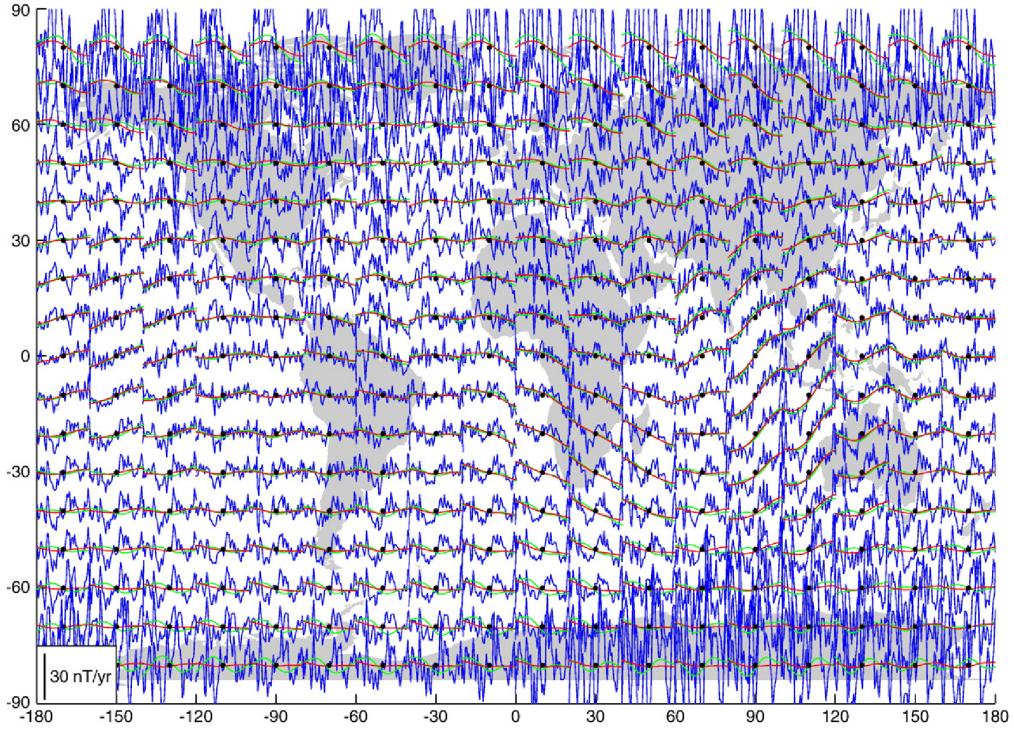

Figure 3.1: Example of the construction of a grid of virtual observatories by Olsen and Mandea (2007). Represented at each grid point (*black dots*) are the time series of the dZ/dt at 400 km altitude, for the time interval 2001–2005. Also shown are satellite data (*blue*), predicted values by the CHAOS model (*red*) and predicted values of the VO derived model (*green*), both for internal part only.

The distance l (see Fig. 3.2) between the dipole and the observation location is

$$l = (r_d^2 + r^2 - 2r_d r cos(\zeta))^{\frac{1}{2}}, \tag{3.2}$$

with ζ been the angle between observation and dipole locations:

$$cos(\zeta) = cos(\theta)cos(\theta_d) + sin(\theta)sin(\theta_d)cos(\phi - \phi_d). \tag{3.3}$$

The magnetic field at the observation point due to a dipole is written

$$\mathbf{B} = -\nabla V = -\left(\frac{\partial V}{\partial r}, \frac{\partial V}{r\partial\theta}, \frac{\partial V}{rsin(\theta)\partial\phi}\right). \tag{3.4}$$

The magnetic field as measured at one point is the sum of the magnetic fields created by all

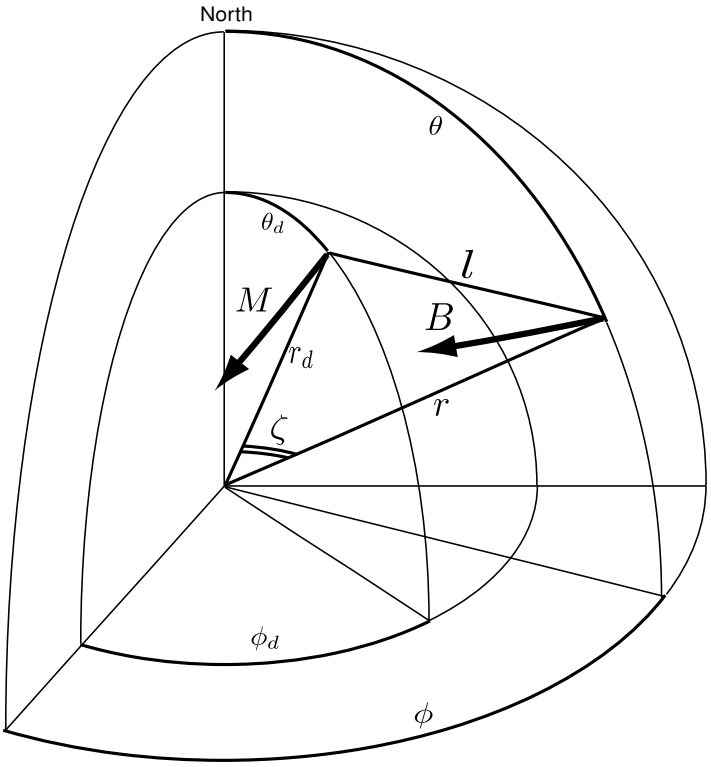

Figure 3.2: Geometry for one dipole point and one observation point in a spherical coordinate system (see text for details). Adapted from Dyment and Arkani-Hamed (1998).

the dipoles placed on a grid at a given altitude. Using measured magnetic components B_r, B_θ and B_ϕ the equivalent magnetization M_r, M_θ and M_ϕ for each dipole on the grid is calculated by a least-square fit in an iterative conjugate inversion scheme.

The potential of Eq. 3.1 can be written as:

$$V = \frac{M_r(rA_1 - r_d) - M_\theta r B_1 + M_\phi r C_1}{l^3}, \tag{3.5}$$

where l is the distance defined in Eq. 3.2 and the coefficients are

$$A_1 = cos(\theta)cos(\theta_d) + sin(\theta)sin(\theta_d)cos(\phi - \phi_d), \tag{3.6}$$

$$B_1 = cos(\theta)sin(\theta_d) - sin(\theta)cos(\theta_d)cos(\phi - \phi_d), \tag{3.7}$$

$$C_1 = sin(\theta)sin(\phi - \phi_d). \tag{3.8}$$

Following Eq. 3.4, the partial derivatives of the above listed coefficients are calculated (Langlais

et al., 2004):

$$A_2 = \frac{\partial A_1}{\partial \theta} = -sin(\theta)cos(\theta_d) + cos(\theta)sin(\theta_d)cos(\phi - \phi_d) \quad (3.9)$$

$$B_2 = \frac{\partial B_1}{\partial \theta} = -sin(\theta)sin(\theta_d) - cos(\theta)cos(\theta_d)cos(\phi - \phi_d) \quad (3.10)$$

$$C_2 = \frac{\partial C_1}{\partial \theta} = cos(\theta)sin(\phi - \phi_d) \quad (3.11)$$

$$A_3 = \frac{\partial A_1}{sin(\theta)\partial \phi} = -sin(\theta_d)sin(\phi - \phi_d) \quad (3.12)$$

$$B_3 = \frac{\partial B_1}{\sin(\theta)\partial \phi} = cos(\theta_d)sin(\phi - \phi_d) \quad (3.13)$$

$$C_3 = \frac{\partial C_1}{\sin(\theta)\partial \phi} = cos(\phi - \phi_d) \quad (3.14)$$

$$(3.15)$$

Finally, using the substitutions $D_1 = r - r_d A_1$, $D_2 = -R_d A_2$, $D_3 = -R_d A_3$, $F_1 = rA_1$, $F_2 = -rB_1$ and $F_3 = rC_1$, we can write the full expression for the magnetic field components:

$$B_r = M_r \frac{\frac{3D_1F1}{l^2} - A_1}{l^3} + M_\theta \frac{\frac{3D_1F_2}{l^2} + B_1}{l^3} + M_\phi \frac{\frac{3D_1F_3}{l^2} + C_1}{l^3}, \quad (3.16)$$

$$B_\theta = M_r \frac{\frac{3D_2F1}{l^2} - A_2}{l^3} + M_\theta \frac{\frac{3D_2F_2}{l^2} + B_2}{l^3} + M_\phi \frac{\frac{3D_2F_3}{l^2} + C_2}{l^3}, \quad (3.17)$$

$$B_\phi = M_r \frac{\frac{3D_3F1}{l^2} - A_3}{l^3} + M_\theta \frac{\frac{3D_3F_2}{l^2} + B_3}{l^3} + M_\phi \frac{\frac{3D_3F_3}{l^2} + C_3}{l^3}. \quad (3.18)$$

To solve are the vector components of the dipole moment (M_r, M_θ, M_ϕ), given the coefficients and the observations. This inverse problem can be written as (Purucker et al., 1996)

$$\tilde{\mathbf{b}} = \tilde{\mathbf{D}}\mathbf{x} + \tilde{\nu} \quad (3.19)$$

where:

- $\tilde{\mathbf{b}}$ is the vector containing N magnetic field observations (or $3 \times N$ observed magnetic components),
- $\mathbf{x}$ is the vector containing the magnitude of M dipoles moments to be determined (or $3 \times M$ unknowns),
- $\tilde{\mathbf{D}}$ is the geometric source function matrix ($3N \times 3M$) relating $\mathbf{x}$ to $\tilde{\mathbf{b}}$, whose elements

are given by Eq. 3.16, 3.17 and 3.18, and

- $\tilde{\nu}$ is the observation noise vector (of zero mean and covariance matrix $\mathbf{W}^{-1}$).

If each observation is weighted by the variance $w_i = \frac{1}{\sigma_i^2}$, which is the same as normalize $\tilde{\mathbf{b}}$ by multiplying Eq. 3.19 by $\mathbf{W}^{1/2}$, it gives

$$\mathbf{b} = \mathbf{D}\mathbf{x} + \nu. \tag{3.20}$$

This is solved by seeking to minimize the quantity $\mathbf{L}(\mathbf{x}) = \nu^T\nu$, which corresponds to solving

$$\mathbf{D}^T\mathbf{D}\mathbf{x} = \mathbf{D}^T\mathbf{b} \tag{3.21}$$

The minimum of $\mathbf{L}$ is reached when $\nabla\mathbf{L} = \mathbf{D}\mathbf{x} - \mathbf{b}$ goes to zero (Press et al., 1992). To solve this one can use the Conjugate Gradients method (Shewchuk, 1994), an iterative technique that generates at each iteration k a new solution $\mathbf{x}_{k+1} = \mathbf{x}_k + \alpha_k\mathbf{p}_k$, where $\mathbf{p}_k$ is a vector of search directions and α_k is a scalar that minimizes $\mathbf{L}(\mathbf{x}_{k+1})$ along the direction of $\mathbf{p}_k$:

$$\alpha_k = \frac{\mathbf{r}_k^T\mathbf{r}_k}{\mathbf{p}_k^T\mathbf{D}^T\mathbf{D}\mathbf{p}_k} \tag{3.22}$$

where $\mathbf{r}_k$ is the vector of residuals after the kth iteration:

$$\mathbf{r}_k = \mathbf{D}^T\mathbf{b} - \mathbf{D}^T\mathbf{D}\mathbf{x}_k. \tag{3.23}$$

In the method of Conjugate Gradients each new residual is orthogonal to all the previous residuals and search directions; and each new search direction is constructed from the residuals to be orthogonal to all previous residuals and search directions.
The explicit calculation of $\mathbf{D}^T\mathbf{D}$ in Eq. 3.22 is numerically expensive. If the following identity is used

$$\mathbf{p}_k^T\mathbf{D}^T\mathbf{D}\mathbf{p}_k = (\mathbf{D}\mathbf{p}_k)^T\mathbf{D}\mathbf{p}_k, \tag{3.24}$$

it is possible to replace the calculation of $\mathbf{D}^T\mathbf{D}$ directly by only $\mathbf{D}$. This is called the design matrix approach (Van der Sluis and Van der Vorst, 1987). The matrix $\mathbf{D}$ should be pre-conditioned

to make the inversion faster. The change from $\mathbf{r}_k$ to $\mathbf{r}_{k+1}$ is conjugate or perpendicular to all preceding search directions $\mathbf{p}_k$. This technique is guaranteed to converge in at most M steps. The root mean square weighted residual (or misfit)

$$\sigma_k = \sqrt{\frac{(\mathbf{b} - \mathbf{D}x_k)^T(\mathbf{b} - \mathbf{D}x_k)}{N}}, \tag{3.25}$$

is calculated after each iteration and used as a convergence criterion. Usually, and for simplicity, all measurements are attributed the same weight. From the estimated equivalent magnetization for each of the M dipoles, the forward problem is used to predict the magnetic field components (B_r, B_θ, B_ϕ) using Eq. 3.16, 3.17 and 3.18 at the desired location (r_o, θ_o, ϕ_o).

3.1.3 Definition of the VO-ESD approach

The virtual observatory approach previously mentioned uses a geomagnetic field model to extract the magnetic measurements at a fixed altitude. A more ideal solution would be a method which does not need any a priori model.

The equivalent source dipole technique can be used as an alternative to reduce to a constant altitude all measurements made within a VO volume for a given time interval. The VO-ESD approach idea is the following: for each VO a dipole grid is placed at a defined depth, and with a certain number of dipoles; from all the satellite measurements made inside the VO, during a given time period, the equivalent magnetization of each one of the dipoles is computed by an iterative least-square conjugate gradient inversion; then, the prediction is done at the centre of the VO location, at the chosen fixed altitude. This procedure is done for each one of the VO, placed on a global grid, and for each one of the time period (e.g., one month). A time series is then obtained at each VO location.

To implement this new approach the methodology had to be defined: the geometry, size of the dipole mesh, its depth, the time interval used for the inversion, etc. All these parameters had to be set. That work is described in the following pages.

3.2 Comparing SV at ground and satellite altitudes

To begin with, it is important to have an idea of the field behaviour for:

- the same location but at two distinct altitudes (surface and satellite altitude);
- two close locations i.e., the spatial change of the field's time variations.

Figure 3.3 shows time series of the three magnetic components measured at the CLF observatory and at satellite altitude. It is an example of a VO data volume, obtained from Swarm measurements taken within a 3^o diameter and $\sim$50 km altitude cylinder centred on the CLF location. The satellite data is much more scattered than the ground data due to the satellite movements within the VO region where the magnetic field changes spatially. Therefore, the smooth trend seen in the ground data cannot be inferred from satellite data (at least for this short period: 13 months). Note also that the satellite data were taken at two different altitude "layers" (cf. Section 1.6.3). This shows that even within a small region the difference of signal scatter between ground-based data and satellite data is very significant.

Figure 3.4 shows the magnetic field and its secular variation at one location at the Earth's surface and at satellite altitude (490 km) just above, given by an SH model. It shows the differences in the MF and SV trends at those two altitudes. The magnetic field components vary at the ground more than at satellite altitude e.g., for the X component the variation at the ground is about 150 nT and at satellite altitude is 120 nT. For the vertical component (Z), the field increases about 300 nT at the ground and "only" 160 nT at satellite altitude. Furthermore, at different times the differences between ground and satellite values change. For example, for the Z component the difference at 2000 is about 8520 nT and at 2011 is of 8620 nT, 100 nT more. However, the general trend of the curves is very similar at both altitudes. The same can be seen for the SV prediction, where the curves are even more similar for both altitudes. The SV at the ground is always larger than at satellite altitude, as expected. The dX/dt increases by about 8 nT.yr^{-1} from 2005 to 2007.5 at the ground, but only increases by 6 nT.yr^{-1} at satellite altitude, for the same time period. So, as with the MF, for distinct time intervals, the SV changes differently at both altitudes. These comparisons express the differences between a

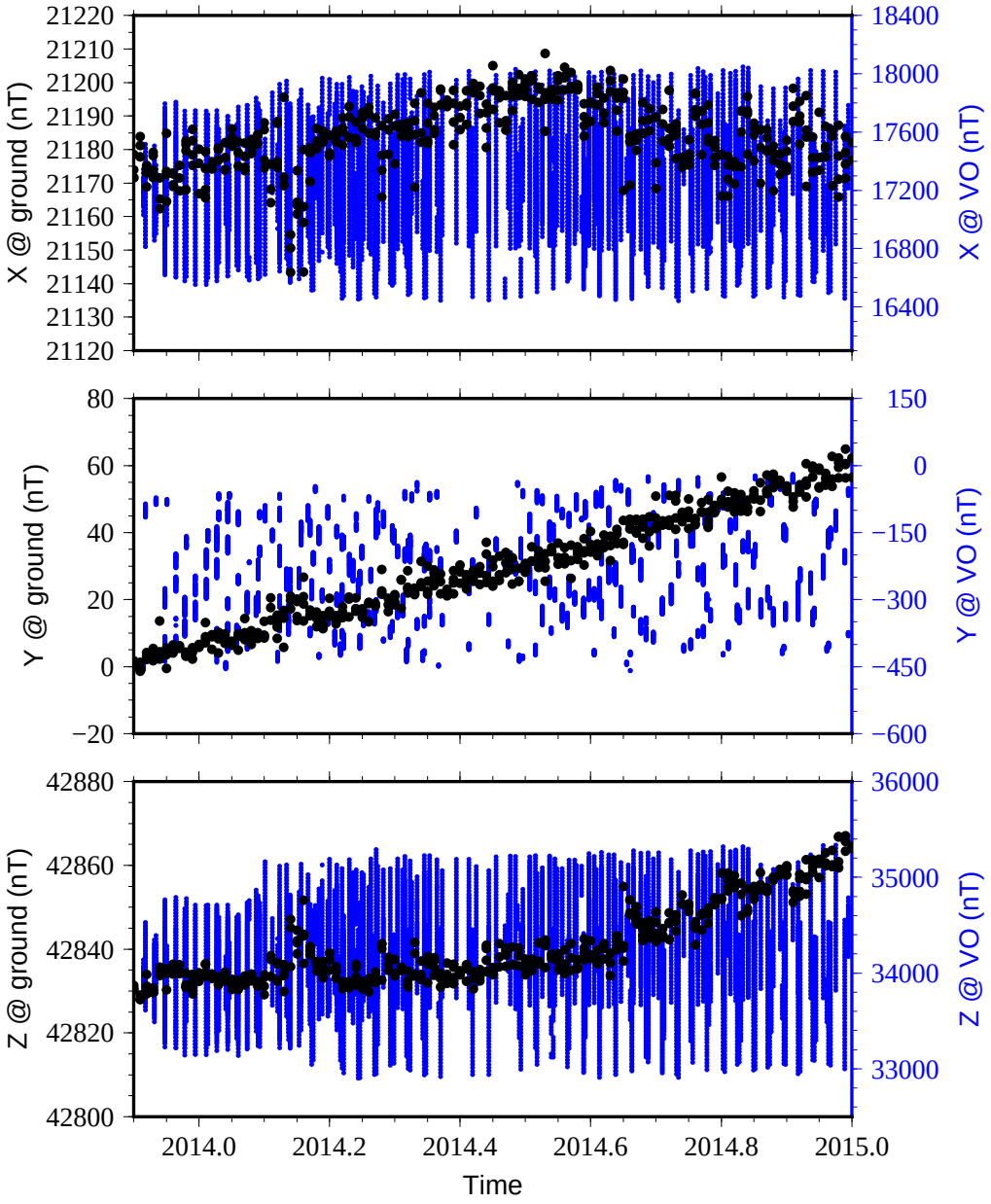

Figure 3.3: Time series of the X, Y and Z magnetic components at the CLF observatory (*black*) and Swarm measurements within a cylinder centred at the CLF location (*blue*).

time series at the ground and at satellite altitude. The curve behaviour of the magnetic field and its secular variation are similar, and the differences between them are not constant in time. These differences can be of 2 to 10 nT.yr^{-1} for the SV. Note that CHAOS-4 only accounts for the main field contribution. At satellite altitude the short-term temporal and spatial variations are expected to contribute in a stronger way to the measured field.

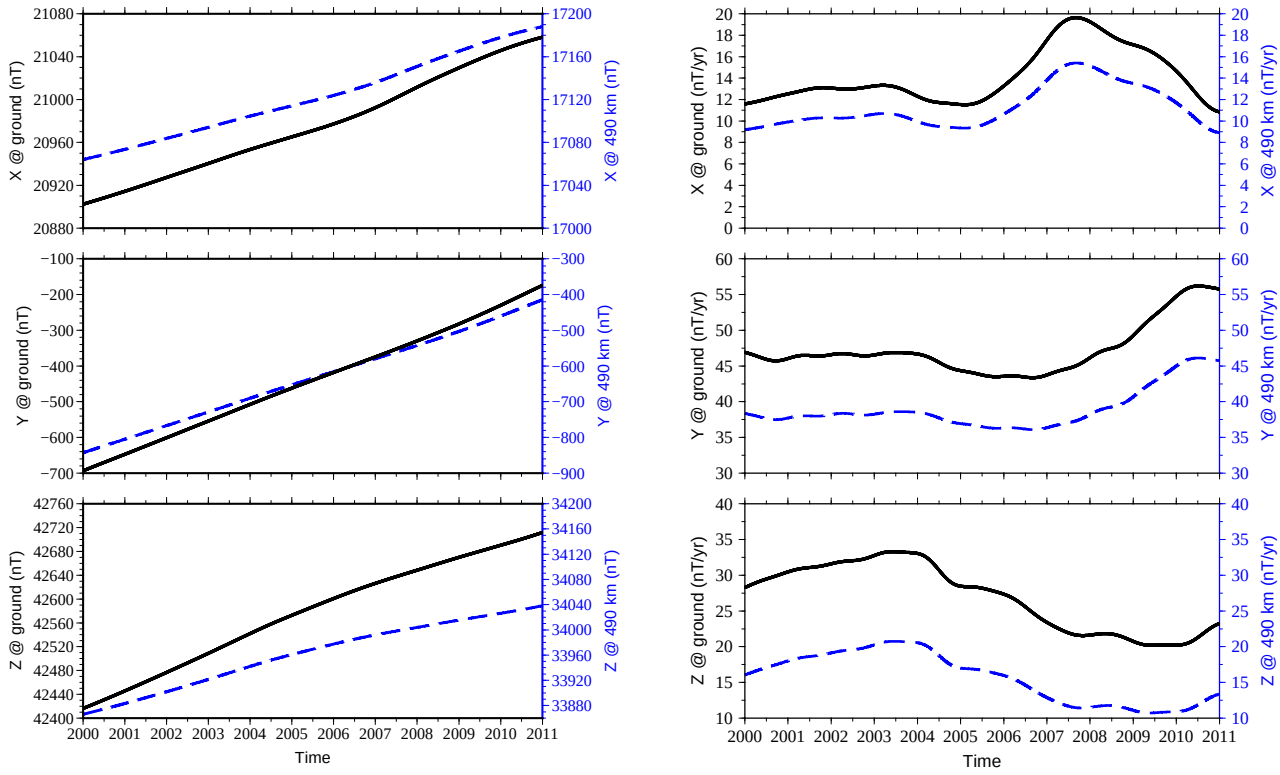

Figure 3.4: Time series of the magnetic field (*left*) and the first time derivative (*right*) for the X, Y and Z magnetic components at the CLF observatory (*black line*) and at satellite altitude (490 km, *blue dotted line*), as given by the CHAOS-4 model. Note that for the SV, the range scale for each magnetic component is the same both at the surface and at satellite altitude.

Figure 3.5 shows the magnitude of the horizontal vector gradient for the SV for the three magnetic components. The direction was calculated clockwise from north toward east, and at each point of a global mesh with 1^o resolution. It can be seen that the spatial change of the first time derivative within 1^o ($\sim$ 111 km) can be of 8 nT.yr^{-1}.degree, but the more probable value is below 2 nT.yr^{-1}.degree. The vertical component horizontal gradient exibits the highest values of spatial change of SV. The higher values of the spatial changes of SV are seen at the south Atlantic and Indian oceans. The Pacific Ocean and Europe exibit the smaller values. Therefore, between two VOs, for example 3^o apart, the spatial difference of SV can range 6 to 24 nT.yr^{-1}.

In summary, in order for the VO-ESD approach to extract short-term temporal variations at a regional scale resolution, the ESD technique should have, at least, a minimal resolution of 2 nT. This has to be taken into account during the validation procedure.

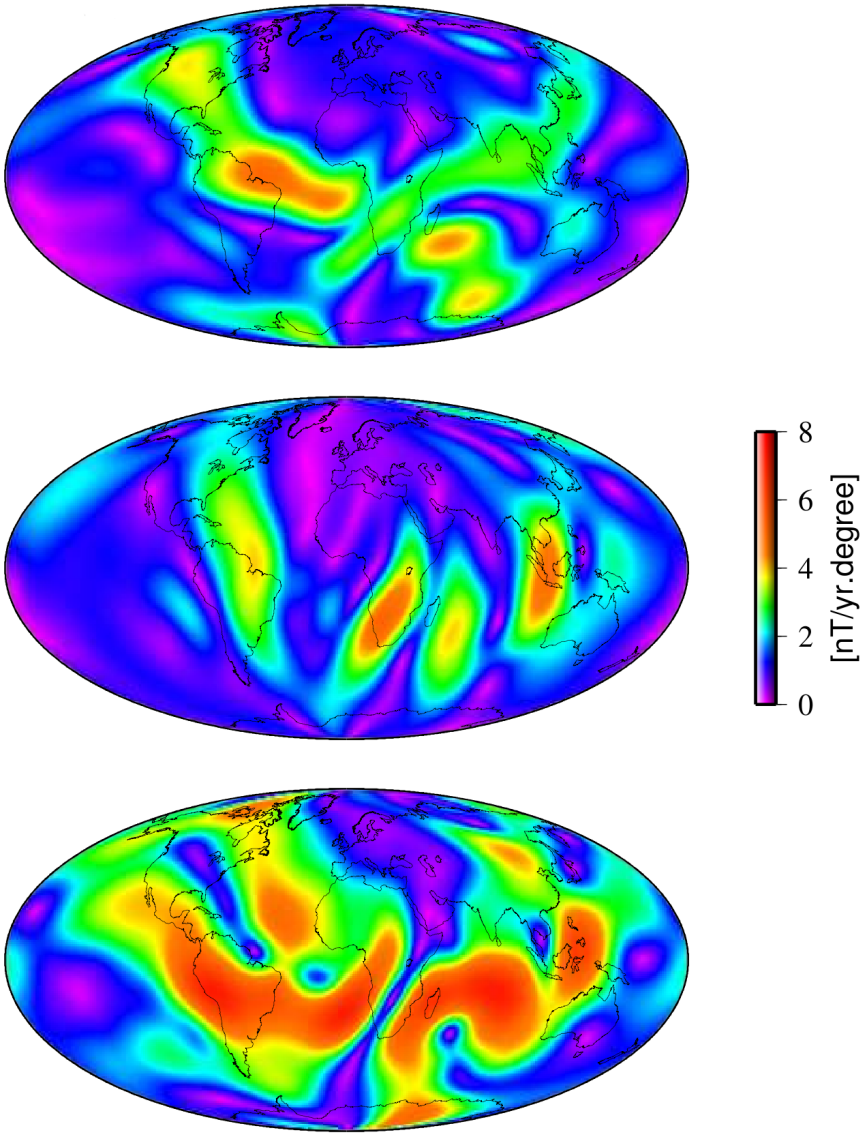

Figure 3.5: Magnitude of the horizontal vector gradient of SV for the X, Y and Z magnetic components (i.e., $\frac{\partial}{\partial t}|\bigtriangledown_h X|$, $\frac{\partial}{\partial t}|\bigtriangledown_h Y|$ and $\frac{\partial}{\partial t}|\bigtriangledown_h Z|$, at *top*, *middle* and *bottom*, respectively), at the Earth's surface and at epoch 2002.0, as given by the CHAOS-4 model truncated at SH degree 13.

3.3 Validation of the VO-ESD approach by application to synthetic data

It is necessary to account for the effectiveness of the new approach. Is the ESD technique able to recover the magnetic field from a small volume of data and predict an equivalent field at that volume central location? Synthetic tests were performed to respond to this question. For that end a global geomagnetic model was used to construct a synthetic data set. Furthermore for the application of the ESD technique several parameters had to be defined. The description of those parameters and the search for their optimal values in a virtual observatories case is described in this section.

3.3.1 Synthetic data

The synthetic data is obtained by means of a global SH magnetic model, the CHAOS-4 (Olsen et al., 2014) internal field model, truncated to degree 13. For all testing cases, predictions for the three magnetic components (X, Y, Z) at different satellite altitudes were used. Tests were made for a data set with and without SV. The measurements were mapped either on a regular grid (regular points on latitude, longitude and altitude, see Fig. 3.7), on sparse grids or on synthetic orbits mimicking Swarm satellite measurements (see Fig. 3.30). The initial tests were performed on cubic VO volumes. Later a cylindrical volume was preferred.

3.3.2 Input parameters

There are several solutions (in space) of dipole magnetizations that can explain the observed magnetic measurements. This non-uniqueness forces one to carefully select the ESD technique modelling parameters. These parameters have to be established a priori, as the non-linearity makes it difficult to solve for all at the same time. The parameters needed to be defined for the ESD technique were:

- the geometry of the dipole mesh (i.e., the dipoles distribution within the mesh, their mean distance (d)),
- the number of dipoles of the mesh (M),
- the depth at which the dipole mesh is placed.

The assumed thickness of the dipole mesh (the dipoles thickness) does not significantly affect the results: only the vertically integrated magnetization is actually computed. On the other hand, when dealing with ESD the geographical distribution of the dipoles on the mesh should be as homogeneous as possible in order to minimize the sources instabilities (Covington, 1993). In the VO approach, the measurements are confined in a volume, thus the problem lives on a spatial regional scale. The chosen dipole mesh geometry should be homogeneous on this spatial scale.

Other parameters, related with the VO approach, also had to be defined such as:

- the geometry of the VO volume (a cylinder, a cube...),
- the size of the VO volume,
- the time interval, or duration of the data (T), chosen to separate the VO measurements to perform at each inversion,

The choices of the VO size and the time interval must consider that:

- there is enough data to describe the field temporal and spatial variations, and
- the region is small enough to capture the small spatial scales changes of the field.

In Fig. 3.6 an example of the VO-ESD application is shown, with a dipole mesh below a VO volume of satellite data. The parameters values are obtained by analysing their impact on the results of the inversion. The idea is to infer the sensitivity of the solution to the dipole mesh geometry, number of dipoles (M) and mean distance between dipoles (d). An interval of values is considered for each parameter, and then the rms residuals of the solution are observed.

The rms residuals (σ) between the observation (this case the synthetic data) and the prediction of a magnetic component (Eq. 3.25) is computed at each iteration k of the inversion scheme.

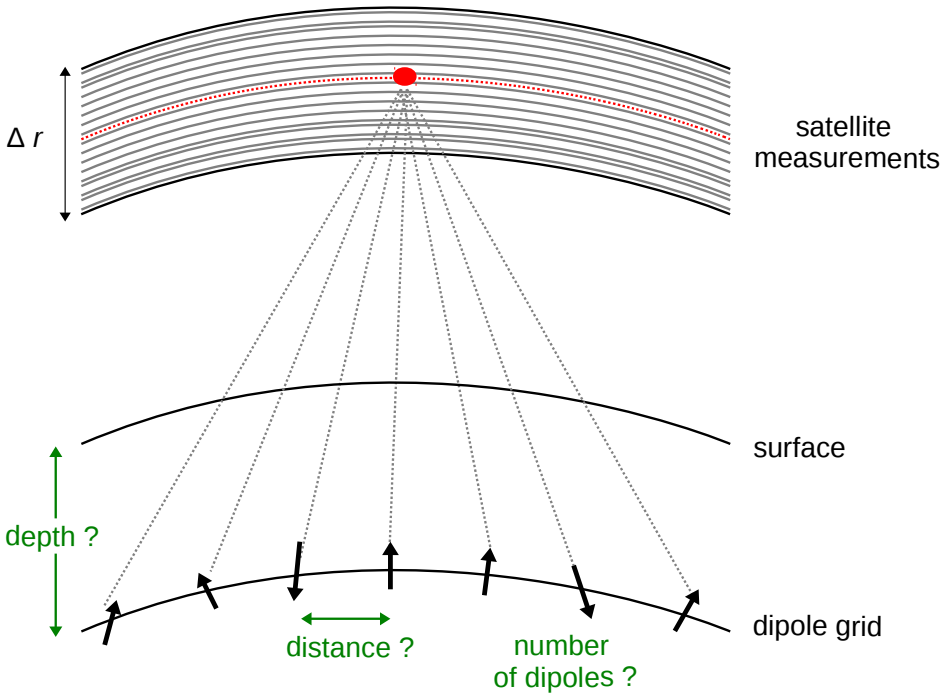

Figure 3.6: Scheme of the VO-ESD approach application. The parameters needed to be defined are shown, as well as the mean altitude (*red line*) of the satellite measurements (*black lines*) and the centre of the VO volume (*red point*).

More precisely, σ is computed for the three magnetic components X, Y and Z (using Eq. 2.17) and also for the field intensity as:

$$\sigma_{F_k} = \sqrt{\frac{\sum_{i}^{N} \left[(B_{\theta_i} - B_{\theta_{i,k}})^2 + (B_{\phi_i} - B_{\phi_{i,k}})^2 + (B_{r_i} - B_{r_{i,k}})^2 \right]}{N}}, \tag{3.26}$$

where k is the iteration number, and $B_{\theta_{i,k}}, B_{\phi_{i,k}}, B_{r_{i,k}}$ are the magnetic components (in spherical coordinates, see Eq. 2.17) of the observation i as predicted by the iteration k solution ($\mathbf{M}_k$). The numerical inversion is stopped when σ_k $<10^{-10}$ nT or after 100 iterations (maximum), whichever came first. A decision was also to be done regarding the choice of the solution iteration. The criterion has changed throughout this work. Initially, during the tests regarding the ESD parameters, a visual inspection was thought sufficient, but later, as the number of inversions increased (as one had to invert to a number of months and VOs) an automatic criteria had to be chosen. This will be presented at the proper time.

3.3.3 Initial tests with a local dipole mesh

3.3.3.1 Dipole mesh and VO volume definition

The initial tests followed the idea presented in Fig. 3.6. The dipole mesh was placed below the location of a VO volume synthetic data centre. This volume was assumed as a cube of $1^o \times 1^o \times 300$ km, with altitudes ranging from 450 to 750 km, with a spacing of 0.20^o in latitude and longitude, and $N = 400$ points (see Fig. 3.7).

An important assumption at this stage was that the dipole mesh had the same horizontal extend as the VO volume, at maximum. The idea was that the observed magnetic field within one region may be explained by sources located immediately below that region. From this, the dipole mesh size was constrained by the VO volume synthetic data. The chosen dipole mesh had an hexagonal distribution of the dipoles, as used for example in Langlais and Purucker (2007). Several input dipole meshes were tested, by increasing the number of sources (for a same mean distance between sources, see Fig. 3.8), or increasing the mean distance between sources (for the same number of sources, see Fig. 3.9). The depth at which the dipole mesh was placed was also tested for an interval of values. The tested intervals of values of the parameters are listed in Table 3.1. As already referred, the rms residuals of the predictions are analysed to infer the dependence of the technique with the different parameters.

Table 3.1: Intervals of values of the dipole mesh parameters.

Parameter	Interval of values
M - number of dipoles	1; 7; 19; 37; 61; 91
d - mean distance	0.050; 0.075; 0.100; 0.125; 0.150
Depth	3020; 3070; 4020;. . . ; 6370

3.3.3.2 Results: why it did not work

Figure 3.10 shows an example of the rms residuals σ for a case with $M = 19$, $d = 0.125^o$ and placed at a depth of 4370 km. The input data is the VO volume presented in Fig. 3.7. The number of iterations to find a suitable solution is small, as only seven iterations are needed.

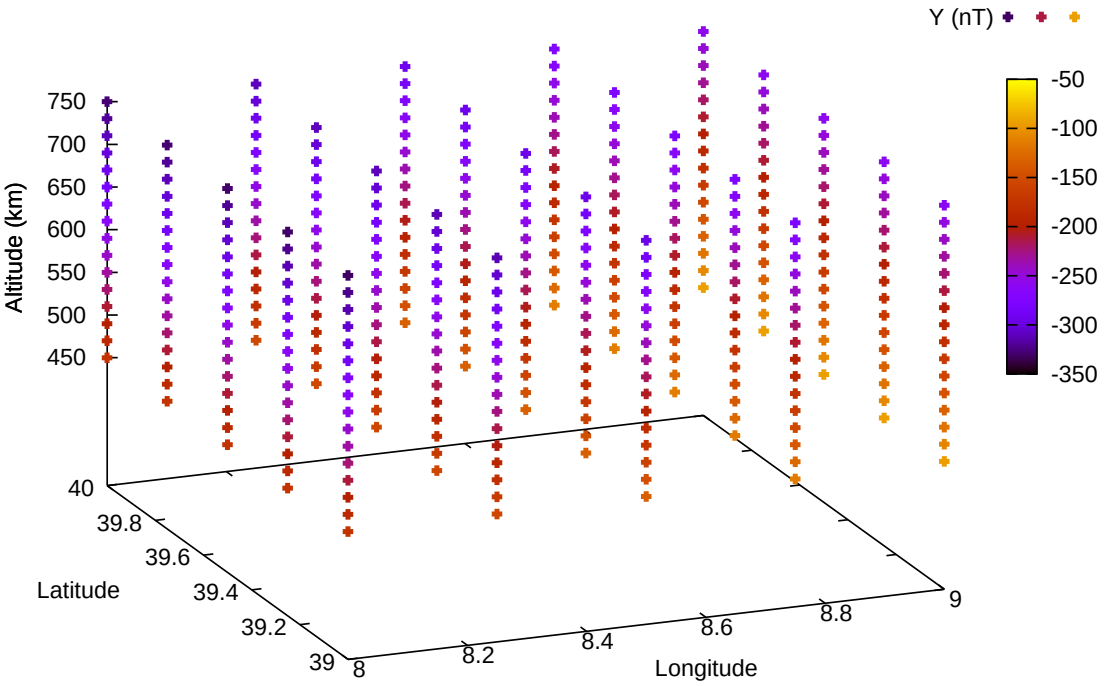

Figure 3.7: Synthetic data VO volume of $1^o \times 1^o \times$ 300 km, centred at 39.5^{o}N 8.5^{o}E. As an example, the horizontal east-west magnetic field component is plotted.

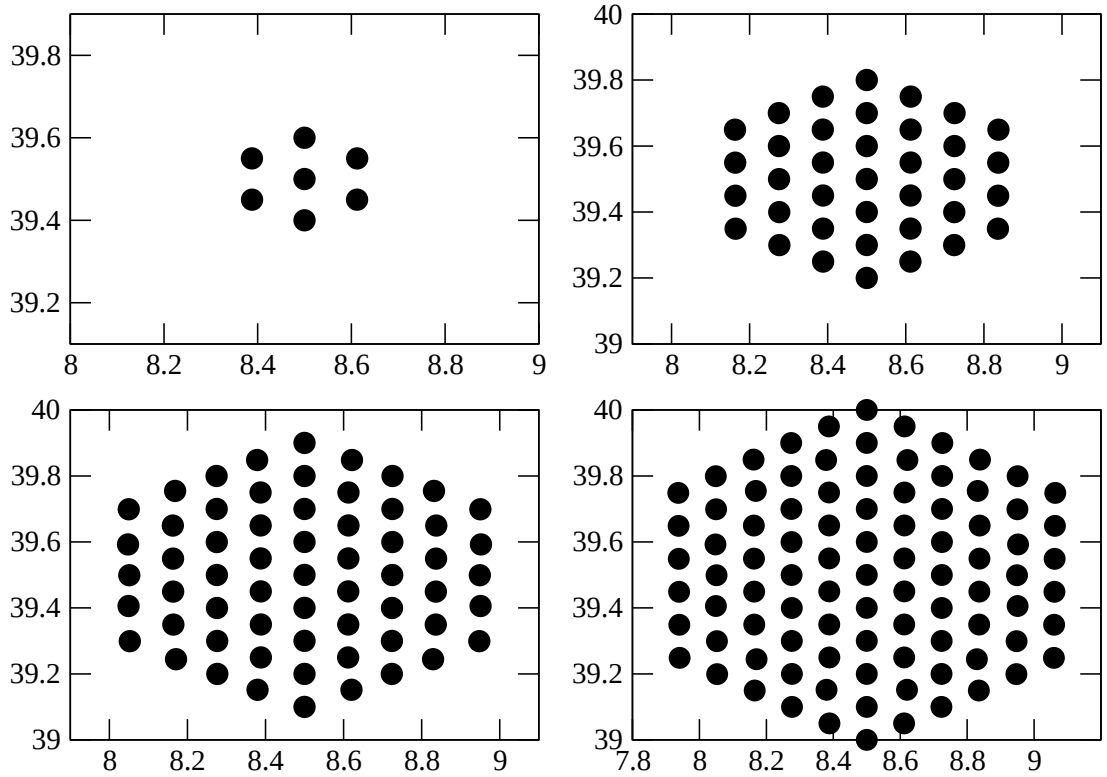

Figure 3.8: Example of four hexagonal dipole meshes with $d = 0.100^o$, and four different number of dipoles, $M = 7$, 37, 61 and 91.

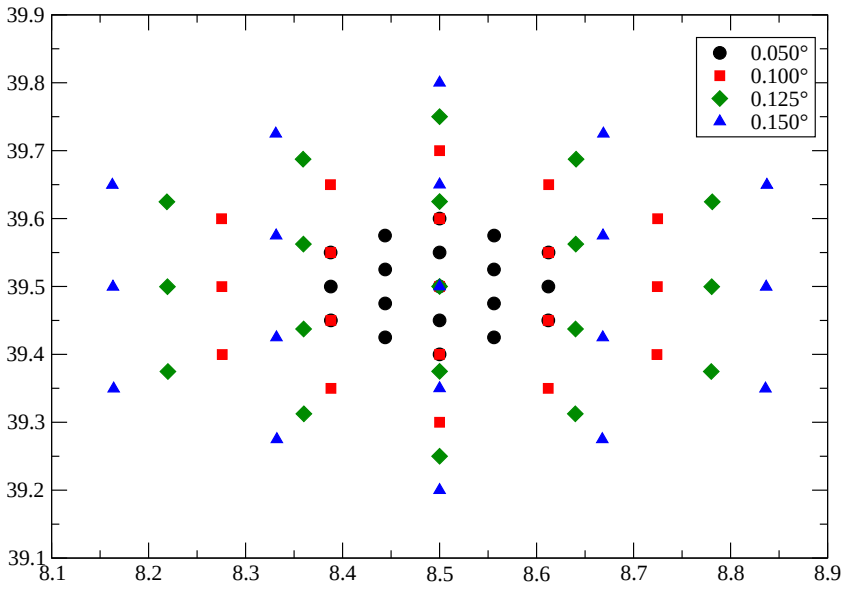

Figure 3.9: Example of four hexagonal dipole meshes with $M = 19$ and four different mean distance between dipoles, $d = 0.050^o$, 0.100^o, 0.125^o and 0.150^o.

The rms residuals of the last iterations for the three magnetic components are between 5 and 8 nT, and around 12 nT for the field intensity. Figures 3.11 to 3.13 show other three examples of the obtained rms residuals for three different dipole meshes tested. These examples proved to have a σ never inferior to 5 nT, and usually above 10 nT. These values of σ were obtained very fast during the inversion, at the 4th or 5th iterations.

The ESD technique was not able, with these parameters for the dipole meshes, to obtain better values of σ. For some tested dipole meshes the rms residuals obtained during the inversion were always bigger than 100 nT for all magnetic components. Figure 3.14 illustrates this, by showing the last iteration σ values, for the three magnetic components as a function of the number of dipoles placed on the dipole mesh. The values are always very large, even if they slightly decrease for higher values of M.

Figure 3.15 shows the rms residuals dependence on the mean distance d between dipoles. Slightly smaller intervals of σ are seen for the higher values of d. Figure 3.16 shows the dependence on the number of dipoles for four different cases of mean distance and depth. It seems, from these examples, that a higher number of dipoles resolves more adequately the inversion problem, i.e., a higher number of unknowns improves the final fit to the input data. Nevertheless, the misfits are always higher than desired, which is at maximum around 2 nT.

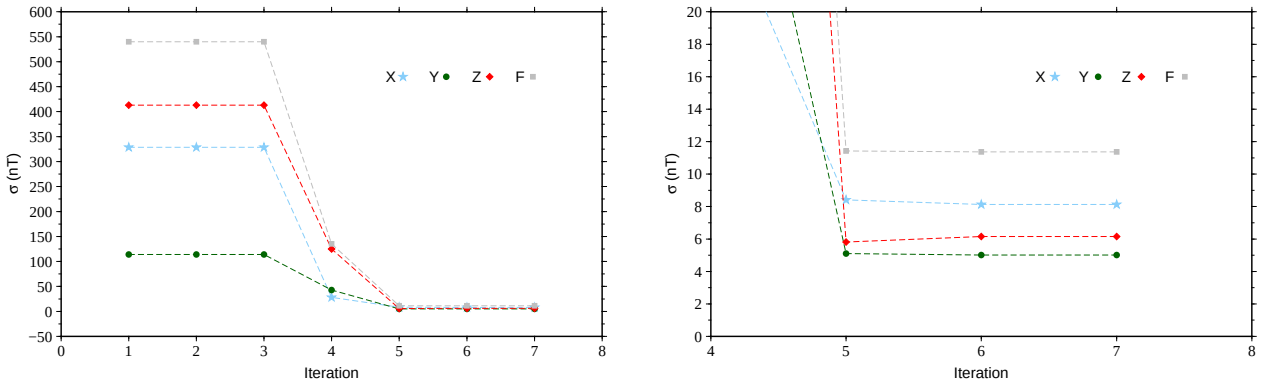

Figure 3.10: Example of the obtained rms residuals between synthetic data and predictions of each iteration by each magnetic component and the field intensity, (*left*) for all inversion iterations and (*right*) for a zoom around the last iterations, for the case of a dipole mesh with $M = 19$, $d = 0.125^o$ and placed at a depth of 4370 km.

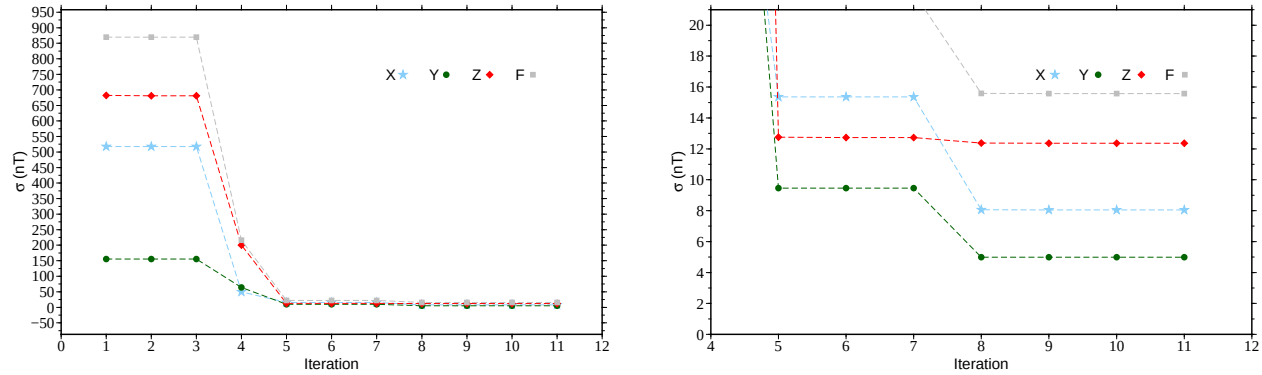

Figure 3.11: As in Fig. 3.10, for a dipole mesh with $M = 37$, $d = 0.150^o$ and placed at a depth of 3670 km.

As mentioned above, the dipole mesh should be within the region of the VO volume, thus for higher number of dipoles the mean distance between dipoles was limited. Because of this, there are no tested dipole meshes with d above 0.075^o for $M = 61$ and $M = 91$.

Figure 3.17 shows the obtained rms residuals as a function of the depth at which the dipole mesh is placed, for all tested ensemble of parameters. One part of the curves shows the smaller values for the higher depths, around 6000-6010 km, and the other part also shows small misfits for the depths 4020 and 4070 km. Thus, different dipole mesh parameters (M and d) for the same depth can produce completely different values of σ. Figure 3.18 shows again the misfit

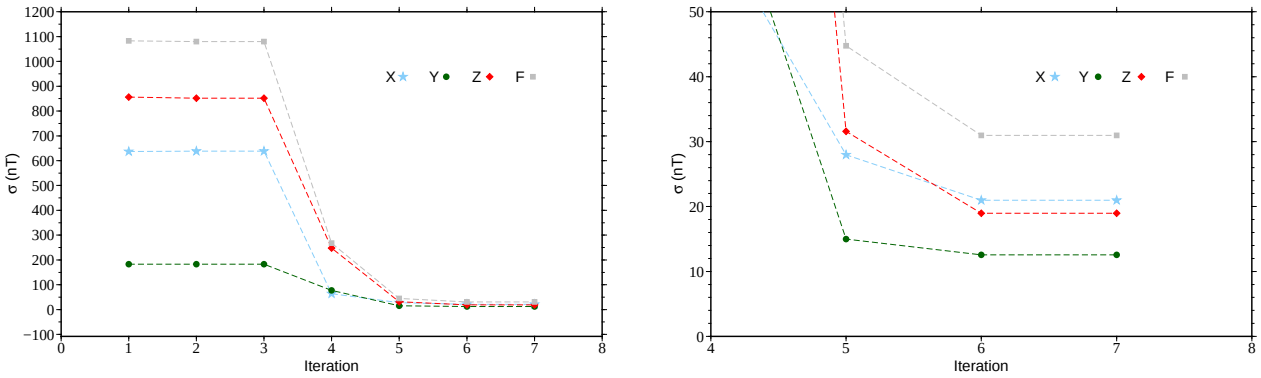

Figure 3.12: As in Fig. 3.10, for a dipole mesh with $M = 7$, $d = 0.150^o$ and placed at a depth of 3320 km.

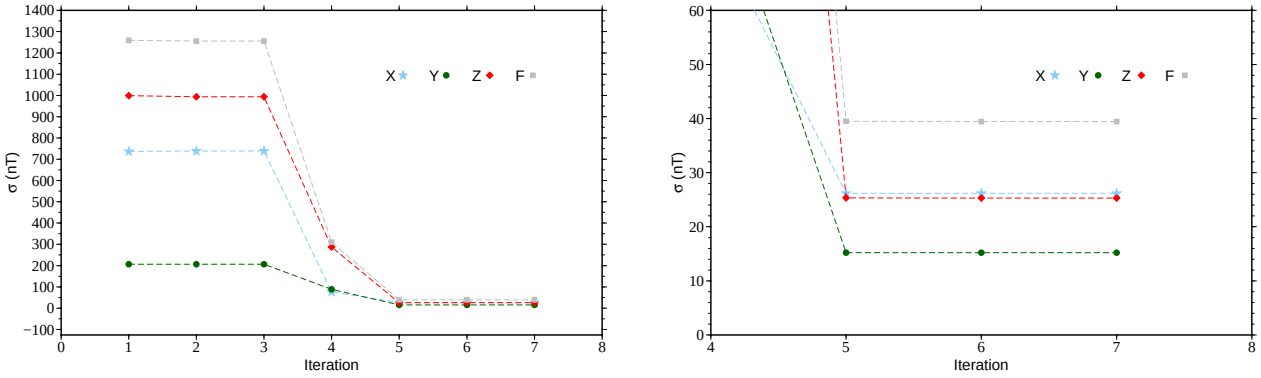

Figure 3.13: As in Fig. 3.10, for a dipole mesh with $M = 61$, $d = 0.075^o$ and placed at a depth of 3070 km.

obtained for four examples of M, as a function of the distance d. The higher values of d for the higher values of M seem to be the pair with smaller rms residuals.

The same tests were performed for other two regions, one centred at the geographic equator and the other at 76.5^{o}N 14.5^{o}E. The results are alike, with similar values of rms residuals and an unclear dependence on the tested parameters. It also seemed probable the existence of a regional dependency (on the location of the VO) of the resulting rms residuals.

Other tested idea was to invert not for the magnetisation M_θ, M_ϕ and M_r, but for the total magnetization of each one of the dipoles, with imposed values of inclination (I) and declination (D) during the inversion. First, the values of I and D were computed from the inversion of a

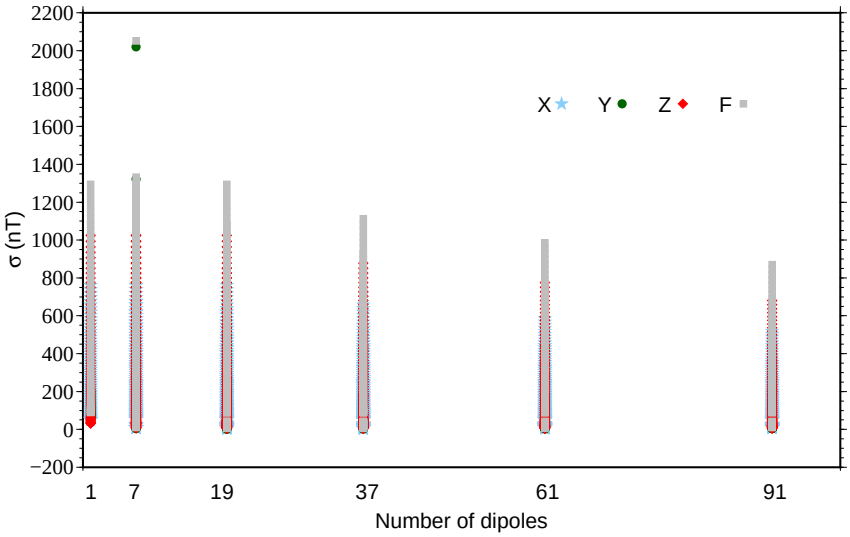

Figure 3.14: Rms residuals as a function of the number of dipoles for all cases tested. Note that the values for each case correspond to the last iteration solution.

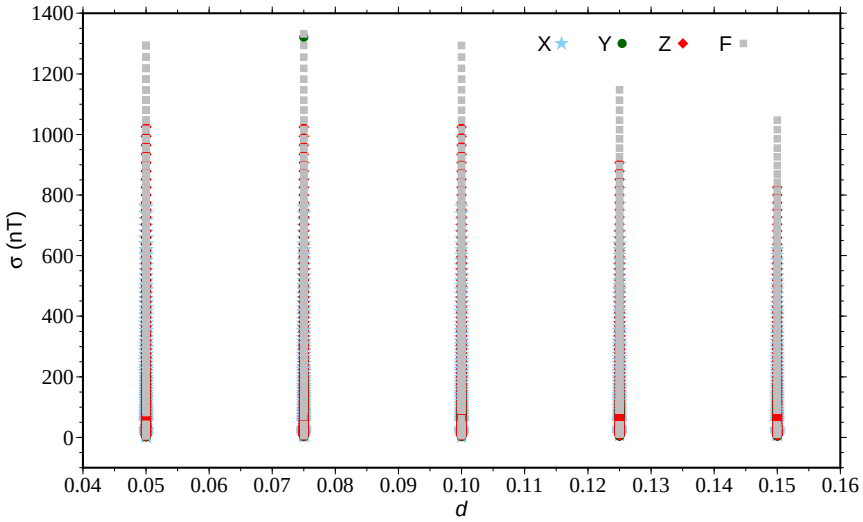

Figure 3.15: Rms residuals as a function of the mean distance between dipoles within a dipole mesh, for all cases tested. Note that the values for each case correspond to the last iteration solution.

single dipolar source centred at the dipole mesh and responsible for the input synthetic data. Then, D and I were included as an a priori parameter in the inversion for the magnetization of all dipoles within a mesh. Hence, for a given VO and respective dipole mesh the values of I and D were fixed. The results of this approach were not encouraging. The forcing of I and

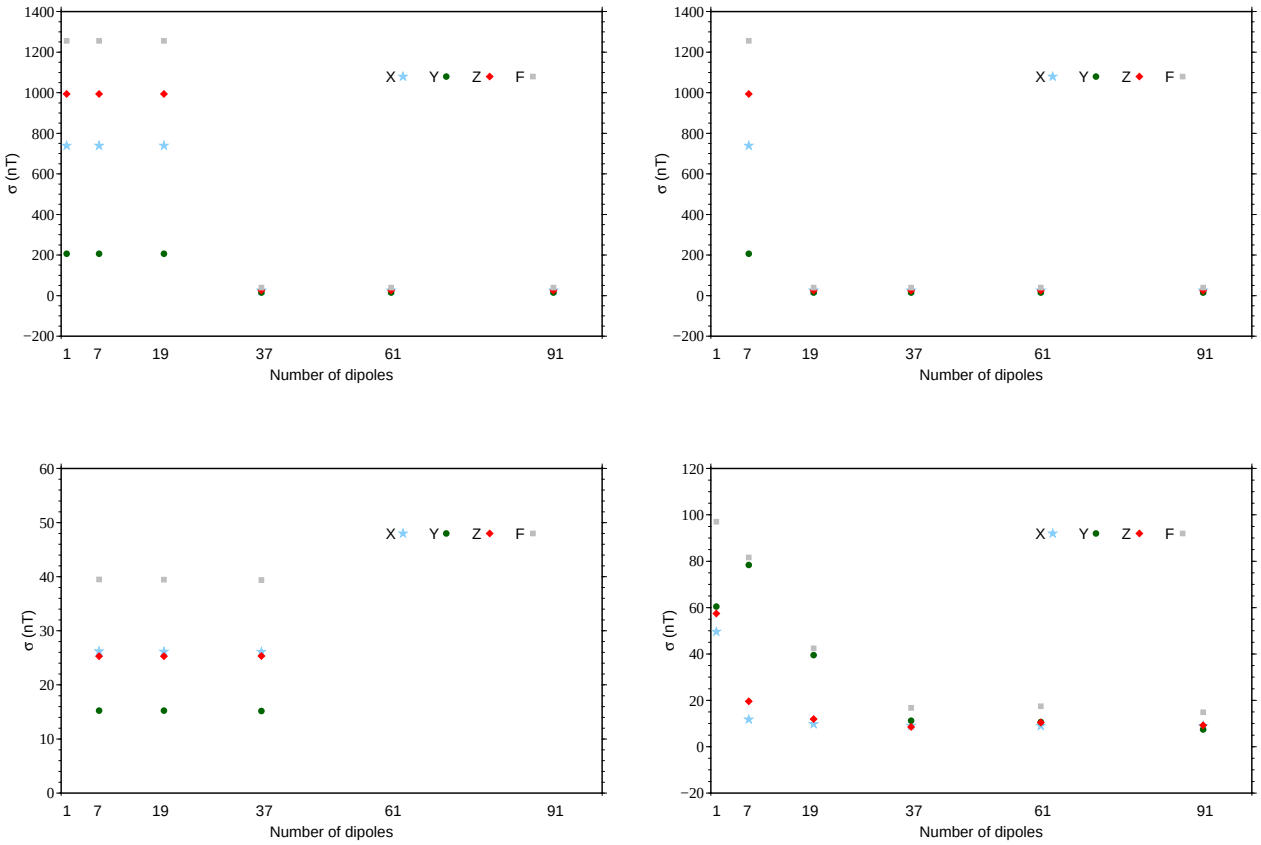

Figure 3.16: Rms residuals as a function of the number of dipoles (M) for four different dipole mesh cases: (*top left*) $d = 0.050^o$ and depth of 3070 km, (*top right*) $d = 0.075^o$ and depth of 3070 km, (*bottom left*) $d = 0.150^o$ and depth of 3070 km, and (*bottom right*) $d = 0.050^o$ and depth of 6320 km.

D on the ESD inversion did not improve the results and the misfit obtained continued to be higher than desired.

From all these results it was clear that it was not possible to obtain the desired rms residuals ($\leq$ 2 nT) by any of the tested ensemble of parameters and with the defined idea of a small dipole mesh of the size of the VO volume horizontal extend. The rms residuals obtained until now were too high. A new direction had to be taken.

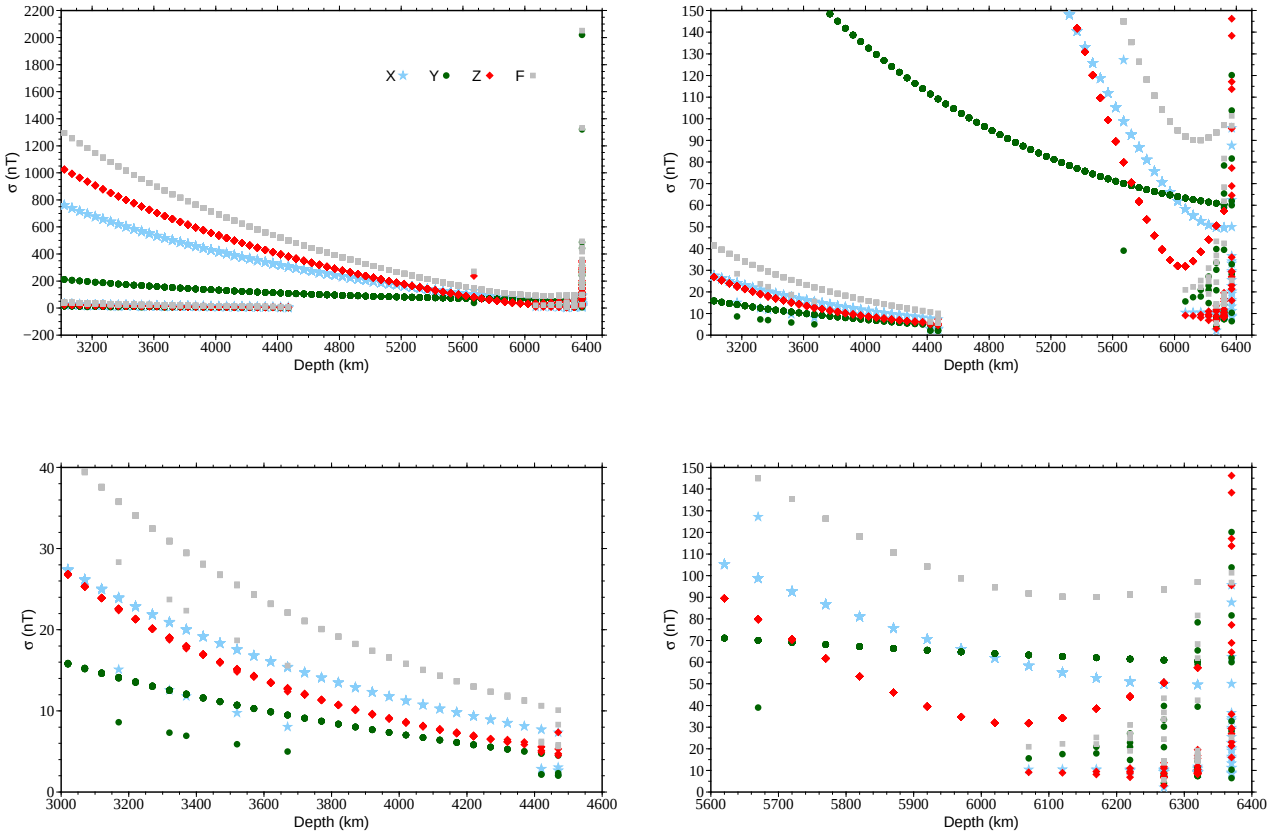

Figure 3.17: Rms residuals as a function of the depth at which the dipole mesh is placed. Three plots are zooms of the first one, focusing on different intervals of depth.

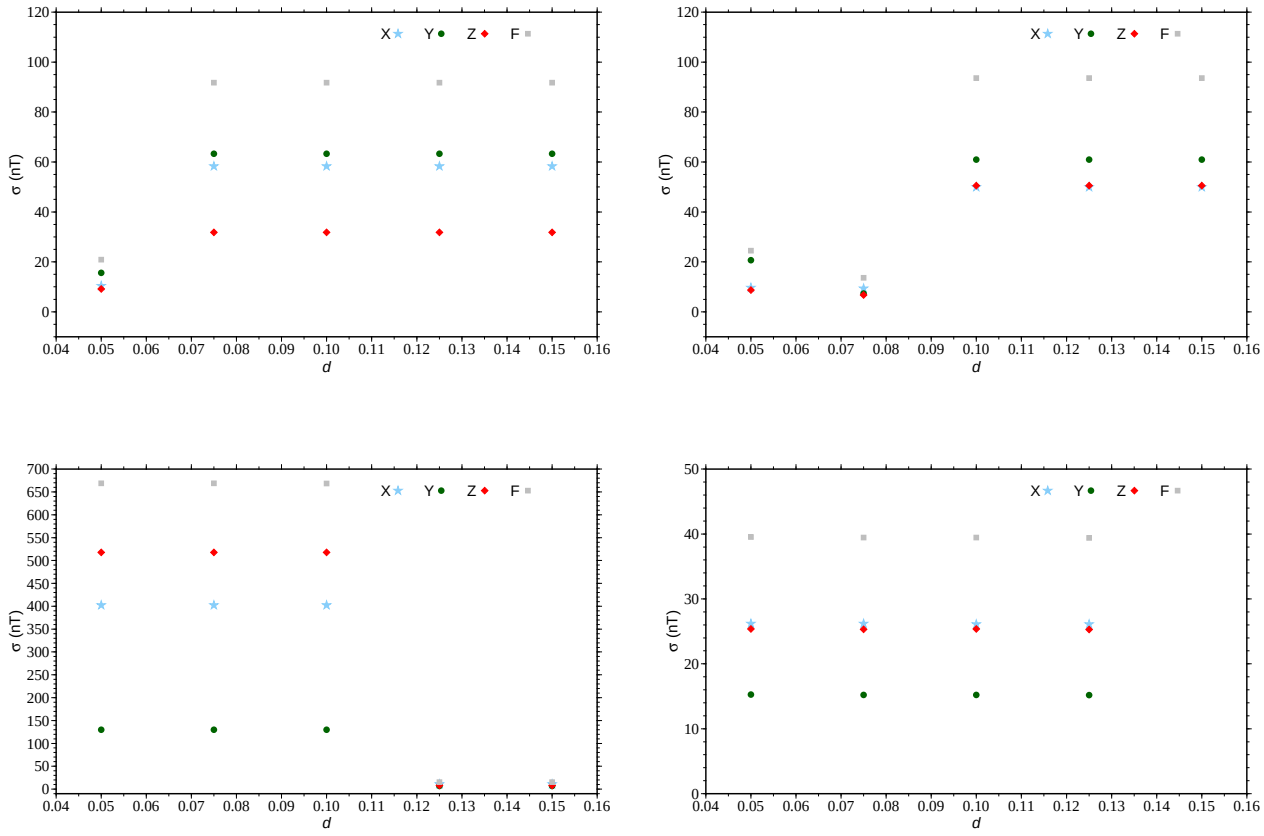

Figure 3.18: Rms residuals as a function of the mean distance (d) between dipoles within the dipole mesh, for four different dipole mesh cases: (*top left*) $M = 7$ and depth of 6070 km, (*top right*) $M = 19$ and depth of 6270 km, (*bottom left*) $M = 37$ and depth of 4070 km, and (*bottom right*) $M = 61$ and depth of 3070 km.

3.3.4 Different approach with a hemispherical dipole mesh

From the above mentioned tests it was obvious that the chosen dipole parameters were not adequate. The question of the effectiveness of the new VO-ESD approach was posed. A new direction was taken. Now the idea was to employ a dipole mesh on a larger scale, i.e., with the size of half a hemisphere or more. The following of this new idea was to place the mesh on a more "physically meaningful" depth, i.e., the CMB's depth, around 2900 km below the Earth's surface, but always centred at the VO location. The goal was still for an adequate misfit between the input synthetic data and the correspondent ESD predictions. A prediction at the centre of the VO volume for each time interval continued to be the objective. The synthetic data was the same as before. The possible time and spatial dependence of the method to the new parameters was also tested.

3.3.4.1 The new dipole mesh

A dipole mesh which covers half a hemisphere or maybe more should have a larger number of dipoles than before. The first idea was to define a dipole mesh with a spherical icosahedral discretization (Vestine et al., 1963), with equal spacing and area arrangement. This is the dipole mesh distribution used in Purucker et al. (2000); Langlais et al. (2004). A first step to obtain such a distribution is to project on the sphere twelve vertices: one at the North Pole, five equiangular distributed points at 30^oN and five other at 30^oS, and one at the South Pole. These twelve points form a mesh of twenty equal spherical triangles, bounded by thirty geodesic arcs. The discretization can be increased by the connection of equidistant point on the arcs, thus resulting in smaller triangles. If the number of subdivisions per arc is m_d it comes that the total number of mesh points on the surface of the spherical icosahedron is $M = 10(m_d - 1)^2 + 2$.

The tested dipole mesh consisted on a half icosahedron extended over one hemisphere. At first, the dipole mesh is placed at the North Pole location then a rotation on a sphere is made to bring it to the location of each VO volume. Hence from an a priori icosahedral dipole mesh, all dipole meshes for all desired VO volumes can be computed. A test was made to infer if

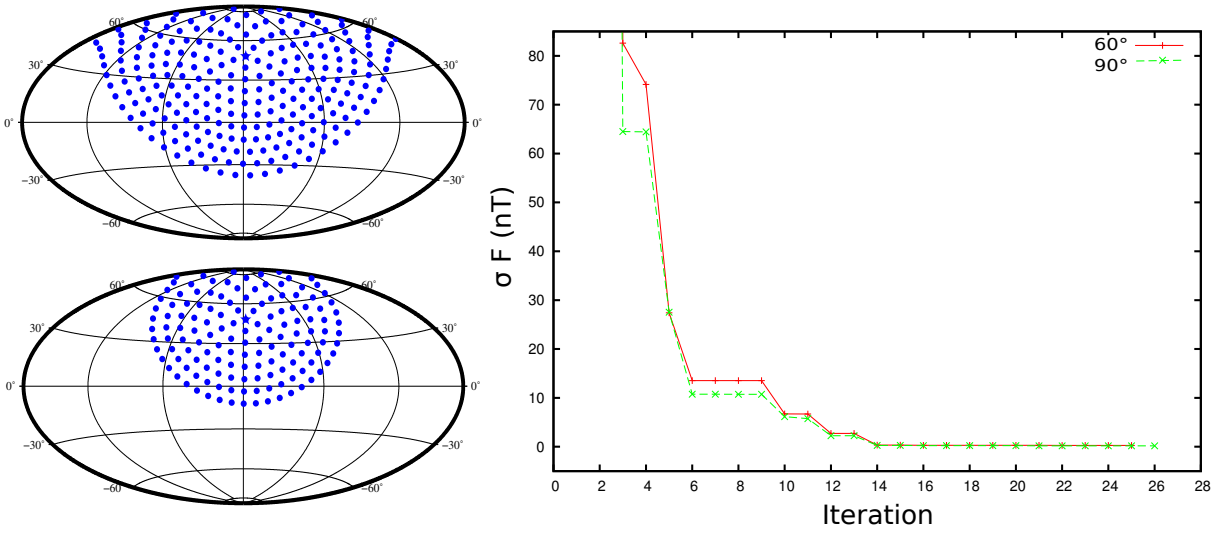

Figure 3.19: (*Left*) Half of an icosahedral dipole mesh centred at the location of the ground magnetic observatory of Chambon-la-Forêt, France (CLF) for a latitudinal extend of 90^o (*top*) and 60^o (*bottom*). (*Right*) Rms residuals between synthetic data and predictions for each iteration for the field intensity over a 30-day period for a cubic grid of 500 points and for the two dipole meshes on the left.

a latitudinal extent of 60^o (less than half of the initial icosahedron) or 90^o (half of the initial icosahedron) was more adequate. The VO volume data grid previously used continues to be considered here. As showed in Fig. 3.19 there is no significant difference on the rms residuals curve behaviour. The slightly lower values for the case of 90^o made the choice. From this, various tests were taken for a half icosahedron dipole mesh for different values of dipole mesh resolution i.e., for different m_d (from 5 to 12). The point was to infer the minimal necessary number of subdivisions on the dipole mesh for adequate rms residuals values. However, the obtained rms residuals were strongly dependent on the value of m_d.

The quality of a dipole mesh geometry can be tested using Runcorn's theorem (Runcorn, 1975) with a spherical shell and an internal dipole field. The result of this should be a zero field in a perfectly even mesh geometry. Purucker (2004) performed this test and showed that the icosahedral distribution approach showed bands of non-zero values at the connections of the spherical triangles at 30^oN and 30^oS, and near the poles. This test was performed for a global mesh, however on a regional scale the mesh still has an uneven distribution. For this reason

the icosahedral mesh distribution was abandoned and a return to the hexagonal dipole mesh was decided. Contrary to the icosahedron, the hexagonal dipole mesh is much more regular, even at a regional scale.

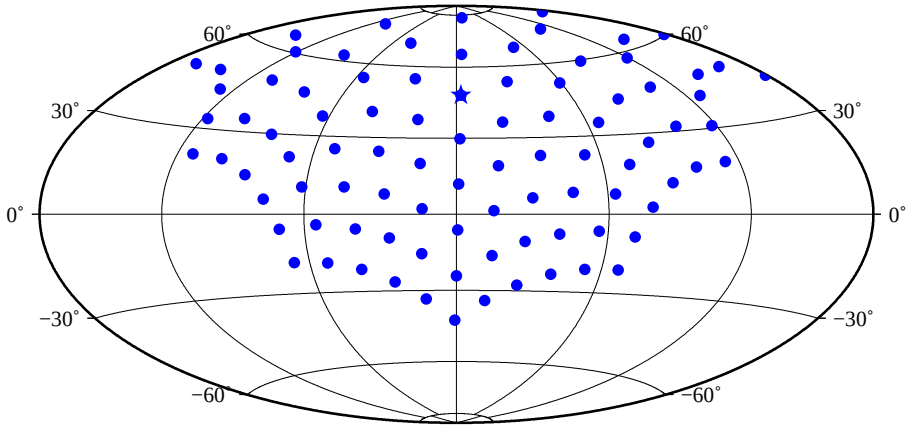

Figure 3.20: Example of an hexagonal dipole mesh, with $M = 91$ and $d = 18^o$, centred at the location of the ground magnetic observatory of Chambon-la-Forêt, France (CLF).

However, this time the hexagonal dipole mesh would have a much bigger size. Figure 3.20 shows an example of the hexagonal dipole mesh used. The hexagonal dipole mesh consists on $M = 91$ equally spaced dipoles discretized over half a sphere and 2900 km depth from the Earth's surface. The definition of such a dipole mesh for a specific VO volume is made in similar fashion as for the icosahedral: from an already defined dipole mesh at the North Pole, a rotation on the sphere is made to the centre of the VO location.

3.3.4.2 The new tests

The first tests on the new hexagonal mesh were made using the same regular cubic volume of synthetic data as the tests before (cf. Fig. 3.7). Note that this data corresponds to main field contributions only with secular variation. The results were far more encouraging. Figure 3.21 shows an example of the rms residuals obtained for a $N = 500$ points grid and a time interval of $T = 30$ days. The rms residuals for this case are closer to zero, ranging from 0.27 nT (for Z) to 1.18 nT (for F).

From these encouraging results a new step was made and a new synthetic dipole mesh definition

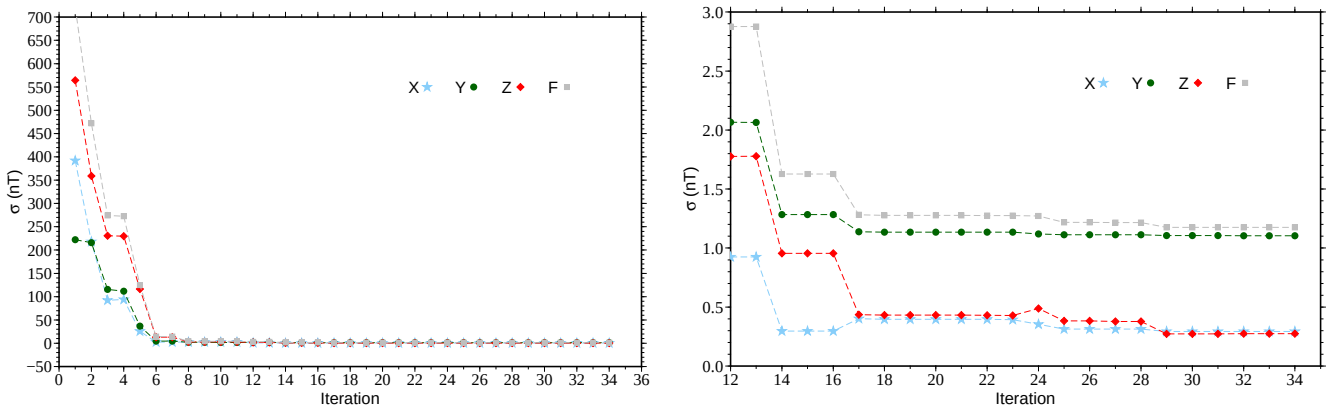

Figure 3.21: Rms residuals between synthetic data and predictions of each iteration for each magnetic component and the field intensity, (*left*) for all inversion iterations and (*right*) for a zoom around the last iterations, over a 30-day period for a cubic data volume of 500 points centred at the location of the ground magnetic observatory of Chambon-la-Forêt, France (CLF).

was chosen. A VO volume became a cylinder of radius $r_c = 1.5^o$ ($\sim$ 170 km) with N points ($\times$ 3 vector field components) distributed over a defined time period T. The cylinder was centred at a chosen VO location (r_{vo},ϑ_{vo},ϕ_{vo}), between altitudes of 463 and 517 km, which mimics the Swarm two main altitudes, with a mean altitude of 490 km (see Fig. 3.22). The number of points within a cylinder (VO) was randomly distributed in latitude, longitude and altitude. To obtain the random positions a white noise generator was used to create a series of values between the intervals of latitude, longitude and altitude, i.e.

$$\vartheta_{vo} \pm r_c, \tag{3.27}$$

$$\phi_{vo} \pm r_c, \tag{3.28}$$

$$(r_{vo} = a + 490) \pm 27km. \tag{3.29}$$

A cylinder was constructed for each time interval T, i.e., with values spanning a time interval of for example one month. Tests were also performed using different random locations of points for each time period. Thus, due to the randomly generated location points, when different locations points were used for each time period, each cylinder time period had a different spatial distribution. White noises of 2 nT (standard deviation SD = 1.16), 5 nT (SD = 2.92) or 10 nT (SD = 5.78) were also added to the various example tests in order to mimic the external field contributions and other noise sources at satellite altitude. Even thought these signals are

not identical to white noise, this was the only way found to test them. In the next pages the results of various tests for a cylindrical VO with $N = 800$ points and with data within the time interval of $T = 30$ days are presented. The VO is centred at the location of the ground magnetic observatory of Chambon-la-Forêt, France (CLF) at 48.02^{o}N 3.27^{o}E.

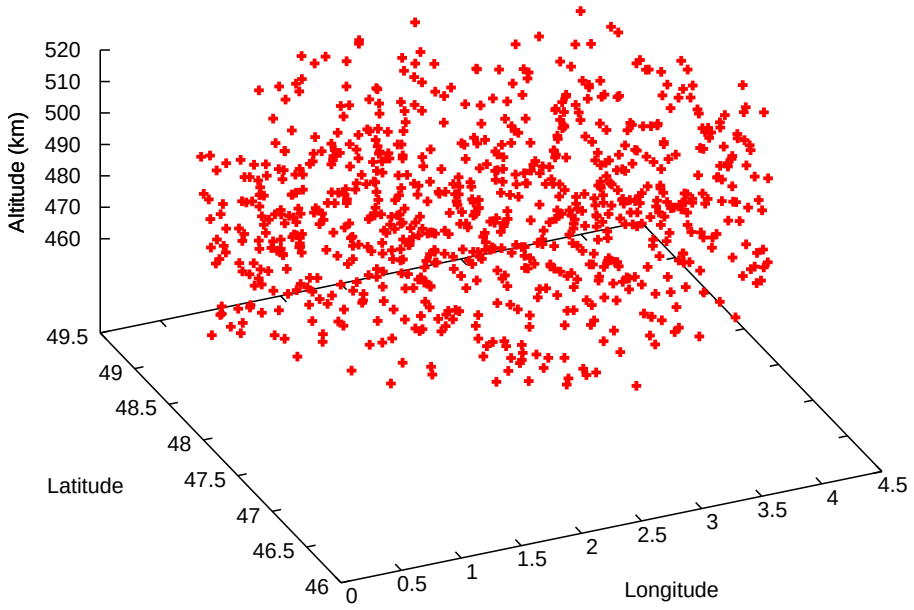

Figure 3.22: Example of a 800 points VO volume cylinder centred at the location of the ground magnetic observatory of Chambon-la-Forêt, France (CLF), spanning a 30-day time period.

3.3.4.2.1 First automatic iteration selection criterion

A first automatic criterion to choose the solution iteration from the ESD inversion was defined here. The idea was simply to search for the iteration $k + 1$ where

$$\sigma_{k+1} - \sigma_k < 0, \tag{3.30}$$

for all the three magnetic components and field intensity (i.e., for all four σ). When this criterion was found, the iteration k was the chosen one. Afterwards, a prediction at the centre of a VO volume was performed using the solution of the selected iteration. This criterion is based on the idea that once the solution iteration rms residuals are stable (do not change more with the iteration), a good solution is found.

3.3.4.2.2 Cylindrical volume without noise, without secular variation

An initial test of synthetic data with no secular variation was performed. Without SV, σ for field intensity is below 0.1 nT and below 0.06 nT for all three magnetic components (see Table 3.2 and Fig. 3.23). It is the Y component that exhibits the smaller rms residuals (below 0.05 nT).

Even if the case of no SV is not physically meaningful, this test allows a comparison with the next tests using SV within the data and properly account for the SV's effect in the results. All the following tests use synthetic data with secular variation.

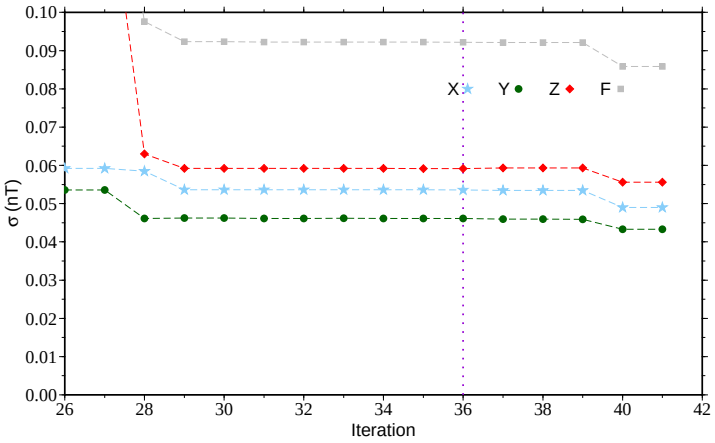

Figure 3.23: Rms residuals between synthetic data and predictions of each iteration for each magnetic component and the field intensity over a 30-day period and a cylindrical 800 points VO volume **without SV** and centred at CLF. The selected iteration solution is highlighted with a violet vertical dotted line.

3.3.4.2.3 Cylindrical volume without noise

For a synthetic time varying data volume the resulting distribution of rms residuals (σ), follows a behaviour which is illustrated in Fig. 3.24. The rms residuals for this case are of the order of 1 to 1.5 nT (see Table 3.2). These values are, as expected, greater than the ones for the case without SV. They can be explained by both

- the spatial variation of the field over the considered VO volume, and
- the temporal variation of the field which takes place during the 30-day period.

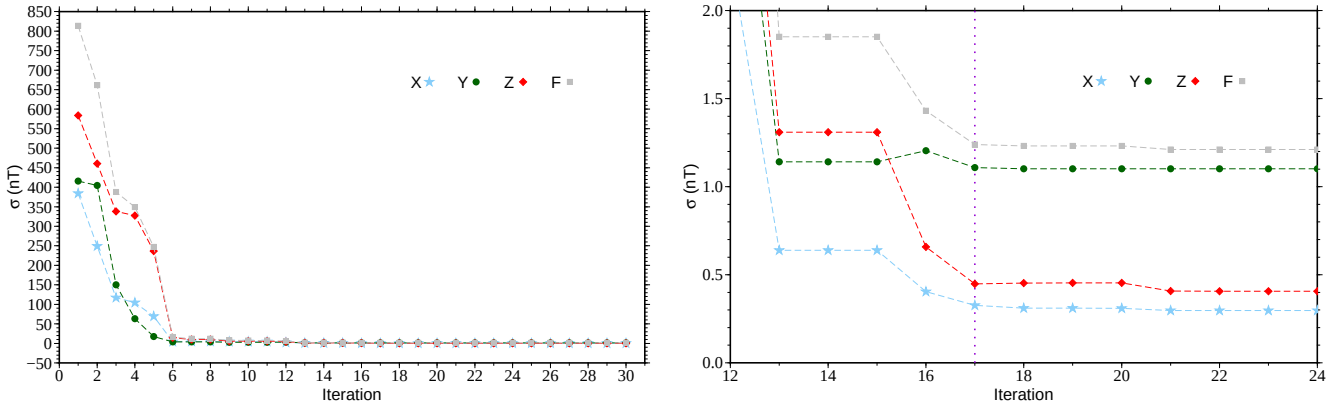

Figure 3.24: Rms residuals between synthetic data and predictions of each iteration for each magnetic component and the field intensity over a 30-day period and for a cylindrical 800 points VO volume centred at CLF **without noise** added; (*left*) for all inversion iterations and (*right*) for a zoom around the selected iteration solution. The selected iteration solution is highlighted with a violet vertical dotted line.

Interestingly σ for Y component is now more important (for the three magnetic components), indicating that the SV strongly influences this component. Despite these values of rms residuals, the prediction of the VO-ESD approach at the VO centre and mean time is very satisfactory as can be seen in Fig. 3.25. This figure displays the predictions of the ESD technique at the centre of the VO volume for each 30-day period and respective selected iteration solution, during one year. A comparison between the ESD prediction and the CHAOS-4 model prediction at the same time and location is made. The differences between the model and the ESD predictions are displayed in green on the right-side of each plot. It can be seen that the differences are mainly close to zero, with values $\leq \pm$ 0.1 nT. Contrary to what could be expected, after displaying the higher σ (compared to X and Z, cf. Fig. 3.24), the Y component is the one with smaller differences, constantly very close to zero.

3.3.4.2.4 Cylindrical volume with noise

As expected, the addition of noise to the synthetic data volume increased the rms residuals. Figure 3.26 presents the rms residuals for the three examples of added white noises (2, 5 and 10 nT) for the same 30-day period and VO volume. For the case of 2 nT noise, the three magnetic components have σ around the value of SD of the noise (1.16 nT). Considering the

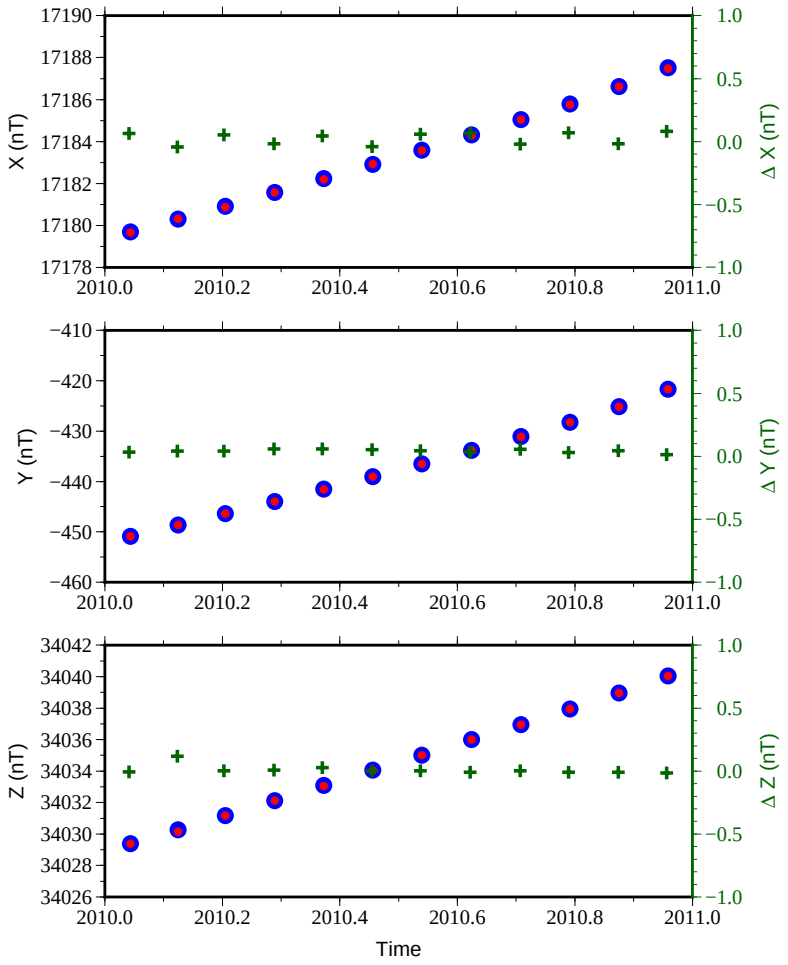

Figure 3.25: Predictions by the ESD technique (*red*) for the three magnetic components at the centre of the VO for each 30-day period and a cylindrical 800 points VO volume centred at CLF **without noise** added. Also showed are the predictions by a SH model at the middle of the time period (*blue*). The residuals between the model and the ESD predictions are also shown (*green*), with its axis on the right.

5 nT noise case, the rms residuals are of the order of 3 nT, also corresponding to the noise SD. The same can be seen for the 10 nT noise case, where σ is around 5.7 nT. The east-west component (Y) has the higher values of σ for the first two cases. In the last case (10 nT noise) it is the vertical component who has the higher σ (see Table 3.2).

Despite these larger rms residuals, the quality of the VO-ESD predictions is not altered for almost all cases (Figs. 3.27, 3.28 and 3.29). The differences between the model used as input and the ESD predictions are $\leq \pm 0.4$ nT for the 2 nT case and $\leq \pm 0.5$ nT for the 5 nT case. For the 10 nT case, differences can be as close as 2.5 nT for the vertical component. In fact for the 10 nT white noise case, the vertical component is less well predicted by the ESD technique. The disturbance in the data due to this noise becomes important and affects the ESD effectiveness.

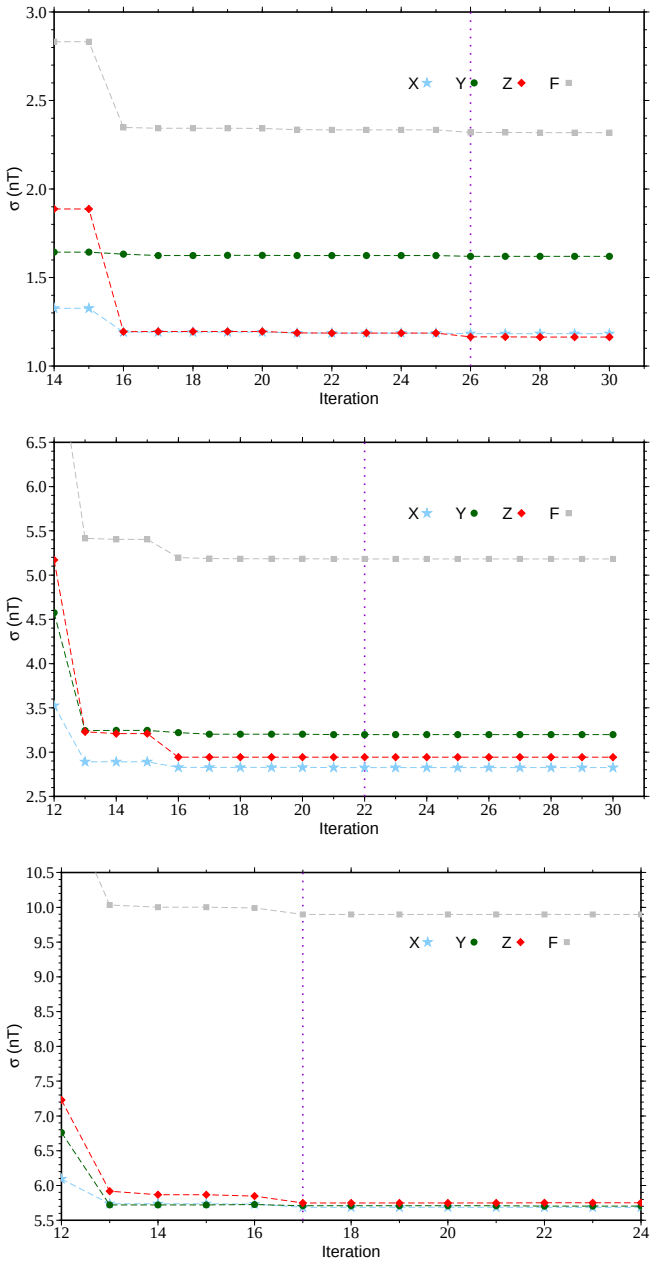

Figure 3.26: Rms residuals between synthetic data and predictions for iterations around the selected one, for each magnetic component and the field intensity over a 30-day period and a cylindrical 800 points VO volume centred at CLF. Presented are the cases (*top*) with **2 nT** white noise, (*middle*) **5 nT** white noise, and (*bottom*) **10 nT** white noise. The selected iteration solutions are highlighted with a violet vertical dotted line.

Tests were also performed for identical position values as well as identical noise values for all time periods. The results show that the ESD technique is not significantly dependent of the spatial distribution of the data points or of the different values of added noise. The obtained rms residuals are very close to the ones of the case showed here.

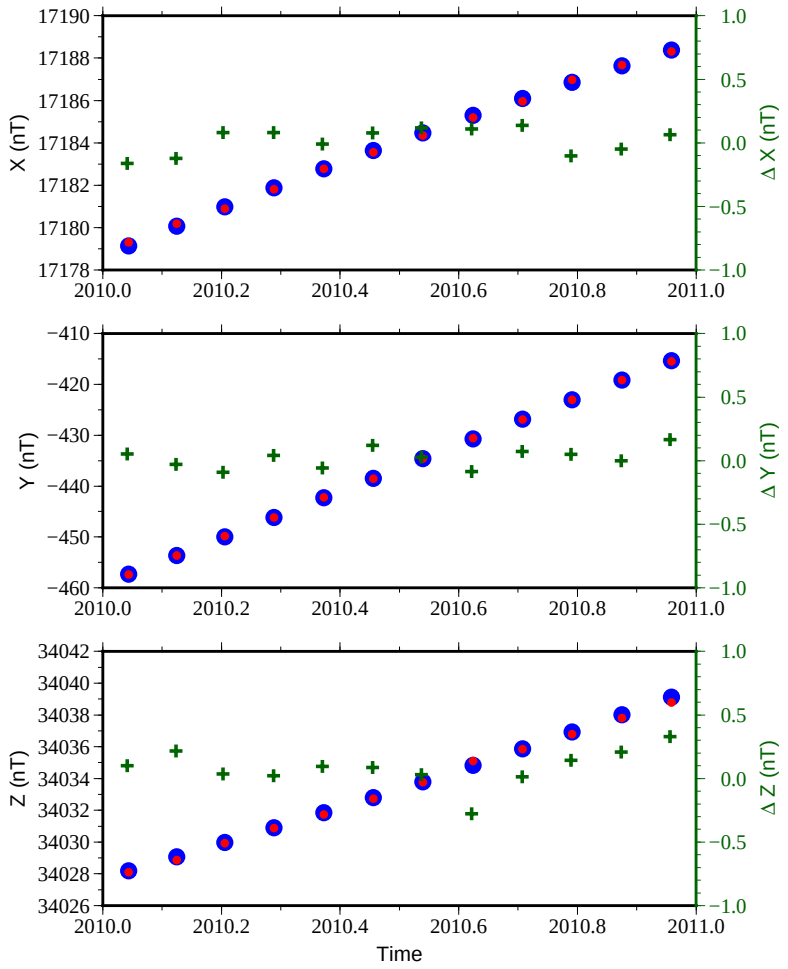

Figure 3.27: Predictions by the ESD technique (*red*) for the three magnetic components at the centre of the VO for each 30-day period and a cylindrical 800 points VO of synthetic data with 2 nT white noise added. Also showed are the predictions by an SH model at the middle of the time period (*blue*). The residuals between the model and the ESD predictions are also shown (*green*), with its axis on the right.

3.3.4.2.5 Synthetic orbits without noise

The next step was to apply the VO-ESD approach to synthetic Swarm orbits. These orbits consisted on predictions of an SH model (CHAOS-4) along the Swarm orbits positions, spanning the first thirteen months of the mission, from November 2013 to December 2014. Figure 3.30 shows examples of the spatial distribution of Swarm orbits within a cylindrical VO volume and for a time period of 30 days. It is clear that for different periods the spatial distribution of the data changes significantly. The VO volume geometry did not change. The fixed altitude for all VO was later reconsidered during the application of the VO-ESD approach to Swarm measurements (see Section 4.5.1).

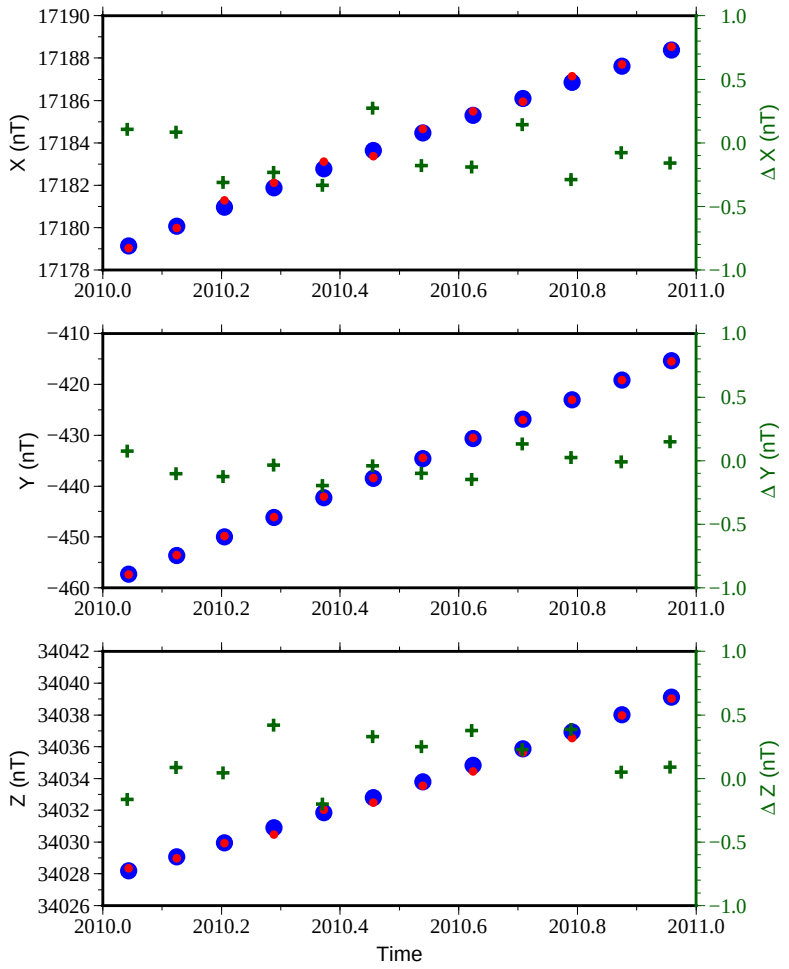

Figure 3.28: As in Fig. 3.27, for 5 nT white noise.

Rms residuals for X, Y, Z and F are of the order of 0.4, 1.2, 0.4 and 1.3 nT respectively (Fig. 3.31), varying slightly for different periods of 30-days. The reason for the higher value of σ for the Y component may be linked to the effect of the SV on this component (cf. Sections 3.3.4.2.2 and 3.3.4.2.3). Comparing these results with the ones from the case of a cylindrical VO volume (without noise) it can be seen that the rms residuals are very similar and even a little smaller. Thus, the rms residuals values are not significantly affected by changing the spatial distribution of the orbit positions.

For this case, the differences between the input synthetic data and the VO-ESD predictions vary from ± 0.1 to ± 0.5 nT (Fig. 3.32). The X component is the one with greater number of small differences, while the Z component presents the higher number of high differences. The prediction is however still satisfactory, only some periods for the vertical component have less ideal results (like the last period shown).

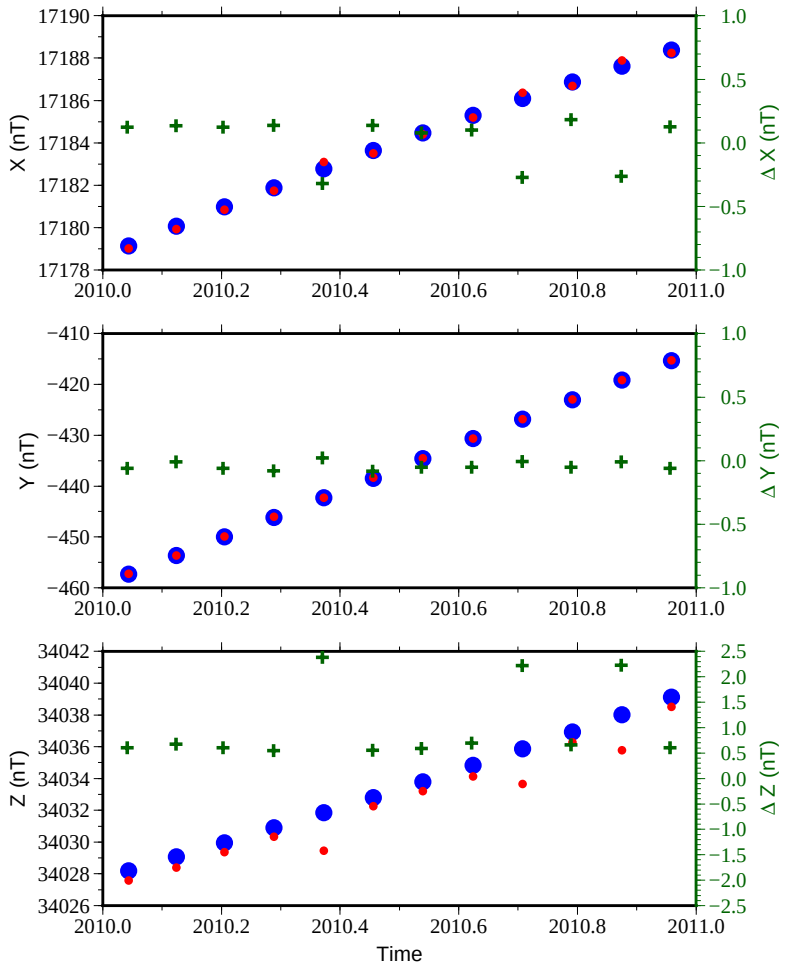

Figure 3.29: As in Fig. 3.27, for 10 nT white noise.

3.3.4.2.6 Synthetic orbits with noise

As before, the rms residuals increase with the addition of white noise to the synthetic data, but still within the expected values (Fig. 3.33). Here only the examples for 5 and 10 nT noise are shown. As with the case without noise, it is the Y component which presents the higher values of rms residuals. The rms residuals for the case of 5 nT are of the order of 3.2 nT for X, Y and Z components and of 5.5 nT for the field intensity. For the 10 nT case the rms residuals are of the order of 5.9 nT for the X, Y and Z components and 10.3 nT for F (Table 3.2). These values of rms residuals do not significantly change for different periods. Again, the rms residuals values are not significantly affected by the spatial distribution of the orbit positions neither by the addition of the white noise.

The introduction of noise increased the differences of the predictions at the centre of the VO,

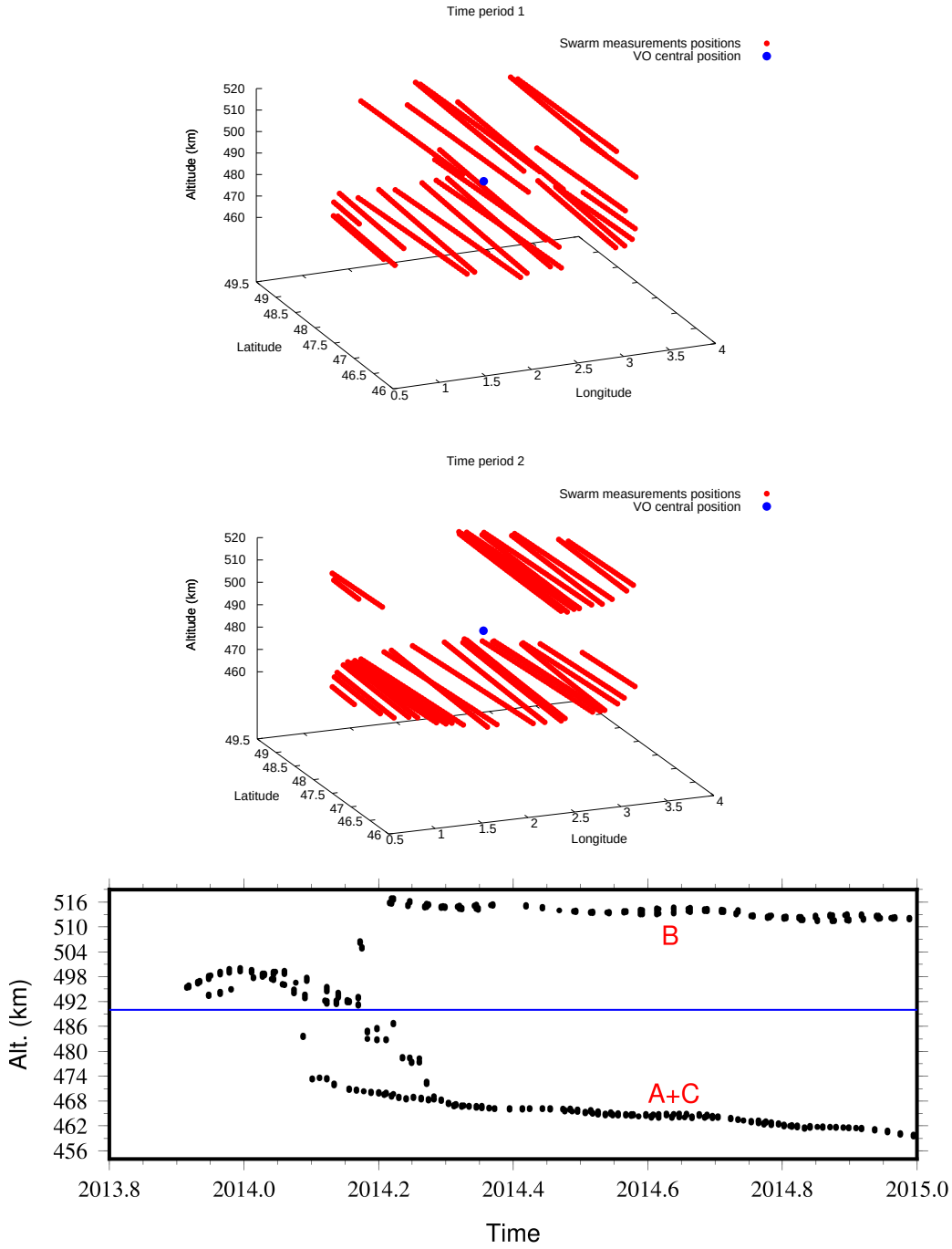

Figure 3.30: (*Top and middle*) Examples of Swarm orbits within a cylindrical VO volume for two different time periods of 1-month. (*Bottom*) Evolution of the altitude of Swarm orbits for the same VO cylindrical volume represented on top. The VO central position altitude ($r_{vo} = 490$ km) is outlined as a blue line and the satellite names are marked.

as expected. Nevertheless, the addition of white noise to the synthetic orbits data set does not significantly change the prediction effectiveness (Figs. 3.34 and 3.35). It is on the vertical component that the differences are higher. In the 10 nT white noise case the predictions are less ideal for some periods. However, they are still satisfactory.

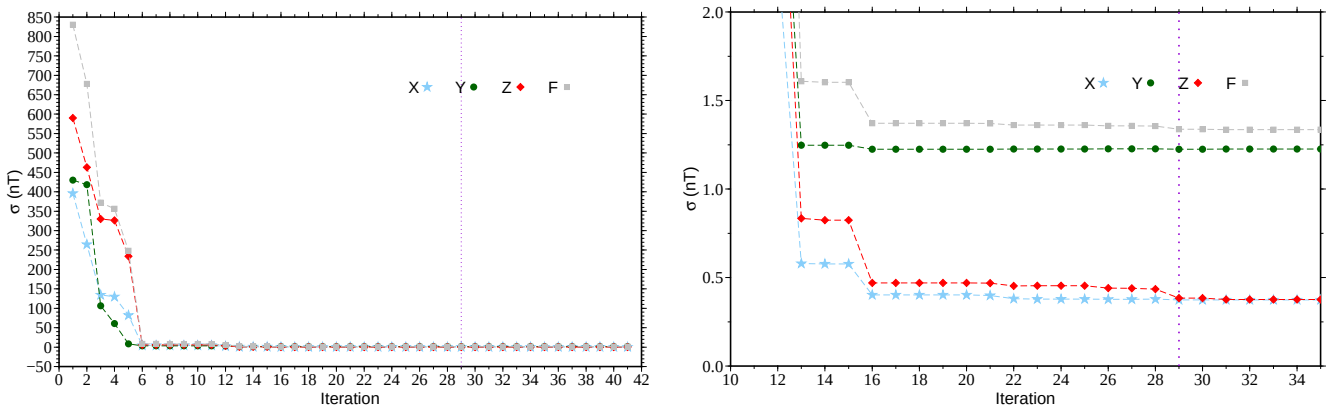

Figure 3.31: Rms residuals between synthetic data and predictions for (*left*) all inversion iterations and (*right*) for a zoom around the selected iteration solution, for each magnetic component and the field intensity for the case of **synthetic Swarm orbits without noise** within a VO volume centred at CLF. The selected iteration solution is highlighted with a violet vertical dotted line.

3.3.4.2.7 Dependence with the number of points

As the satellite measurements cannot be available for all times due to satellite movements or any kind of problems in the instruments, the number of points within a VO volume for a given time period can vary significantly. A procedure continually performed during the validation tests was testing the variation of the results with the parameter N. The objective was to infer the dependence of the VO-ESD approach with the chosen dipole mesh and VO volume geometry to this parameter.

Figure 3.36 shows an example for $N = 500$ on a cylindrical volume and a hexagonal dipole mesh, without noise added to the synthetic data. Comparing with Fig. 3.24 we see that the component Y continues to be the one less explained by the technique. The values of rms residuals are very similar for both cases. The change of the number of points within the volume does not significantly changes the results.

Other values of N were tested and no significant changes were noted in the results. Table 3.3 shows the rms residuals for different examples of N. For the cylindrical VO volume and a hexagonal dipole mesh the values increase for a larger number of points, but they are still acceptable.

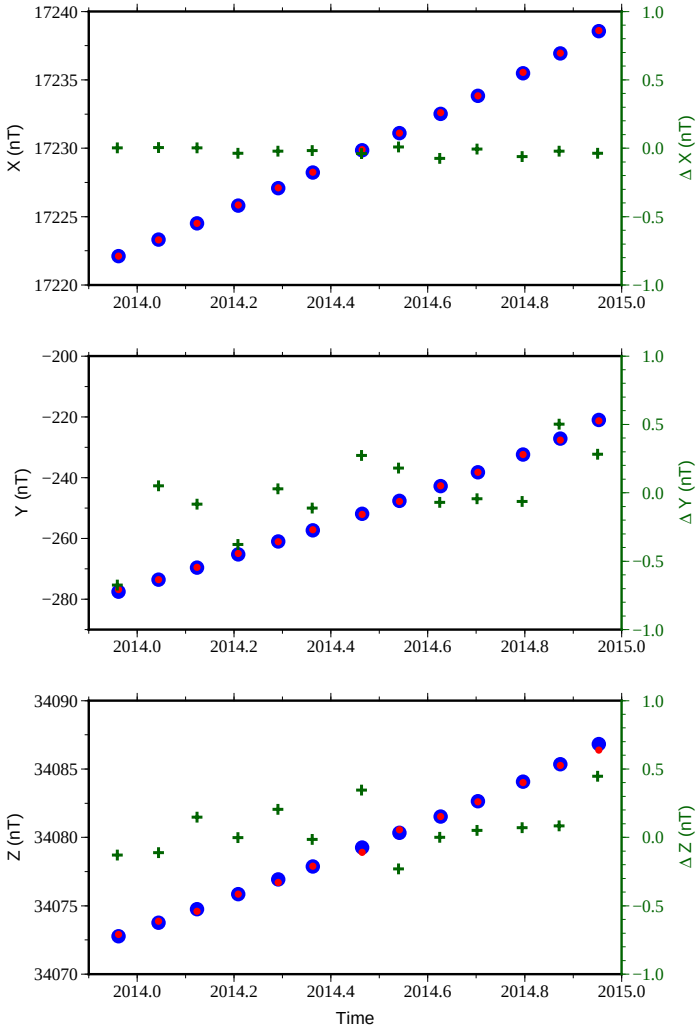

Figure 3.32: Predictions by the ESD technique (*red*) for the three magnetic components at the centre of the VO for each 30-day period and for the case of **synthetic Swarm orbits without noise** within a VO volume centred at CLF. Also shown are the predictions by an SH model at the middle of the time period (*blue*). The residuals between the model and the ESD predictions are also shown (*green*), with its axis on the right. Note the change of the right side axis interval for the Z component.

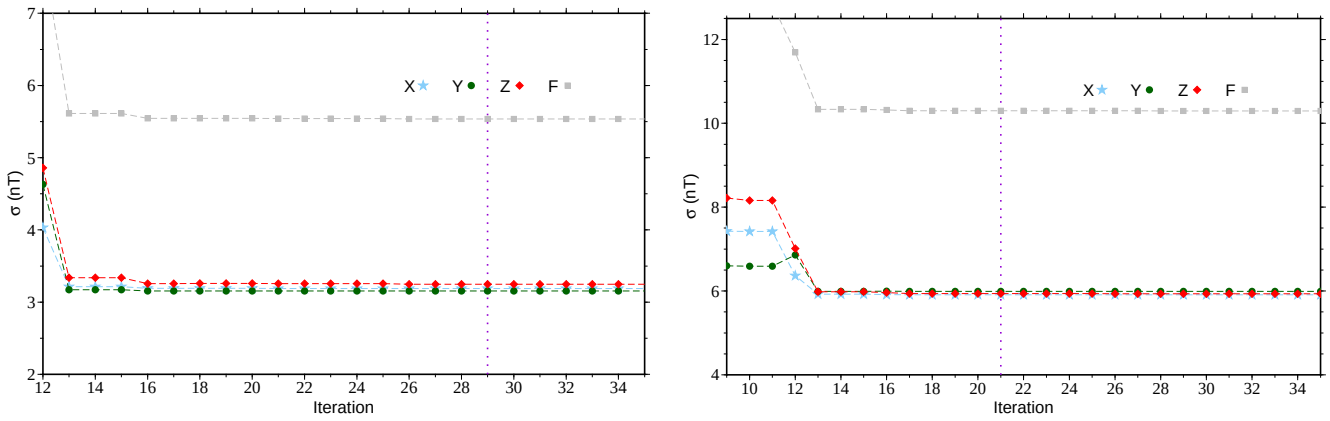

Figure 3.33: Same as Fig. 3.31, for a case with (*left*) **5 nT** and (*right*) **10 nT** noise added.

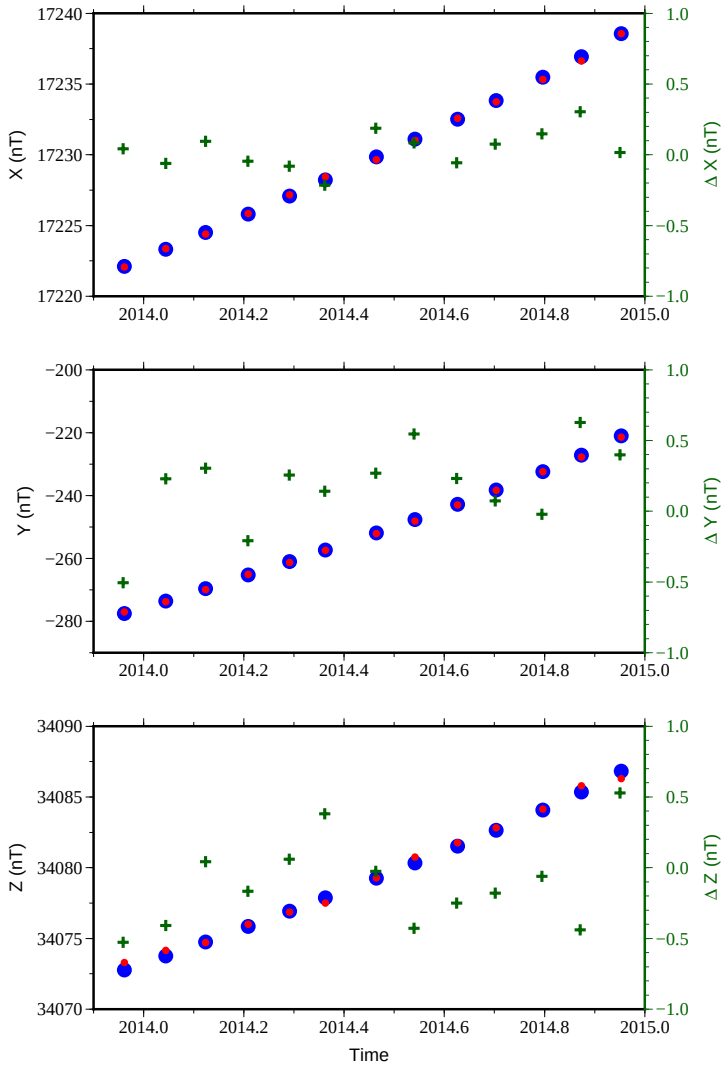

Figure 3.34: As in Fig. 3.32, for a case with **5 nT** noise added. Note the change of the right side axis interval for the Z component.

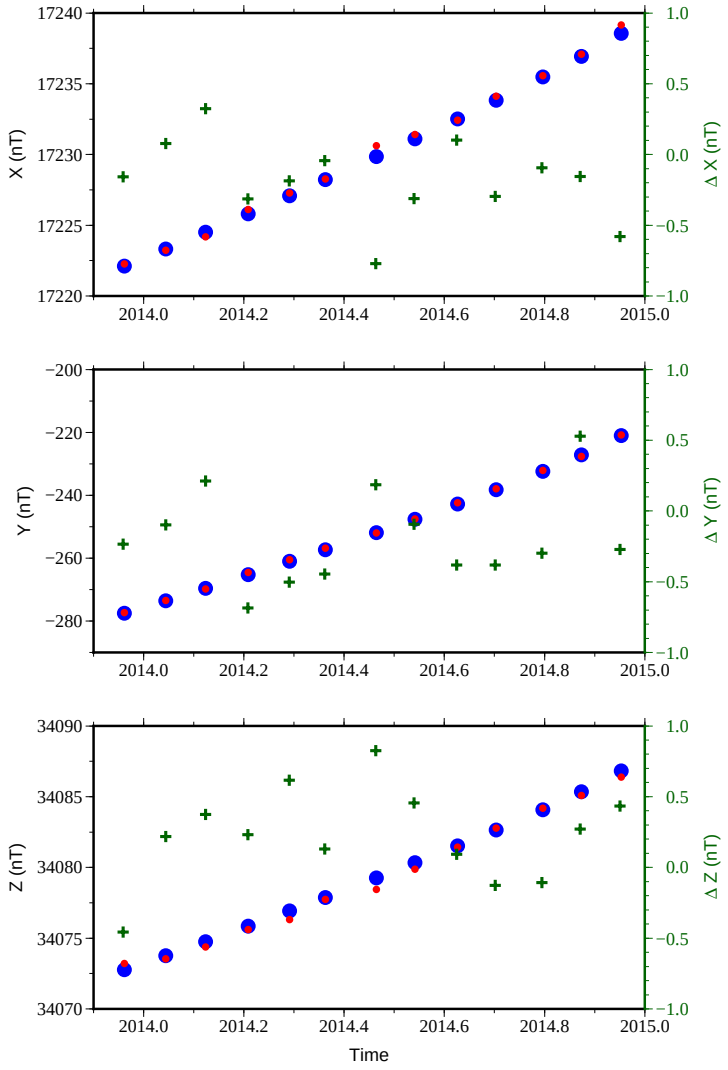

Figure 3.35: As in Fig. 3.32, for a case with **10 nT** noise added. Note the change of the right side axis interval for the Z component.

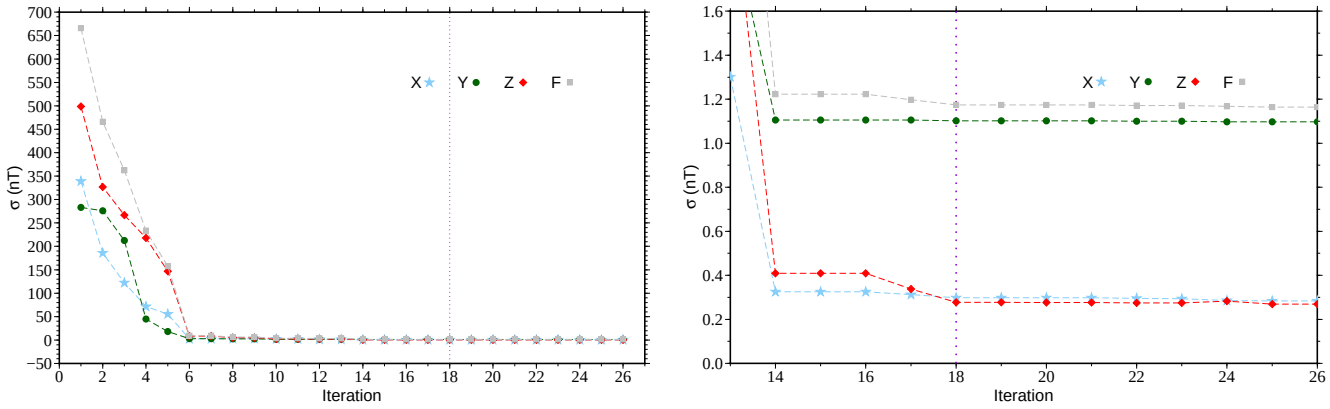

Figure 3.36: Same as Fig. 3.24, for a case with 500 points.

Table 3.2: Rms residuals between synthetic data and predictions of the selected iteration solution for each magnetic component and the field intensity over a 30-day period and for different VO volumes examples. See text for details.

	σ (nT)			
	X	Y	Z	F
Cylindrical volume without SV	0.054	0.046	0.059	0.092
Cylindrical volume without noise	0.327	1.108	0.448	1.239
Cylindrical volume with noise (2 nT)	1.183	1.620	1.165	2.319
Cylindrical volume with noise (5 nT)	2.825	3.197	2.942	5.183
Cylindrical volume with noise (10 nT)	5.687	5.708	5.748	9.898
Synthetic orbits without noise	0.374	1.225	0.384	1.338
Synthetic orbits with noise (5 nT)	3.188	3.153	3.248	5.537
Synthetic orbits with noise (10 nT)	5.908	5.992	5.937	10.298

Table 3.3: Rms residuals between synthetic data and predictions of the selected iteration solution for each magnetic component and the field intensity over a 30-day period and for different examples of the number of points in the VO data volume. See text for details.

N	VO volume	Dipole mesh	Year	σ (nT)			
				X	Y	Z	F
300	cube	icosahedron	2010	0.308	1.087	0.379	1.192
400	cube	icosahedron	2010	0.317	1.090	0.360	1.191
500	cube	icosahedron	2010	0.297	1.284	0.955	1.627
500	cylinder	hexagonal	2010	0.298	1.102	0.277	1.174
1000	cylinder	hexagonal	2010	0.327	1.108	0.448	1.239
1000	cylinder	hexagonal	2014	0.374	1.205	0.302	1.297
1125	cylinder	hexagonal	2014	0.535	1.750	0.481	1.892

3.3.5 Discussion and conclusions of the validation tests

The initial tests using a local and narrow dipole mesh revealed inadequate results. The obtained rms residuals were higher than desirable. The assumption that a mesh of sources at a local scale, just above the VO volume would be appropriate to explain the measurements proved to be incorrect. The ESD technique with such a narrow dipole mesh was not capable to properly reduce the measurements to a common altitude.

The ESD technique has been successfully used on a local scale, essentially for crustal and local problems (Mayhew et al., 1980; Langlais et al., 2004). However, for a global and complex magnetic field (with a multitude of sources) as the Earth's, a local group of sources is not adequate to explain it and describe it, even for measurements at a local scale.

With the change of approach to a hemispherical dipole mesh the results become more encouraging. Hence, the input data was better explained by a mesh of sources well distributed and distant from the data location.

From the initial idea of a cubic VO data volume, a change of approach was also taken to a cylindrical VO volume. The notion was that with the new geometry the farthest data points were closely at the same distance from the VO centre. It appeared a more balanced approach.

As for the altitude of a VO, it was decided after some months of measurements of the Swarm mission, to fix it to 490 km, the mean altitude of both orbital planes of the constellation satellites. This decision was later redefined (see next chapter).

Nevertheless, for a VO volume of synthetic measurements and with the following characteristics:

- cylindrical with $r_c = 1.5^o$,
- centred at 490 km altitude, and
- with data spanning a period of 30 days,

the ESD technique is capable to reduce to a common altitude and time the magnetic field measurements acquired inside the VO volume, using the following dipole mesh parameters:

- depth of 2900 km,
- $M = 91$ dipoles, and
- $d = 18^o$ of mean spacing between dipoles.

The tests which validated these parameters were performed using as input data the model CHAOS-4 (Olsen et al., 2014). First for randomly distributed data points within the cylindrical volume for all months of the year 2010. This corresponded to 12 periods for which the inversion was computed. Later, the approach was applied to orbital positions of the first thirteen months of the Swarm mission. On both tests the approach's inversion technique delivered satisfactory rms residuals values.

For cylindrical volumes of data and the without noise cases, the rms residuals values were under 0.5 nT for the X and Z components of the field and only above 1 nT for the Y component. One test was also performed for data without secular variation, delivering rms residuals inferior to 0.1 nT, even for the field intensity. This test demonstrated that the temporal variation of the data increases the obtained rms residuals of the inversion.

The SH model used as input data only describes the internal field contributions. But, at satellite altitude the external field contributions are important. To mimic these contributions and/or others, white noise was added to the input data. The addition of noise did not significantly alter the ability of the approach to predict the magnetic field for a given time interval at a fixed altitude. The increase of the rms residuals values corresponded to the standard deviation of the added white noise, as expected. The obtained predictions of the VO-ESD approach at satellite altitude at the mean time of the data periods was also very close to the input data model predictions at the same locations. These predictions were very satisfactory.

Even the utilization of Swarm orbits positions, leading to a significant change on the spatial distribution of the data did not transform the technique results. The obtained rms residuals and the predictions at satellite altitude were similar to the ones obtained for the randomly distributed points, and thus satisfactory.

The spatial distribution of the data does not significantly affects the inversion technique results.

The number of points within the VO volume is also not significantly important. From all these results the VO-ESD approach was considered validated.

Nevertheless, the inversion technique needs a minimum number of data points. The unknowns of the inversion correspond to $M \times 3$ dipoles magnetisation. Thus at least the same number of data points is needed at each period (if no regularization is added).

The tests were performed using a model describing only the main field contributions. Even with the addition of white noise to mimic the external sources of the field, the results can still differ using real magnetic measurements. This is performed and the results are described in the next chapter.

Chapter 4

Application of the VO-ESD approach to Swarm measurements

The VO-ESD approach described in the previous chapter was applied to Swarm measurements. This chapter presents the results of these applications. First a comparison is made between a limited number of ground magnetic time series with the ones obtained at satellite altitude using the VO-ESD approach. Second, a comparison is made with a global SH model. Then, using a global grid of virtual observatories global field models are constructed. Finally, the results are discussed.

4.1 Data

Two data sets were used: ground magnetic observatory data and satellite magnetic measurements provided by the first months of the Swarm mission.

4.1.1 Observatory data

The first data set consists on monthly mean time series from ground magnetic observatories, spanning from November 2013 to December 2014. The monthly means are defined as an

average of all days of a month and all hours of a day. All data components (X, Y and Z) were transformed from the geodetic to the geocentric coordinate system. This procedure is necessary to make them comparable to satellite data. Quasi-definitive data was available for a reduced number of observatories due to the very recent time interval that was chosen. Figure 4.1 displays the locations of the ground magnetic observatories and Table 4.1 presents their (geocentric) coordinates.

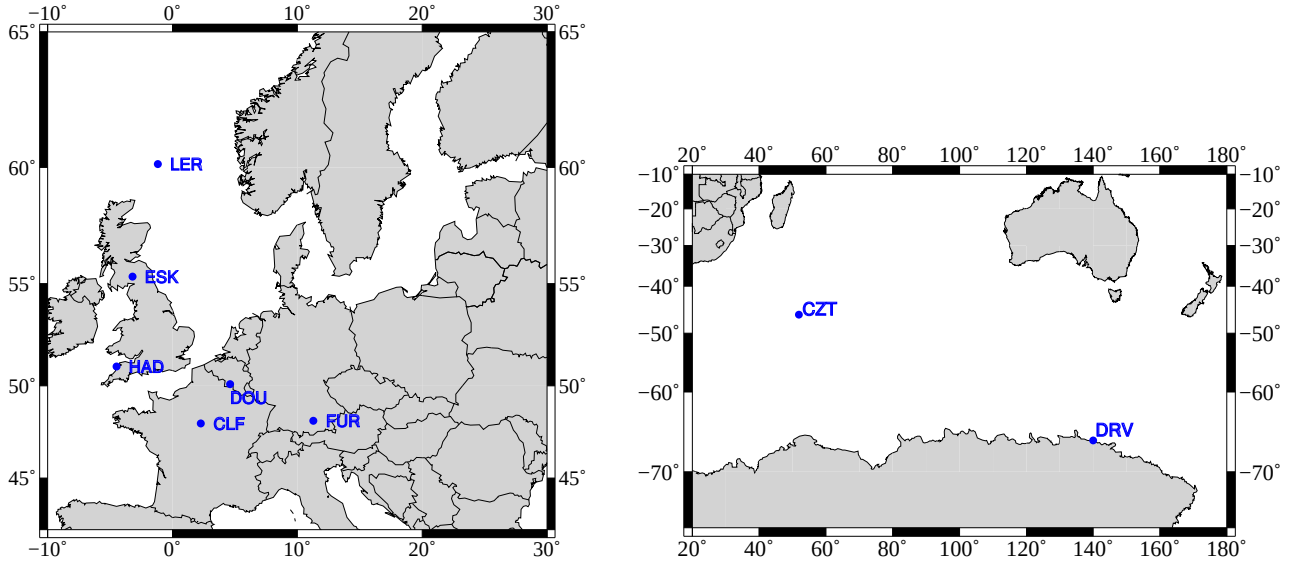

Figure 4.1: Location of the eight ground magnetic observatories whose time series were used for comparison on this study.

4.1.2 Satellite data

The Swarm mission (cf. Section 1.6.3) measurements spanning from November 2013 to June 2015 compose the second data set. The data consist on the latest release by ESA of magnetic vector measurements (X, Y, Z) with 1 Hz sampling rate. In ESA's Swarm product files each measurement is associated with flags describing the performance of the instruments at the time where measurements were taken. Based on such flags a selection of data was performed (Tøffner-Clausen, 2013):

- `Flags_B`: 0 or 1 (VFM is nominal or ASM is turned off);
- `Flags_F`: 0 or 1 (ASM is nominal or running in Vector mode);

- `Flags_q`: between 0 and 6, or between 16 and 22 (at least two CHUs nominal);
- `Flags_Platform`: 0 or 1 (nominal telemetry or thrusters not activated).

From the selected data, virtual observatories volumes were built. As can be seen in Fig. 1.15, Swarm satellites fly between 460 and 524 km altitude (extreme values). During (approximately) the first 3 months of the mission all three satellite flew together. Then after some weeks of flight manoeuvres, two satellites joined the lower flight altitude and the third one took the higher altitude. This, as already demonstrated in the last chapter, will be important to the data spatial distribution within each VO. During the first months all measurements cluster around 505 km altitude as opposed to the latter months where there are two "layers" of measurements separated by about 50 km. To make it comparable to the way ground magnetic data is treated no data selection is done on geomagnetic indices or local time. Note that the Swarm mission 3 satellites cover all 24 hours of local time every 7-10 months (Olsen et al., 2006a).

4.2 Iteration selection criterion

A more efficient iteration criterion was needed for the application to Swarm measurements. It was observed that an adequate iteration could be considered within the first twenty iterations of the inversion. In addition, for the same VO and for all periods (thus, for all inversions) the selected iteration could always be the same. These observations were the base for the following iteration selection criterion. For a given time period, after the respective inversion, the rms residuals of the first twenty iterations are checked. Their relative difference is computed:

$$d\sigma_k = \frac{\sigma_k - \sigma_{k-1}}{\sigma_k} \times 100, \tag{4.1}$$

and then the iteration where

$$d\sigma_k \leq \varepsilon, \tag{4.2}$$

is searched. This operation is applied to the rms residuals of the field intensity (σF). A satisfying value of $\varepsilon = 1.5\%$ was empirically found. It was observed that for most periods

(i.e., around 70%) the same iteration was selected. For consistency we decided to use the most frequent iteration number for all periods.

Figure 4.2 shows an example of the application of this method for eighteen periods of 30-day each. Each curve corresponds to a different period. The iteration highlighted by a vertical dotted line was the selected iteration (the 14th on this case). When the initially selected iteration was different from the 13th, the iteration is highlighted by a black circle. It can be said that the 13th iteration is adequate for all period's inversions. On a total of eighteen periods, only six had a different initial choice of iteration solution. The difference of the rms residuals between the initial chosen iteration solution and the final one (when different) is always small. For the example given in Fig. 4.2 the mean differences are, for X, Y, Z and F, 0.05, 0.21, 0.30 and 0.17 nT; with the larger difference being 0.96 nT.

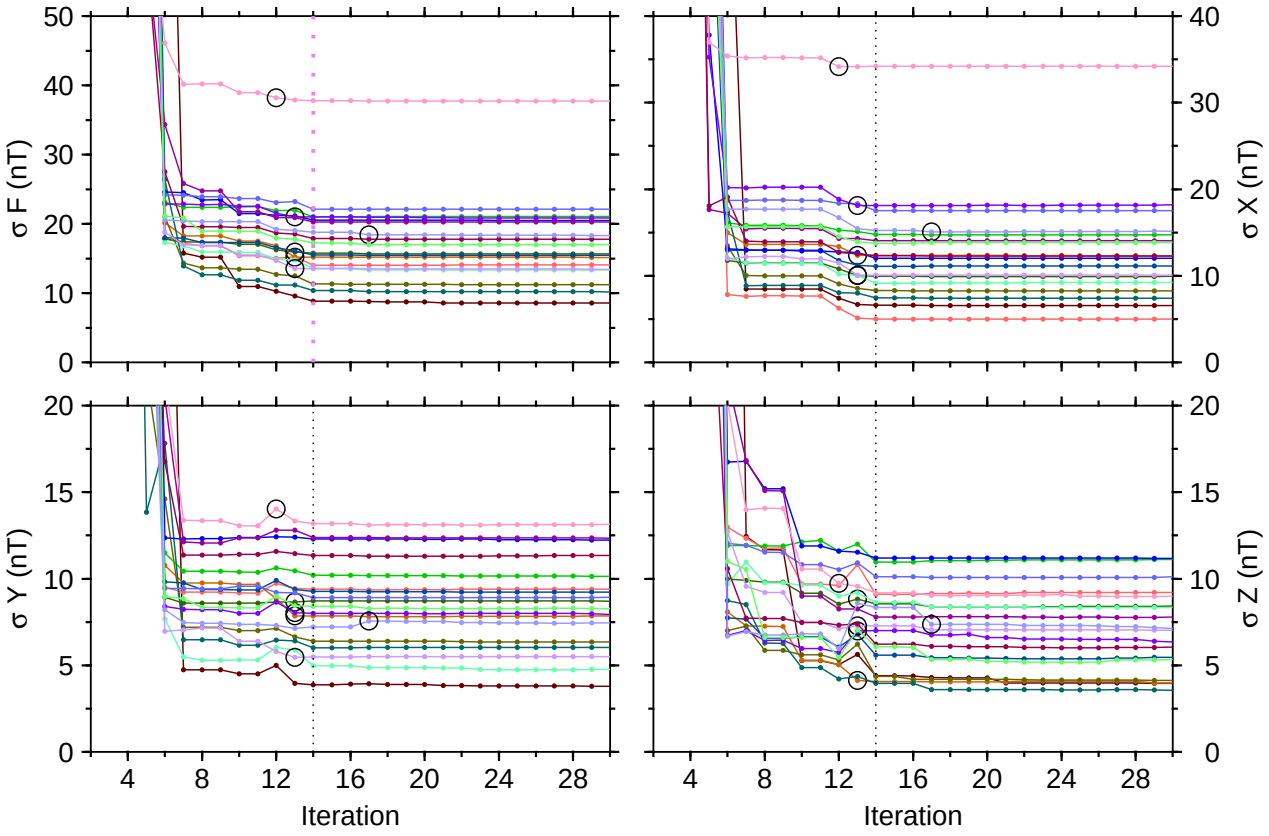

Figure 4.2: Rms residuals between synthetic data and predictions as a function of the inversion solution iteration, around the final selected one. This example corresponds to the application of the VO-ESD approach to a VO centred at $\vartheta_{vo} = 21.25^o$, $\phi_{vo} = 54.67^o$ and for eighteen time periods with duration of 30 days.

4.3 Dependence on time interval

A question arose on the dependence of the VO-ESD approach on the choice of the time interval T. Tests were performed by changing the time interval T. Four case examples for the value of T were considered:

Case 1: $T = 30$ days, and the periods overlap each 15 days, so one measurement coexists in two consecutive periods;

Case 2: $T = 30$ days, but the periods do not overlap;

Case 3: $T = 27$ days, following the solar cycle period;

Case 4: $T = 1$ month, i.e., following the calendar months, thus some data intervals have 30 days, while others 31 or 28 days.

For this test Swarm measurements were considered until the end of 2014, for a VO volume centred again at the CLF location and with all parameters fixed and with values as described in Section 3.3.5. The only changing parameter was T.

Figure 4.3 presents the misfit for each case, and for one period around 2014.5. All cases found an adequate solution by iteration $k = 13$. Cases 1 and 2 have the same rms residuals behaviour, because around a certain epoch (2014.5 in this case) the input measurements are the same (the same 30 days). The rms residuals do not significantly change from case to case. The case 4 presents the smaller values for all three magnetic components and field intensity. Specifically, all rms residuals of the three magnetic components are ≤ 8 nT. In these examples, the horizontal magnetic components are less well described in cases 1,2 and 3, than in case 4. However these behaviours can change for different inversions, i.e., for other periods. For all four cases the effectiveness of the ESD description of the magnetic components depends on the period data. For one period the horizontal components may be less well described than the vertical one, and that for the following period all components have rms residuals alike.

From analysis of the rms residuals of the field intensity for all periods (Fig. 4.4) it is clear that the interval of values of misfit is comparable for all four cases. There are two time intervals with

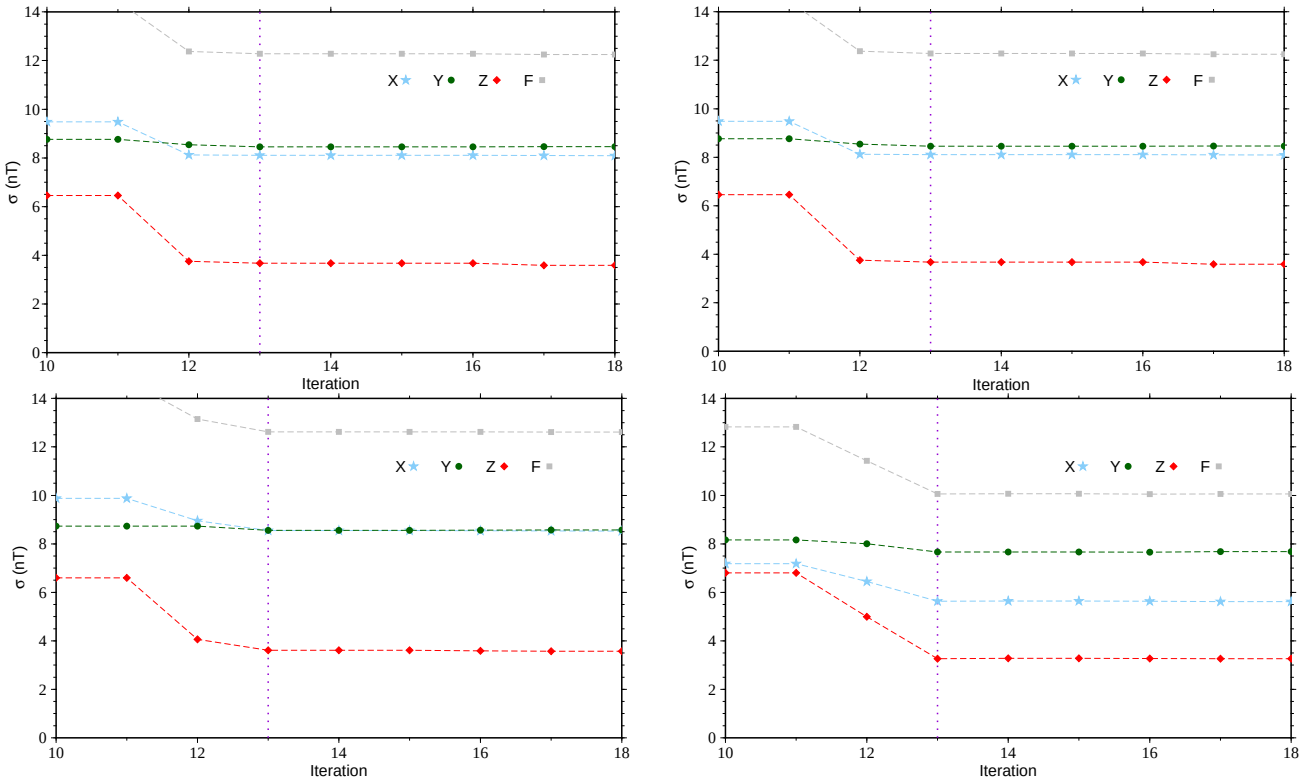

Figure 4.3: Rms residuals between synthetic data and predictions per iteration (a zoom around the selected iteration), for the three magnetic components and the field intensity, for four different case examples of the time interval, T: (*top left*) case 1, (*top right*) case 2, (*bottom left*) case 3, (*bottom right*) case 4. These examples correspond to a period around 2014.5. See text for details.

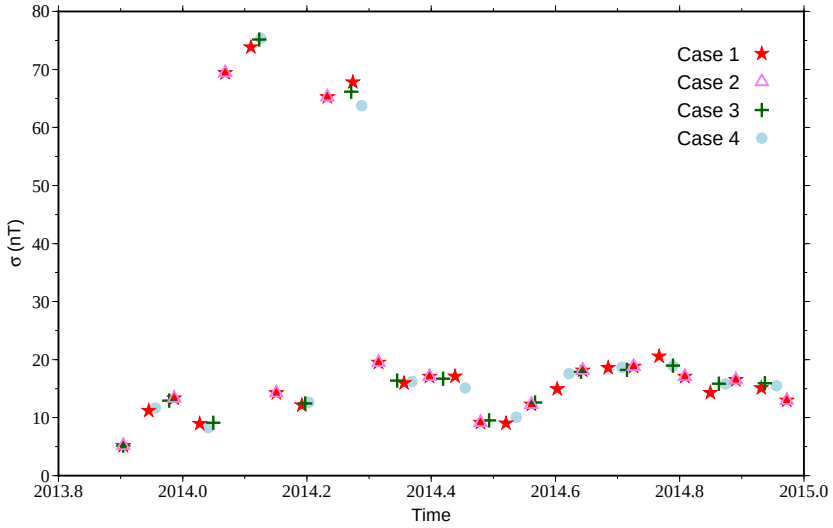

Figure 4.4: Rms residuals between synthetic data and the prediction given by the selected iteration solution for the field intensity, as a function of time, for the four case examples for T.

larger rms residuals, between 65 and 75 nT, around 2014.1 and 2014.3. These larger residuals could be related with a more heterogeneous spatial distribution of the Swarm measurements due to the satellites' movements during these periods, or any problem with the data. Another possibility is the presence of a very large field variation due to external field currents, which the ESD technique is not able to describe. For the other periods, all four cases rms residuals follow similar behaviours. No case emerges as more adequate than the others.

Figures 4.5 and 4.6 present the four cases results. Case 1 has 27 periods, case 2 has 14, case 3 has 15 periods and case 4 has 13 periods. Note that each prediction was made at the mean time of the respective period, which depends on the temporal distribution of the Swarm measurements within the cylindrical volume during the period. This is the reason why the predictions are not evenly distributed in time, e.g., for case 1 the longer time space between the 3rd and 4th periods. From the analysis of the predictions and comparison with a SH model (CHAOS-5, Finlay et al. (2015)), it can be seen that the curve behaviour of the four cases is very similar. The difference between the SH model and the VO-ESD prediction, seen in Figs. 4.7 and 4.8 are also similar. The periods with high or smaller differences values are the same for the four cases. For example, on the X component smaller differences at the end of 2013 and around 2014.45 are recurrent. The vertical component usually has low differences on those periods. In contrast, the Y component has always high differences at the end of 2013. Like with the rms residuals values, the predictions do not show preference to a particular T value. Thus, the prediction does not seem to significantly depend on the time period T. The 30-day period was chosen to be used for all applications of the VO-ESD approach. This choice was made because

- the constant number of days of the period allows to a more coherent distribution of measurements for different periods, and
- it is still easy to compare the obtained time series with ground observatory monthly means.

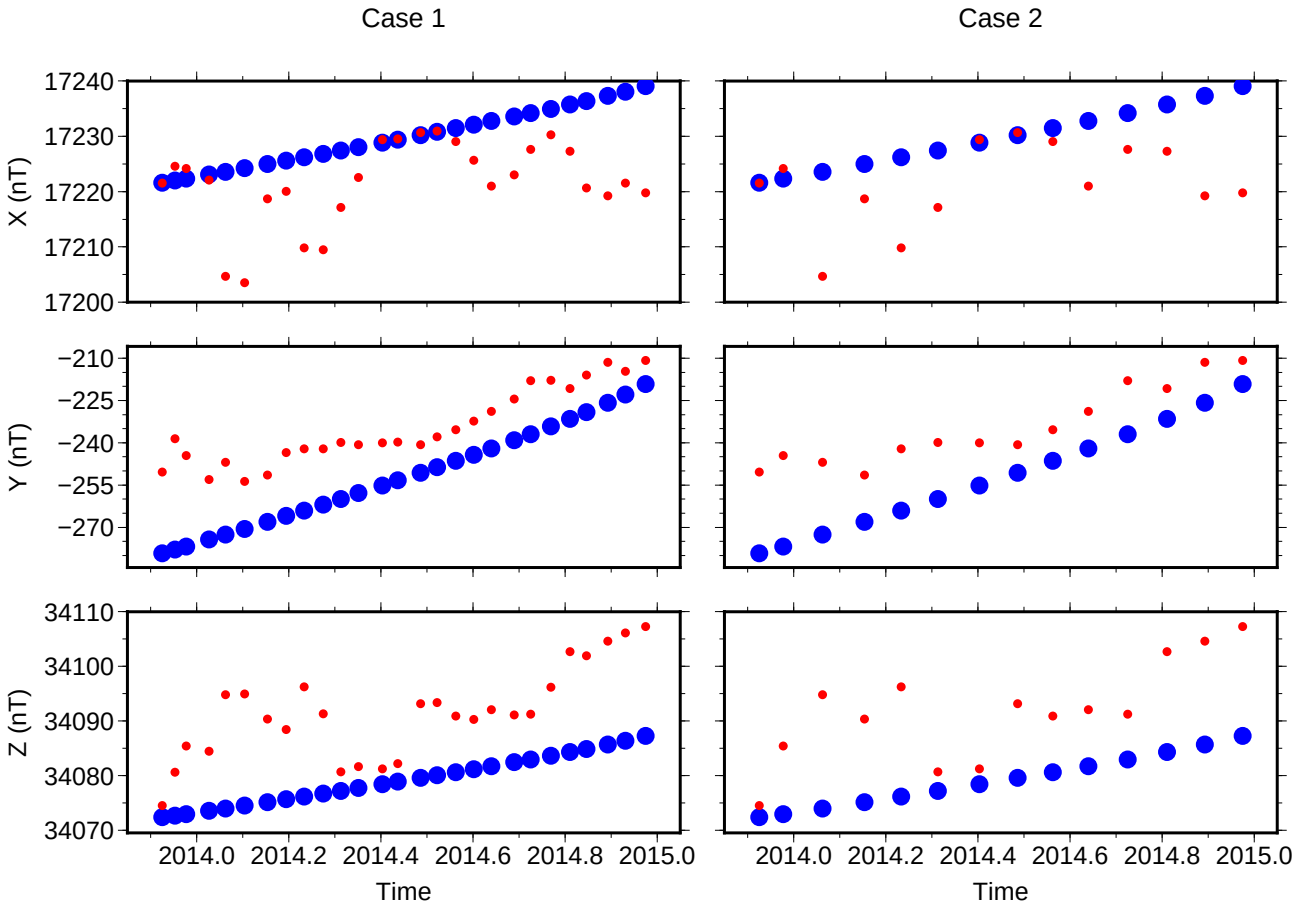

Figure 4.5: Predictions by the VO-ESD approach (*red*) for the three magnetic components at the centre of the VO, and the predictions by an SH model at the mean time of the time period (*blue*) for different values of T: (*left*) case 1 and (*right*) case 2. For each magnetic component (each line) the y-axis are the same.

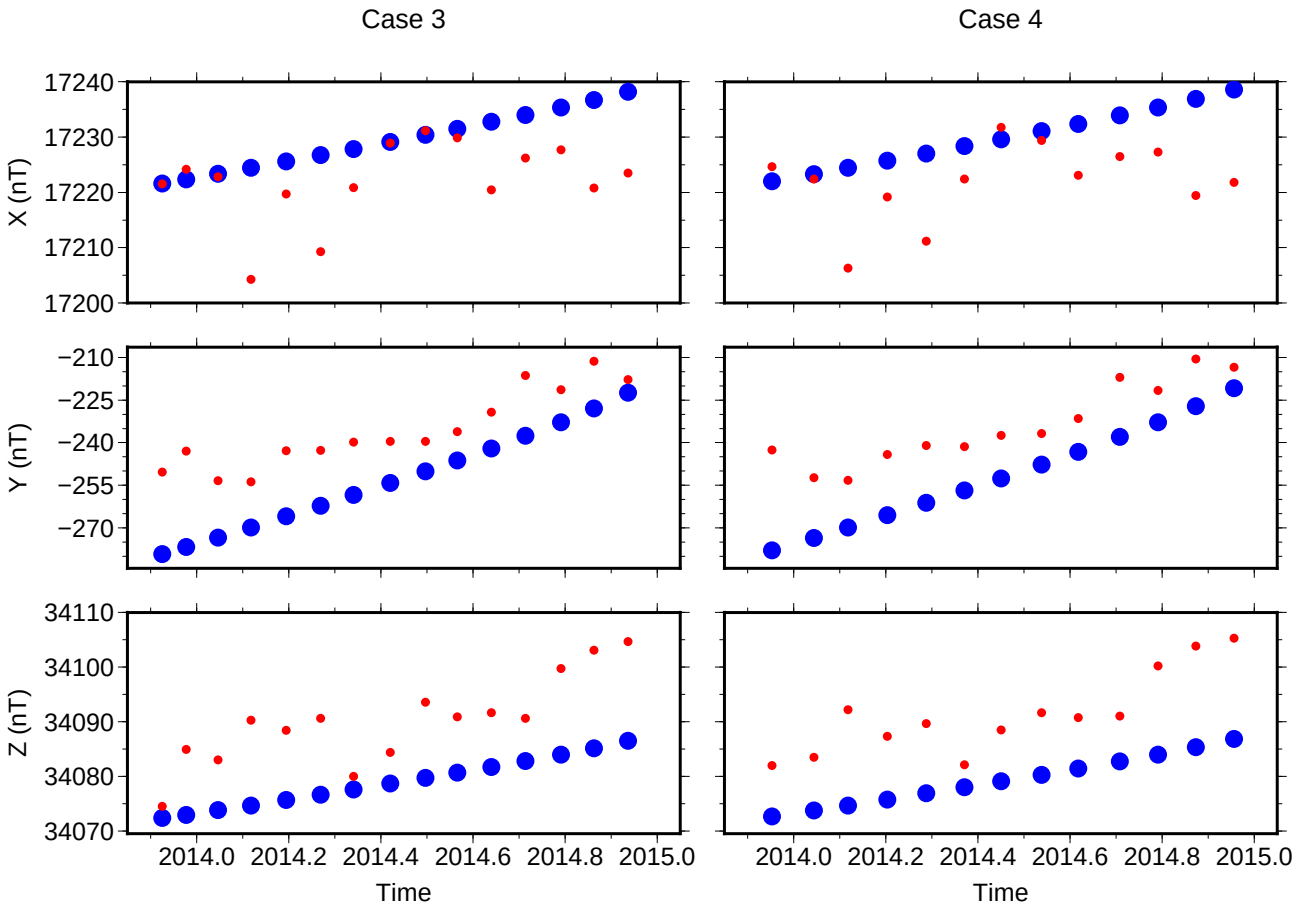

Figure 4.6: As in Fig. 4.5, for cases 3 (*left*) and 4 (*right*).

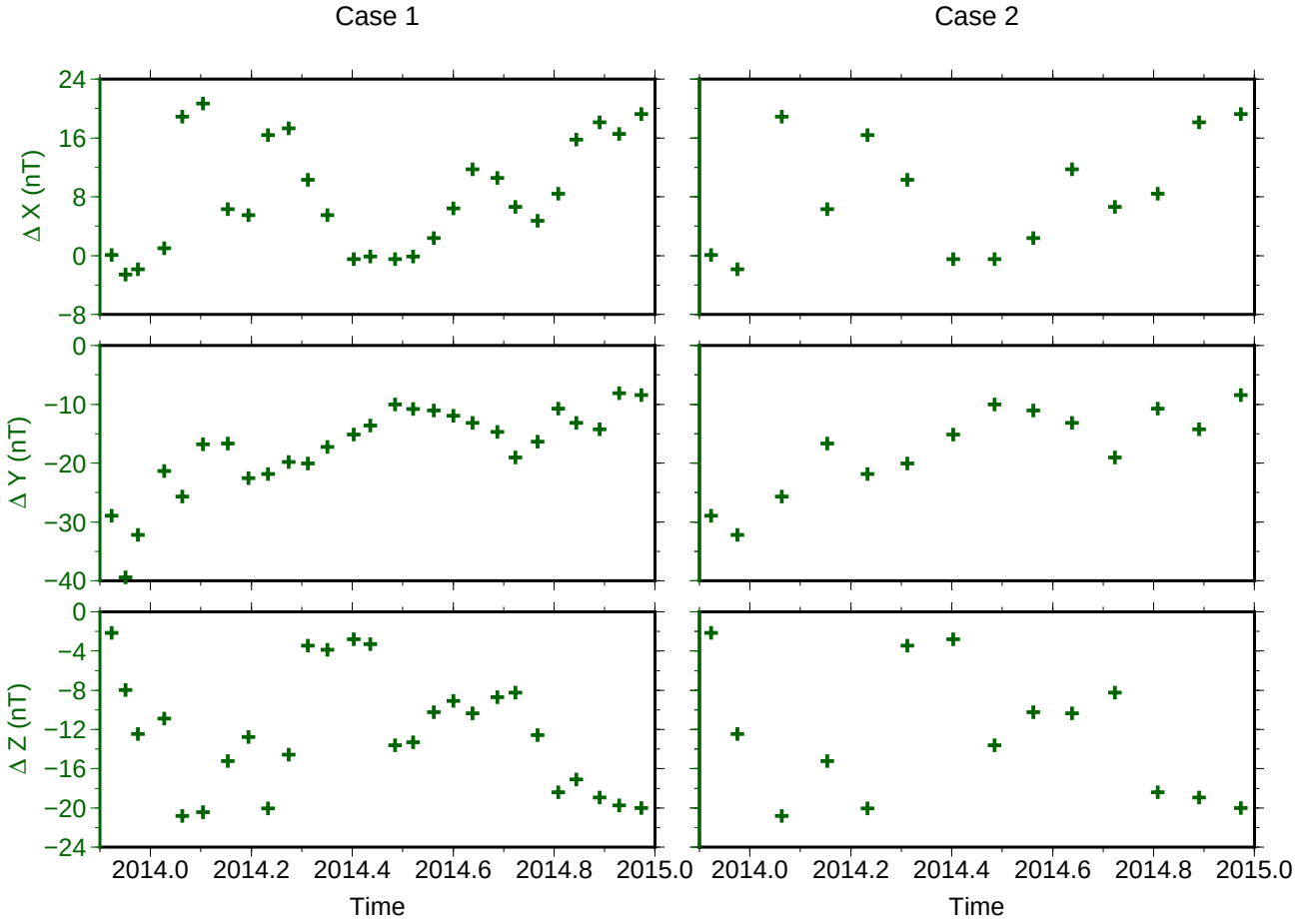

Figure 4.7: Differences between the predictions by an SH model and the VO-ESD approach at each mean time (predictions showed in Fig. 4.5), for different values of T: (*left*) case 1 and (*right*) case 2.

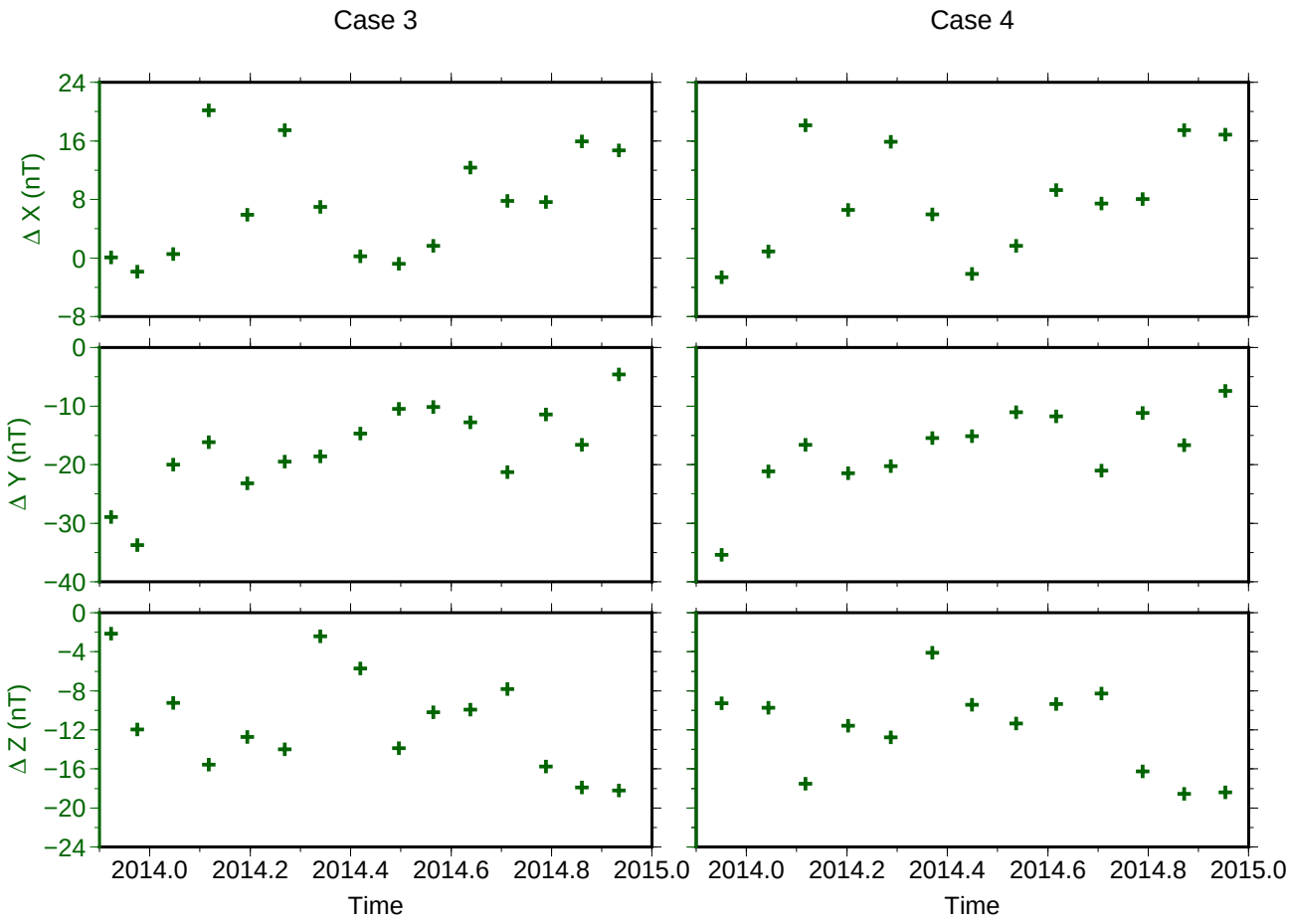

Figure 4.8: As in Fig. 4.7, for cases 3 (*left*) and 4 (*right*).

4.4 Comparison with ground observatory time series

4.4.1 Method

In a first step, I looked for a similar behaviour between temporal variations at the Earth's surface, measured by ground observatory time series and the temporal variations at satellite altitude recovered by the VO-ESD approach. For each ground magnetic observatory a corresponding VO was constructed. For example, for the CLF ground observatory, all Swarm measurements within a cylinder of 1.5^o radius and centred at the CLF location consisted the virtual CLF observatory volume, as illustrated in Fig. 3.3.

The VO-ESD approach is applied to the Swarm measurements and a prediction is made at the mean time of each successive 30-day period. The comparison is made until the end of the year 2014. The ESD parameters employed are the ones discussed in Section 3.3.5 and the iteration solution criteria is the one described in Section 4.2.

4.4.2 Inversion results

Figure 4.9 displays the rms residuals obtained for the eight ground observatories considered on this comparison (see Table 4.1). The rms residuals are always above 2 nT and generally under 30 nT. The virtual observatory at the location of the ground observatory DRV presents a more irregular rms residual behaviour than the others. For some periods it is as high as 170 nT for the field intensity and 150 nT for the Y component. These high rms residuals are related to the high latitudinal location of the VO, where the external current's signals are significant and may not be completely described by the ESD technique.

Figure 4.10 presents the differences between each Swarm measurement and the ESD technique, as a function of time, for three different VO locations. The geographically close VO, CLF and DOU, present similar magnetic field and hence similar rms residual time dependence, with larger values around 2014.1 and 2014.3. This is exactly the same that is observed with ground based magnetic observatories. In contrast, the third VO, on the southern hemisphere, displays

higher rms residuals also for the 2014.1 and 2014.3 periods as well as between 2014.6 and the end of the year.

Figures 4.11 to 4.14 compare the VO-ESD predictions and the corresponding eight ground observatories time series. Generally, ground observatory and VO time series are strongly correlated. The X component presents the smallest resemblance for all examples. The similarity between ground and satellite altitude time series is most evident for the Y component. For all cases, the VO-ESD time series are less smooth than the observations at the surface, containing more short-term temporal variations. This is clearly related to external contributions at satellite altitude, as no data selection was made which the ESD technique may not be capable to describe. But, in general the VO-ESD time series follow the ground time series. Just like with ground observatories, geographically close virtual observatories time series are very similar, as is clear with the CLF and DOU observatories.

The higher differences (in the curve behaviour) between ground and VO time series seem to occur at different times for different VOs and for different components. Therefore it is difficult to establish a relation between those differences and an external field events (like geomagnetically disturbed days or a geomagnetic storm) during the considered year. Nevertheless, at some VOs

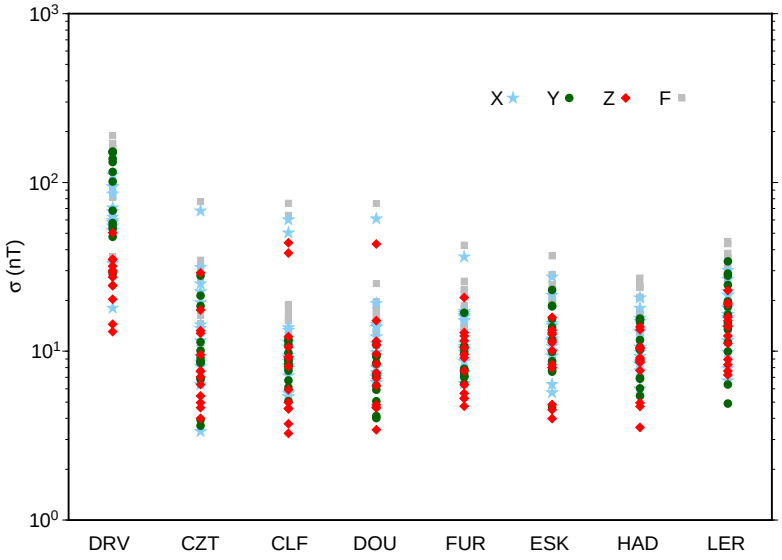

Figure 4.9: Rms residuals between all Swarm measurements and the ESD technique given by the selected iteration solution for the three magnetic components and field intensity, for the eight considered ground magnetic observatory locations at satellite altitude.

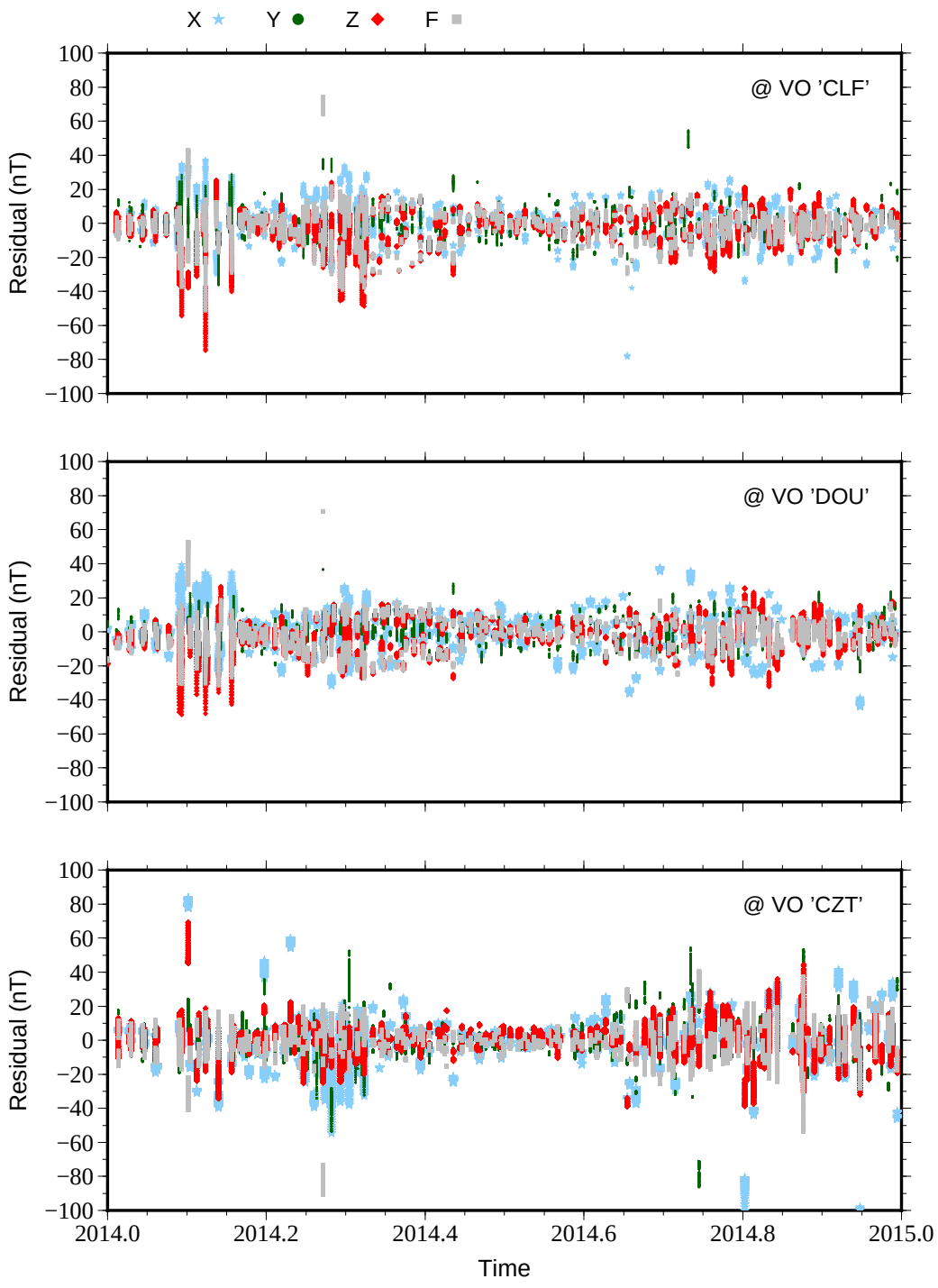

Figure 4.10: Residuals between Swarm measurements and the ESD technique for the three magnetic components and field intensity, at three VO, as a function of time.

a periodic signal seems to exist in the results. For example in DOU and FUR, particularly at the Y and Z components, changes in the behaviour of the curves (in comparison with the ground observatory curves) occur around 2014.3 and 2014.7.

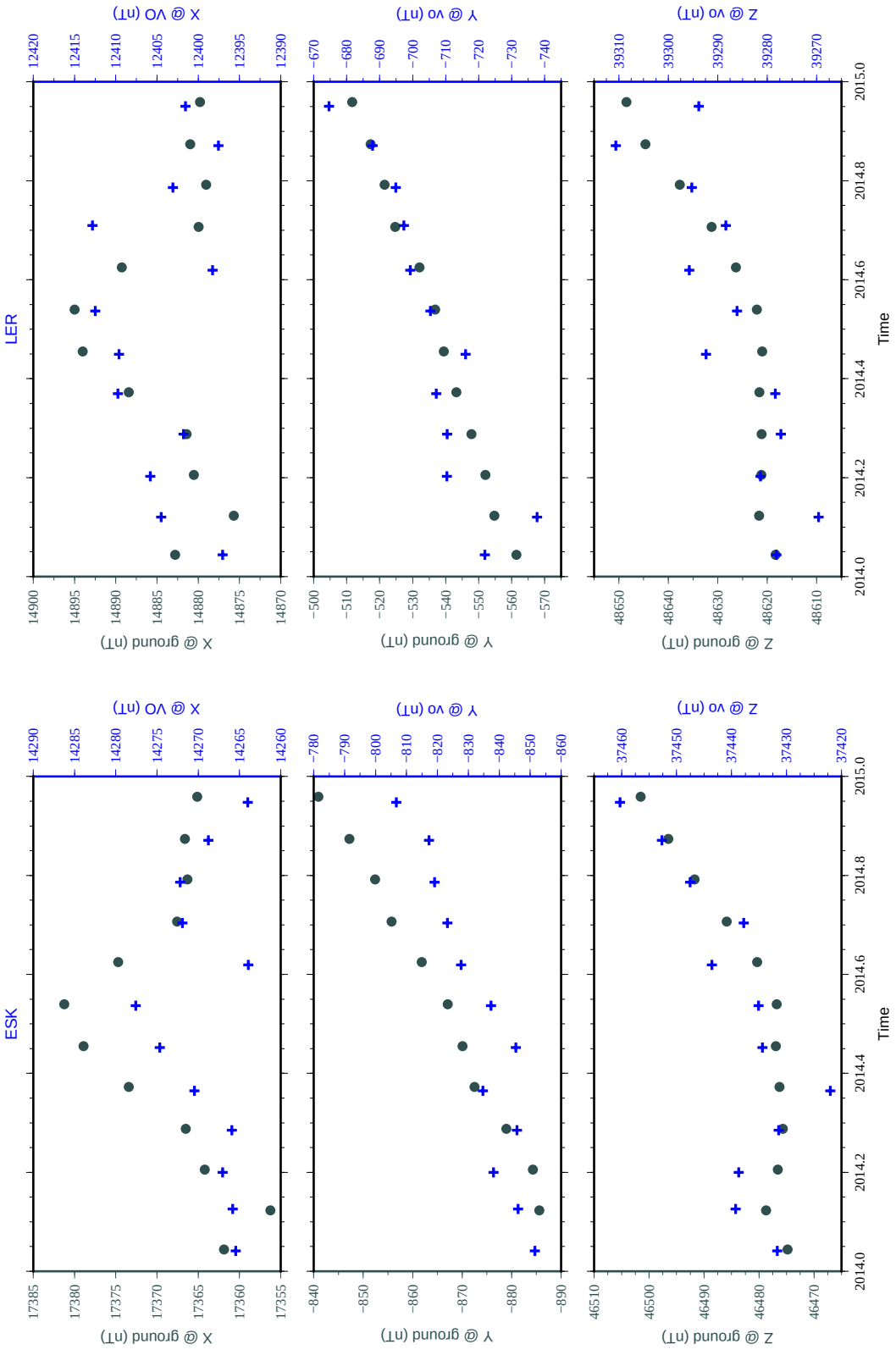

Figure 4.11: Time series of the three magnetic components at LER and ESK ground magnetic observatory (*grey circles*) and corresponding VO given by the VO-ESD approach (*blue pluses*). Note that the difference between maximum and minimum in the y-axis is the same both at the ground and satellite altitude, for each magnetic component.

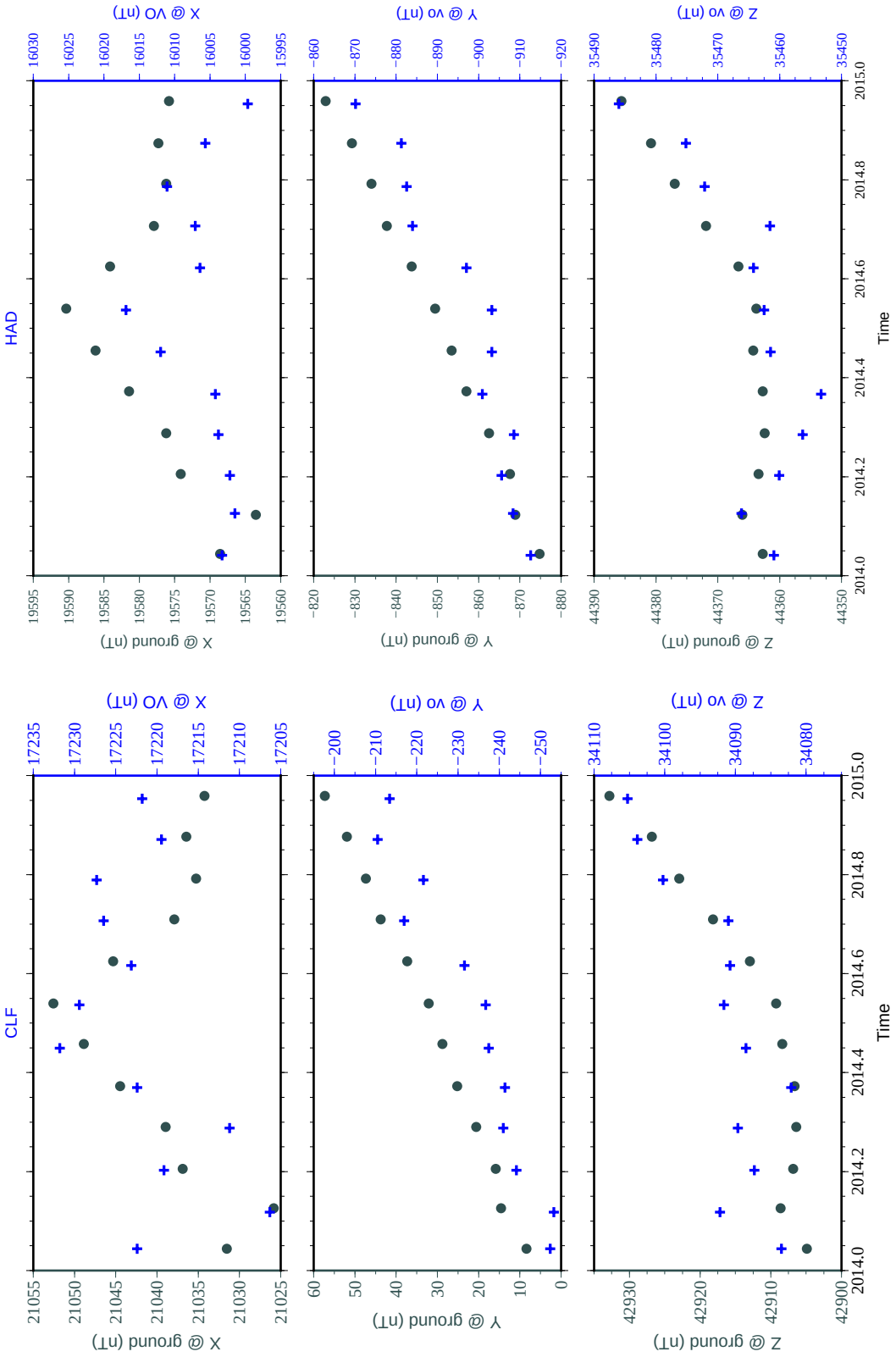

Figure 4.12: As in Fig. 4.11, for HAD and CLF ground observatories.

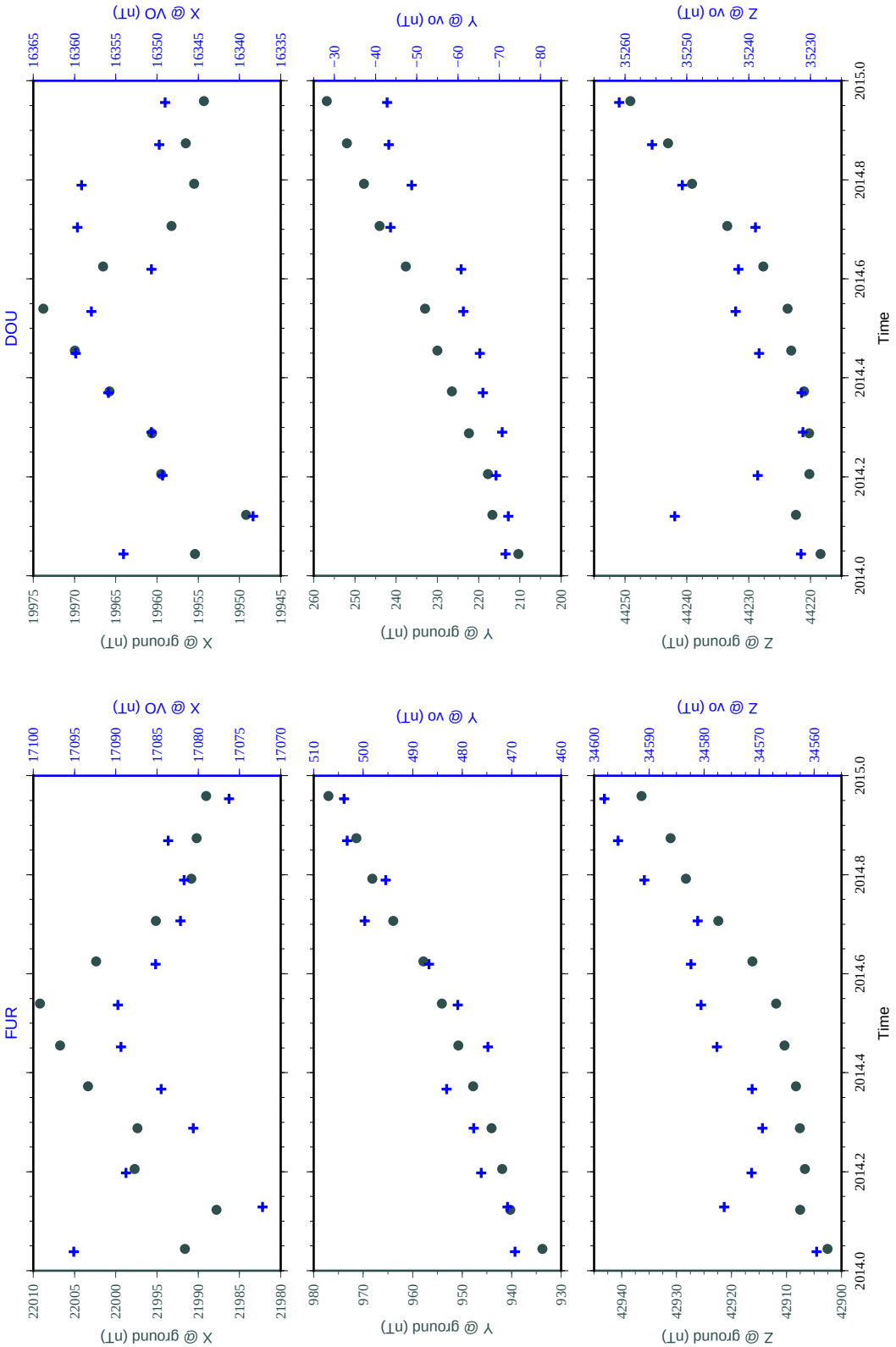

Figure 4.13: As in Fig. 4.11, for DOU and FUR ground observatories.

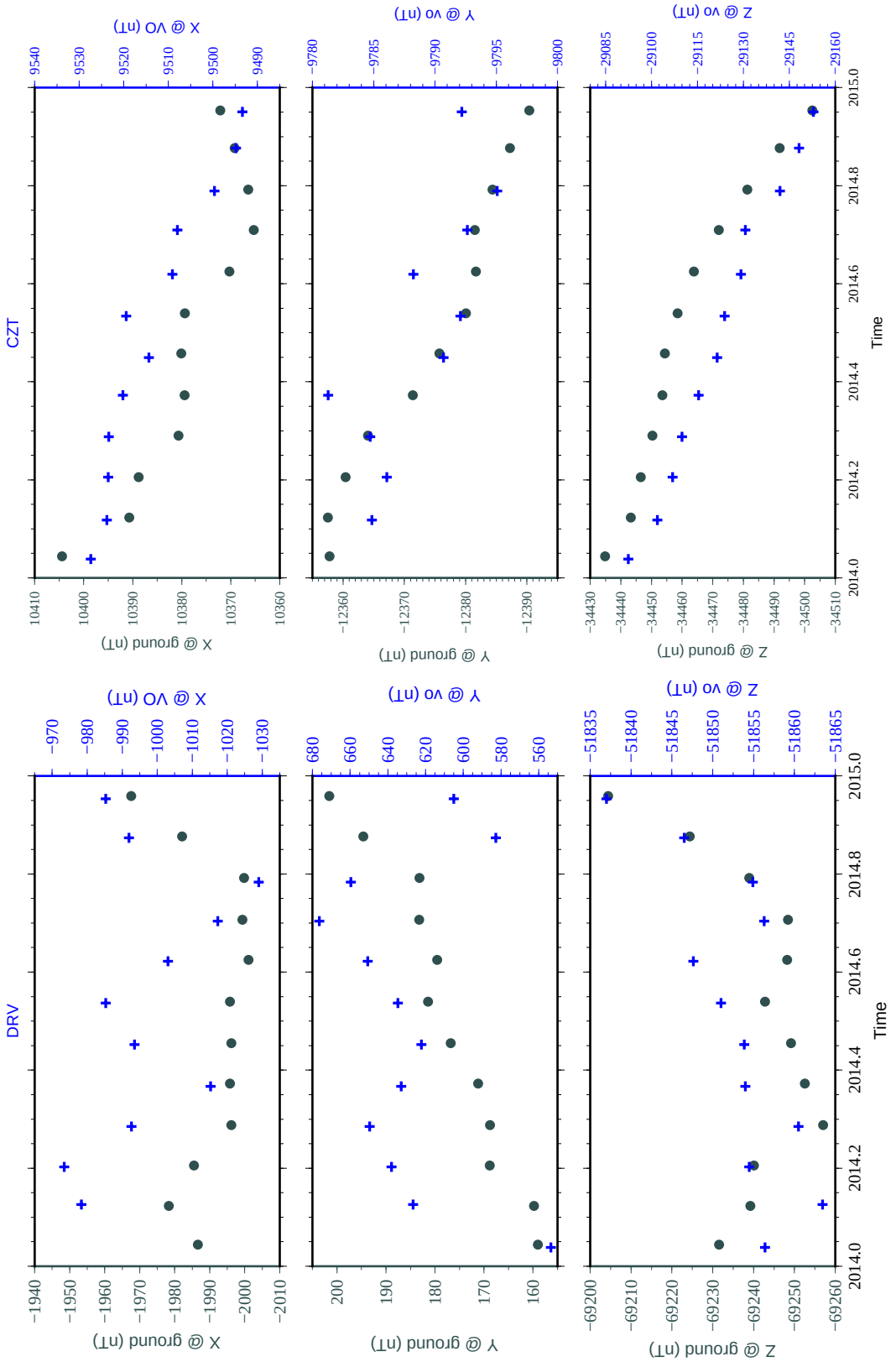

Figure 4.14: As in Fig. 4.11, for CZT and DRV ground observatories.

4.4.3 Statistical analysis

The Pearson's correlation coefficient was computed between ground and VO time series for each magnetic component (see Table 4.1). The east-west component presents the highest correlations, always equal or greater than 0.90, except for the DRV and CZT observatories. The correlations for the X component are the lowest, however, they are superior to 0.55, except for the LER observatory ($\rho_X = 0.38$). The correlations for the DRV observatory are lower than the other observatories. This could be related to external contributions to the measurements, which are large at high latitudes (close to the magnetic pole) as the one of this observatory (66.53^o S), and may not be described by the ESD tehcnique, but leaking to the results. The north ground observatory considered in Europe, LER, has also poorer correlations, which could also be related to the high latitude external contributions.

Table 4.1: Ground magnetic observatories location and the correlation coefficient between their time series and the respective virtual observatory.

Observatory	ϑ (^{o})	ϕ (^{o})	ρ_X	ρ_Y	ρ_Z
CLF	47.83	2.26	0.66	0.97	0.93
DOU	49.91	4.60	0.58	0.95	0.83
FUR	47.97	11.28	0.53	0.95	0.95
ESK	55.14	356.80	0.66	0.94	0.89
HAD	50.81	355.52	0.74	0.95	0.92
LER	59.97	358.82	0.38	0.90	0.74
DRV	-66.53	140.01	0.59	0.06	0.70
CZT	-46.24	51.87	0.80	0.81	0.98

A first approximation for the secular variation was computed for each one of the time series by linear regression. The trend was computed both at the ground and at satellite altitude from the observations and VO-ESD time series and also for the CHAOS-5 model. The purpose here is not to obtain an idential secular variation both at the ground and at satellite altitude, as it should not be exactly the same (different altitudes, see Fig. 3.4) but similar. The idea is rather to compare both computed trends with the ones from CHAOS-5 and infer if they similarly resemble the model. Table 4.2 presents the computed linear trends for all cases, and Figs. 4.15

Table 4.2: Linear secular variation (first time derivative for 1-year time interval, in $nT.yr^{-1}$) for the considered ground observatories monthly means time series (OMM) and respective VO-ESD predicted (VO) time series, and both at the ground (CH) and at satellite altitude (CHS) given by the CHAOS-5 model.

Observatory	dX/dt		dY/dt		dZ/dt	
	VO	CHS	VO	CHS	VO	CHS
CLF	10.29	16.66	47.16	56.93	19.79	14.22
DOU	5.97	13.12	36.86	55.69	21.65	18.30
FUR	-6.16	9.56	39.21	52.61	34.94	24.75
ESK	2.54	15.93	43.25	58.45	25.14	11.72
HAD	3.66	20.06	42.29	59.57	21.14	7.31
LER	-0.37	57.10	49.58	57.10	31.17	15.92
DRV	-35.57	-18.50	21.59	43.23	17.05	12.41
CZT	-38.01	-26.20	-16.90	-26.74	-61.66	-65.60
	OMM	CH	OMM	CH	OMM	CH
CLF	4.73	21.06	52.40	70.49	27.79	26.79
DOU	0.78	16.32	49.60	68.43	31.22	31.33
FUR	-2.87	12.23	44.95	63.95	35.04	38.53
ESK	6.44	19.76	53.29	73.12	26.14	23.40
HAD	9.96	25.17	55.77	74.97	22.59	18.22
LER	-0.03	13.25	52.48	70.76	30.20	28.46
DRV	1.93	-27.70	41.19	63.17	21.24	8.53
CZT	-34.03	-42.20	-38.50	-45.19	-65.82	-101.45

to 4.18 show the linear trends superposed to the times series of the ground observatories monthly means and VO-ESD time series. The figures show that sometimes the two time series behave very similarly (LER or CZT), but others have significant differences (DRV or the Y component in ESK). Table 4.2 shows that in general the difference between the ground monthly mean trend and CHAOS-5 trend at the surface is similar to the difference between VO-ESD trend and CHAOS-5 trend at satellite altitude, with some exceptions.

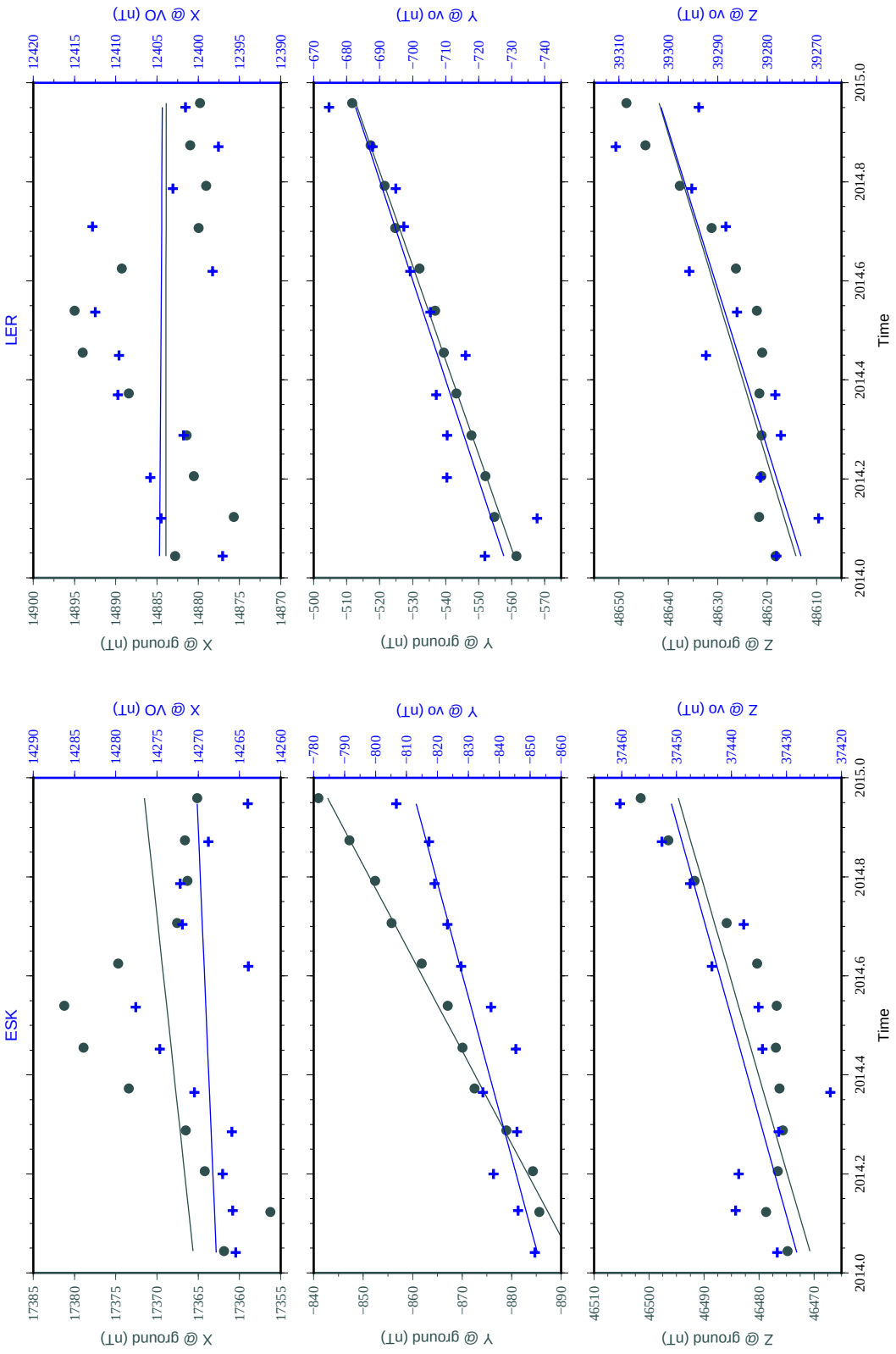

Figure 4.15: As in Figs. 4.11 to 4.14 but with the addition of linear fits to the time series, representing the computed linear secular variation, for LER and ESK ground observatories.

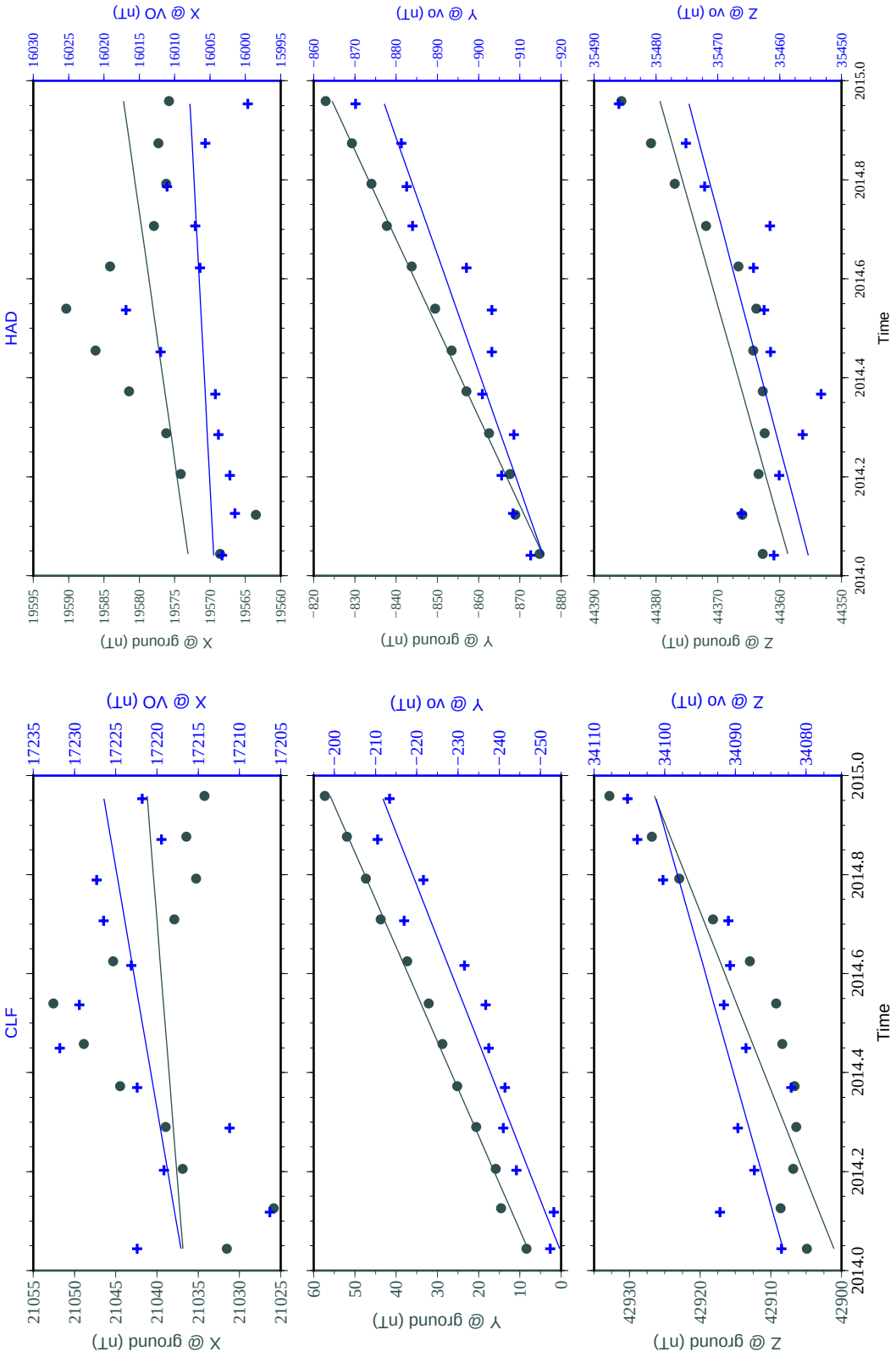

Figure 4.16: As in Fig. 4.15, for HAD and CLF ground observatories.

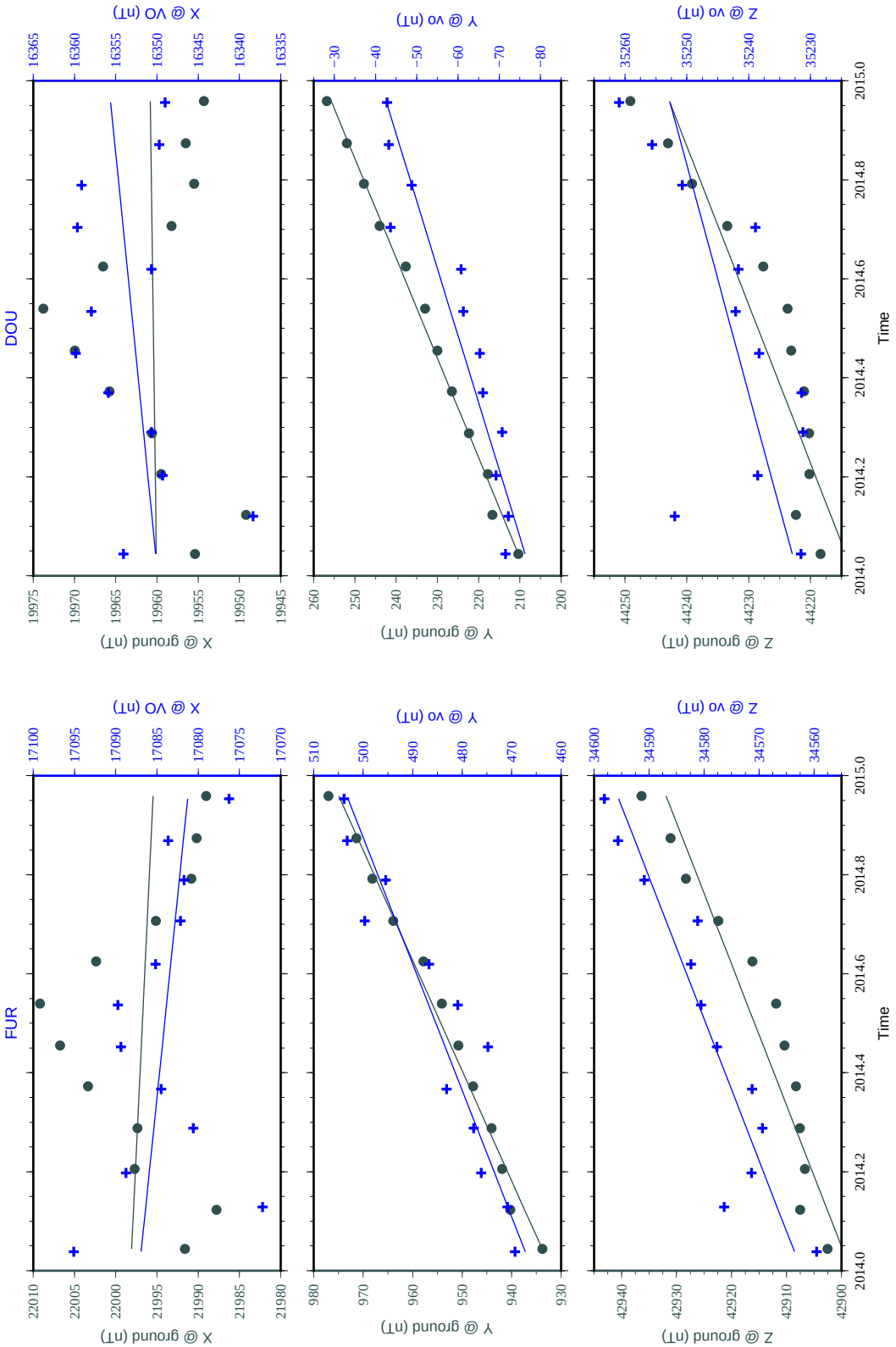

Figure 4.17: As in Fig. 4.15, for DOU and FUR ground observatories.

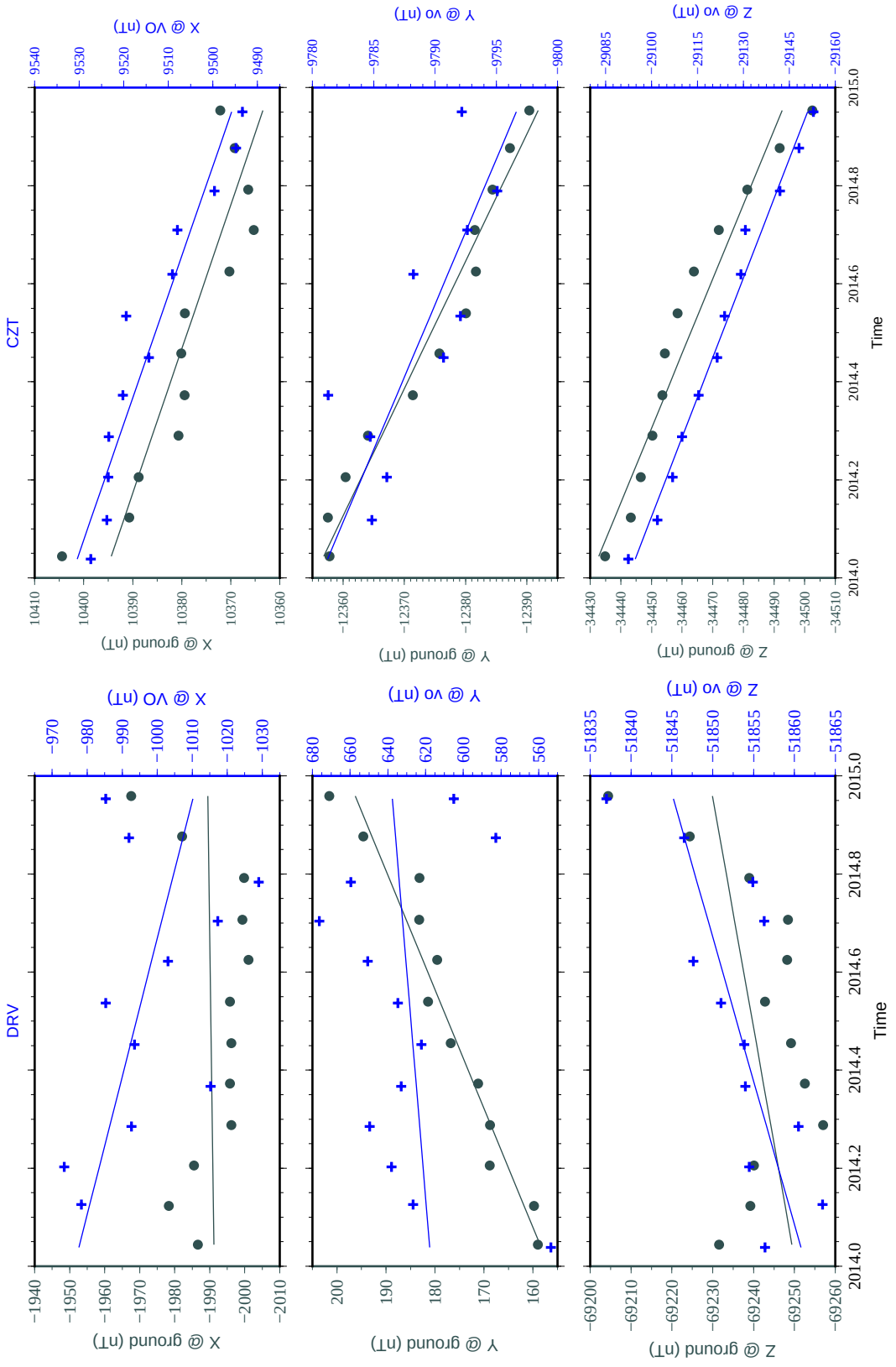

Figure 4.18: As in Fig. 4.15, for CZT and DRV ground observatories.

4.4.4 Discussion

The results of the application of the VO-ESD approach to Swarm measurements are encouraging. It exist resemblance between ground observatories monthly means time series and the 30-days period VO-ESD time series. The correlation between both time series is strong, particularly for the Y and Z components, with values frequently above 0.80. For the X component the correlations are between 0.38 and 0.80.

The linear regression was computed for the ground observatory, the VO-ESD predictions and the model CHAOS-5 both at the ground and at satellite altitude. This linear variation represents a rough value of the secular variation during 1.5 year. The difference between the VO derived time series and the CHAOS-5 at satellite altitude is similar to the difference between the ground observatories and the model temporal variations. The meaning is that the VO derived time series are comparable to the ones obtained at the ground, as their temporal behaviours are similar. This result together with the computed correlations and the visual analysis of the VO time series supports the validity of the VO-ESD approach.

At high latitudes (above 60^o) the influence of external currents on the results is strong. High latitudinal electrical currents are continually present at all local times and possess high temporal frequency. The magnetic signal of these currents is significant and diminishes the validity of the VO-ESD approach there.

The temporal variations of the VO time series are generally faster than at the respective ground observatory. This is most probably due to the presence of external contributions. Even the application of the technique for a 30-day period data does not average or smooth the external field contributions. Thus, the separation of the external contributions from the VO time series is difficult.

4.5 A global mesh of virtual observatories

A global mesh of virtual observatories (VO) was constructed at satellite altitude. From the resulting mesh the temporal variation of the magnetic field was extracted at local scales, as it is done with ground observatories. The short-period changes of the magnetic field can then be studied at local scale and at satellite altitude.

4.5.1 Method

The VO-ESD approach is applied to global Swarm measurements. An equal area mesh was chosen, where each VO volume has 3^o of diameter and in latitude the VO centres are separated by 2.5^o, thus the volumes overlap in space. We define 72 latitudinal bands, with $\vartheta_{vo} = 1.25^o, 3.75^o, 6.25^o, ..., 88.75^o$. In each band, the longitude ϕ_{vo} of each VO and the number of longitudinal divisions, $N\phi_{vo}$, are chosen so that:

$$N\phi_{vo} = \frac{360}{2.5} \cos \vartheta_{vo} \tag{4.3}$$

Hence, at the equator there are 144 virtual observatories, at $\vartheta_{vo} = 48.75^o$ there are 95 and at $\vartheta_{vo} = 88.75^o$ only 4. The resulting mesh contains 6644 VOs. Figure 4.19 displays the locations of all virtual observatories in the mesh. This equal area mesh was preferred over an equiangular one mainly because the latter would introduce a latitudinal dependency for the number of measurements per VO volume.

A mistake had been made by using a constant altitude for the centre of all VO. The problem can be understood by the analysis of Figs. 1.15 or 3.30, showing the daily mean altitude of all three Swarm satellites. If one looks at the first two to three months of the mission, it becomes clear that the altitude of 490 km is outside the range of altitudes where measurements were made. However, an inversion using the ESD technique should only be used to predict the field within the zone were the actual observations were made. Thus, modelling the magnetic field at the altitude of 490 km for the first months of the Swarm mission is not adequate. Therefore, for

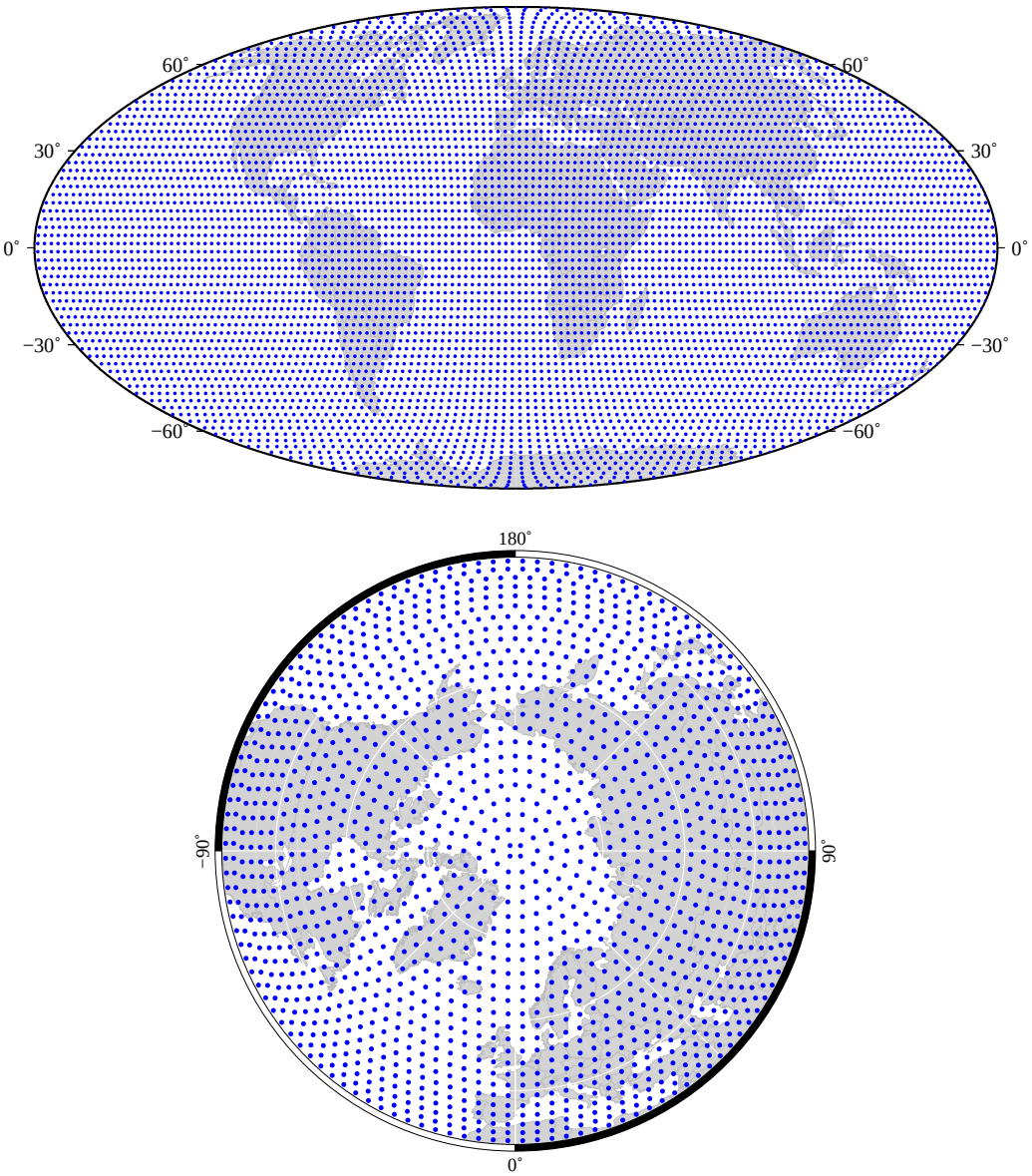

Figure 4.19: (*Top*) Global mesh of virtual observatories. (*Bottom*) Polar view of the northern hemisphere, with $30^o \leq \vartheta_{vo} \leq 90^o$.

each VO we searched for an altitude which lies always (during the time interval of the available measurements) within the altitude range of the measurements during the first two months of the mission. The selected altitude will always be within the altitude range of the following months of the mission. Then, all predictions of the VO are made for the chosen altitude. With this approach each VO has a different altitude. This can still be compared with the magnetic ground observatories which are placed at different altitudes, as the surface of the Earth is far from a perfect sphere. The obtained distribution of altitudes is shown on Fig. 4.20. The altitude depends strongly on the latitude of the centre of the VO. All three satellites are closer to the

Earth's surface in the Northern Hemisphere.

The approach was applied to all Swarm data, without selection, from November 2013 to June 2015, which covers $T = 18$ periods of 30 days. The parameters are the same as in the previous section. Thus, the inversion with the ESD technique was applied to 6644 VOs for 18 periods (roughly 18 months), which sums 119 592 inversions.

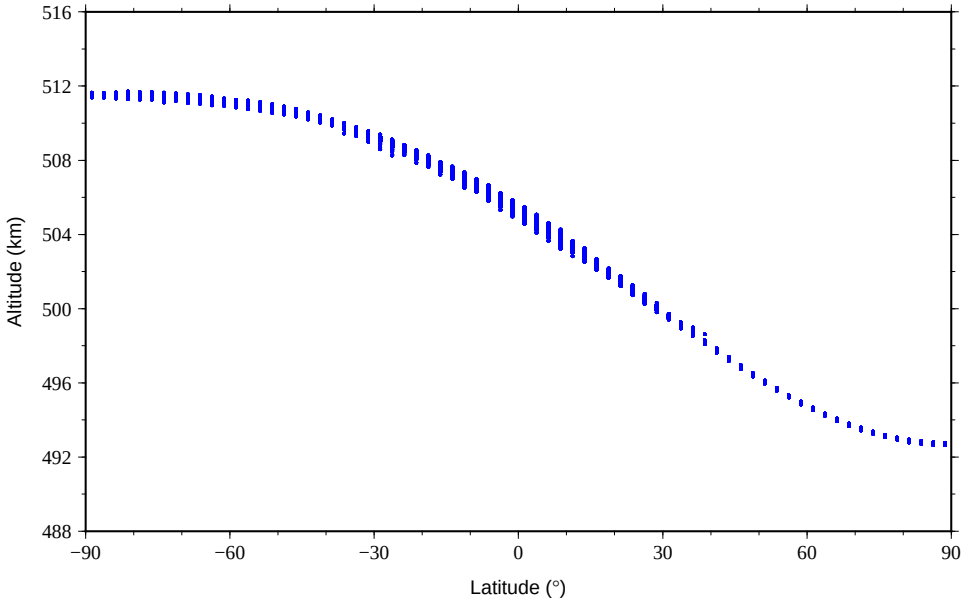

Figure 4.20: Altitude for all VOs as a function of the latitude of the VO centre.

4.5.2 Results

Figure 4.21 displays the rms residuals of the selected solutions for all 18 periods and for all VOs as a function of the latitude of the VO. It is clear that for high latitudes ($\sim 60^o$) the rms residual is usually much higher for the X and Y components. Also their minimum values increase when the VO centre location latitude is above $\pm 70^o$. This compares with what was seen during the comparison of VO results with ground based observatories and discussed in Section 4.4.4. However, the vertical component has an opposite behaviour, with its higher residuals at low latitudes. Both hemispheres present the same results.

Figures 4.22 to 4.27 show the VO-ESD predictions of the three components of the field with the field intensity, for twelfth VOs distributed all over the world (see Table 4.3). In general the predictions exhibit faster temporal changes on the X component. The Y and Z components are smoother.

High latitude virtual observatories display greater changes of the magnetic field, as expected. This can be seen for example in the VO in Fig. 4.25. The closer a VO is from the geographic pole, more noise it appears in its field.

All the VO's on Figs. 4.22 to 4.27 display, to a greater or lesser extent, a temporal cycle of around 5 or 6 months of half period (then, closely an annual cycle). This signal is most likely related to external contributions, as it is stronger (more evident) than the signals registered at the ground magnetic observatories (see e.g., Fig. 4.11).

Geographically nearby VO exhibit similar curve behaviours, as can be seen from the VOs on Figs. 4.22 (VO on the right) and 4.23, which are adjacent VOs and share mutual measurements. Figure 4.23 curves are very similar for all magnetic components. On the X and Z components the field increases rapidly around epochs 2014.1, 2014.5 and 2014.8 on both VO's, except the last increase which is only seen in the most northern VO ($\vartheta_{vo} = 6.25^o$, $\phi_{vo} = 8.75^o$) . The 15th and 16th period predictions on the same VO are also significantly different.

In Fig. 4.27 three geographically nearby VO, north, near and south of the magnetic equator also display very similar curves. At these locations the vertical component of the field is very smooth, in contrast to the north-south component which varies faster and also displays the 5 to 6 months cycle.

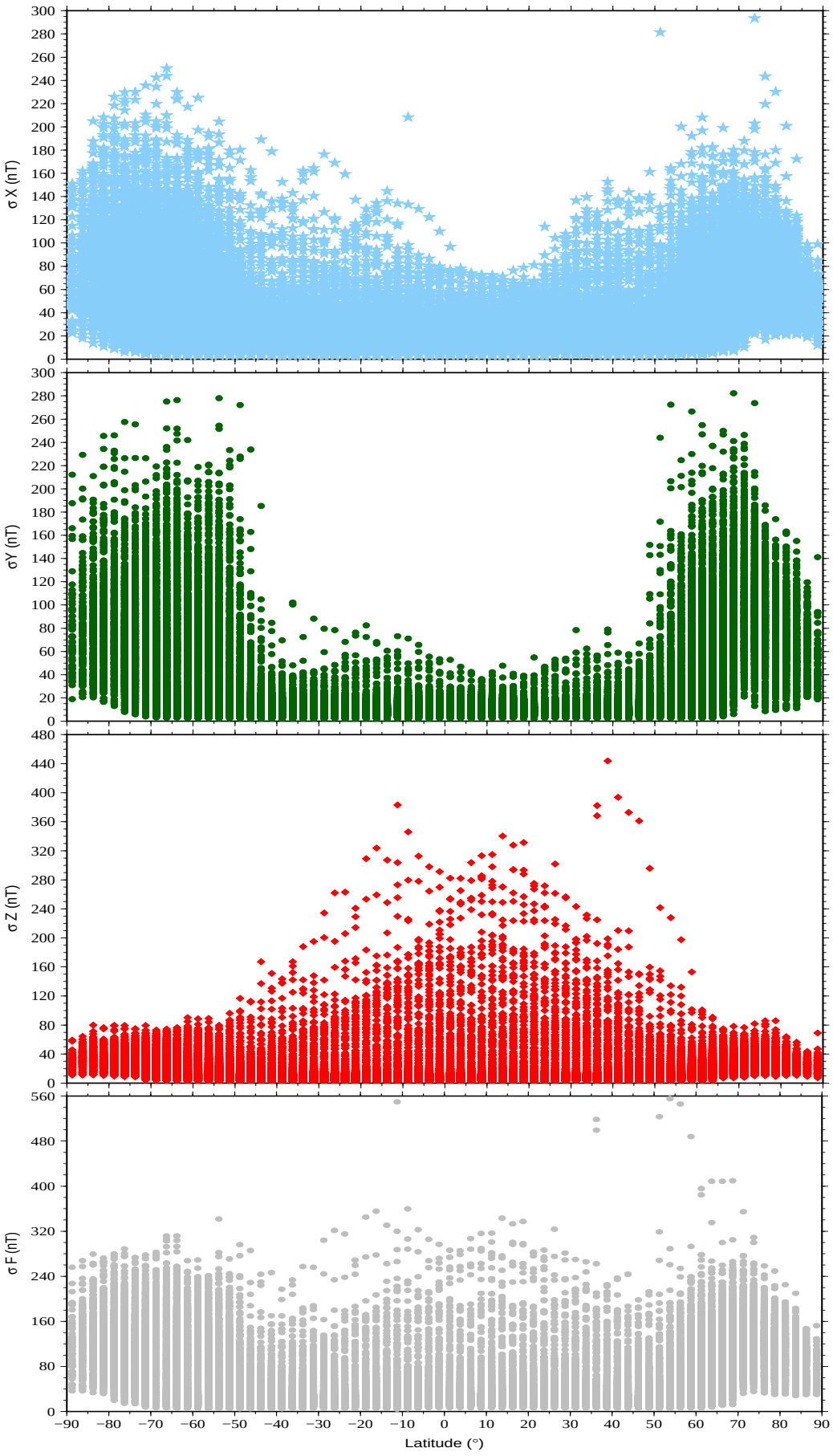

Figure 4.21: Rms residuals between Swarm mesurements and the ESD predictions given by the selected iteration solution for all 18 periods and all VOs as a function of the VO latitude.

4.6 Comparison with an SH model

The VO-ESD magnetic field time series computed at each virtual observatory were compared with a recent global SH geomagnetic field model. This comparison was made also with a B-spline description of the VO time series.

4.6.1 Method

For each VO of the constructed mesh the VO-ESD approach predictions were compared with the CHAOS-5 (cf. Section 2.5.1, Finlay et al. (2015)). These were computed at each VO's centre location, and at the mean time of each period between November 2013 and December 2014, resulting in 13 predictions per component and per VO. The CHAOS-5 model is defined between 1997.0 and 2015.0 (Finlay et al., 2015), then it was evaluated only until the end of 2014. To compute the CHAOS-5 model predictions, only the time-dependent internal field up to spherical harmonic 20 was used[1].

The VO time series were described by cubic B-splines. For this step all 18 periods of the VO time series were considered (from 2013.96 to 2015.37). A ten-knot description was used with a six-month knot separation, corresponding to four exterior equal knots at each endpoint, 2013.96 and 2015.37, and two interior knots at the points 2014.46 and 2014.95. This yields a cubic B-spline function $M_l(t), l = 1, ..., 6$, used to represent the time change of each magnetic component at each VO. The purpose of the application of splines to the VO time series was to observe their time dependence with on another perspective and compare with the SH model, which also used B-splines to describe the time dependence of the Gauss coefficients (sixth-order splines with a 0.5 year knot spacing).

[1]The spline coefficients were retrieved from the model website: `http://www.spacecenter.dk/files/magnetic-models/CHAOS-5/`.

4.6.2 Comparison

Figures 4.22 to 4.27 represent, for twelfth VOs (see Table 4.3) VO-ESD and CHAOS-5 predictions, even if the latter is only until the end of 2014. Also on those figures, the B-spline descriptions of the VO-ESD predictions are displayed. The showed results belong to VO distributed all over the globe. The VO-ESD predictions were already discussed (Section 4.5.2). The simple B-spline representation adjusts satisfactorily to the predictions. The geographically close VOs on Fig. 4.23 exhibit a B-spline representation very alike, especially for the horizontal components.

As expected the CHAOS-5 model is much smoother than the VO-ESD time series. Their temporal variations correspond roughly to a linear increase or decrease of the magnetic field, thus to a constant secular variation. In general, the absolute variation (increase/decrease) of the magnetic field during the 13 periods interval predicted by CHAOS-5 is larger than the one given by the VO-ESD predictions. For example, the X component of the VO on the left in Fig. 4.22 increases 50 nT in the model prediction, while the VO-ESD prediction only increases approximately 25 nT for the same period of time. However, at high latitudes opposite situation appears as the VO-ESD magnetic field changes are larger than the ones given by CHAOS-5 (e.g., Fig. 4.24).

Figure 4.27 represents the predictions for three VO's located north, very near and south of the magnetic equator. As with the geographically close VO on Fig. 4.24, the predictions are very similar for all components and field intensity. The variations of the magnetic field on the three VOs are similar. Contrary to the high latitude VOs, the temporal variations are smoother. Nevertheless, the influence of the external field can still be observed mostly in the horizontal components, and as a consequence in the field intensity.

Table 4.3: Location and reason of selection for the VOs compared in Sections 4.5 and 4.6.

ϑ (^{o})	ϕ (^{o})	Observations
-33.75	88.50	southern location, South Indian Ocean
46.25	1.80	central France and close to CLF
6.25	6.25	equatorial location and close to VO D
6.25	8.75	equatorial location and close to VO C
-73.75	136.10	polar latitude location, South East Antarctica
88.75	225.00	polar latitude location, North America continent
-31.25	332.42	southern location, South Atlantic
31.25	123.39	northeast location, East China Sea
-36.25	26.15	southern location, near South Africa
8.75	66.71	north of magnetic equator
6.25	66.25	very near of magnetic equator
1.25	66.25	south of magnetic equator

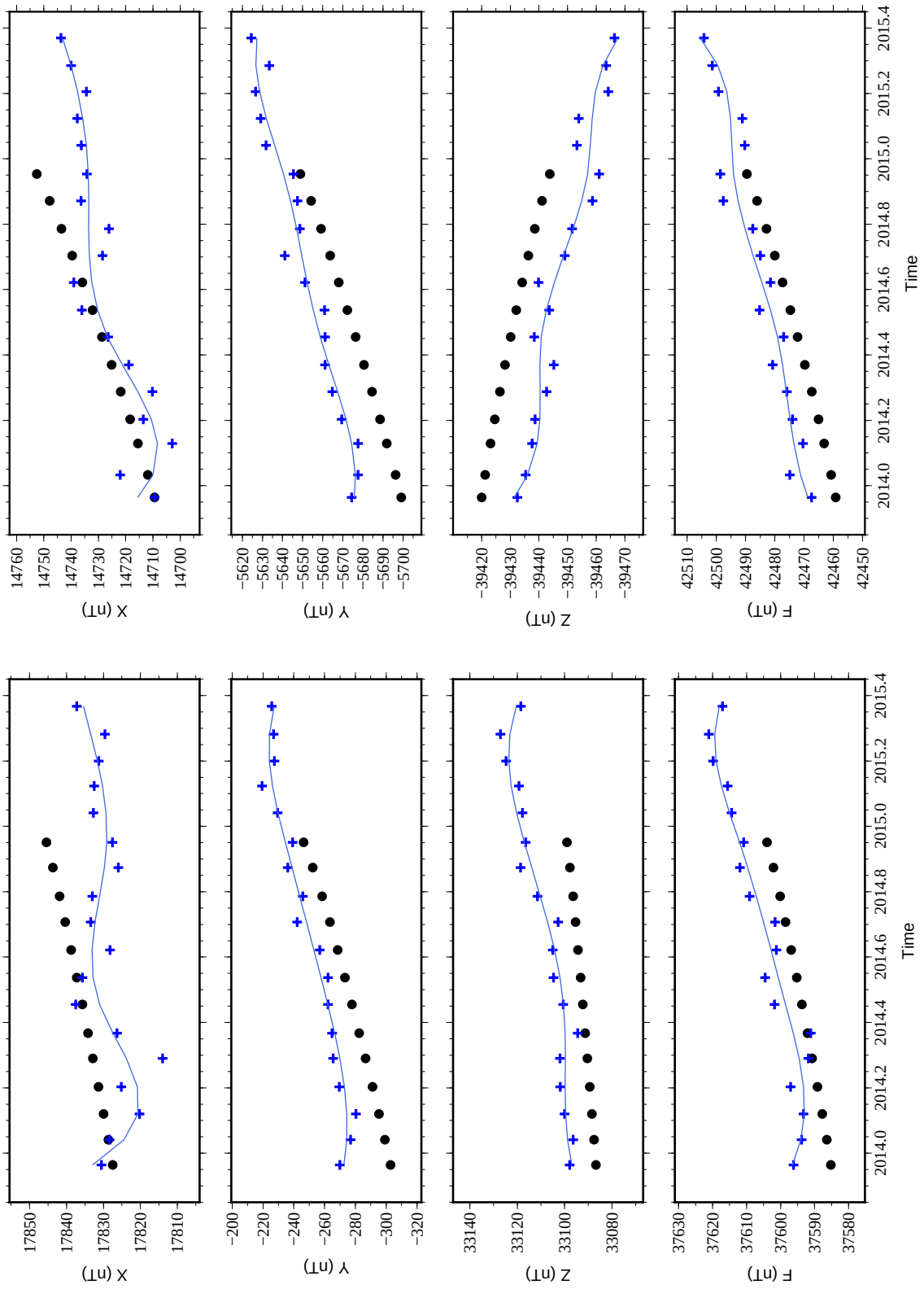

Figure 4.22: VO-ESD predictions (*blue pluses*) with a cubic B-spline description (*blue lines*), and the CHAOS-5 predictions (*black dots*), for two VO located at: (*top*) $\vartheta_{vo} = -33.75^o$, $\phi_{vo} = 88.50^o$ and (*bottom*) $\vartheta_{vo} = 46.25^o$, $\phi_{vo} = 1.80^o$.

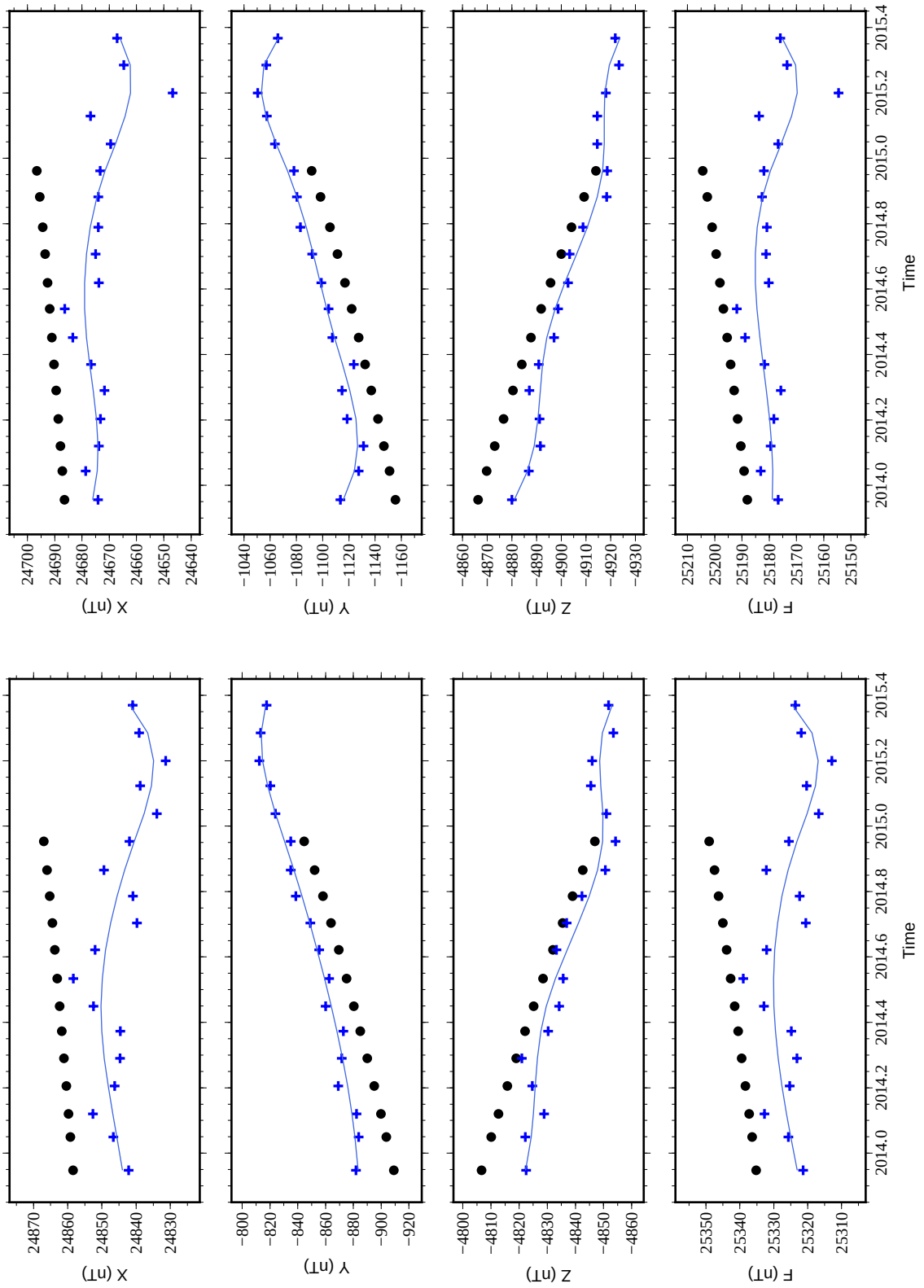

Figure 4.23: As in Fig. 4.22, for two nearby VO located at: (*top*) $\vartheta_{vo} = 6.25^o$, $\phi_{vo} = 6.25^o$ and (*bottom*) $\vartheta_{vo} = 6.25^o$, $\phi_{vo} = 8.75^o$.

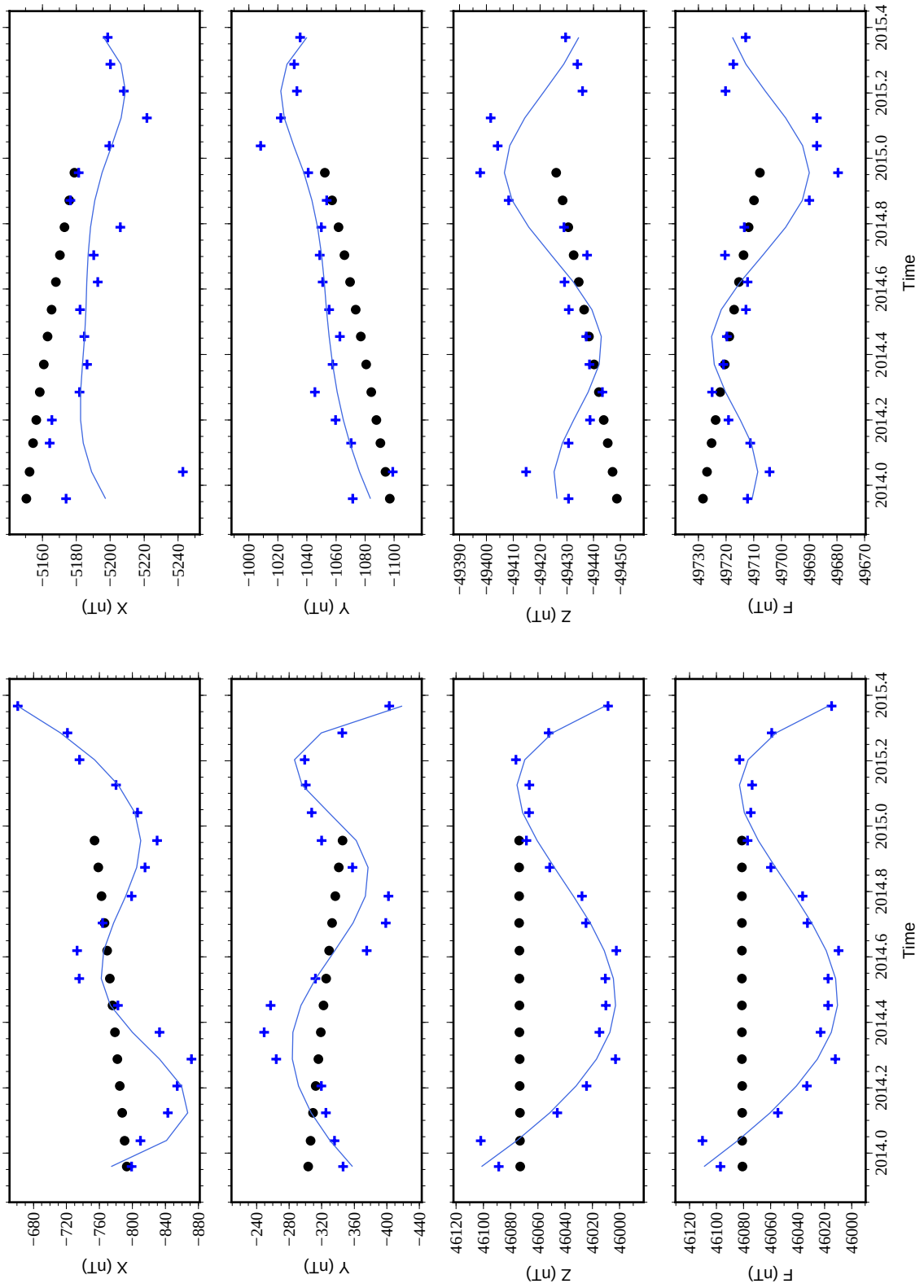

Figure 4.24: As in Fig. 4.22, for two VO located at: (*top*) $\vartheta_{vo} = -73.75^o$, $\phi_{vo} = 136.10^o$ and (*bottom*) $\vartheta_{vo} = 88.75^o$, $\phi_{vo} = 225.00^o$.

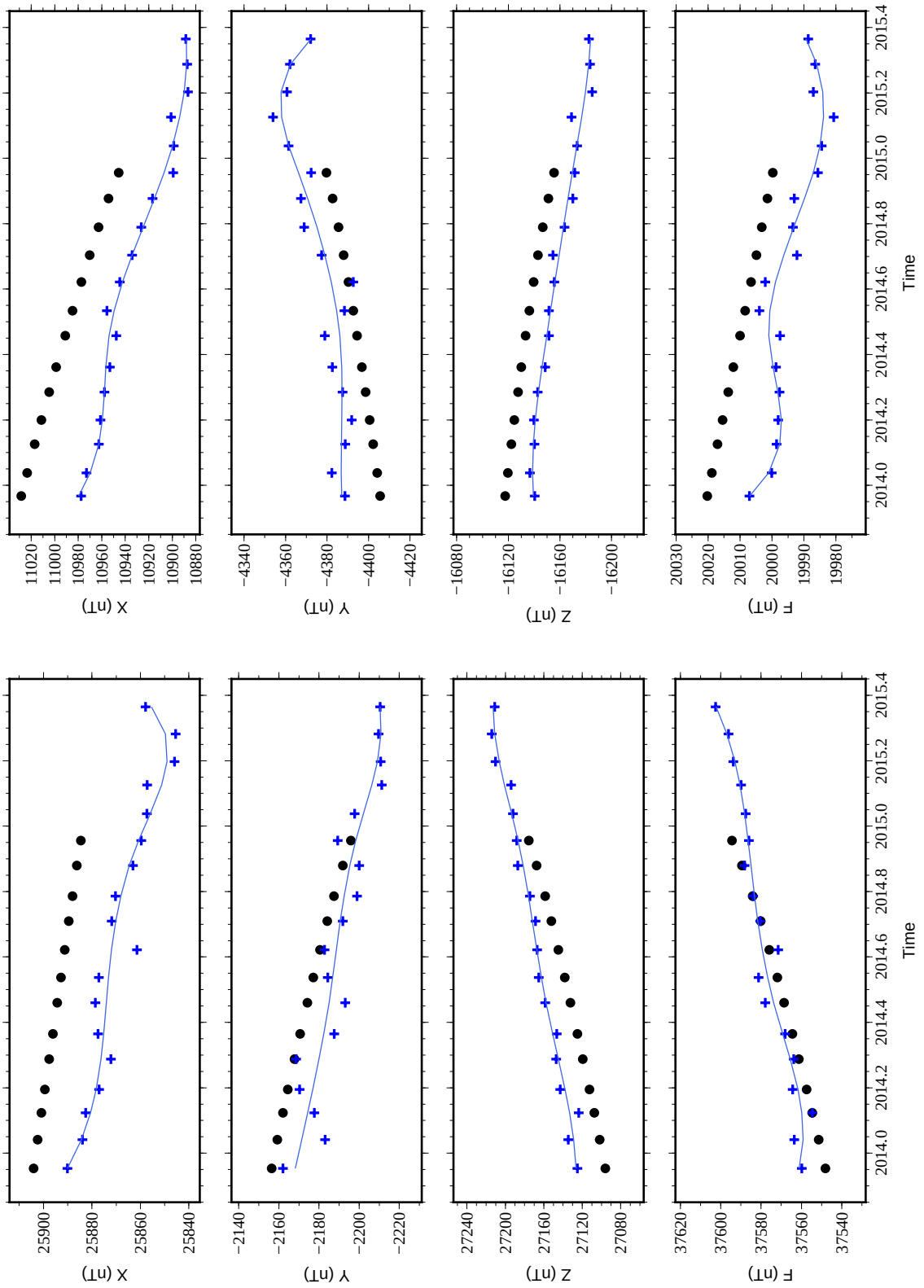

Figure 4.25: As in Fig. 4.22, for two VO located at: (*top*) $\vartheta_{vo} = -31.25^o$, $\phi_{vo} = 332.42^o$ and (*bottom*) $\vartheta_{vo} = 31.25^o$, $\phi_{vo} = 123.39^o$.

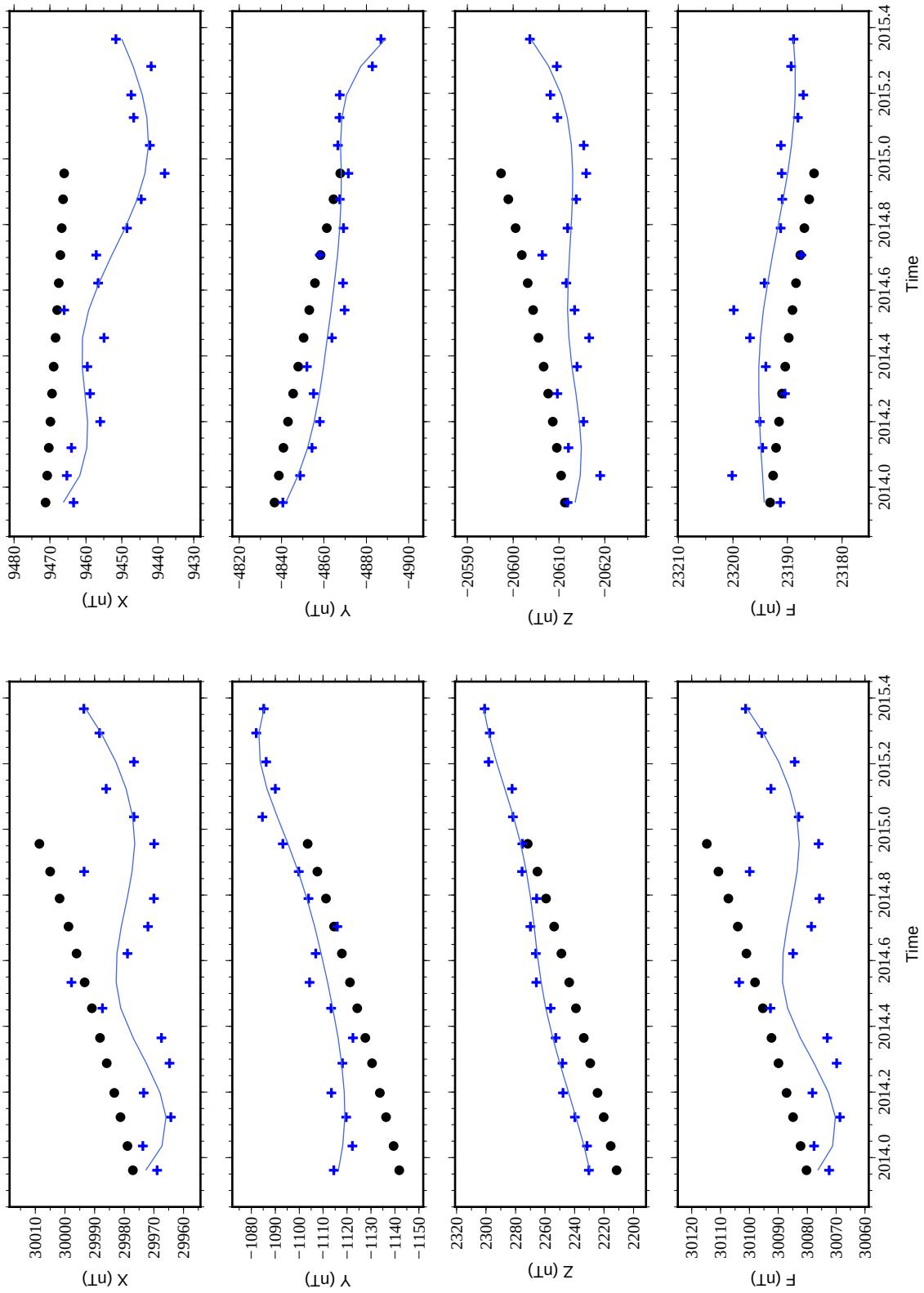

Figure 4.26: As in Fig. 4.22, for two VO located at: (*top*) $\vartheta_{vo} = -36.25^o$, $\phi_{vo} = 26.15^o$ and (*bottom*) $\vartheta_{vo} = 8.75^o$, $\phi_{vo} = 66.71^o$,

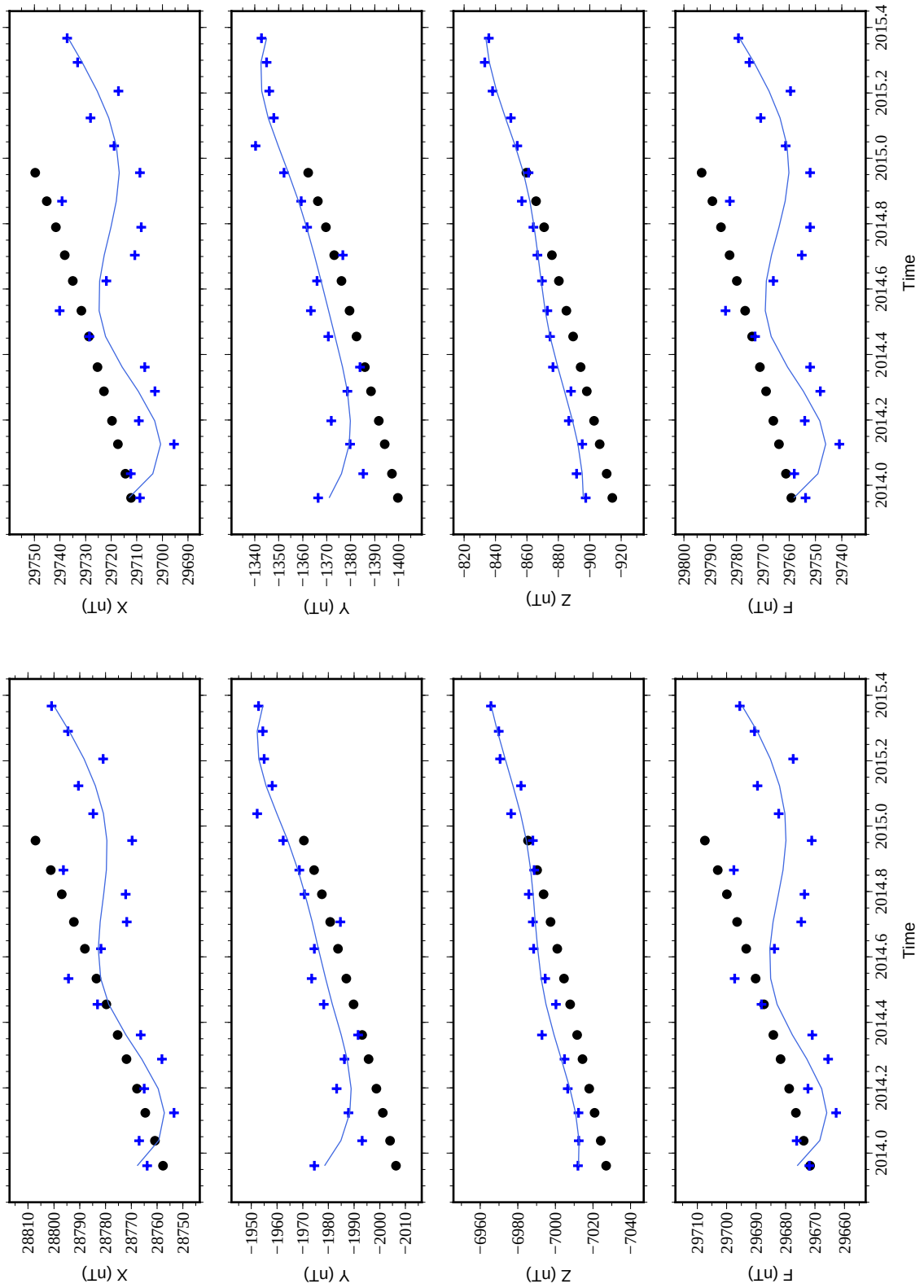

Figure 4.27: As in Fig. 4.22, for two VO located at: (*top*) $\vartheta_{vo} = 6.25^o$, $\phi_{vo} = 66.25^o$ and (*bottom*) $\vartheta_{vo} = 1.25^o$, $\phi_{vo} = 66.25^o$.

4.7 Discussion and conclusions of the application of the VO-ESD approach

The application of the VO-ESD approach to Swarm measurements revealed encouraging and interesting results.

From the first tests a new iteration selection criteria, more efficient and consistent for each VO was redefined. The Swarm measurements were then used to constrain other parameters of the VO-ESD approach e.g., the time interval of the inversion input data. Different intervals were tested but no important dependence was found, neither with the rms residuals nor with the differences between the input SH model and the VO-ESD approach predictions. However, it was found that for some periods of time (2014.1 and 2014.3, Fig. 4.4) the obtained rms residuals were significantly higher than for other periods. A relation may exist with the operation manoeuvres on the three Swarm satellites. In fact, during the first months of the mission several manoeuvres were applied to the three satellites, especially from the end of January to the beginning of March[2]. These manoeuvres as well as torque corrections may have biased the magnetic measurements taken during that period of time. Futhermore a relation was also searched with the external field contributions, but no evident dependence was found.

I compared the VO predictions with eight ground magnetic time series. The rms residuals are similar for all VOs, with higher values for the VOs at higher latitudes. The obtained VO time series strongly resemble to the corresponding ground observatories. The correlation computed between the series on the ground and at satellite altitude is significant, especially for the Y and Z components of the field. Both on the ground and at satellite altitude the annual tendency is alike and geographically close VO present similar magnetic field time series as it is observed with nearby ground magnetic observatories.

Mandea and Olsen (2006) computed correlations between their obtained time series of the secular variation at satellite altitude and at ground observatories. They found significant cor-

[2]The information on the Swarm Mission manoeuvres can be found in `https://earth.esa.int/documents/10174/1568455/Swarm_manoeuvres`.

relations for the dX/dt and dZ/dt components, whereas the correlations for dY/dt were not significant. The same kind of correlations cannot yet be computed for our VO-ESD time series, as the number of points (18) is still low. However, based on the computed correlations for the field time series, we may expect to obtain good correlations for the three magnetic components of the secular variation. This is supported by the observation that the annual tendency of the temporal variation of the field is also generally alike between the ground observatories and the respective VO predictions. Nevertheless, a resemblance exists between the annual tendency of the derived VO time series and the CHAOS-5 model (Finlay et al., 2015), which is similar to the resemblance between ground observatories time series and the model predictions at those locations.

From this result, the approach was applied to all Swarm measurements for a global mesh of virtual observatories. Time series of the magnetic field were then obtained at 6644 locations for a total of 18 periods of 30 days. The altitude of each VO was computed as the mean value of the altitude range of Swarm satellites during the first two months of the mission. Thus, due to the Swarm satellites orbits, the altitude of the VO depends on the latitude, decreasing from the South to the North.

The rms residuals of all the inversions reveal a dependence with the latitude of the VO position. At polar latitudes the horizontal components of the field present high values of rms residuals, whereas the vertical component has high residuals at low latitudes. At polar latitudes the FAC signals may be responsible for the horizontal components high rms residuals, because the contributions of these currents are dominant compared to the main field contribution there. At low latitudes, around the magnetic equator, it is the vertical component of the main field that is low (and zero at the magnetic equator), thus the contributions of the electrical currents around the magnetic equator are large.

The VO-ESD time series also reflect the influence of the external field. The VO at high latitude locations display greater and faster temporal changes than the ones at lower latitudes. The closer a VO is to the geographic pole, the more noisy its magnetic time series will be. Around the magnetic equator the predictions for the vertical component are not strongly affected by the

high value of rms residuals. The vertical component predictions do not display rapid temporal changes and are very similar to the predictions of the CHAOS-5 model.

The external field contributions in the VO-ESD predictions must be taken into consideration in the construction of a global model of the magnetic field. If one desires input data without these contributions, one can implement a data selection or treatment of the satellite measurements based on geomagnetic indices, as it is commonly done when modelling the geomagnetic main field (cf. section 2.5) .

Chapter 5

Global models using VO-ESD

At this stage, at each VO of the mesh a time series of predictions for 18 periods is built. The construction of a spherical harmonics model representation of the field is performed using these time series. However, even if an adequate description of the main field is possible with such a short time series, an adequate description of the secular variation is more arduous. The classical SH inversion is used to describe the main field, the secular variation and the external field for different combinations of periods and values of the maximum degree of the SH, resulting in several test models, which are discussed and compared in the following pages.

5.1 Parametrization and terminology of the models

In this first section I introduce the model terminology and the modelling parameters. Models will be presented and discussed in the following section. The internal and external fields are described by the potentials from Eqs. 2.8 and 2.9. The time dependence of the Gauss coefficients for the internal field is assumed to be linear, following Eq. 2.18. The maximum degree of each potential was a tested parameter for the different test models.

As the predictions at high latitudes are influenced by external field currents mostly for the horizontal magnetic components, only the field intensity (F) was considered as input data to

Table 5.1: Model terminology, with associated parameters, number of vector ($<55^o$ absolute magnetic latitude) and scalar ($>55^o$) measurements, and associated rms residuals.

Model	Nbr input data		n maximum			σ (nT)			
	Vector	Scalar	MF	SV	Ext.	X	Y	Z	F
VO-ESD_18.30-13-2	97775	21792	30	13	2	9.54	6.38	11.53	9.88
VO-ESD_18.30-18-2	97775	21792	30	18	2	9.45	6.40	11.50	10.09
VO-ESD_18.30-18-3	97775	21792	30	18	3	9.42	6.40	11.49	10.07
VO-ESD_18.30-18-4	97775	21792	30	18	4	9.42	6.40	11.48	10.07
VO-ESD_18.30-10-2	97775	21792	30	10	2	9.47	6.38	11.53	10.16
VO-ESD_16.30-10-2	86905	19374	30	10	2	8.12	5.95	5.91	9.85
VO-ESD_16.30-10-3	86905	19374	30	10	3	8.09	5.95	5.89	9.82
VO-ESD_16.30-10-5	86905	19374	30	10	5	8.07	5.94	5.88	9.81
VO-ESD_6.T01	32604	7260	30	0	2	10.95	8.63	19.13	9.07
VO-ESD_6.T02	32602	7262	30	0	2	10.73	8.17	19.03	9.56
VO-ESD_6.T03	32598	7264	30	0	2	7.52	6.89	9.32	9.68
VO-ESD_6.T04	32598	7266	30	0	2	7.11	6.73	8.96	9.60
VO-ESD_6.T05	32598	7266	30	0	2	8.18	7.62	8.99	9.22
VO-ESD_6.T06	32598	7266	30	0	2	8.41	8.12	8.32	8.69
VO-ESD_6.T07	32598	7266	30	0	2	8.80	7.74	8.39	9.19
VO-ESD_6.T08	32598	7266	30	0	2	9.59	7.33	8.65	11.04
VO-ESD_6.T09	32598	7266	30	0	2	8.13	7.09	8.87	11.44
VO-ESD_6.T10	32598	7266	30	0	2	7.04	7.28	8.72	10.85
VO-ESD_6.T11	32598	7266	30	0	2	8.47	7.31	8.49	10.40
VO-ESD_6.T12	32598	7266	30	0	2	8.02	7.12	8.11	10.06
VO-ESD_6.T13	32573	7266	30	0	2	6.97	6.96	7.90	10.65
VO-ESD_1.T01	5435	1209	30	0	2	7.03	7.99	6.31	6.31
VO-ESD_1.T02	5435	1209	30	0	2	18.68	13.23	36.34	9.37
VO-ESD_1.T03	5435	1209	30	0	2	6.91	4.38	6.02	6.15
VO-ESD_1.T04	5433	1211	30	0	2	4.46	4.25	6.17	4.10
VO-ESD_1.T05	5433	1211	30	0	2	6.15	4.97	8.59	4.52
VO-ESD_1.T06	5433	1211	30	0	2	3.93	7.06	3.11	4.00
VO-ESD_1.T07	5433	1211	30	0	2	2.72	3.43	2.19	3.42
VO-ESD_1.T08	5433	1211	30	0	2	2.34	2.17	2.26	3.36
VO-ESD_1.T09	5433	1211	30	0	2	4.47	4.29	2.95	4.69
VO-ESD_1.T10	5433	1211	30	0	2	4.06	7.25	2.93	5.05
VO-ESD_1.T11	5433	1211	30	0	2	3.91	5.70	2.94	4.72
VO-ESD_1.T12	5433	1211	30	0	2	4.20	3.32	2.65	4.92
VO-ESD_1.T13	5433	1211	30	0	2	4.76	4.28	2.87	5.84
VO-ESD_1.T14	5433	1211	30	0	2	4.17	5.25	3.43	5.13
VO-ESD_1.T15	5433	1211	30	0	2	4.18	5.27	3.69	4.61
VO-ESD_1.T16	5433	1211	30	0	2	6.49	4.75	3.83	5.87
VO-ESD_1.T17	5433	1211	30	0	2	3.81	3.32	2.63	4.42
VO-ESD_1.T18	5408	1211	30	0	2	4.22	4.57	2.83	4.63

the inversion above the 55^o magnetic absolute latitude. Below this latitude only the vectorial components (X, Y, Z) were considered. Figure 5.1 shows the distribution of the VO data for three different periods, the first, the fourth and the last one. Even if the number of VOs based on vector data changed slightly from the first to the fourth periods, the distribution of data is always globally homogeneous. However for the last period some VO are absent, especially around the equator.

The first computed models are snapshots of the magnetic field for only one period and all VOs, leading to 18 snapshots models. For these models the internal field is considered static up to degree 30 and the external field is described up to degree 2. Table 5.1 presents the characteristics of the computed models, the number of observations, the maximum degree of expansion and the corresponding rms residuals to the VO-ESD predictions. The snapshot models for one period are named VO-ESD_1.TX where X is the number of the model period, with 01 corresponding to 2013.956 and 18 to 2015.369.

Snapshot models constrained by data from 6 consecutive periods are also computed. They are named VO-ESD_6.X, where X goes from 01 to 13. VO-ESD_6.T01 corresponds to the first six periods (from 2013.956 to 2014.369), VO-ESD_6.T02 contains data from the second period to the seventh (2014.041 to 2014.455) and so on.

Finally models using predictions from all 18 periods and including a time changing magnetic field were computed. The secular variation is computed with a SH maximum degree of 13 or 18. The external field is computed up to degree 2, 3 or 5. The main field is computed to SH degree 30. These models are named VO-ESD_18.A-B-C, where A, B and C are the maximum degree of the SH expansion for the main field, secular variation and external field, respectively.

From the observation of the results of the snapshots models, especially their spectra (Figs. 5.2 and 5.3), it is also decided to compute models using only the last 16 periods, the VO-ESD_16.X models. Also from analysis of the secular variation spectra of the models VO-ESD_18.A-B-C, the secular variation is computed up to degree 10 only. The external field coefficients are computed for degree up to 2, 3 or 5 (see Table 5.1). The spectra of these models are shown in Figs. 5.4 and 5.5.

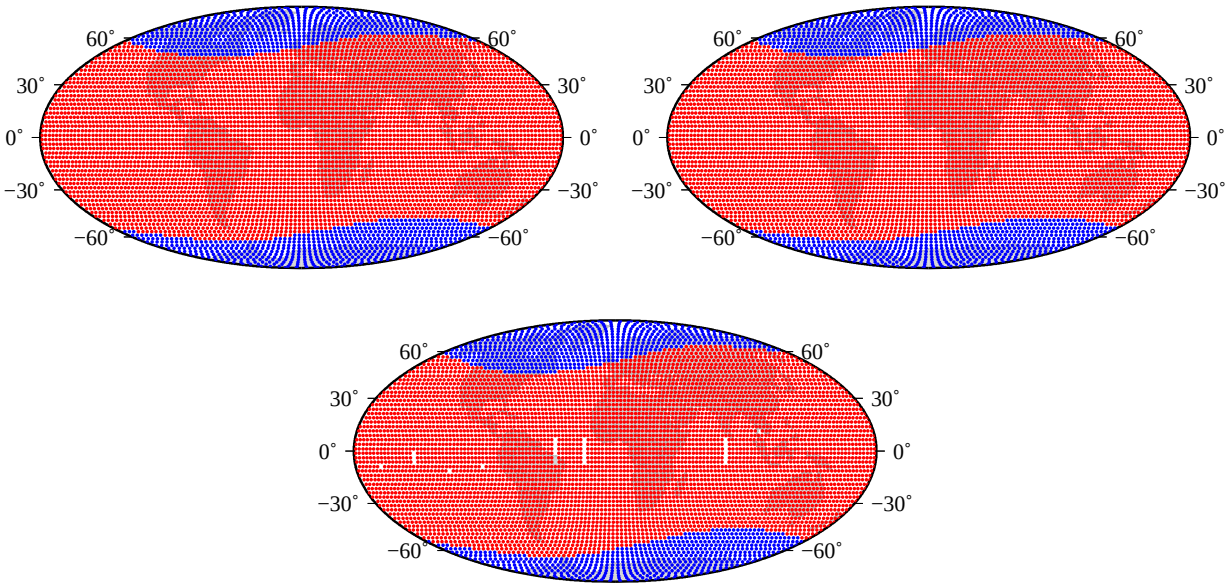

Figure 5.1: Distribution of vector (*red*) and scalar (*blue*) measurements for three periods (2013.956, 2014.203 and 2015.369) of the VO-ESD time series, used as input data to the different models.

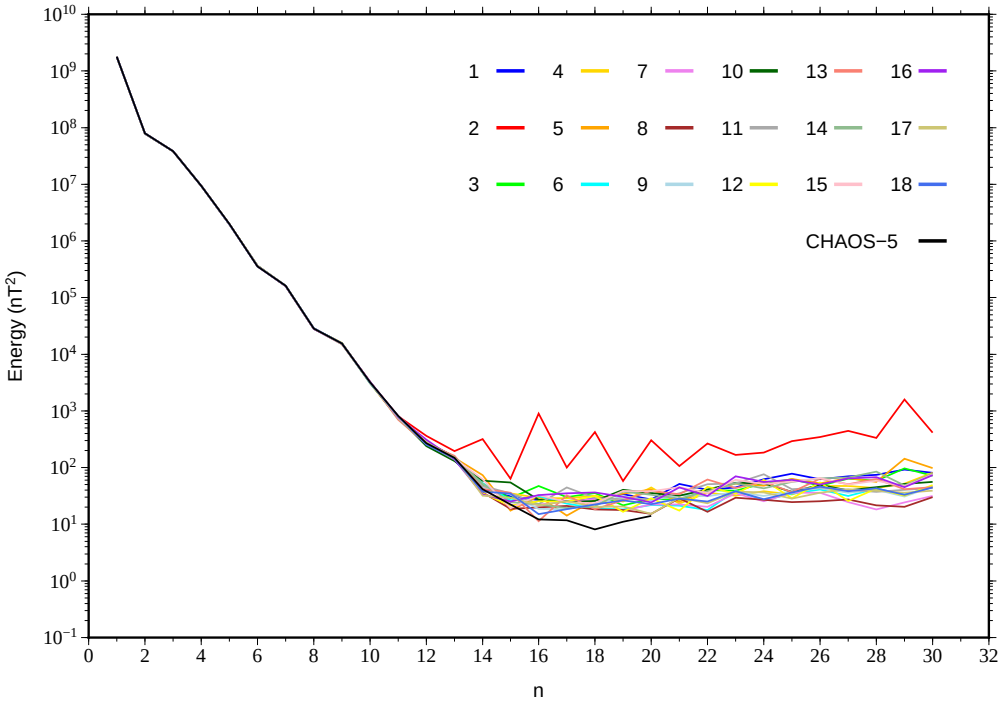

Figure 5.2: Magnetic energy spectra of the geomagnetic field at the Earth's surface, for all eighteen 1-period snapshot models, VO-ESD_1.TX, and for the CHAOS-5 model (for $n \leq 20$ and epoch 2014.70).

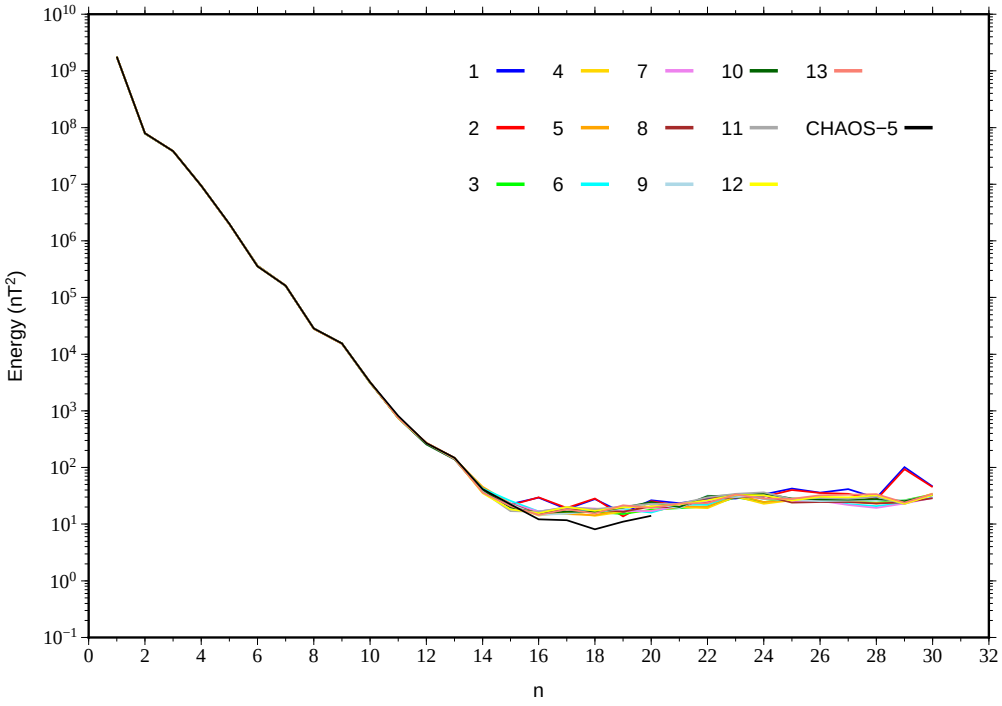

Figure 5.3: Magnetic energy spectra of the geomagnetic field at the Earth's surface, for all thirteen 6-period models, VO-ESD_6.TX, and for the CHAOS-5 model (for $n \leq 20$ and epoch 2014.70).

5.2 Results

5.2.1 Statistics, spectra and comparison with an SH model

Statistics for the rms residuals between all models and the VO-ESD time series used to derive them are gathered in Table 5.1. The geomagnetic spectra (cf. Section 2.4) are also plotted for all models (Figs. 5.2 to 5.5).

The 1-period snapshot models, each one with observations of a 30-day period, allow to perform a first test on the VO-ESD derived time series. From the rms residuals of these models (Table 5.1) and the corresponding geomagnetic spectra (Fig. 5.2) it is found that the first two 30-day periods have a different behaviour. These models (VO-ESD_1.T01 and VO-ESD_1.T02) present the higher rms values, about 7 nT (horizontal components) for the first and about 36 nT (vertical component) for the second. All 1-period models have similar spectra up to degree 11. Thereafter the first two 1-period models spectra have high values, with abrupt changes with the degree, increasing with larger degree and are significantly different from the other sixteen models. It

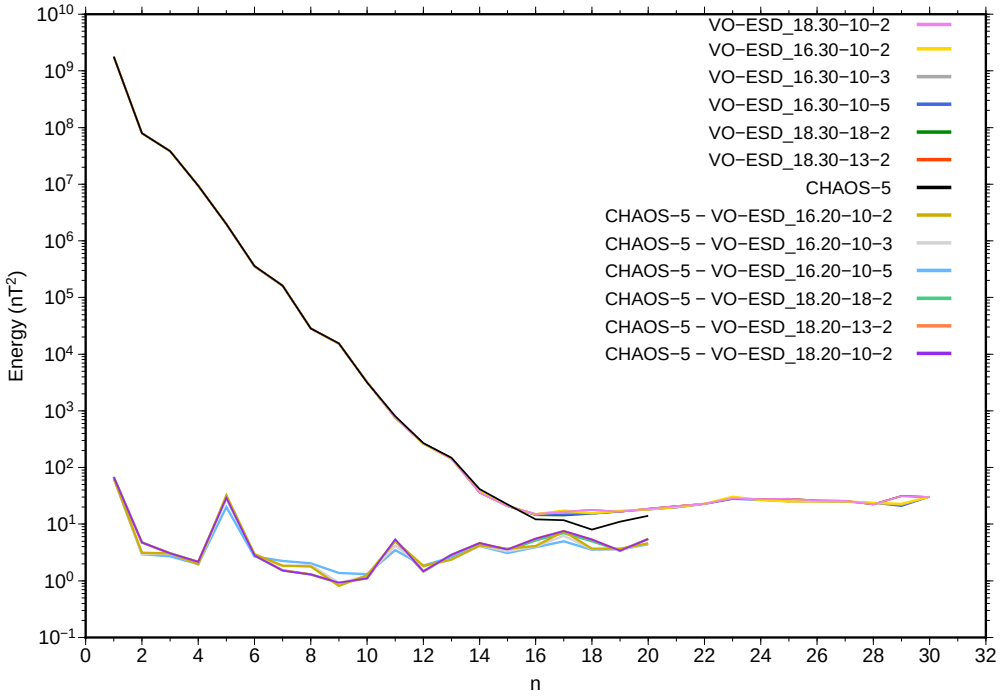

Figure 5.4: Magnetic energy spectra of the geomagnetic field at the Earth's surface, for the different computed models using 16 or 18 periods, and the CHAOS-5 model (for $n \leq 20$) at epoch 2014.70. Also shown are the differences between CHAOS-5 and the other models (for $n \leq 20$). Note that some curves do superimpose.

must be also noted that all the sixteen model spectra have slightly larger values than the CHAOS-5 model spectrum, above degrees 15 or 16.

Model VO-ESD_1.T03 to VO-ESD_1.T18 spectra are almost constant (for $n > 13$), with a small increase towards the higher degrees. The difference of the first two models with the other sixteen is also noted if one looks at the residuals between the model predictions and the VO-ESD input data used to derive them (Fig. 5.6). Visually it is clear that the residuals associated with the first two models are much higher than the ones from the tenth one. All the residual maps are given in Appendix C, Fig. C.1.

The 6-period models describe only the main field and the external field, and the secular variation through the six periods (roughly six months) is neglected. All models spectra are superimposed up to degree 13 (Fig. 5.3). The first two models (VO-ESD_6.T01 and VO-ESD_6.T02) have again the larger rms residuals, especially for the X and Z components (above 10 and 19 nT, respectively). The spectra from these two models differ from the other 6-period models spectra

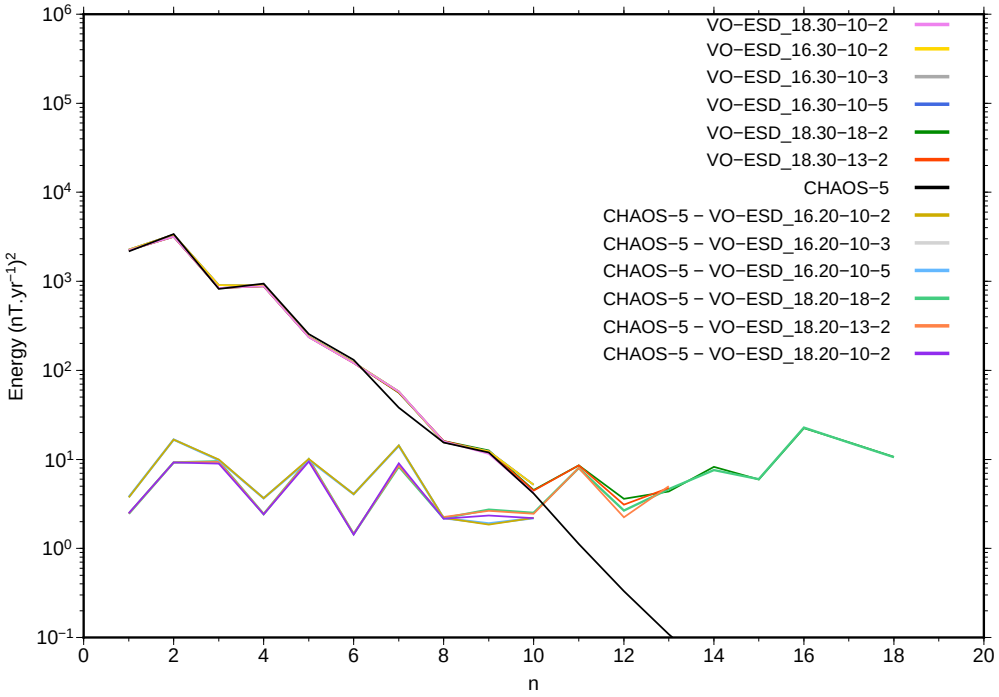

Figure 5.5: Magnetic energy spectra of the first time derivative (secular variation) of the geomagnetic field at the Earth's surface, for the different computed models using 16 or 18 periods, and the CHAOS-5 model (for $n \leq 20$), at epoch 2014.7. Also shown are the differences between CHAOS-5 and the other models (for $n \leq 18$). Note that some curves do superimpose, like the differences for models VO-ESD_16, and the differences for models VO-ESD_18.

from degree 16 onward (Fig. 5.3). Figure 5.7 shows the residuals for two models of this series, VO-ESD_6.T01 and VO-ESD_6.T10. The residuals patterns are alike for both models, but the higher residuals for VO-ESD_6.T01 are clear. As for the 1-period models, maps of the residuals are given in Appendix C, Fig. C.2.

The model using all eighteen periods and describing the secular variation up to degree 18 has rms residuals between 6.40 and 11.50 nT. The tests with different expansions for the external field, from 2 to 5, do not affect the rms residual values. These different model spectra are very similar. Figure 5.4 shows the spectra of the VO-ESD_18.30-18-2 model as an example. A comparison between our models spectra and the CHAO-5 spectrum is also made. As CHAOS-5 coefficients are only known up to degree $n = 20$, we truncate our models to degree 20 for comparison purposes. With a description of the secular variation limited to degree 13 the rms residuals are very similar, between 6.38 and 11.53 nT (see Table 5.1). The spectra of these models are also alike (Fig. 5.4).

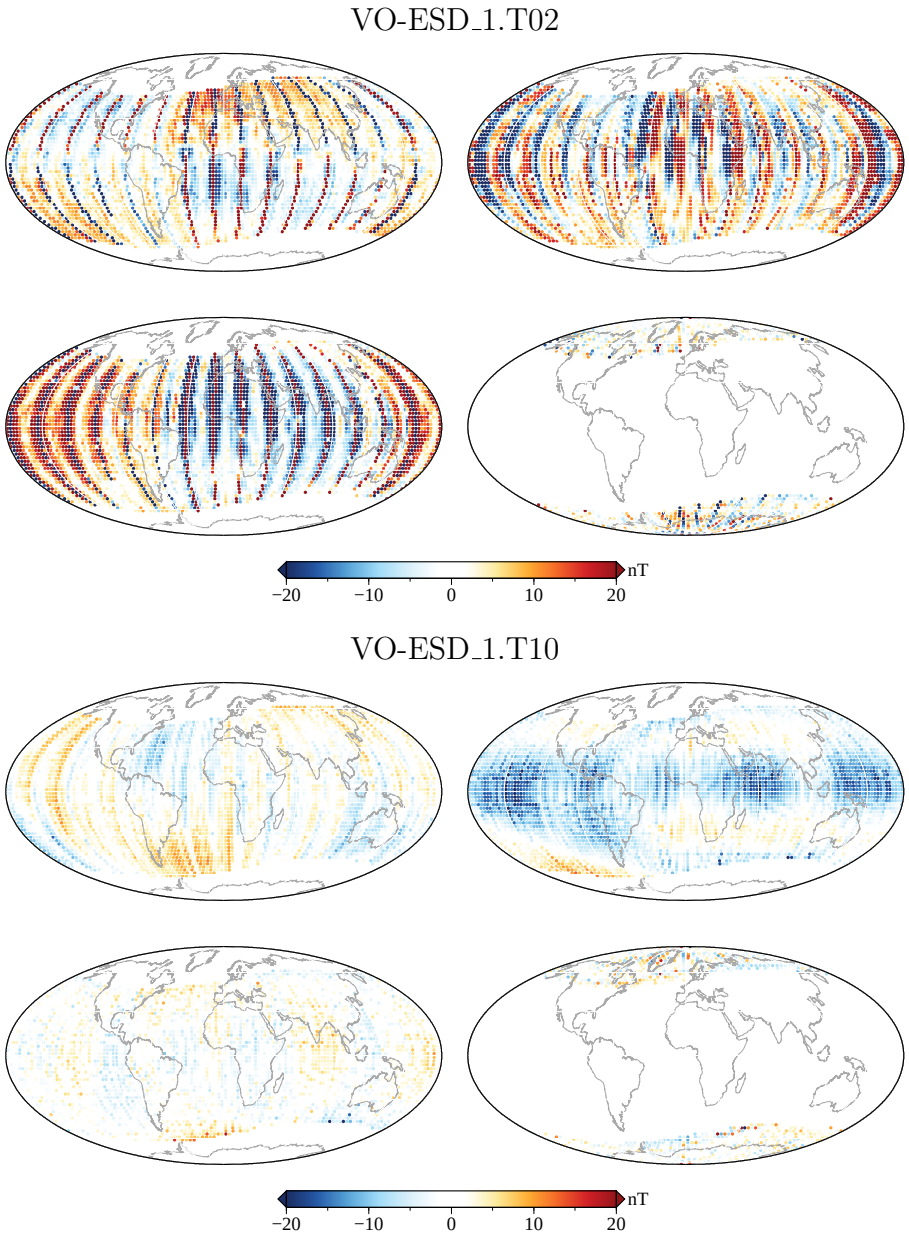

Figure 5.6: Residuals between the VO-ESD time series used as input data and the models (*top*) VO-ESD_1.T02 (epoch 2014.041) and (*bottom*) VO-ESD_1.T10 (epoch 2014.707). From (*top left*) to (*bottom right*), X, Y, Z, and F, respectively.

Residuals between VO-ESD time series on one hand and models VO-ESD_18.30-18-3, VO-ESD_18.30-18-2, VO-ESD_16.30-10-2, VO-ESD_16.30-10-3 and VO-ESD_16.30-10-5 predictions on the other hand, for epoch 2014.707, are shown in Figs. 5.8 and 5.9. The spatial patterns are very alike for the different models. Several features are always present: the longitudinal zones of opposite signal in X, the opposite signal between the Pacific and the Indian areas, the equatorial antisymmetry as well as the presence of the higher residuals in the polar areas for Z.

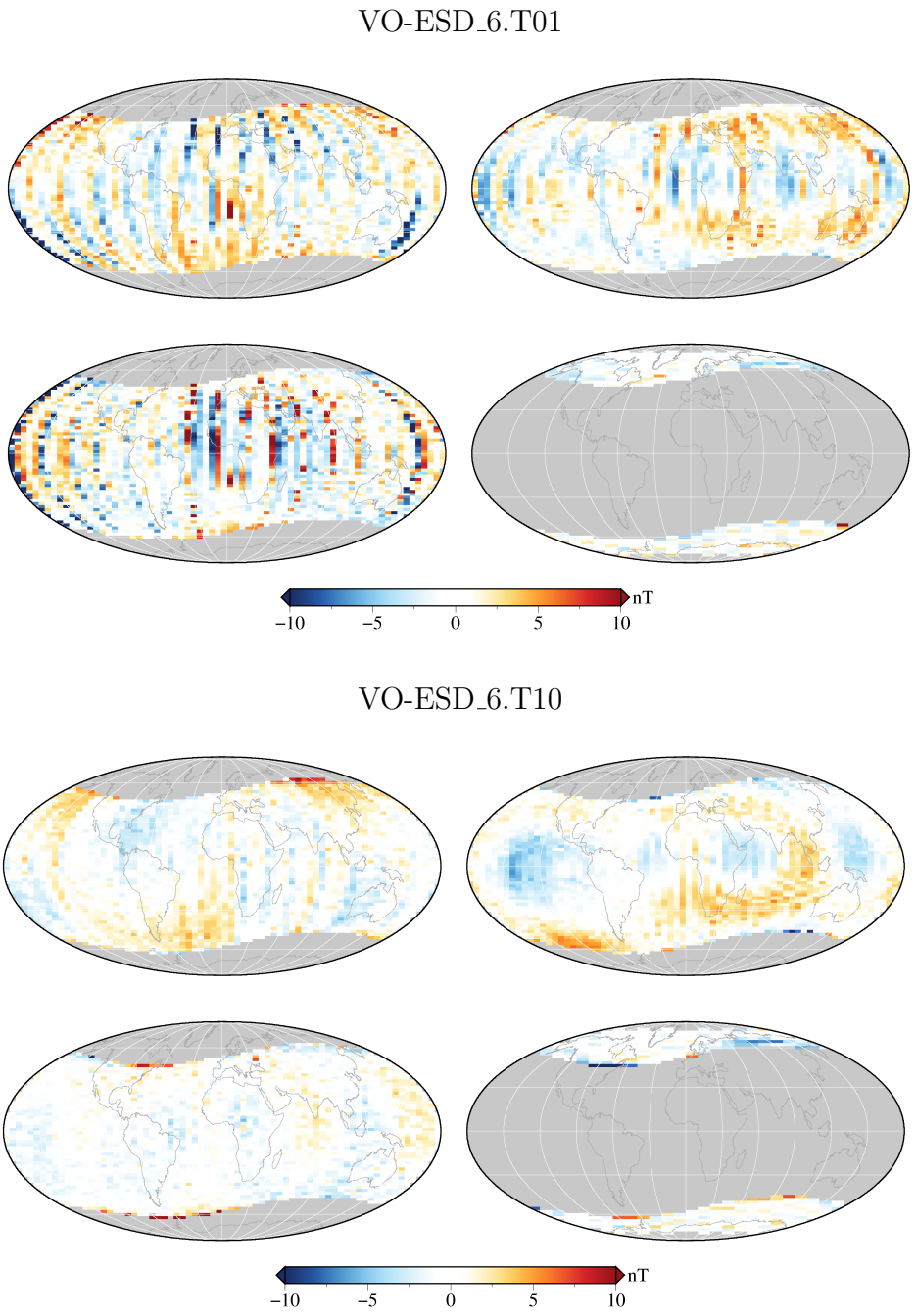

Figure 5.7: Residuals between the VO-ESD time series used as input data and the models (*top*) VO-ESD_6.T01 (mean epoch 2014.16) and (*bottom*) VO-ESD_6.T10 (mean epoch 2014.92). Each value corresponds to the mean of the residuals during the six periods over a $5^o \times 2.5^o$ surface for vector and $10^o \times 2.5^o$ surface for scalar components. From (*top left*) to (*bottom right*), X, Y, Z, and F, respectively.

Figure 5.5 shows the spectra of the secular variation for several computed models and the difference between them and the CHAOS-5 model at epoch 2014.70. For SH degrees above 10 the differences between models with secular variation expansion up to 13 and 18 and CHAOS-5 are of the same order of their own spectra. Their spectra are also too high for degrees larger

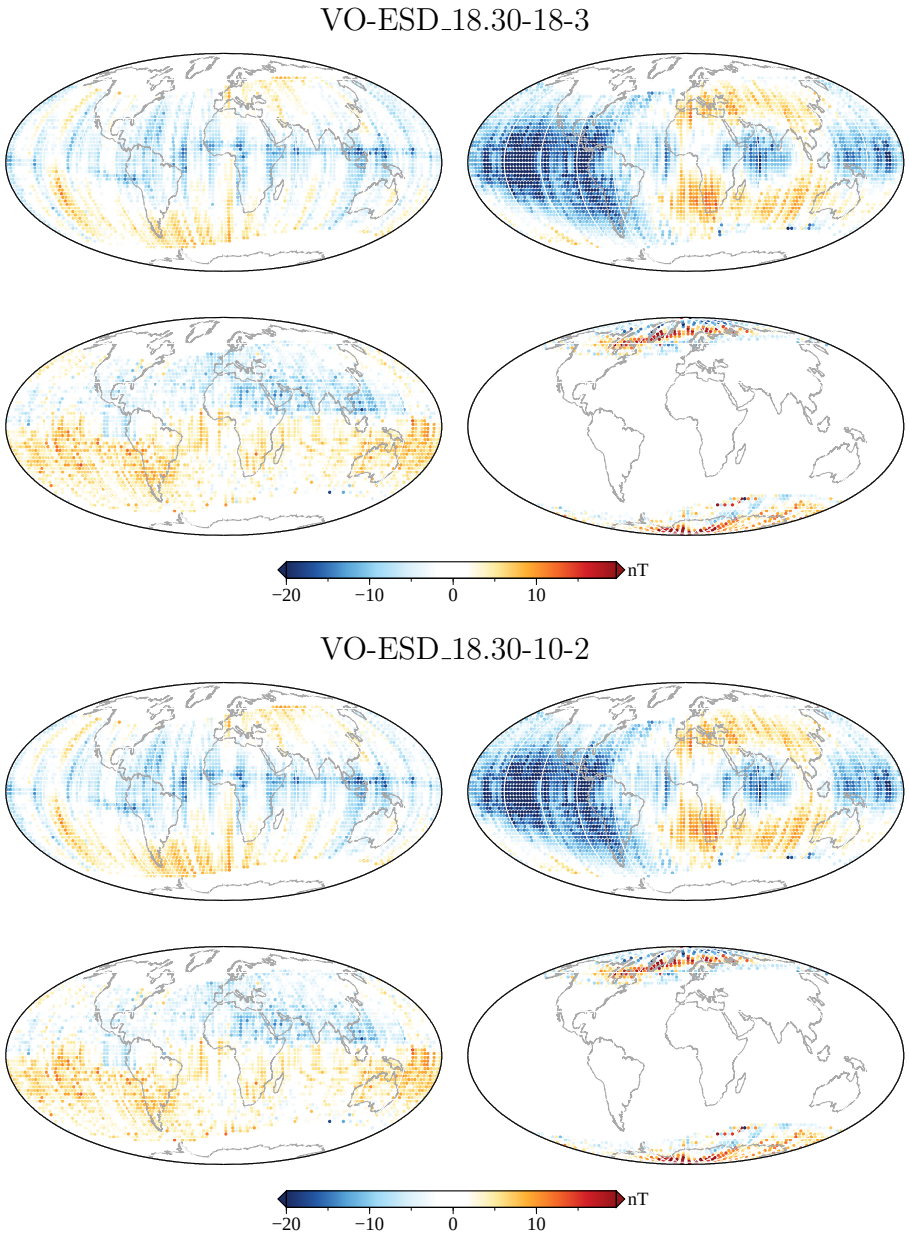

Figure 5.8: Residuals between the VO-ESD time series used as input data and the models (*top*) VO-ESD_18.30-18-3 and (*bottom*) VO-ESD_18.30-10-2 at epoch 2014.707. From (*top left*) to (*bottom right*), X, Y, Z, and F, respectively.

than 10. We conclude from this that the input data and the applied model parametrization do not allow the secular variation to be properly described for degrees above $n = 10$. For this reason a model is computed with a secular variation expansion up to degree 10 and up to degree 2 for the external field, hereafter denoted VO-ESD_18.30-10-2.

From the conclusions made from the 30-day snapshot models it is decided to compute a model with only the last sixteen periods. The main field is computed up to degree $n = 30$, the

secular variation up to degree $n = 10$ and the external contributions are computed for different expansions, $n = 2$, 3 or 5. This results in the models VO-ESD_16.30-10-C, where C is the maximum degree for the external field. The rms residuals improve with increasing maximum degree for the external field expansion (Table 5.1). However, the spectra of the three models are similar as well as their differences to CHAOS-5 spectrum. The model VO-ESD_16.30-10-2 displays the lowest differences to CHAOS-5 for most degrees, except for $n = 3$, 5, 11 and 17. At those same degrees the model VO-ESD_18.30-10-2 has the largest differences, while at other degrees ($n = 7$, 8, 12 and 19) this model difference is the lowest.

All main field model spectra have an important difference with the one of CHAOS-5 for degree 5. This is especially visible when looking at the differences coefficient by coefficient, as shown in Figs. 5.10 and 5.11. For the main field, differences larger than 1 nT are found for coefficients g_1^0, h_1^1, g_5^0 and h_5^1 for all models; a fifth coefficient, g_2^0, has also such a large difference for model VO-ESD_18.30-10-2. Figures 5.12, 5.13 and 5.14 show the differences, at the Earth's surface and epoch 2014.7, between CHAOS-5 and the VO-ESD_16.30-10-2, VO-ESD_16.30-10-5 and VO-ESD_18.30-10-2 models truncated at $n = 20$. All figures present the same spatial patterns with high differences at the polar areas, an equatorial antisymmetric difference in Z and a antisymmetric difference between Atlantic and Pacific areas in Y. The X component also presents important differences along the magnetic dip equator. These may be due to external contributions. The prediction given at the Earth's surface by four largest coefficient differences (g_1^0, h_1^1, g_5^0 and h_5^1), explains 55% of the signal of the differences between CHAOS-5 and model VO-ESD_16.30-10-2, as it can be seen in Fig. 5.15. The result is similar for VO-ESD_16.30-10-5 and VO-ESD_18.30-10-2.

Contrary to the case of the main field, the subtraction of the first two periods to the input data (with the computation of the VO-ESD_16 models) leads to a slight increase of the difference between the model and the CHAOS-5 for the secular variation spectrum (Fig. 5.5). The differences are more important for the 16-period models for all SH degrees $n \leq 8$. The differences coefficient by coefficient (Fig. 5.11) do not shown any particular pattern. The differences between these models are smaller than 1 nT for all coefficients but three, and reaches almost 2 nT for coefficient g_2^0. For the 18-period model the differences exceed 1 nT only for coefficient

h_2^1.

The difference between the 6-period models separated by six periods of 30 days (thus not overlapping in time) is also computed, in an attempt to evaluate a possible secular variation. There are seven such models. Each model is computed at its mean data time. Figure 5.16 shows the difference between VO-ESD_6.T01 and VO-ESD_6.T13, thus corresponding to the difference of the field during one year. Figure 5.17 shows the difference computed between the models VO-ESD_6.T03 and VO-ESD_6.T09 at their data mean time. Color scales on Figs. 5.16 and 5.17 differ by a factor of 2, to highlight the similitude of the patterns of magnetic field changes for all magnetic components as well as for the field intensity. The differences during one year are twice as large, as expected. This result is similar when looking at the differences between other 6-period models separated by six periods (not shown). Strong variations are seen above the Indian Ocean, North America, south-east Asia and south of Atlantic. The secular variation predicted by model VO-ESD_16.30-10-2 (Fig. 5.18) at the epoch (2014.66) is similar to the difference between models shown in Fig. 5.16.

Because of the spurious behaviour of the residuals and spectra associated with the first two 30-day periods and the insignificant change of results with an external field expansion higher than degree 2, the model VO-ESD_16.30-10-2 is the model we consider hereafter. Figure 5.19 shows the radial component and its secular variation at the CMB and epoch 2014.7 given by the VO-ESD_16.30-10-2 model truncated at $n = 13$.

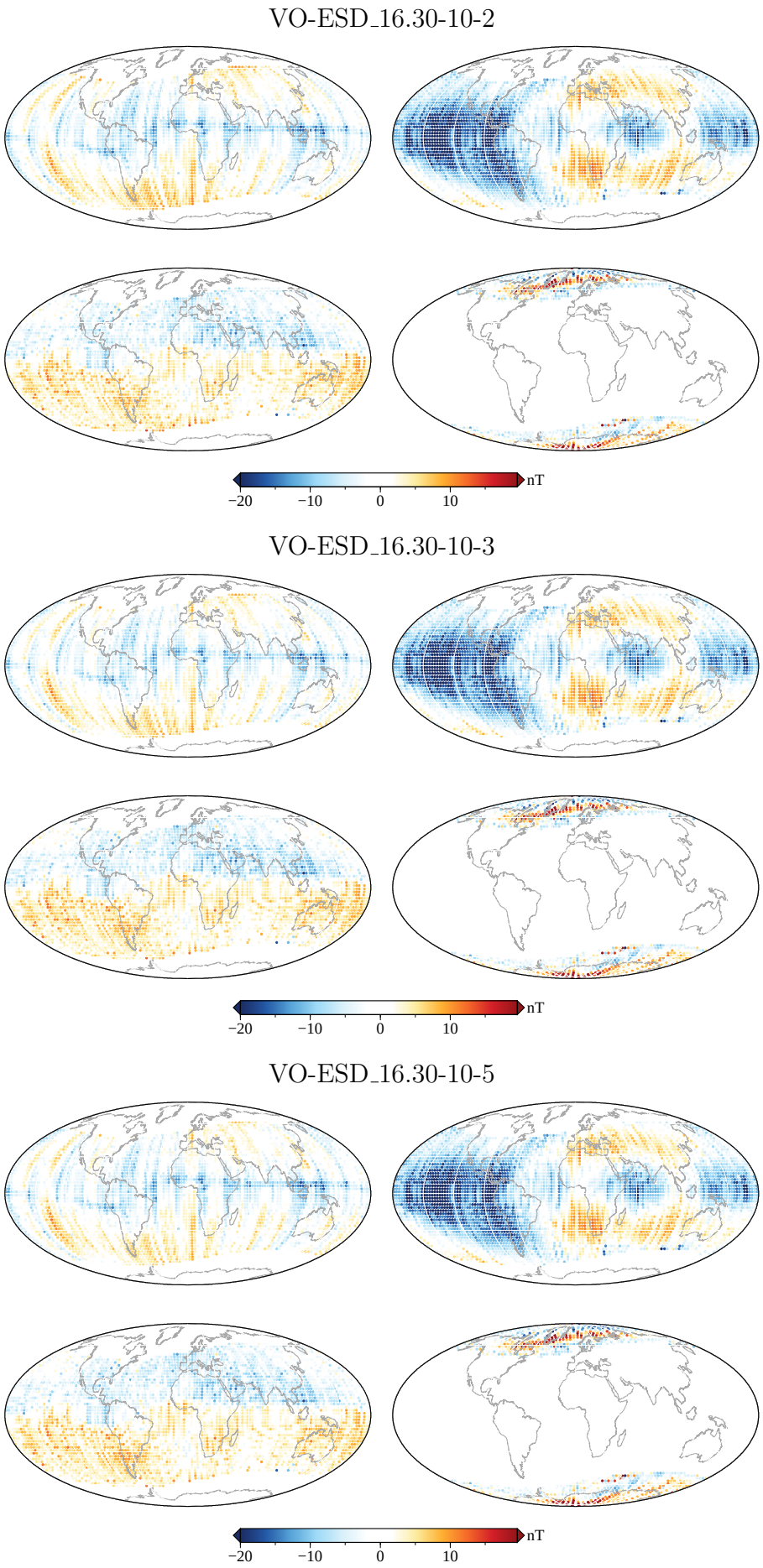

Figure 5.9: As in Fig. 5.8, for models (*top*) VO-ESD_16.30-10-2, (*middle*) VO-ESD_16.30-10-3 and (*bottom*) VO-ESD_16.30-10-5.

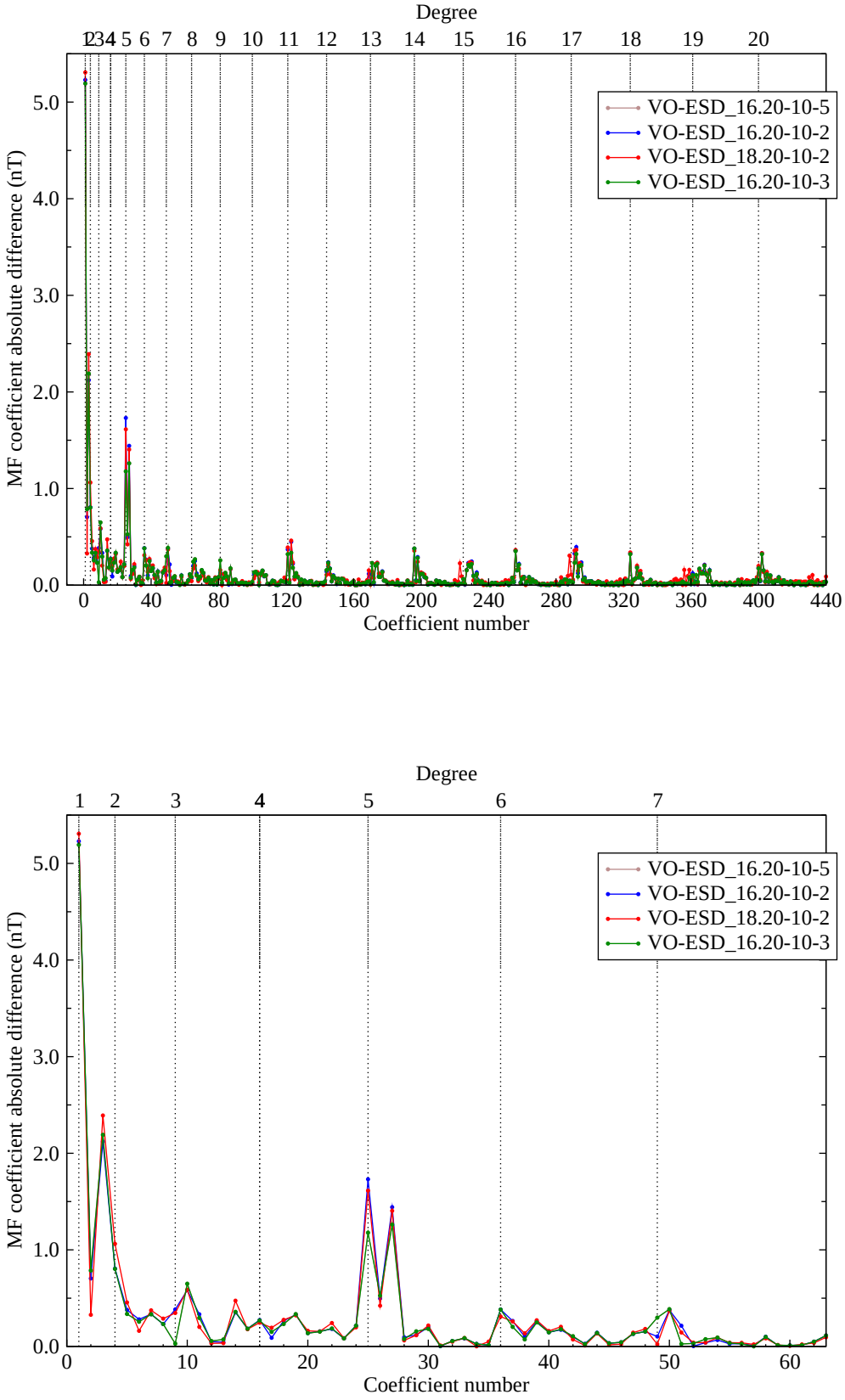

Figure 5.10: Absolute difference of Gauss coefficients between some computed models and the CHAOS-5 model for (*top*) $n \leq 20$ and (*bottom*) $n \leq 7$ at epoch 2014.70. Note that the green and brown curves are superimposed.

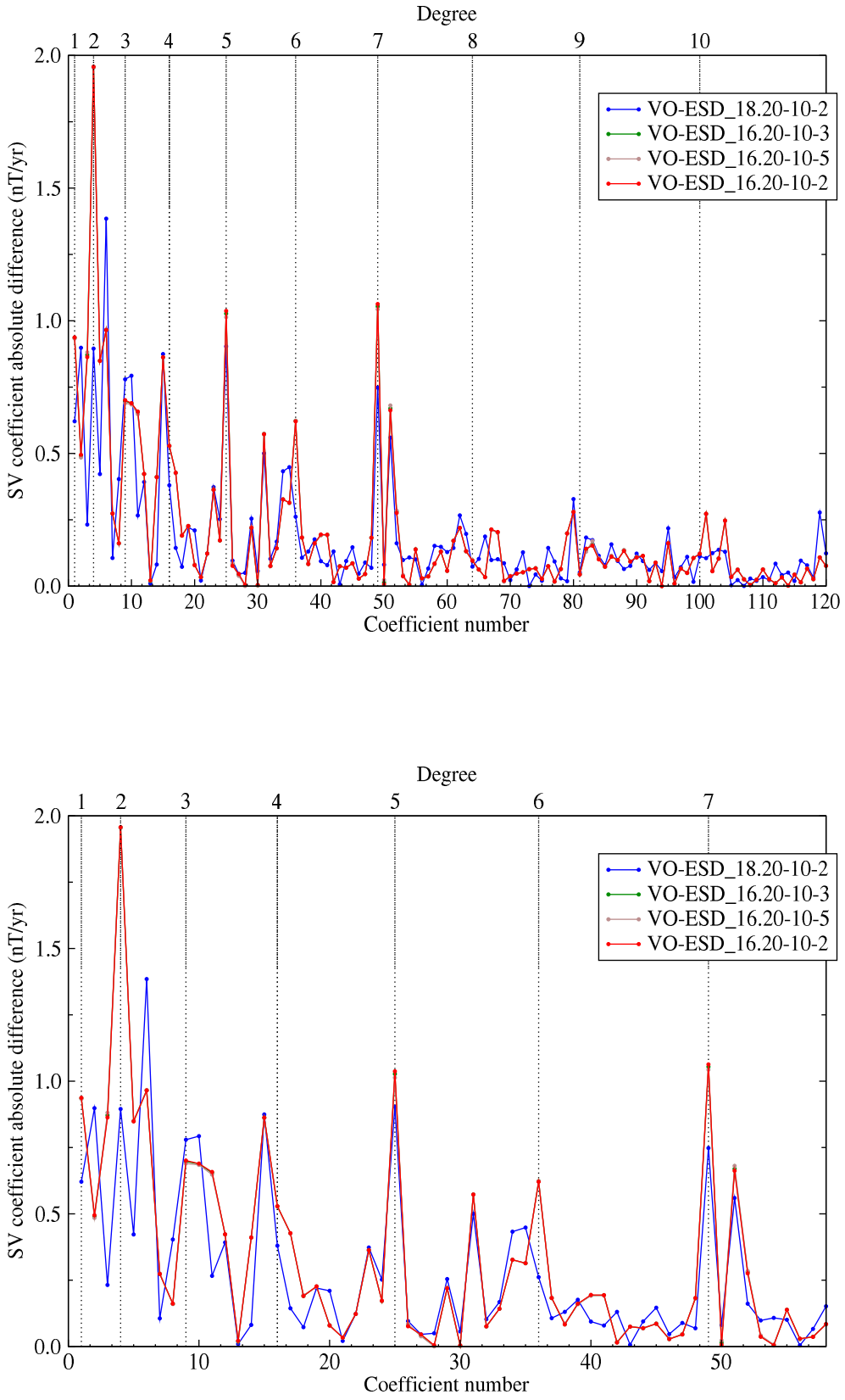

Figure 5.11: Absolute difference of Gauss coefficients between some computed models and the CHAOS-5 model for (*top*) $n \leq 10$ and (*bottom*) $n \leq 7$ at epoch 2014.70. Note that the red, green and brown curves are superimposed.

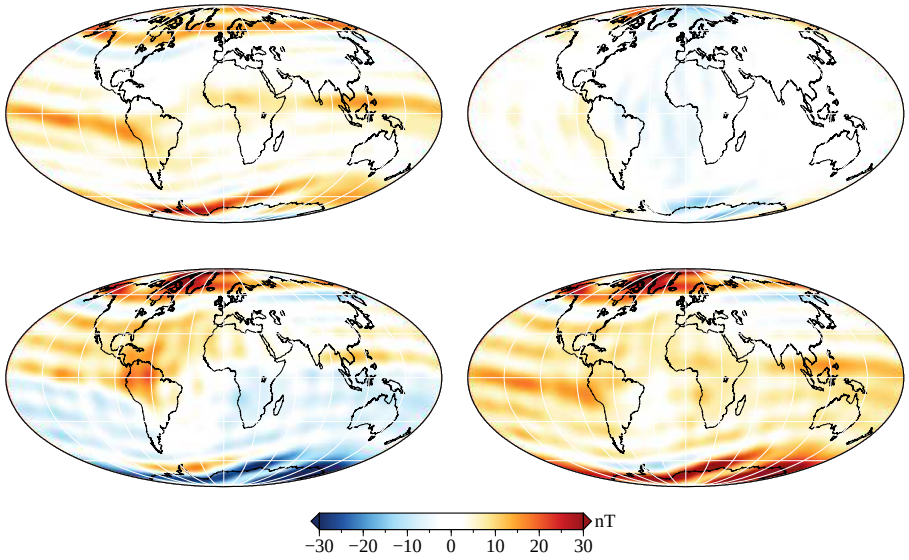

Figure 5.12: Difference at Earth's mean radius between CHAOS-5 and VO-ESD_16.30-10-2 models at epoch 2014.70 and truncated for $n \leq 20$. From (*top left*) to (*bottom right*), X, Y, Z, and F, respectively.

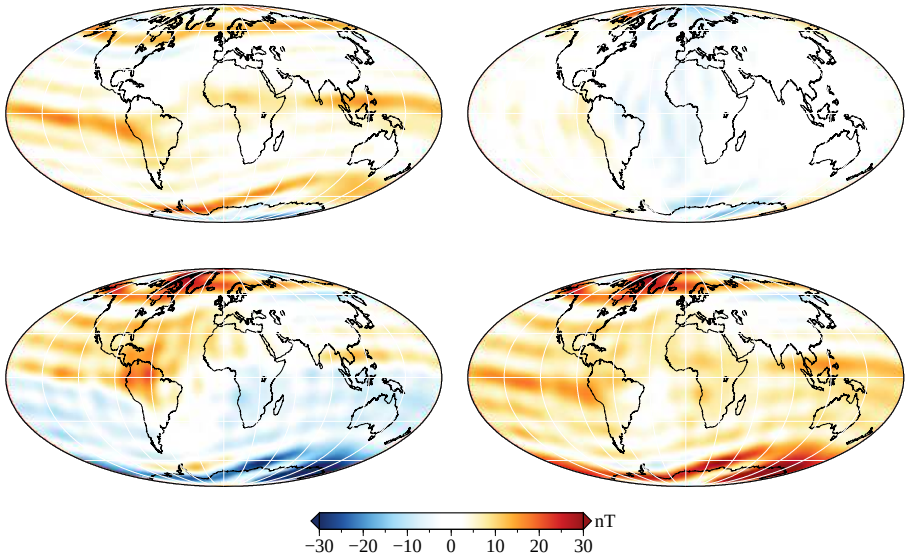

Figure 5.13: Same as Fig. 5.12 between CHAOS-5 and VO-ESD_16.30-10-5.

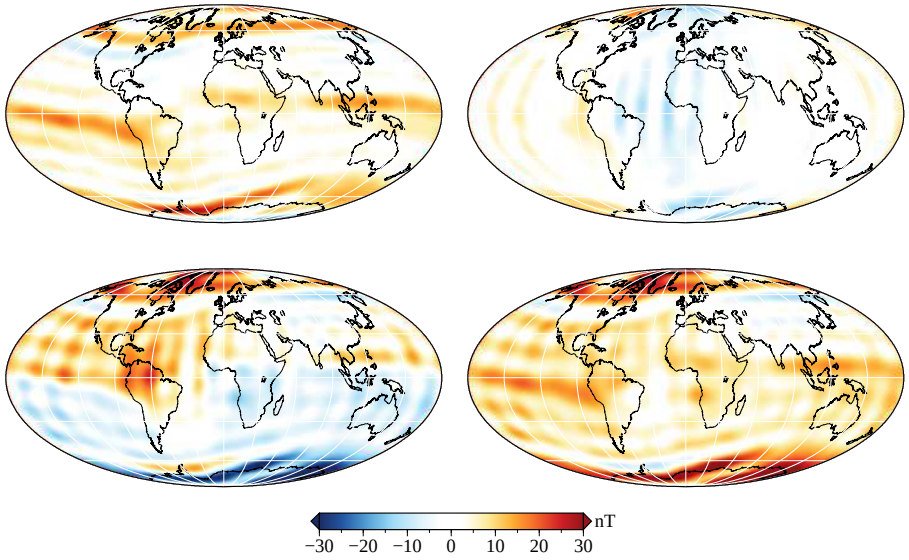

Figure 5.14: Same as Fig. 5.12 between CHAOS-5 and VO-ESD_18.30-10-2.

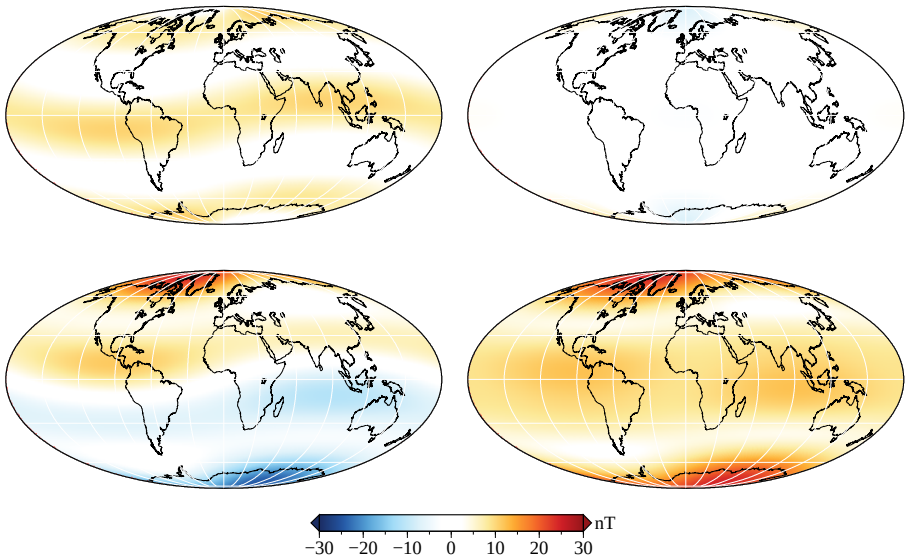

Figure 5.15: Magnetic field given by the differences of the g_1^0, h_1^1, g_5^0 and h_5^1 coefficients between CHAOS-5 and VO-ESD_16.30-10-2 at epoch 2014.70. From (*top left*) to (*bottom right*), X, Y, Z, and F, respectively.

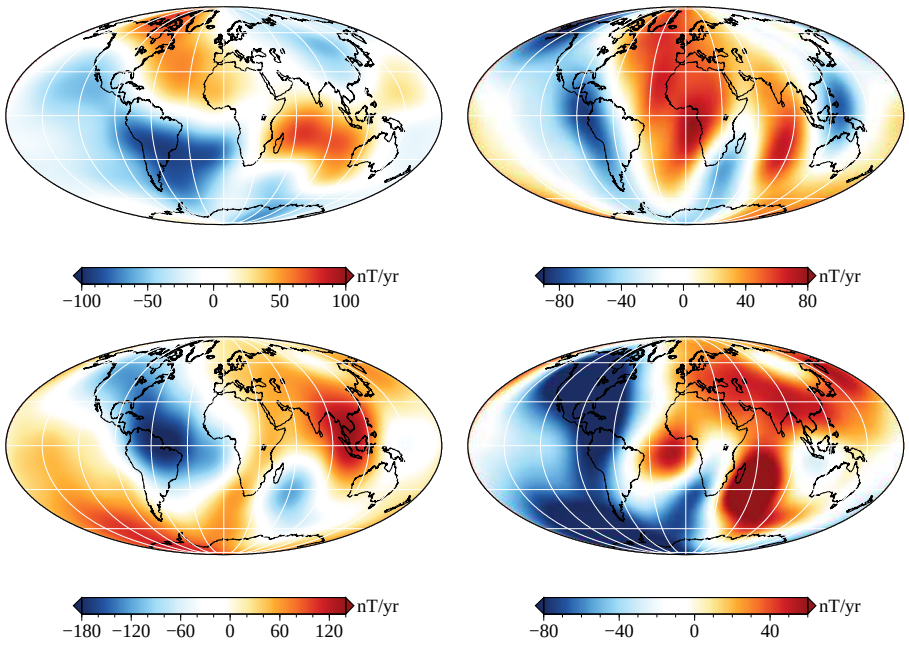

Figure 5.16: Difference between models VO-ESD_6.T01 and VO-ESD_6.T13 at their mean time, corresponding to the variation of the field during one year. From (*top left*) to (*bottom right*), X, Y, Z, and F, respectively.

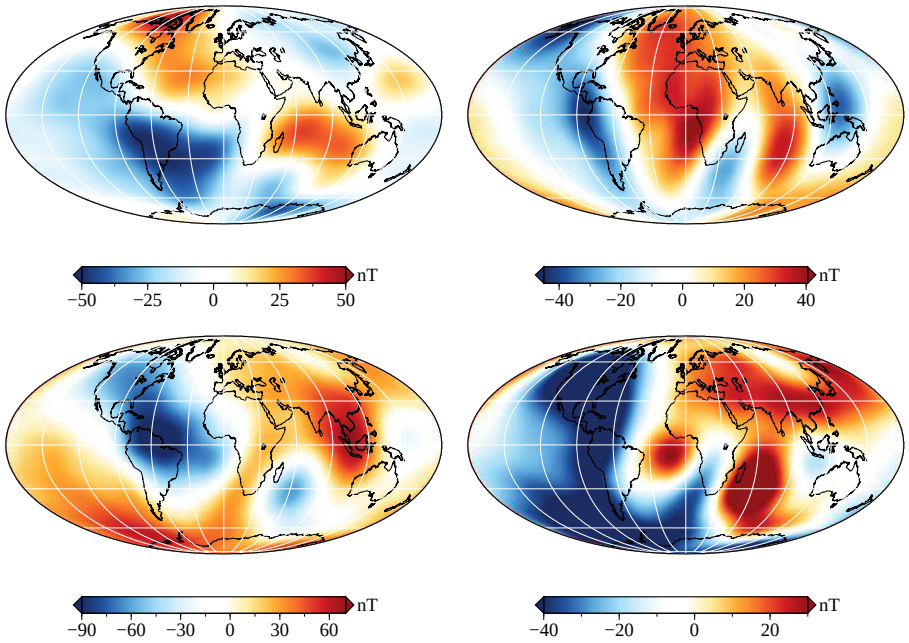

Figure 5.17: Diffference between models VO-ESD_6.T03 and VO-ESD_6.T09 at their mean time, corresponding to the difference during six periods of 30 days (approximately six months). From (*top left*) to (*bottom right*), X, Y, Z, and F, respectively.

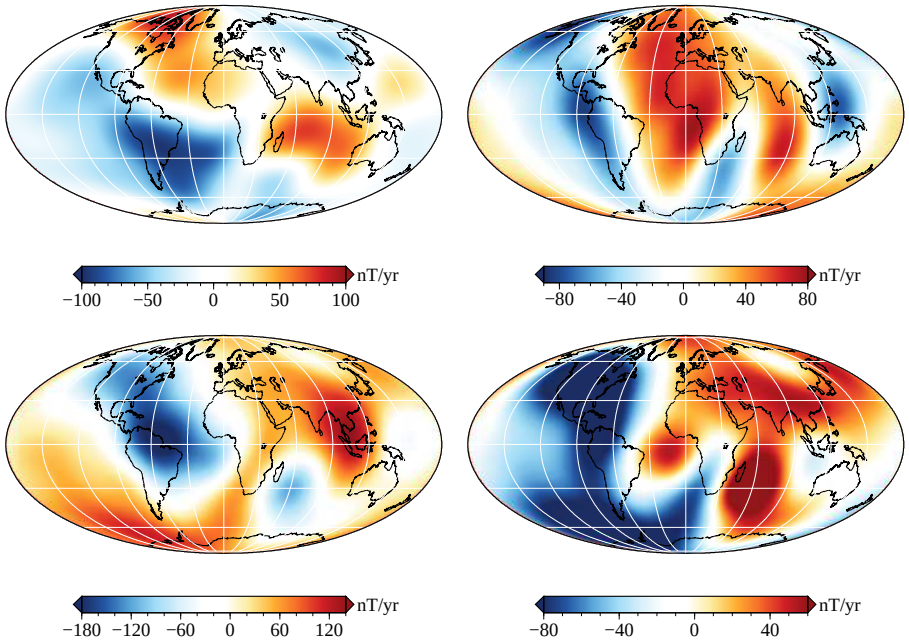

Figure 5.18: Secular variation given by model VO-ESD_16.30-10-2 at epoch 2014.66, which corresponds to the epoch of the difference of Fig. 5.16. From (*top left*) to (*bottom right*), X, Y, Z, and F, respectively.

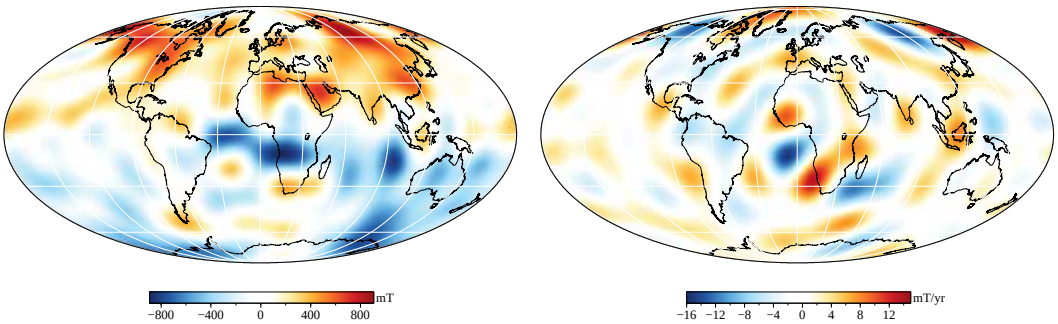

Figure 5.19: Vertical component (Z) of the (*left*) main field and (*right*) secular variation at the CMB as given by the VO-ESD_16.30-10-2 model at epoch 2014.70 and truncated at $n = 13$. From (*top left*) to (*bottom right*), X, Y, Z, and F, respectively.

5.2.2 Fit to observatory monthly means

Magnetic field predictions by the model VO-ESD_16.30-10-2 are compared to observatory monthly mean time series from the same eight ground observatories as in Section 4.4. Also plotted are predictions by the CHAOS-5 model until the end of 2014. The y axis are not identical for both measurements and model predictions as observatory crustal biases are not subtracted from the monthly means.

For all observatories the X component presents the higher variability in time. A constant secular variation may be not adequate for this component. On the contrary, an almost constant value of secular variation seems adequate for the Y component in all observatories and for Z component in some observatories (like ESK or CZT). An increase of the X component of the field is observed at the beginning of 2014 (around 2014.2-2014.4) at CLF, DOU, FUR, ESK and HAD, of about 20 nT. Another increase is observed at the same component at the end of 2014 for CLF, DOU, ESK, HAD and LER. At the same time a strong increase is also seen in the vertical component on HAD, LER and DRV observatories, of about 30 nT. These rapid variations are not described by our constant secular variation nor by the CHAOS-5 model.

Table 5.2 presents secular variation trends computed directly from the eight monthly means observatories and from the predictions by model VO-ESD_16.30-10-2, for each magnetic component. Values associated with the CHAOS-5 model are taken as the mean secular variation predicted in 2014 only. These comparisons aim only to test whether VO-ESD_16.30-10-2 is capable to describe the general trend of the field at the ground. For observatories CLF, DOU and DRV the trends from the VO-ESD_16.30-10-2 model and all observatories monthly means are very alike, especially for the Y component. But for ESK and HAD the trends are different, for example in the X component in HAD. For most cases, the estimation for the vertical component is more distant from the observations than the ones for the horizontal components.

Overall the VO-ESD model describes relatively well the trend of the magnetic field at the surface. Furthermore, this description is slightly better than CHAOS-5 for the 2014 trend. The time series of data used for the VO-ESD_16.30-10-2 models helps to constrain the trend

of the field up to the end of the considered period, and leads to changes of the trend. Nearby observatories trends are described slightly differently by our model when compared to CHAOS-5, following more closely the observed monthly means. For example, the Y component monthly means trend at CLF and DOU differ by about 1 nT.yr^{-1}. The corresponding trends given by our model differ only 1.5 nT.yr^{-1} (see Table 5.2). A similar comparison can be made with HAD and LER observatories.

Table 5.2: Linear secular variation (first time derivative, in nT.yr^{-1}) for the considered ground observatories monthly means time series (O(all)) and given by model VO-ESD_16.30-10-2 (M16) for the period 2013.9-2015.4; by CHAOS-5 model (CH) and for the observatory montly means (O(12)) for the year 2014 (cf. Table 4.2).

Obs.	dX/dt				dY/dt				dZ/dt			
	O(all)	M16	O(12)	CH	O(all)	M16	O(12)	CH	O(all)	M16	O(12)	CH
CLF	7.7	13.2	4.7	21.1	53.4	53.4	52.4	70.5	28.9	21.4	27.8	26.8
DOU	4.0	9.3	0.8	16.3	52.4	51.7	49.6	68.4	29.8	23.5	31.2	31.4
FUR	-4.8	5.9	-2.9	12.2	49.7	48.6	44.9	64.0	39.9	29.9	35.0	38.5
ESK	20.6	13.7	6.4	19.8	56.2	54.9	53.3	73.1	22.1	14.4	26.1	23.4
HAD	-0.1	16.3	10.0	25.2	57.2	56.7	55.8	75.0	28.6	13.5	22.6	18.2
LER	22.9	13.1	-0.1	13.3	53.7	52.5	52.5	70.8	23.7	16.7	30.2	28.5
DRV	-15.9	-20.8	1.9	-27.7	44.5	45.8	41.2	63.2	12.6	13.1	21.2	8.5
CZT	-36.6	-39.9	-34.0	-42.2	-31.9	-35.0	-65.8	-45.2	-80.1	-66.6	-65.8	-101.5

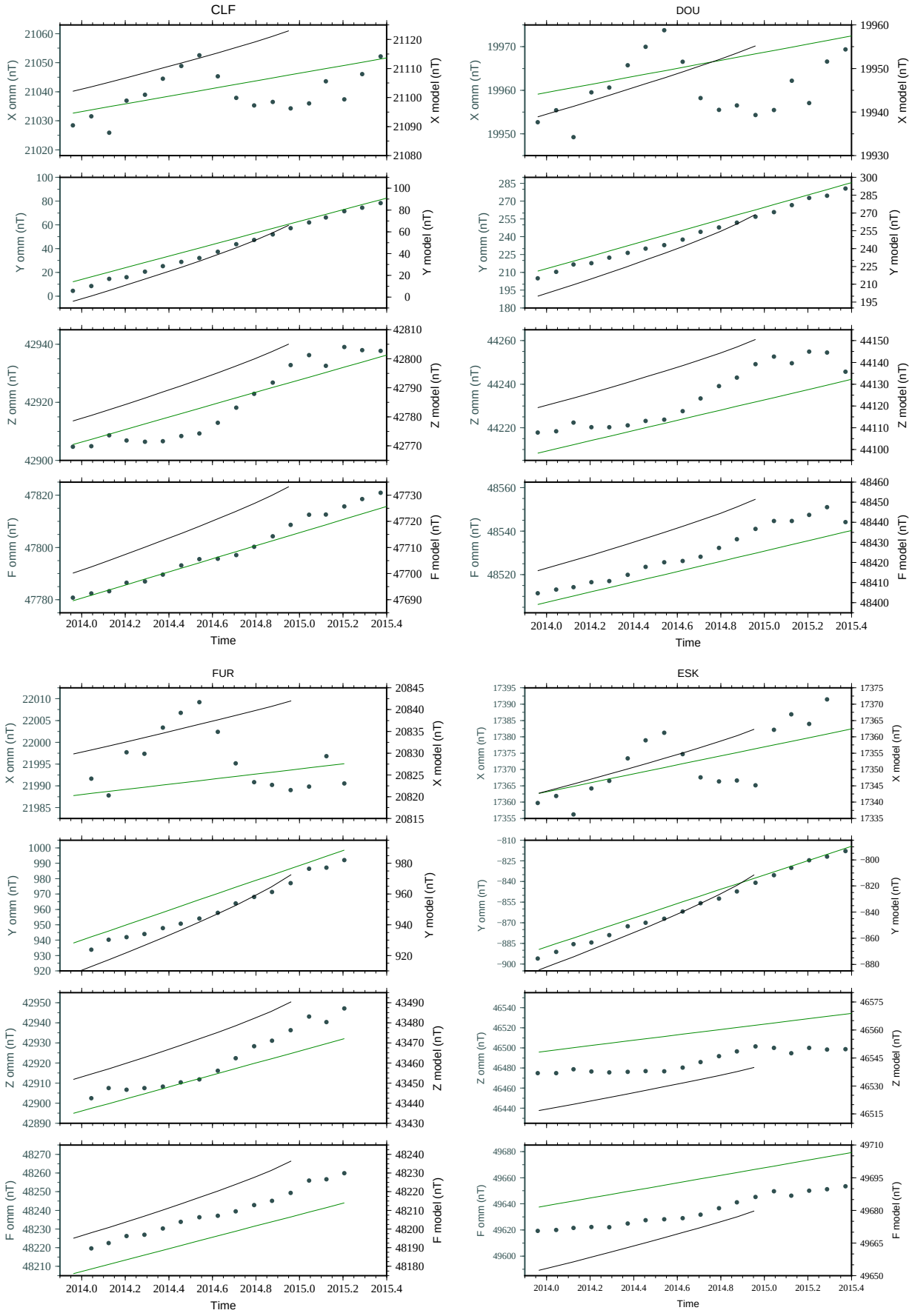

Figure 5.20: Observatory monthly means (*black dots and left axis*) and model CHAOS-5 (*black line and right axis*) and VO-ESD_16.30-10-2 (*green line and right axis*) at ground observatory locations (Table 5.2). Left and right axis have both the same scale range for each component and observatory.

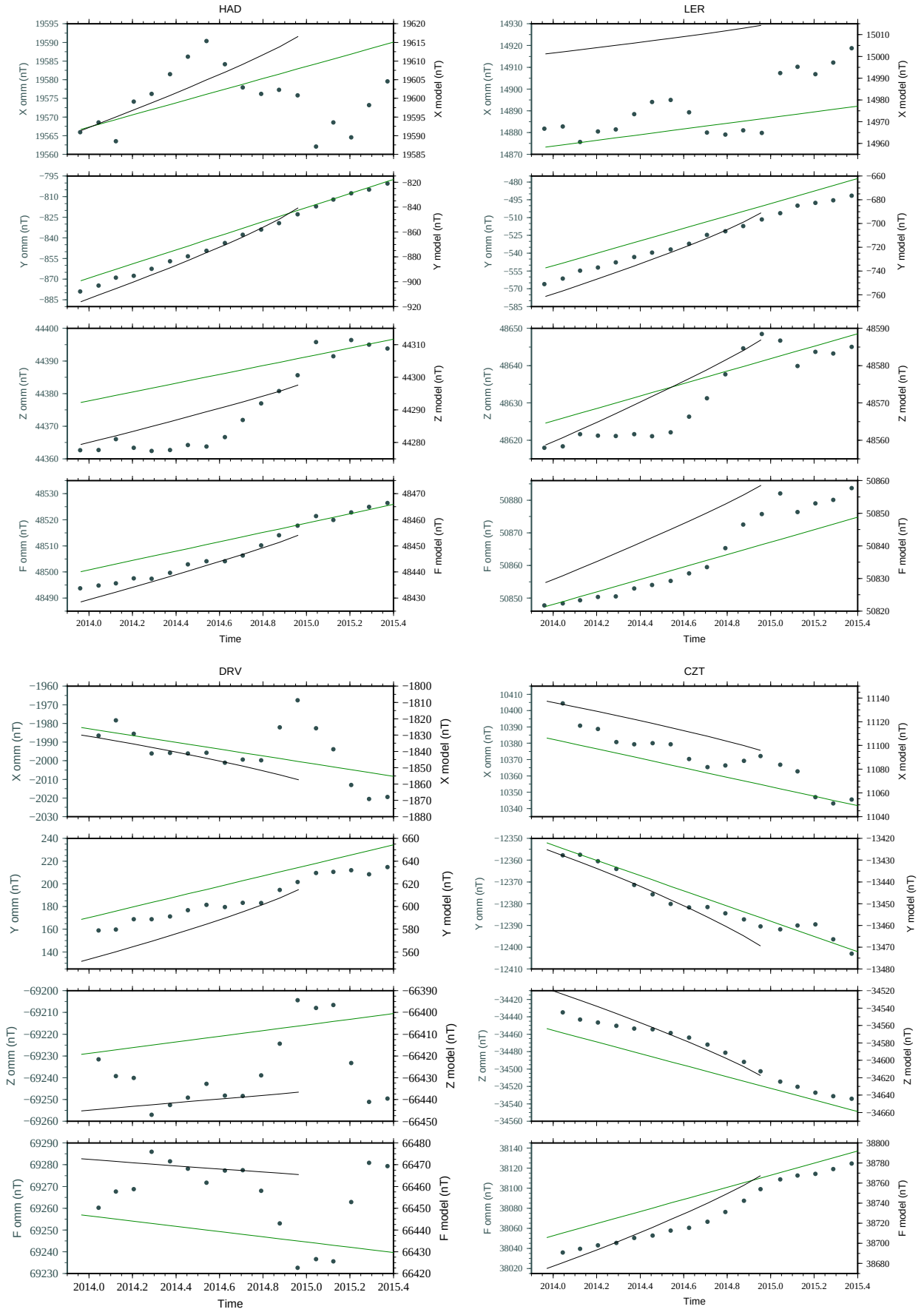

Figure 5.20: (cont.)

5.3 Discussion and conclusions

From the VO-ESD derived time series global models are computed, using a simple parametrization with spherical harmonics. We observe some differences with respect to CHAOS-5 which are discussed below.

The first two 30-day periods (approximately 60 days) of Swarm measurements and corresponding VO-ESD time series are found to be not adequate to the elaboration of a global field model. This may be related to satellite manoeuvres (altitude changes and operations), which were frequent during that period and already mentioned in the previous chapter 4.7.

Residuals between VO-ESD input data and the longer period models VO-ESD_18 and VO-ESD_16, present an equatorial antisymmetry in the vertical component. This antisymmetry is not seen for the snapshot models neither for the other magnetic components. This means that these features are not present in the data for short periods or that they are modelled as internal field in the snapshot models. Residuals at the polar areas, for the field intensity (magnetic latitude above 55^o) are always larger than for other components and latitudes, as it is often the case for satellite based models (Finlay et al., 2015).

The spatial pattern of differences between CHAOS-5 and our models, like VO-ESD_16.30-10-2, is explained mostly by differences in the coefficients g_1^0, h_1^1, g_5^0 and h_5^1 (Fig. 5.15). This may be connected with the referred antisymmetry of the vertical component residuals of the VO-ESD_18 and VO-ESD_16 models. This is illustrated when looking at some candidate models of the magnetic field at epoch 2015.0 for the IGRF-12 (Thébault et al., 2015a). All these candidates used different data sets as well as different modelling strategies. For instance, the candidate model by the IZMIRAN team is the only model using both day and night time magnetic field measurements. It presents large differences from the mean of the candidate models, the largest one being for g_5^0 (see Fig. 5 of Thébault et al., 2015a). It also presents spatial structures of residuals (to the mean model) at low latitudes. These were suggested to be due to the ionospheric equatorial electrojet (EEJ). These differences are comparable to the differences between our model and CHAOS-5. Because we also use day and night time data it

is likely that ionospheric EEJ leaks into our internal field model too.

The model by ISTerre team (Gillet et al., 2015) presents a significant deviation for SH degree 1 (Thébault et al., 2015a). This candidate model is derived from a rather complex parametrization for the internal field, but its external field is explained by a single coefficient, the axial dipole in geomagnetic coordinates. Thus the commonly used Dst dependence (see Eq. 2 of Saturnino et al., 2015) is not applied. This simple parametrization of the external component may be related with the higher differences observed for degree 1. Our model does have an external contribution parametrization up to degree 2 or more, but without data selection nor Dst dependence. The observed differences of our model with respect to CHAOS-5, as well as those between the ISTerre candidate models and the mean of candidate models, may be connected with this.

Regarding the internal field, the secular variation is constrained up to SH degree $n = 10$ with the available eighteen points of the VO-ESD time series. This period is probably too short to constrain the SV to higher degrees. Nevertheless VO-ESD_16.30-10-2 model can describe the trend of the magnetic field at the surface.

If one goes deeper, a possible direct application of the model is to estimate the radius of the outer core, following Langlais et al. (2014). They propose two new expressions to model the spatial power spectrum of the magnetic field at the CMB and thus to derive an independent estimate of the core radius, using all degrees between 1 and 13. They identified two subfamilies which have a constant magnetic field spectrum at the CMB, the non-zonal ($m \neq 0$) and the quadrupole ($n + m$ even) families. We show in Table 5.3 estimates of the core radius based on our model VO-ESD_16.30-10-2, the CHAOS-5 model coefficients at epoch 2014.7 and the IGRF-12 model coefficients at epoch 2015.0. The commonly adopted radius from seismic studies is 3481.7 km (Dziewonski and Anderson, 1981). The core radius estimated using our model is always smaller and closer to the seismic value than the ones obtained from the other two models, with differences ranging between 2 and 5 km.

Taking into account the possible external field issues, as well as the similarity between observed and predicted SV trends, we nonetheless conclude that our VO time series can be used to

Table 5.3: Core radius estimates (in km) given by the two expressions proposed by Langlais et al. (2014) and the VO-ESD_16.30-10-2, CHAOS-5 and IGRF-12 field models.

Model	Non-zonal family	Quadrupole family
VO-ESD_16.30-10-2	3483.3	3491.8
CHAOS-5	3486.4	3493.3
IGRF-12	3487.6	3497.3

compute global SH geomagnetic field models. Our first models use a simple parametrization. No data selection is applied and all day and night satellite measurements are used. The external field contributions description does not take into account the Dst dependence (magnetosphere) nor the ionospheric currents. The secular variation is described as constant and up to degree 10.

Chapter 6

General conclusions and perspectives

The numerical description of the magnetic field has the difficult task of describing a multitude of sources which overlap on temporal and spatial scales. The geomagnetic field description is an important and essential tool for the understanding of the Earth's interior. It constrains the possible physical processes of core field generation. An accurate description of the spatial variation of the short-term temporal variations can help to constrain the magnetic core field generation.

Through this work a new approach to process magnetic satellite measurements has been proposed, validated and applied to the first Swarm satellite measurements. It follows the virtual observatories approach, which aims at extracting time series of the SV from satellite data as it would be done at ground observatories. A global and homogeneous distribution of time series of the field temporal changes is then obtained. In order to downward or upward continue all satellite measurements to a constant altitude, the Equivalent Source Dipoles (ESD) technique is applied. This technique is widely used to model satellite magnetic data at a regional or global scale, on the Earth or on other planets. It is based on the expression of magnetic field caused by a distribution of magnetic dipoles located below the altitude of the measurements.

The validation of the approach was arduous at the beginning. The initial parameters designed to apply the ESD technique were not adequate. A local dipole mesh placed at a given depth in the Earth is not capable to describe and predict the Earth's complex magnetic field. The

prediction obtained using a local dipole mesh was always inaccurate for the different depth and mesh geometries we tested. A dipole mesh with a hemispherical extent was therefore tested. With a reasonnable number of dipoles (91) placed at the CMB, it is possible to describe and predict the magnetic field observations at satellite altitude. With these parameters, the ESD technique can then be used to process Earth satellite magnetic data at different altitudes and bring them to a fixed one. Furthermore, for a time interval around 30-days (27 days, one calendar month, etc.) the technique is able to predict a "mean" magnetic value at the fixed altitude and at the centre location of the observation volume.

The approach application to Swarm measurements revealed a similar time series behaviour for geographically nearby VOs as it is seen with ground observatories. VO-ESD time series are also similar to the corresponding time series at ground observatories. Good correlations were found between both time series, particularly for Y and Z components of the field. Furthermore, the differences between VO-ESD derived time series and an SH model predictions at satellite altitude are close to the differences between ground observatories and the model predictions at the surface. We conclude that the VO-ESD derived time series are comparable to the ones obtained at the ground.

All satellite measurements without any data selection were used. External field contributions may thus leak into the VO-ESD time series. Particularly at high latitudes, the time series show more rapid variations than at other latitudes. For several VOs the time series also show cyclic variations with a period close to 5 to 6 months. These VO-ESD time series can be used to derive global field models. A B-spline representation proved to be a good description of the local temporal changes of the VO-ESD derived time series.

The first global SH models derived using VO-ESD time series were snapshot models for one or six 30-days periods. From these models we concluded that the use of the first two months of Swarm measurements is not adequate to the elaboration of geomagnetic field models with our approach.

We also built global field models using sixteen or eighteen 30-day periods VO-ESD time series. These models are comparable to CHAOS-5 up to degree 14 for the main field. Using a simple

parametrization, the models are capable to describe the trend of the magnetic field both at satellite altitude and at the Earth's surface. The secular variation is described as constant and up to degree 10. The model using only the last sixteen periods, and with a description of the external field up to degree 2, has rms residuals between 5.9 and 9.8 nT. However external contributions are still visible in the computed models. They correspond to differences between our models and CHAOS-5 model in degrees 1 and 5 coefficients. They are associated with spatial patterns which may be caused by the ionospheric Sq and EEJ variations and the magnetospheric axial dipole which leak into our model. From these results it is concluded that the no data selection option may not be adequate.

There remain open questions about the technique implementation. We have however some ideas about how tackle these. These questions and possible ways for data treatment or for different utilisation of the obtained VO-ESD predictions are presented below.

Data selection to reduce external contribution

The description of the external fields should be more adequate. A data selection can be made to the initial satellite measurements before the application of the VO-ESD approach. This is important especially for the polar and dip equator areas where the magnetic field has great contributions from the external electrical currents.

One option is to select only night time measurements, which contain fewer ionospheric contributions (Olsen et al., 2005a). Another is to select quiet time data using geomagnetic indices (Olsen et al., 2006b; Lesur et al., 2008). One additional possibility is to used an a priori correction for the external field with or without a dependence on the Dst. This correction would allow to subtract part of the external field signal from the measurements before the application of the ESD technique.

All these options but the last one have the disadvantage of reducing the number of observations for a given VO. This implies that in order to be able to perform the inversion for 91 dipoles, longer time intervals (more than 30 days) or larger VO surface (larger than a circle of 3^o) would be needed.

Definition of the VO altitude and other parameters

The global mesh of virtual observatories constructed during this work does not have a constant altitude, due to the differences of the Swarm satellites orbits between the first months and remaining of the mission. Still, each VO has a constant altitude. The altitude dependence on the latitude of the VO may include a bias in the global model constructed with the VO-ESD time series. This possibility has not yet been tested. A different approach will be to define a constant altitude for all VOs, as at the beginning of the validation process. For the specific case of Swarm measurements this can be achieved if only the measurements after the second month are used. A longer time interval of measurements (i.e., after mid 2015) will allow to exclude the first two months of the Swarm mission and construct a VO global mesh at constant altitude.

Other parameters that could be still tested are the size and density of the VO mesh, i.e., the distance between each VO centre or the mesh geometry, e.g., a regular mesh in latitude and longitude, not constant in area. Does the distribution of the VO centres influence global models derived from VO-ESD time series?

Application to other measurements

The VO-ESD approach can obviously be applied to other past satellite mission measurements. A comparison with the VO mesh time series obtained by Olsen and Mandea (2007) may be performed for the CHAMP and Ørsted satellites measurements. The two altitude layers of both satellites allow to apply our VO-ESD approach for the same time period. Olsen and Mandea (2007) only used CHAMP data therefore they needed an a priori model to reduce the measurements to a constant altitude.

Mandea and Olsen (2006) computed correlations between their obtained time series of the secular variation at satellite altitude and at ground observatories. They found significant correlations for the dX/dt and dZ/dt components, whereas the correlations for dY/dt were not significant. The same kind of correlations cannot yet be computed for our VO-ESD time series, as the number of points (18) is still short. However, based on the computed correlations for the field time series, we may expect to obtain good correlations for the three magnetic components

of the secular variation. This is supported by the observation that the annual tendency of the temporal variation of the field is also alike between the ground observatories and the respective VO predictions.

Global models parametrization

The VO-ESD approach may show more interesting results for a longer time series of satellite data. The secular variation would be better constrained in global field models and time series of the SV could then be compared with the ones at ground observatories. The VO-ESD time series can be described locally by B-splines. The obtained series can then be used to construct a global field model.

A global field model can also be estimated using not only VO-ESD time series but also ground magnetic observatories time series. The separation of internal and external contributions could then be made using the two altitudes of measurements, i.e., surface and satellite. Again, a special care should be made concerning the ionospheric contribution. This contribution is confined to a region between ground observatories and satellite measurements. This could be used to separate it from other signals within the data, following the proposed methods of comprehensive models, e.g., Sabaka et al. (2002).

Other applications of the approach

The approach developed during this work has the purpose of better constraining locally the secular variation of the magnetic field as it is done at ground observatories. An utilization of this would be the study of magnetic field features like geomagnetic jerks. The global mesh of virtual observatories would allow to study locally the secular variation of the field on a global scale, which can not be done with current ground based observatories, due to their uneven spatial distribution. The use of VO-ESD time series from the following months/years may help to confirm or not the occurrence of the 2014 jerk as proposed by Torta et al. (2015).

Another application of this approach is the derivation of core flow models from the VO-ESD secular variation time series, following the work of Beggan et al. (2009). However, an adequate

description and separation of the external contributions should be done before this application.

Finally, the VO-ESD approach can also be applied to satellite measurements from other planets, and help the study of the spatial and temporal variations of their magnetic field.

Appendix A

Inverse problem

Given a set of observations of the geomagnetic field one seeks to determine the source responsible for those observations. This consists of an inverse problem. The searched source is the scalar potential given by Gauss coefficients. Here the classical expressions for this inverse problem are described.

Let $C(p; r, \theta, \phi, t)$ represent any component of the magnetic field (X, Y, Z, I, D, F or H) where p is the set of parameters (g_n^m,h_n^m,q_n^m,s_n^m) to be solved for and $(\mathbf{r}, t) = (r, \theta, \phi, t)$ the coordinates in time and space (Langel, 1987). For each measure C_i we seek, in a least squares process, to minimize the cost function

$$\Upsilon^2 = \sum_i \left[C_i - C(p; \mathbf{r}_i)\right]^2 w_i \tag{A.1}$$

with respect to p and where w_i represents the weighting factor for each measure. C is expanded around an approximate solution C_0, in a Taylor expansion, where all but the linear term is neglected:

$$C(p; \mathbf{r}_i) \simeq C_0 - \sum_{k=1}^{n} \left(\frac{\partial C(\mathbf{r}_i)}{\partial p_k} \right)_{p_0} \delta_{p_k} \tag{A.2}$$

giving

$$\Upsilon^2 = \sum_i \left[C_i - C_0 - \sum_{k=1}^{n} \left(\frac{\partial C(\mathbf{r}_i)}{\partial p_k} \right)_{p_0} \delta_{p_k} \right]^2 w_i. \tag{A.3}$$

One seeks the solution

$$\left(\frac{\partial \Upsilon^2}{\partial p_k}\right)_{p_k} \simeq \left(\frac{\partial \Upsilon^2}{\partial p_k}\right)_{p_0} = 0 \tag{A.4}$$

from which come n normal equations

$$\sum_{j=1}^{n} \delta_{p_j} \sum_i \left(\frac{\partial C}{\partial p_j}\right)_{p_0} \left(\frac{\partial C}{\partial p_k}\right)_{p_0} w_i = \sum_i (C_i - C_0) \left(\frac{\partial C}{\partial p_k}\right)_{p_0} w_i, \qquad k = 1, ..., n. \tag{A.5}$$

In matrix notation, let $\mathbf{C}$ be a vector column of the measurements, $\delta\mathbf{c}$ the column vector of the differences $C_i - C_0$, $\mathbf{p}$ the column vector of the spherical harmonic coefficients to be determined, $\mathbf{A}$ the matrix of partial derivatives

$$A_{ij} = \left(\frac{\partial \mathbf{C}(\mathbf{r}_i)}{\partial p_j}\right)_{p_0}, \tag{A.6}$$

and $\mathbf{W}$ the weights

$$W_{ij} = w_i \delta_{ij}, \tag{A.7}$$

the normal equations will then come as

$$(\mathbf{A}^T \mathbf{W} \mathbf{A}) \delta\mathbf{p} = \mathbf{A}^T \mathbf{W} \delta\mathbf{c} \tag{A.8}$$

with solution

$$\delta\mathbf{p} = (\mathbf{A}^T \mathbf{W} \mathbf{A})^{-1} \mathbf{A}^T \mathbf{W} \delta\mathbf{c}. \tag{A.9}$$

An a priori estimate of the Gauss coefficients, $\mathbf{p}_0$, is considered. The choice of this initial set of parameters has no effect on the final result as long as it is close enough to the actual field, such as a model at a different epoch (see e.g., Langlais et al., 2003). Hence the problem is solved by an iterative inversion scheme. An a priori covariance matrix $\mathbf{\Omega}_0$ can also be included:

$$\delta\mathbf{p}_{n+1} = (\mathbf{A}^T \mathbf{W} \mathbf{A} + \mathbf{\Omega}_0^{-1})^{-1} [\mathbf{A}^T \mathbf{W} \delta\mathbf{c}_n + \mathbf{\Omega}_0^{-1} (\mathbf{p}_0 - \mathbf{p}_n)], \tag{A.10}$$

where the estimate at the $(n+1)$th iteration is

$$\mathbf{p}_{n+1} = \mathbf{p}_n + \delta\mathbf{p}_{n+1}. \tag{A.11}$$

For spherical coordinates the A_{ij} can be found directly from Eq. 2.16, for e.g.:

$$\frac{\partial B_r}{\partial g_n^m} = \left(\frac{a}{r}\right)^{n\,+2} (n+1)\cos(m\phi)P_n^m(\theta). \tag{A.12}$$

The magnetic components X, Y and Z are linearly related to the Gauss coefficients, as the Eq. A.12 shows, however that is not the case of all the others (D, I, H and F), which poses a nonlinear inverse problem. They must be derived from the partials of $\mathbf{A}$ (e.g., the partial of Eq. A.12) and using the relations already presented in Section 1.2.

The expressions for the inverse problem described here are valid for the internal and external potentials.

Appendix B

Appendix

B.1 International Geomagnetic Reference Field: the 12th generation

The article concerning the 12th generation of the IGRF model is reproduced here.

Thébault *et al. Earth, Planets and Space* (2015) 67:79
DOI 10.1186/s40623-015-0228-9

Earth, Planets and Space
a SpringerOpen Journal

LETTER Open Access

International Geomagnetic Reference Field: the 12th generation

Erwan Thébault[1*], Christopher C Finlay[2], Ciarán D Beggan[3], Patrick Alken[4,5], Julien Aubert[6], Olivier Barrois[7], Francois Bertrand[8,9], Tatiana Bondar[10], Axel Boness[8,9], Laura Brocco[6], Elisabeth Canet[11], Aude Chambodut[12], Arnaud Chulliat[4,5], Pierdavide Coïsson[6], François Civet[1], Aimin Du[13], Alexandre Fournier[6], Isabelle Fratter[14], Nicolas Gillet[7], Brian Hamilton[3], Mohamed Hamoudi[15,19], Gauthier Hulot[6], Thomas Jager[8,9], Monika Korte[15], Weijia Kuang[16], Xavier Lalanne[6], Benoit Langlais[1], Jean-Michel Léger[8,9], Vincent Lesur[15], Frank J Lowes[17], Susan Macmillan[3], Mioara Mandea[18], Chandrasekharan Manoj[4,5], Stefan Maus[4], Nils Olsen[2], Valeriy Petrov[10], Victoria Ridley[3], Martin Rother[15], Terence J Sabaka[16], Diana Saturnino[1], Reyko Schachtschneider[15], Olivier Sirol[6], Andrew Tangborn[20], Alan Thomson[3], Lars Tøffner-Clausen[2], Pierre Vigneron[6], Ingo Wardinski[15] and Tatiana Zvereva[10]

Abstract

The 12th generation of the International Geomagnetic Reference Field (IGRF) was adopted in December 2014 by the Working Group V-MOD appointed by the International Association of Geomagnetism and Aeronomy (IAGA). It updates the previous IGRF generation with a definitive main field model for epoch 2010.0, a main field model for epoch 2015.0, and a linear annual predictive secular variation model for 2015.0-2020.0. Here, we present the equations defining the IGRF model, provide the spherical harmonic coefficients, and provide maps of the magnetic declination, inclination, and total intensity for epoch 2015.0 and their predicted rates of change for 2015.0-2020.0. We also update the magnetic pole positions and discuss briefly the latest changes and possible future trends of the Earth's magnetic field.

Keywords: Geomagnetism; Field modeling; IGRF

Correspondence/Findings

Introduction

The International Geomagnetic Reference Field (IGRF) is a series of mathematical models describing the large-scale internal part of the Earth's magnetic field between epochs 1900 A.D. and the present. The IGRF has been maintained and produced by an international team of scientists under the auspices of the International Association of Geomagnetism and Aeronomy (IAGA) since 1965 (Zmuda 1971). It results from a collaborative effort between magnetic field modelers and institutes involved in collecting and disseminating magnetic field data from magnetic observatories (see the Appendix for the list of World Data Centers), ground surveys, and low Earth orbiting (LEO) satellites. The IGRF is used by scientists in a wide variety of studies, for instance, concerning the dynamics of the Earth's core field, space weather, or local magnetic anomalies imprinted in the Earth's crust. It is also used by commercial organizations and individuals as a source of orientation information.

The IGRF model must be regularly revised in order to follow the continuous temporal changes of the geomagnetic field generated in the Earth's outer core. The period between revisions is however sufficiently short to preserve its utility as a reference model in applications requiring a fixed reference standard. Table 1 provides the nomenclature and a summary of the history of previous generations of the IGRF. At present, each generation consists of three constituent models. One constituent is designated a Definitive Geomagnetic Reference Field (DGRF). The term 'definitive' is used because any further improvement of these retrospectively determined models is unlikely. The second constituent model, referred to as

*Correspondence: erwan.thebault@univ-nantes.fr
[1] Laboratoire de Planétologie et Géodynamique de Nantes, University of Nantes, UMR 6112 CNRS, 1 chemin de la Houssiniére F-44322, Nantes, France
Full list of author information is available at the end of the article

Table 1 Summary of IGRF generations, their intervals of validity, and related references

Full name	Short name	Valid for	Definitive for	Reference
IGRF 12th generation	IGRF-12	1900.0-2020.0	1945.0-2010.0	Thébault et al., this article
IGRF 11th generation	IGRF-11	1900.0-2015.0	1945.0-2005.0	Finlay et al. (2010a)
IGRF 10th generation	IGRF-10	1900.0-2010.0	1945.0-2000.0	Maus et al. (2005)
IGRF 9th generation	IGRF-9	1900.0-2005.0	1945.0-2000.0	Macmillan et al. (2003)
IGRF 8th generation	IGRF-8	1900.0-2005.0	1945.0-1990.0	Mandea and Macmillan (2000)
IGRF 7th generation	IGRF-7	1900.0-2000.0	1945.0-1990.0	Barton (1997)
IGRF 6th generation	IGRF-6	1945.0-1995.0	1945.0-1985.0	Langel (1992)
IGRF 5th generation	IGRF-5	1945.0-1990.0	1945.0-1980.0	Langel et al. (1988)
IGRF 4th generation	IGRF-4	1945.0-1990.0	1965.0-1980.0	Barraclough (1987)
IGRF 3rd generation	IGRF-3	1965.0-1985.0	1965.0-1975.0	Peddie (1982)
IGRF 2nd generation	IGRF-2	1955.0-1980.0	–	IAGA (1975)
IGRF 1st generation	IGRF-1	1955.0-1975.0	–	Zmuda (1971)

an IGRF model, is non-definitive - it will eventually be replaced by a definitive model in a future revision of the IGRF. The final constituent, referred to as the secular variation (SV), is provided to predict the time variation of the large-scale geomagnetic field for the 5 years following the latest revision of the IGRF. Readers interested in the history of the IGRF should consult Barton (1997), and users can find legacy versions of the IGRF at the online archive located at http://www.ngdc.noaa.gov/IAGA/vmod/igrf_old_models.html. These may prove useful for those wishing to recover data from which a previous generation of the IGRF has been subtracted or who wish to use the latest generation of the IGRF to carry out revised analyses. Here, attention will focus on the most recent 12th-generation IGRF, hereafter referred to as IGRF-12, that provides a DGRF model for epoch 2010.0, an IGRF model for epoch 2015.0, and a predictive SV model covering the epochs 2015.0-2020.0. IGRF-12 was agreed in December 2014 by a task force of the IAGA Working Group V-MOD. The purpose of this note is to document the release of IGRF-12, to act as a permanent published record of the IGRF-12 set of model coefficients, and to briefly describe some major features of the geomagnetic field at the Earth's surface as revealed by the updated model.

Mathematical formulation of the IGRF model

The IGRF is a series of mathematical models of the internal geomagnetic field $\overrightarrow{B}(r,\theta,\phi,t)$ and its annual rate of change (secular variation). On and above the Earth's surface, the magnetic field $\overrightarrow{B}$ is defined in terms of a magnetic scalar potential V by $\overrightarrow{B} = -\nabla V$ and where in spherical polar co-ordinates V is approximated by the finite series

$$V(r,\theta,\phi,t) = a\sum_{n=1}^{N}\sum_{m=0}^{n}\left(\frac{a}{r}\right)^{n+1} \times \left[g_n^m(t)\cos(m\phi) + h_n^m(t)\sin(m\phi)\,P_n^m(\cos\theta)\right], \quad (1)$$

with r denoting the radial distance from the center of the Earth, $a = 6,371.2$ km being the geomagnetic conventional Earth's mean reference spherical radius, θ denoting geocentric co-latitude, and ϕ denoting east longitude. The functions $P_n^m(\cos\theta)$ are the Schmidt quasi-normalized associated Legendre functions of degree n and order m. The Gauss coefficients g_n^m, h_n^m are functions of time and are conventionally given in units of nanotesla (nT).

In the IGRF-12 model, the Gauss coefficients g_n^m and h_n^m are provided for the main field (MF) at epochs separated by 5 years between 1900.0 and 2015.0 A.D. The time dependence of the Gauss coefficients is assumed to be linear over 5-year intervals and is specified by the following expression

$$g_n^m(t) = g_n^m(T_0) + \dot{g}_n^m(T_0).(t - T_0), \quad (2)$$

$$h_n^m(t) = h_n^m(T_0) + \dot{h}_n^m(T_0).(t - T_0), \quad (3)$$

where $\dot{g}_n^m$ $\left(\text{respectively } \dot{h}_n^m\right)$ given in units of nT/year represent the 5-year average first time derivative (the linear secular variation) of the Gauss coefficients. t is the time of interest in units of year and T_0 is the epoch preceding t which is an exact multiple of 5 years, such that $T_0 \le t < (T_0 + 5.0)$. When MF models exist for both T_0 and $T_0 + 5.0$, then coefficients $\dot{g}_n^m(T_0)$ can be computed as $[g_n^m(T_0 + 5.0) - g_n^m(T_0)]/5.0$. For the final 5 years of the model validity (between 2015.0 and 2020.0 for IGRF-12),

Table 2 Magnetic observatories contributing data used in the construction of IGRF-12

Supporting Agencies	Country	Observatory IAGA code
Centre de Recherche en Astronomie, Astrophysique et Geophysique	Algeria	TAM
Universidad Nacional de la Plata	Argentina	TRW
Servicio Meteorologico Nacional	Argentina	ORC
Geoscience Australia	Australia	ASP, CKI, CNB, CSY, CTA, DVS, GNA, GNG, KDU, LRM, MAW, MCQ
Zentralanstalt für Meteorologie und Geodynamik	Austria	WIK
Institut Royal Météorologique	Belgium	DOU, MAB
CNPq-Observatorio Nacional	Brazil	VSS
Academy of Sciences	Bulgaria	PAG
Geological Survey of Canada	Canada	ALE, BLC, CBB, FCC, IQA, MEA, OTT, PBQ, RES, STJ, VIC,YKC
Centro Meteorológico Regional Pacifico	Chile	IPM
Academy of Sciences	China	BMT
China Earthquake Adminstration	China	CDP, GLM, GZH, KSH, LZH, MZL, QGZ, QIX, QZH, SSH, THJ, WHN
Academy of Sciences	Czech Republic	BDV
Danish Technical University-Space	Denmark	TDC
Addis Ababa University	Ethiopia	AAE
Finnish Meteorological Institute	Finland	NUR
Geophysical Observatory	Finland	SOD
Institut de Physique du Globe de Paris	France	AAE, BOX, CLF, KOU, IPM, LZH, MBO, PHU, QSB, PPT, TAM
Ecole et Observatoire des Sciences de la Terre	France	AMS, CZT, DMC, DRV, PAF, TAN
Institut Français de Recherche Scientifique pour le Développement	France	BNG, MBO
Academy of Sciences	Georgia	TFS
Universität München	Germany	FUR
Alfred-Wegener-Institute for Polar Marine Research	Germany	VNA
GFZ Hemholtz Centre Potsdam	Germany	NGK, TDC, WNG
Universität Stuttgart	Germany	BFO
Institute of Geology and Mineral Exploration	Greece	PEG
Academy of Sciences	Hungary	NCK
Eötvös Loránd Geophysical Institute	Hungary	THY
University of Iceland	Iceland	LRV
Indian Institute of Geomagnetism	India	ABG, PND, SIL, TIR, VSK
National Geophysical Research Institute	India	HYB
Meteorological and Geophysical Agency	Indonesia	KPG, PLR, TND
Meteorological Service	Ireland	VAL
Survey of Israel	Israel	AMT, BGY, ELT
Instituto Nazionale di Geofisica e Vulcanologia	Italy	AQU, DMC
Japan Coast Guard	Japan	HTY
Japan Meteorological Agency	Japan	CBI, KAK, KNY, MMB
Geographical Survey Institute	Japan	ESA, KNZ, MIZ
Institute of the Ionosphere	Kazakhstan	AAA

Table 2 Magnetic observatories contributing data used in the construction of IGRF-12 *(Continued)*

National Centre for Geophysical Research	Lebanon	QSB
Université d'Antananarivo	Madagascar	TAN
Gan Meteorological Office/ETH Zurich	Maldives/Switzerland	GAN
Universidad Nacional Autonoma de México	Mexico	TEO
Institute of Geological and Nuclear Sciences	New Zealand	API, EYR, SBA
University of Tromsø	Norway	BJN, DOB, TRO
Instituto Geofisico del Peru	Peru	HUA
Academy of Sciences	Poland	BEL, HLP, HRN
Directorate General of Telecommunications	Republic of China	LNP
Instituto Nacional de Geologia	República de Moçambique	LMM
Geological Survey of Romania	Romania	SUA
Academy of Sciences	Russia	ARS, BOX, LVV, MOS, NVS
Institute of Solar-Terrestrial Physics	Russia	IRT
Dept. of Agriculture, Forestry, Fisheries & Meteorology	Samoa	API
Geomagnetic College Grocka	Serbia and Montenegro	GCK
Slovenska Akademia Vied	Slovakia	HRB
National Research Foundation	South Africa	HBK, HER, KMH, TSU
Observatori de l'Ebre	Spain	EBR, LIV
Real Instituto y Observatorio de la Armada	Spain	SFS
Instituto Geográfico Nacional	Spain	GUI, SPT
Sveriges Geologiska Undersökning	Sweden	ABK, LOV, LYC, UPS
Swedish Institute of Space Physics	Sweden	KIR
Bŏgaziçi University	Turkey	IZN
Academy of Sciences	Ukraine	AIA
British Geological Survey	United Kingdom	ASC, ESK, HAD, JCO, KEP, LER, PST, SBL
US Geological Survey	United States	BRW, BOU, BSL, CMO, DLR, FRD, FRN, GUA HON, NEW, SIT, SJG, SHU, TUC
Academy of Science and Technology	Vietnam	PHU

the coefficients $\dot{g}_n^m(t)$ and $\dot{h}_n^m(t)$ of the predictive average SV are explicitly provided. The geocentric components of the geomagnetic field in the northward, eastward, and radially inwards directions (X, Y and Z) are obtained from the model coefficients using Equation 1 and by taking the gradient of V in spherical polar co-ordinates

$$X = \frac{1}{r}\frac{\partial V}{\partial \theta}, \quad Y = -\frac{1}{r\sin\theta}\frac{\partial V}{\partial \phi}, \quad Z = \frac{\partial V}{\partial r}. \tag{4}$$

For some applications, the declination D, the inclination I, the horizontal intensity H, and the total intensity F are required. These components are calculated from X, Y, and Z using the relations,

$$\begin{aligned} &H = \sqrt{X^2 + Y^2}, \quad F = \sqrt{X^2 + Y^2 + Z^2}, \\ &D = \arctan(Y/X), \quad I = \arctan(Z/H). \end{aligned} \tag{5}$$

In Equation 1, the maximum spherical harmonic degree of the expansion N may vary from one epoch to another. The maximum degree N of the series is equal to 10 up to and including epoch 1995.0 and the coefficients are quoted to 1-nT precision. For epoch 2000, the coefficients are provided to degree and order 13 and quoted to 0.1-nT precision, and from epoch 2005 onwards they are quoted to 0.01-nT precision for the DGRF (and 0.1 nT for the latest non-definitive IGRF), to take advantage of the higher data quality and good coverage provided by the LEO satellite missions (Finlay et al. 2010a). The maximum truncation degree $N = 13$ for epochs after 2000 is defined so as not to include the crustal magnetic field contributions that dominate at higher degrees (see e.g., Langel and Estes 1982).

The predictive SV coefficients $\dot{g}_n^m(t)$ and $\dot{h}_n^m(t)$ are given to degree and order 8 to 0.1-nT/year precision. Because

of these changes in precision and nomenclature, it is recommended to always use the term 'IGRF-gg,' where gg represents the generation, in order to keep track of the coefficients that were actually used in applications. This is a simple way to standardize studies carried out at different epochs that makes it apparent whether the results are 'predictive' and therefore less accurate or 'definitive'. For example, one cannot recover the original full-field measurement from an aeromagnetic anomaly map if one does not know which generation of the IGRF was used. This issue has important consequences when comparing magnetic surveys carried out at different epochs (e.g., Hamoudi et al. 2007; Hemant et al. 2007; Maus et al. 2007).

Equation 1 is expressed in the geocentric system of co-ordinates, but it is sometimes necessary to work in geodetic co-ordinates. When converting between geocentric and geodetic co-ordinates (see for instance Hulot et al. 2007), it is recommended to use the World Geodetic System 1984 (WGS84) datum as present-day satellite magnetic data are often positioned using it. The WGS84 spheroid is defined with major (equatorial) radius A = 6,378.137 km at the equator and a reciprocal flattening f = 1/298.257223563 (the polar semi-minor axis is therefore B = A(1-f)≃6,356.752 km).

The 12th-generation IGRF

IGRF-12, the 12th generation of IGRF, is derived from candidate models prepared by international teams who answered a call issued by the IGRF-12 task force in May 2014. This call requested candidates for the Definitive Geomagnetic Reference Field (DGRF) for epoch 2010, for a provisional IGRF model for epoch 2015, and for a predictive SV model for the interval 2015.0-2020.0. The IGRF-12 model coefficients remain unchanged for epoch 2005 and earlier.

The number of institutions participating in IGRF-12 was larger than for any previous generation. This reflects the constructive effect of open and unconditional cooperation between scientists involved in modeling the magnetic field, the institutions archiving and disseminating the ground magnetic data, and the national and the European space agencies who actively worked to distribute their expertise, computer programs, and magnetic satellite data with documentation. This latter point was especially important for the MF for epoch 2015.0 given the short period that elapsed between the launch of the Swarm satellites (in November 2013) and the submission of IGRF candidate models by October 2014. The European Space Agency provided prompt access to the Swarm satellite measurements, including detailed documentation and information on the operational status of the instruments (https://earth.esa.int/web/guest/missions/esa-operational-eo-missions/swarm). This allowed the teams producing candidate models to rapidly use the Swarm data and helped IGRF-12 to be delivered on time. The collection of ground-based magnetic observatory measurements (see Table 2) and the availability of other satellite measurements, from the CHAMP (Reigber et al. 2002), Ørsted (Neubert et al. 2001) and SAC-C missions, were also crucial for IGRF-12.

Seven candidate MF models for the DGRF epoch 2010.0 and ten candidate MF models for the IGRF epoch 2015.0 were submitted. In addition, nine SV models were submitted for the predictive part covering epochs 2015.0-2020.0. Team A was from BGS, UK (Hamilton et al. 2015); team B was from DTU Space, Denmark (Finlay et al. 2015); team C was led by ISTerre, France, with input from DTU Space (Gillet et al. 2015); team D was from IZMIRAN, Russia; team E was from NGDC/NOAA (Alken et al. 2015); team F was from GFZ, Germany (Lesur et al. 2015); team G was led by GSFC-NASA, USA, in collaboration with UMBC; team H was from IPGP (Fournier et al. 2015; Vigneron et al. 2015), France, in collaboration with the CEA-Léti (Léger et al. 2015) and with input from LPG Nantes and CNES, France; team I was led by LPG Nantes, France (Saturnino et al. 2015) with input from CNES; team J was from ETH Zurich, Switzerland. These teams contributed to all or parts of the three model constituents of IGRF. Following the IGRF specifications, the MF candidate models had a maximum spherical harmonic degree $N = 13$ and the predictive SV model had a maximum spherical harmonic degree $N = 8$.

The final IGRF-12 MF models for epochs 2010.0 and 2015.0 as well as the predictive SV model for 2015.0-2020.0 were calculated using a new weighting scheme of the candidate models. For the previous generation of IGRF, fixed weights were assigned to each candidate model based on information gleaned from the evaluations (see Finlay et al. 2010b, for instance) and most weight was given to those models showing the smallest scatter about the arithmetic mean of the candidate models. For IGRF-12, the evidence for significant systematic errors in one or more models was not thought to be sufficient to reject any of the models. A robust weighting scheme was instead applied to the candidate models in space, as agreed by a vote of the IGRF-12 task force. The specification of the candidate models and details of the evaluations and weighting scheme are described in a dedicated paper in this special issue (Thébault et al. 2015).

IGRF-12 model coefficients and maps

Table 3 lists the Schmidt semi-normalized spherical harmonic coefficients defining IGRF-12. In IGRF-12, only coefficients after epoch 2005.0 are modified, but all coefficients are included to serve as a complete record of the model since 1900. This should help to avoid any confusion with previous generations of IGRF, particularly with their provisional parts. The coefficients are given in units of nT

Table 3 12th Generation International Geomagnetic Reference Field

	Degree	Order	IGRF	IGRF	IGRF	IGRF	IGRF	IGRF	IGRF	IGRF	IGRF	DGRF	DGRF	DGRF	DGRF	DGRF	DGRF	DGRF	DGRF	DGRF	DGRF	DGRF	DGRF	IGRF	SV
g/h	n	m	1900.0	1905.0	1910.0	1915.0	1920.0	1925.0	1930.0	1935.0	1940.0	1945.0	1950.0	1955.0	1960.0	1965.0	1970.0	1975.0	1980.0	1985.0	1990.0	1995.0	2000.0	2005.0	2010.0	2015	2015-20
g	1	0	-31543	-31464	-31354	-31212	-31060	-30926	-30805	-30715	-30654	-30594	-30554	-30500	-30421	-30334	-30220	-30100	-29992	-29873	-29775	-29692	-29619.4	-29554.63	-29496.57	-29442.0	10.3
g	1	1	-2298	-2298	-2297	-2306	-2317	-2318	-2316	-2306	-2292	-2285	-2250	-2215	-2169	-2119	-2068	-2013	-1956	-1905	-1848	-1784	-1728.2	-1669.05	-1586.42	-1501.0	18.1
h	1	1	5922	5909	5898	5875	5845	5817	5808	5812	5821	5810	5815	5820	5791	5776	5737	5675	5604	5500	5406	5306	5186.1	5077.99	4944.26	4797.1	-26.6
g	2	0	-677	-728	-769	-802	-839	-893	-951	-1018	-1106	-1244	-1341	-1440	-1555	-1662	-1781	-1902	-1997	-2072	-2131	-2200	-2267.7	-2337.24	-2396.06	-2445.1	-8.7
g	2	1	2905	2928	2948	2956	2959	2969	2980	2984	2981	2990	2998	3003	3002	2997	3000	3010	3027	3044	3059	3070	3068.4	3047.69	3026.34	3012.9	-3.3
h	2	1	-1061	-1086	-1128	-1191	-1259	-1334	-1424	-1520	-1614	-1702	-1810	-1898	-1967	-2016	-2047	-2067	-2129	-2197	-2279	-2366	-2481.6	-2594.50	-2708.54	-2845.6	-27.4
g	2	2	924	1041	1176	1309	1407	1471	1517	1550	1566	1578	1576	1581	1590	1594	1611	1632	1663	1687	1686	1681	1670.9	1657.76	1668.17	1676.7	2.1
h	2	2	1121	1065	1000	917	823	728	644	586	528	477	381	291	206	114	25	-68	-200	-306	-373	-413	-458.0	-515.43	-575.73	-641.9	-14.1
g	3	0	1022	1037	1058	1084	1111	1140	1172	1206	1240	1282	1297	1302	1302	1297	1287	1276	1281	1296	1314	1335	1339.6	1336.30	1339.85	1350.7	3.4
g	3	1	-1469	-1494	-1524	-1559	-1600	-1645	-1692	-1740	-1790	-1834	-1889	-1944	-1992	-2038	-2091	-2144	-2180	-2208	-2239	-2267	-2288.0	-2305.83	-2326.54	-2352.3	-5.5
h	3	1	-330	-357	-389	-421	-445	-462	-480	-494	-499	-499	-476	-462	-414	-404	-366	-333	-336	-310	-284	-262	-227.6	-198.86	-160.40	-115.3	8.2
g	3	2	1256	1239	1223	1212	1205	1202	1205	1215	1232	1255	1274	1288	1289	1292	1278	1260	1251	1247	1248	1249	1252.1	1246.39	1232.10	1225.6	-0.7
h	3	2	3	34	62	84	103	119	133	146	163	186	206	216	224	240	251	262	271	284	293	302	293.4	269.72	251.75	244.9	-0.4
g	3	3	572	635	705	778	839	881	907	918	916	913	896	882	878	856	838	830	833	829	802	759	714.5	672.51	633.73	582.0	-10.1
h	3	3	523	480	425	360	293	229	166	101	43	-11	-46	-83	-130	-165	-196	-223	-252	-297	-352	-427	-491.1	-524.72	-537.03	-538.4	1.8
g	4	0	876	880	884	887	889	891	896	903	914	944	954	958	957	957	952	946	938	936	939	940	932.3	920.55	912.66	907.6	-0.7
g	4	1	628	643	660	678	695	711	727	744	762	776	792	796	800	804	800	791	782	780	780	780	786.8	797.96	808.97	813.7	0.2
h	4	1	195	203	211	218	220	216	205	188	169	144	136	133	135	148	167	191	212	232	247	262	272.6	282.07	286.48	283.3	-1.3
g	4	2	660	653	644	631	616	601	584	565	550	544	528	510	504	479	461	438	398	361	325	290	250.0	210.65	166.58	120.4	-9.1
h	4	2	-69	-77	-90	-109	-134	-163	-195	-226	-252	-276	-278	-274	-278	-269	-266	-265	-257	-249	-240	-236	-231.9	-225.23	-211.03	-188.7	5.3
g	4	3	-361	-380	-400	-416	-424	-426	-422	-415	-405	-421	-408	-397	-394	-390	-395	-405	-419	-424	-423	-418	-403.0	-379.86	-356.83	-334.9	4.1
h	4	3	-210	-201	-189	-173	-153	-130	-109	-90	-72	-55	-37	-23	3	13	26	39	53	69	84	97	119.8	145.15	164.46	180.9	2.9
g	4	4	134	146	160	178	199	217	234	249	265	304	303	290	269	252	234	216	199	170	141	122	111.3	100.00	89.40	70.4	-4.3
h	4	4	-75	-65	-55	-51	-57	-70	-90	-114	-141	-178	-210	-230	-255	-269	-279	-288	-297	-297	-299	-306	-303.8	-305.36	-309.72	-329.5	-5.2
g	5	0	-184	-192	-201	-211	-221	-230	-237	-241	-241	-253	-240	-229	-222	-219	-216	-218	-218	-214	-214	-214	-218.8	-227.00	-230.87	-232.6	-0.2
g	5	1	328	328	327	327	326	326	327	329	334	346	349	360	362	358	359	356	357	355	353	352	351.4	354.41	357.29	360.1	0.5
h	5	1	-210	-193	-172	-148	-122	-96	-72	-51	-33	-12	3	15	16	19	26	31	46	47	46	46	43.8	42.72	44.58	47.3	0.6
g	5	2	264	259	253	245	236	226	218	211	208	194	211	230	242	254	262	264	261	253	245	235	222.3	208.95	200.26	192.4	-1.3
h	5	2	53	56	57	58	58	58	60	64	71	95	103	110	125	128	139	148	150	150	154	165	171.9	180.25	189.01	197.0	1.7

Table 3 12th Generation International Geomagnetic Reference Field *(Continued)*

g	5	3	5	-1	-9	-16	-23	-28	-32	-33	-33	-20	-20	-23	-26	-31	-42	-59	-74	-93	-109	-118	-130.4	-136.54	-141.05	-140.9	-0.1
h	5	3	-33	-32	-33	-34	-38	-44	-53	-64	-75	-67	-87	-98	-117	-126	-139	-152	-151	-154	-153	-143	-133.1	-123.45	-118.06	-119.3	-1.2
g	5	4	-86	-93	-102	-111	-119	-125	-131	-136	-141	-142	-147	-152	-156	-157	-160	-159	-162	-164	-165	-166	-168.6	-168.05	-163.17	-157.5	1.4
h	5	4	-124	-125	-126	-126	-125	-122	-118	-115	-113	-119	-122	-121	-114	-97	-91	-83	-78	-75	-69	-55	-39.3	-19.57	-0.01	16.0	3.4
g	5	5	-16	-26	-38	-51	-62	-69	-74	-76	-76	-82	-76	-69	-63	-62	-56	-49	-48	-46	-36	-17	-12.9	-13.55	-8.03	4.1	3.9
h	5	5	3	11	21	32	43	51	58	64	69	82	80	78	81	81	83	88	92	95	97	107	106.3	103.85	101.04	100.2	0.0
g	6	0	63	62	62	61	61	61	60	59	57	59	54	47	46	45	43	45	48	53	61	68	72.3	73.60	72.78	70.0	-0.3
g	6	1	61	60	58	57	55	54	53	53	54	57	57	57	58	61	64	66	66	65	65	67	68.2	69.56	68.69	67.7	-0.1
h	6	1	-9	-7	-5	-2	0	3	4	4	4	6	-1	-9	-10	-11	-12	-13	-15	-16	-16	-17	-17.4	-20.33	-20.90	-20.8	0.0
g	6	2	-11	-11	-11	-10	-10	-9	-9	-8	-7	6	4	3	1	8	15	28	42	51	59	68	74.2	76.74	75.92	72.7	-0.7
h	6	2	83	86	89	93	96	99	102	104	105	100	99	96	99	100	100	99	93	88	82	72	63.7	54.75	44.18	33.2	-2.1
g	6	3	-217	-221	-224	-228	-233	-238	-242	-246	-249	-246	-247	-247	-237	-228	-212	-198	-192	-185	-178	-170	-160.9	-151.34	-141.40	-129.9	2.1
h	6	3	2	4	5	8	11	14	19	25	33	16	33	48	60	68	72	75	71	69	69	67	65.1	63.63	61.54	58.9	-0.7
g	6	4	-58	-57	-54	-51	-46	-40	-32	-25	-18	-25	-16	-8	-1	4	2	1	4	4	3	-1	-5.9	-14.58	-22.83	-28.9	-1.2
h	6	4	-35	-32	-29	-26	-22	-18	-16	-15	-15	-9	-12	-16	-20	-32	-37	-41	-43	-48	-52	-58	-61.2	-63.53	-66.26	-66.7	0.2
g	6	5	59	57	54	49	44	39	32	25	18	21	12	7	-2	1	3	6	14	16	18	19	16.9	14.58	13.10	13.2	0.3
h	6	5	36	32	28	23	18	13	8	4	0	-16	-12	-12	-11	-8	-6	-4	-2	-1	1	1	0.7	0.24	3.02	7.3	0.9
g	6	6	-90	-92	-95	-98	-101	-103	-104	-106	-107	-104	-105	-107	-113	-111	-112	-111	-108	-102	-96	-93	-90.4	-86.36	-78.09	-70.9	1.6
h	6	6	-69	-67	-65	-62	-57	-52	-46	-40	-33	-39	-30	-24	-17	-7	1	11	17	21	24	36	43.8	50.94	55.40	62.6	1.0
g	7	0	70	70	71	72	73	73	74	74	74	70	65	65	67	75	72	71	72	74	77	77	79.0	79.88	80.44	81.6	0.3
g	7	1	-55	-54	-54	-54	-54	-54	-54	-53	-53	-40	-55	-56	-56	-57	-57	-56	-59	-62	-64	-72	-74.0	-74.46	-75.00	-76.1	-0.2
h	7	1	-45	-46	-47	-48	-49	-50	-51	-52	-52	-45	-35	-50	-55	-61	-70	-77	-82	-83	-80	-69	-64.6	-61.14	-57.80	-54.1	0.8
g	7	2	0	0	1	2	2	3	4	4	4	0	2	2	5	4	1	1	2	3	2	1	0.0	-1.65	-4.55	-6.8	-0.5
h	7	2	-13	-14	-14	-14	-14	-14	-15	-17	-18	-18	-17	-24	-28	-27	-27	-26	-27	-27	-26	-25	-24.2	-22.57	-21.20	-19.5	0.4
g	7	3	34	33	32	31	29	27	25	23	20	0	1	10	15	13	14	16	21	24	26	28	33.3	38.73	45.24	51.8	1.3
h	7	3	-10	-11	-12	-12	-13	-14	-14	-14	-14	2	0	-4	-6	-2	-4	-5	-5	-2	0	4	6.2	6.82	6.54	5.7	-0.2
g	7	4	-41	-41	-40	-38	-37	-35	-34	-33	-31	-29	-40	-32	-32	-26	-22	-14	-12	-6	-1	5	9.1	12.30	14.00	15.0	0.1
h	7	4	-1	0	1	2	4	5	6	7	7	6	10	8	7	6	8	10	16	20	21	24	24.0	25.35	24.96	24.4	-0.3
g	7	5	-21	-20	-19	-18	-16	-14	-12	-11	-9	-10	-7	-11	-7	-6	-2	0	1	4	5	4	6.9	9.37	10.46	9.4	-0.6
h	7	5	28	28	28	28	28	29	29	29	29	28	36	28	23	26	23	22	18	17	17	17	14.8	10.93	7.03	3.4	-0.6
g	7	6	18	18	18	19	19	19	18	18	17	15	5	9	17	13	13	12	11	10	9	8	7.3	5.42	1.64	-2.8	-0.8
h	7	6	-12	-12	-13	-15	-16	-17	-18	-19	-20	-17	-18	-20	-18	-23	-23	-23	-23	-23	-23	-24	-25.4	-26.32	-27.61	-27.4	0.1

Table 3 12th Generation International Geomagnetic Reference Field *(Continued)*

g	7	7	6	6	6	6	6	6	6	6	5	29	19	18	8	1	-2	-5	-2	0	0	-2	-1.2	1.94	4.92	6.8	0.2
h	7	7	-22	-22	-22	-22	-22	-21	-20	-19	-19	-22	-16	-18	-17	-12	-11	-12	-10	-7	-4	-6	-5.8	-4.64	-3.28	-2.2	-0.2
g	8	0	11	11	11	11	11	11	11	11	11	13	22	11	15	13	14	14	18	21	23	25	24.4	24.80	24.41	24.2	0.2
g	8	1	8	8	8	8	7	7	7	7	7	7	15	9	6	5	6	6	6	6	5	6	6.6	7.62	8.21	8.8	0.0
h	8	1	8	8	8	8	8	8	8	8	8	12	5	10	11	7	7	6	7	8	10	11	11.9	11.20	10.84	10.1	-0.3
g	8	2	-4	-4	-4	-4	-3	-3	-3	-3	-3	-8	-4	-6	-4	-4	-2	-1	0	0	-1	-6	-9.2	-11.73	-14.50	-16.9	-0.6
h	8	2	-14	-15	-15	-15	-15	-15	-15	-15	-14	-21	-22	-15	-14	-12	-15	-16	-18	-19	-19	-21	-21.5	-20.88	-20.03	-18.3	0.3
g	8	3	-9	-9	-9	-9	-9	-9	-9	-9	-10	-5	-1	-14	-11	-14	-13	-12	-11	-11	-10	-9	-7.9	-6.88	-5.59	-3.2	0.5
h	8	3	7	7	6	6	6	6	5	5	5	-12	0	5	7	9	6	4	4	5	6	8	8.5	9.83	11.83	13.3	0.1
g	8	4	1	1	1	2	2	2	2	1	1	9	11	6	2	0	-3	-8	-7	-9	-12	-14	-16.6	-18.11	-19.34	-20.6	-0.2
h	8	4	-13	-13	-13	-13	-14	-14	-14	-15	-15	-7	-21	-23	-18	-16	-17	-19	-22	-23	-22	-23	-21.5	-19.71	-17.41	-14.6	0.5
g	8	5	2	2	2	3	4	4	5	6	6	7	15	10	10	8	5	4	4	4	3	9	9.1	10.17	11.61	13.4	0.4
h	8	5	5	5	5	5	5	5	5	5	5	2	-8	3	4	4	6	6	9	11	12	15	15.5	16.22	16.71	16.2	-0.2
g	8	6	-9	-8	-8	-8	-7	-7	-6	-6	-5	-10	-13	-7	-5	-1	0	0	3	4	4	6	7.0	9.36	10.85	11.7	0.1
h	8	6	16	16	16	16	17	17	18	18	19	18	17	23	23	24	21	18	16	14	12	11	8.9	7.61	6.96	5.7	-0.3
g	8	7	5	5	5	6	6	7	8	8	9	7	5	6	10	11	11	10	6	4	2	-5	-7.9	-11.25	-14.05	-15.9	-0.4
h	8	7	-5	-5	-5	-5	-5	-5	-5	-5	-5	3	-4	-4	1	-3	-6	-10	-13	-15	-16	-16	-14.9	-12.76	-10.74	-9.1	0.3
g	8	8	8	8	8	8	8	8	8	7	7	2	-1	9	8	4	3	1	-1	-4	-6	-7	-7.0	-4.87	-3.54	-2.0	0.3
h	8	8	-18	-18	-18	-18	-19	-19	-19	-19	-19	-11	-17	-13	-20	-17	-16	-17	-15	-11	-10	-4	-2.1	-0.06	1.64	2.1	0.0
g	9	0	8	8	8	8	8	8	8	8	8	5	3	4	4	8	8	7	5	5	4	4	5.0	5.58	5.50	5.4	-
g	9	1	10	10	10	10	10	10	10	10	10	-21	-7	9	6	10	10	10	10	10	9	9	9.4	9.76	9.45	8.8	-
h	9	1	-20	-20	-20	-20	-20	-20	-20	-20	-21	-27	-24	-11	-18	-22	-21	-21	-21	-21	-20	-20	-19.7	-20.11	-20.54	-21.6	-
g	9	2	1	1	1	1	1	1	1	1	1	1	-1	-4	0	2	2	2	1	1	1	3	3.0	3.58	3.45	3.1	-
h	9	2	14	14	14	14	14	14	14	15	15	17	19	12	12	15	16	16	16	15	15	15	13.4	12.69	11.51	10.8	-
g	9	3	-11	-11	-11	-11	-11	-11	-12	-12	-12	-11	-25	-5	-9	-13	-12	-12	-12	-12	-12	-10	-8.4	-6.94	-5.27	-3.3	-
h	9	3	5	5	5	5	5	5	5	5	5	29	12	7	2	7	6	7	9	9	11	12	12.5	12.67	12.75	11.8	-
g	9	4	12	12	12	12	12	12	12	11	11	3	10	2	1	10	10	10	9	9	9	8	6.3	5.01	3.13	0.7	-
h	9	4	-3	-3	-3	-3	-3	-3	-3	-3	-3	-9	2	6	0	-4	-4	-4	-5	-6	-7	-6	-6.2	-6.72	-7.14	-6.8	-
g	9	5	1	1	1	1	1	1	1	1	1	16	5	4	4	-1	-1	-1	-3	-3	-4	-8	-8.9	-10.76	-12.38	-13.3	-
h	9	5	-2	-2	-2	-2	-2	-2	-2	-3	-3	4	2	-2	-3	-5	-5	-5	-6	-6	-7	-8	-8.4	-8.16	-7.42	-6.9	-
g	9	6	-2	-2	-2	-2	-2	-2	-2	-2	-2	-3	-5	1	-1	-1	0	-1	-1	-1	-2	-1	-1.5	-1.25	-0.76	-0.1	-
h	9	6	8	8	8	8	9	9	9	9	9	9	8	10	9	10	10	10	9	9	9	8	8.4	8.10	7.97	7.8	-

Table 3 12th Generation International Geomagnetic Reference Field *(Continued)*

g	9	7	2	2	2	2	2	2	3	3	3	-4	-2	2	-2	5	3	4	7	7	7	10	9.3	8.76	8.43	8.7	-
h	9	7	10	10	10	10	10	10	10	11	11	6	8	7	8	10	11	11	10	9	8	5	3.8	2.92	2.14	1.0	-
g	9	8	-1	0	0	0	0	0	0	0	1	-3	3	2	3	1	1	1	2	1	1	-2	-4.3	-6.66	-8.42	-9.1	-
h	9	8	-2	-2	-2	-2	-2	-2	-2	-2	-2	1	-11	-6	0	-4	-2	-3	-6	-7	-7	-8	-8.2	-7.73	-6.08	-4.0	-
g	9	9	-1	-1	-1	-1	-1	-1	-2	-2	-2	-4	8	5	-1	-2	-1	-2	-5	-5	-6	-8	-8.2	-9.22	-10.08	-10.5	-
h	9	9	2	2	2	2	2	2	2	2	2	8	-7	5	5	1	1	1	2	2	2	3	4.8	6.01	7.01	8.4	-
g	10	0	-3	-3	-3	-3	-3	-3	-3	-3	-3	-3	-8	-3	1	-2	-3	-3	-4	-4	-3	-3	-2.6	-2.17	-1.94	-1.9	-
g	10	1	-4	-4	-4	-4	-4	-4	-4	-4	-4	11	4	-5	-3	-3	-3	-3	-4	-4	-4	-6	-6.0	-6.12	-6.24	-6.3	-
h	10	1	2	2	2	2	2	2	2	2	2	5	13	-4	4	2	1	1	1	1	2	1	1.7	2.19	2.73	3.2	-
g	10	2	2	2	2	2	2	2	2	2	2	1	-1	-1	4	2	2	2	2	3	2	2	1.7	1.42	0.89	0.1	-
h	10	2	1	1	1	1	1	1	1	1	1	1	-2	0	1	1	1	1	0	0	1	0	0.0	0.10	-0.10	-0.4	-
g	10	3	-5	-5	-5	-5	-5	-5	-5	-5	-5	2	13	2	0	-5	-5	-5	-5	-5	-5	-4	-3.1	-2.35	-1.07	0.5	-
h	10	3	2	2	2	2	2	2	2	2	2	-20	-10	-8	0	2	3	3	3	3	3	4	4.0	4.46	4.71	4.6	-
g	10	4	-2	-2	-2	-2	-2	-2	-2	-2	-2	-5	-4	-3	-1	-2	-1	-2	-2	-2	-2	-1	-0.5	-0.15	-0.16	-0.5	-
h	10	4	6	6	6	6	6	6	6	6	6	-1	2	-2	2	6	4	4	6	6	6	5	4.9	4.76	4.44	4.4	-
g	10	5	6	6	6	6	6	6	6	6	6	-1	4	7	4	4	6	5	5	5	4	4	3.7	3.06	2.45	1.8	-
h	10	5	-4	-4	-4	-4	-4	-4	-4	-4	-4	-6	-3	-4	-5	-4	-4	-4	-4	-4	-4	-5	-5.9	-6.58	-7.22	-7.9	-
g	10	6	4	4	4	4	4	4	4	4	4	8	12	4	6	4	4	4	3	3	3	2	1.0	0.29	-0.33	-0.7	-
h	10	6	0	0	0	0	0	0	0	0	0	6	6	1	1	0	0	-1	0	0	0	-1	-1.2	-1.01	-0.96	-0.6	-
g	10	7	0	0	0	0	0	0	0	0	0	-1	3	-2	1	0	1	1	1	1	1	2	2.0	2.06	2.13	2.1	-
h	10	7	-2	-2	-2	-2	-2	-2	-2	-1	-1	-4	-3	-3	-1	-2	-1	-1	-1	-1	-2	-2	-2.9	-3.47	-3.95	-4.2	-
g	10	8	2	2	2	1	1	1	1	2	2	-3	2	6	-1	2	0	0	2	2	3	5	4.2	3.77	3.09	2.4	-
h	10	8	4	4	4	4	4	4	4	4	4	-2	6	7	6	3	3	3	4	4	3	1	0.2	-0.86	-1.99	-2.8	-
g	10	9	2	2	2	2	3	3	3	3	3	5	10	-2	2	2	3	3	3	3	3	1	0.3	-0.21	-1.03	-1.8	-
h	10	9	0	0	0	0	0	0	0	0	0	0	11	-1	0	0	1	1	0	0	-1	-2	-2.2	-2.31	-1.97	-1.2	-
g	10	10	0	0	0	0	0	0	0	0	0	-2	3	0	0	0	-1	-1	0	0	0	0	-1.1	-2.09	-2.80	-3.6	-
h	10	10	-6	-6	-6	-6	-6	-6	-6	-6	-6	-2	8	-3	-7	-6	-4	-5	-6	-6	-6	-7	-7.4	-7.93	-8.31	-8.7	-
g	11	0	-	-	-	-	-	-	-	-	-	-	-	-	-	-	-	-	-	-	-	-	2.7	2.95	3.05	3.1	-
g	11	1	-	-	-	-	-	-	-	-	-	-	-	-	-	-	-	-	-	-	-	-	-1.7	-1.60	-1.48	-1.5	-
h	11	1	-	-	-	-	-	-	-	-	-	-	-	-	-	-	-	-	-	-	-	-	0.1	0.26	0.13	-0.1	-
g	11	2	-	-	-	-	-	-	-	-	-	-	-	-	-	-	-	-	-	-	-	-	-1.9	-1.88	-2.03	-2.3	-
h	11	2	-	-	-	-	-	-	-	-	-	-	-	-	-	-	-	-	-	-	-	-	1.3	1.44	1.67	2.0	-

Table 3 12th Generation International Geomagnetic Reference Field *(Continued)*

g	11	3	-	-	-	-	-	-	-	-	-	-	-	-	-	-	-	-	-	-	-	-	-	1.5	1.44	1.65	2.0	-
h	11	3	-	-	-	-	-	-	-	-	-	-	-	-	-	-	-	-	-	-	-	-	-	-0.9	-0.77	-0.66	-0.7	-
g	11	4	-	-	-	-	-	-	-	-	-	-	-	-	-	-	-	-	-	-	-	-	-	-0.1	-0.31	-0.51	-0.8	-
h	11	4	-	-	-	-	-	-	-	-	-	-	-	-	-	-	-	-	-	-	-	-	-	-2.6	-2.27	-1.76	-1.1	-
g	11	5	-	-	-	-	-	-	-	-	-	-	-	-	-	-	-	-	-	-	-	-	-	0.1	0.29	0.54	0.6	-
h	11	5	-	-	-	-	-	-	-	-	-	-	-	-	-	-	-	-	-	-	-	-	-	0.9	0.90	0.85	0.8	-
g	11	6	-	-	-	-	-	-	-	-	-	-	-	-	-	-	-	-	-	-	-	-	-	-0.7	-0.79	-0.79	-0.7	-
h	11	6	-	-	-	-	-	-	-	-	-	-	-	-	-	-	-	-	-	-	-	-	-	-0.7	-0.58	-0.39	-0.2	-
g	11	7	-	-	-	-	-	-	-	-	-	-	-	-	-	-	-	-	-	-	-	-	-	0.7	0.53	0.37	0.2	-
h	11	7	-	-	-	-	-	-	-	-	-	-	-	-	-	-	-	-	-	-	-	-	-	-2.8	-2.69	-2.51	-2.2	-
g	11	8	-	-	-	-	-	-	-	-	-	-	-	-	-	-	-	-	-	-	-	-	-	1.7	1.80	1.79	1.7	-
h	11	8	-	-	-	-	-	-	-	-	-	-	-	-	-	-	-	-	-	-	-	-	-	-0.9	-1.08	-1.27	-1.4	-
g	11	9	-	-	-	-	-	-	-	-	-	-	-	-	-	-	-	-	-	-	-	-	-	0.1	0.16	0.12	-0.2	-
h	11	9	-	-	-	-	-	-	-	-	-	-	-	-	-	-	-	-	-	-	-	-	-	-1.2	-1.58	-2.11	-2.5	-
g	11	10	-	-	-	-	-	-	-	-	-	-	-	-	-	-	-	-	-	-	-	-	-	1.2	0.96	0.75	0.4	-
h	11	10	-	-	-	-	-	-	-	-	-	-	-	-	-	-	-	-	-	-	-	-	-	-1.9	-1.90	-1.94	-2.0	-
g	11	11	-	-	-	-	-	-	-	-	-	-	-	-	-	-	-	-	-	-	-	-	-	4.0	3.99	3.75	3.5	-
h	11	11	-	-	-	-	-	-	-	-	-	-	-	-	-	-	-	-	-	-	-	-	-	-0.9	-1.39	-1.86	-2.4	-
g	12	0	-	-	-	-	-	-	-	-	-	-	-	-	-	-	-	-	-	-	-	-	-	-2.2	-2.15	-2.12	-1.9	-
g	12	1	-	-	-	-	-	-	-	-	-	-	-	-	-	-	-	-	-	-	-	-	-	-0.3	-0.29	-0.21	-0.2	-
h	12	1	-	-	-	-	-	-	-	-	-	-	-	-	-	-	-	-	-	-	-	-	-	-0.4	-0.55	-0.87	-1.1	-
g	12	2	-	-	-	-	-	-	-	-	-	-	-	-	-	-	-	-	-	-	-	-	-	0.2	0.21	0.30	0.4	-
h	12	2	-	-	-	-	-	-	-	-	-	-	-	-	-	-	-	-	-	-	-	-	-	0.3	0.23	0.27	0.4	-
g	12	3	-	-	-	-	-	-	-	-	-	-	-	-	-	-	-	-	-	-	-	-	-	0.9	0.89	1.04	1.2	-
h	12	3	-	-	-	-	-	-	-	-	-	-	-	-	-	-	-	-	-	-	-	-	-	2.5	2.38	2.13	1.9	-
g	12	4	-	-	-	-	-	-	-	-	-	-	-	-	-	-	-	-	-	-	-	-	-	-0.2	-0.38	-0.63	-0.8	-
h	12	4	-	-	-	-	-	-	-	-	-	-	-	-	-	-	-	-	-	-	-	-	-	-2.6	-2.63	-2.49	-2.2	-
g	12	5	-	-	-	-	-	-	-	-	-	-	-	-	-	-	-	-	-	-	-	-	-	0.9	0.96	0.95	0.9	-
h	12	5	-	-	-	-	-	-	-	-	-	-	-	-	-	-	-	-	-	-	-	-	-	0.7	0.61	0.49	0.3	-
g	12	6	-	-	-	-	-	-	-	-	-	-	-	-	-	-	-	-	-	-	-	-	-	-0.5	-0.30	-0.11	0.1	-
h	12	6	-	-	-	-	-	-	-	-	-	-	-	-	-	-	-	-	-	-	-	-	-	0.3	0.40	0.59	0.7	-
g	12	7	-	-	-	-	-	-	-	-	-	-	-	-	-	-	-	-	-	-	-	-	-	0.3	0.46	0.52	0.5	-

Table 3 12th Generation International Geomagnetic Reference Field *(Continued)*

h	12	7	-	-	-	-	-	-	-	-	-	-	-	-	-	-	-	-	-	-	-	-	-	0.0	0.01	0.00	-0.1	-
g	12	8	-	-	-	-	-	-	-	-	-	-	-	-	-	-	-	-	-	-	-	-	-	-0.3	-0.35	-0.39	-0.3	-
h	12	8	-	-	-	-	-	-	-	-	-	-	-	-	-	-	-	-	-	-	-	-	-	0.0	0.02	0.13	0.3	-
g	12	9	-	-	-	-	-	-	-	-	-	-	-	-	-	-	-	-	-	-	-	-	-	-0.4	-0.36	-0.37	-0.4	-
h	12	9	-	-	-	-	-	-	-	-	-	-	-	-	-	-	-	-	-	-	-	-	-	0.3	0.28	0.27	0.2	-
g	12	10	-	-	-	-	-	-	-	-	-	-	-	-	-	-	-	-	-	-	-	-	-	-0.1	0.08	0.21	0.2	-
h	12	10	-	-	-	-	-	-	-	-	-	-	-	-	-	-	-	-	-	-	-	-	-	-0.9	-0.87	-0.86	-0.9	-
g	12	11	-	-	-	-	-	-	-	-	-	-	-	-	-	-	-	-	-	-	-	-	-	-0.2	-0.49	-0.77	-0.9	-
h	12	11	-	-	-	-	-	-	-	-	-	-	-	-	-	-	-	-	-	-	-	-	-	-0.4	-0.34	-0.23	-0.1	-
g	12	12	-	-	-	-	-	-	-	-	-	-	-	-	-	-	-	-	-	-	-	-	-	-0.4	-0.08	0.04	0.0	-
h	12	12	-	-	-	-	-	-	-	-	-	-	-	-	-	-	-	-	-	-	-	-	-	0.8	0.88	0.87	0.7	-
g	13	0	-	-	-	-	-	-	-	-	-	-	-	-	-	-	-	-	-	-	-	-	-	-0.2	-0.16	-0.09	0.0	-
g	13	1	-	-	-	-	-	-	-	-	-	-	-	-	-	-	-	-	-	-	-	-	-	-0.9	-0.88	-0.89	-0.9	-
h	13	1	-	-	-	-	-	-	-	-	-	-	-	-	-	-	-	-	-	-	-	-	-	-0.9	-0.76	-0.87	-0.9	-
g	13	2	-	-	-	-	-	-	-	-	-	-	-	-	-	-	-	-	-	-	-	-	-	0.3	0.30	0.31	0.4	-
h	13	2	-	-	-	-	-	-	-	-	-	-	-	-	-	-	-	-	-	-	-	-	-	0.2	0.33	0.30	0.4	-
g	13	3	-	-	-	-	-	-	-	-	-	-	-	-	-	-	-	-	-	-	-	-	-	0.1	0.28	0.42	0.5	-
h	13	3	-	-	-	-	-	-	-	-	-	-	-	-	-	-	-	-	-	-	-	-	-	1.8	1.72	1.66	1.6	-
g	13	4	-	-	-	-	-	-	-	-	-	-	-	-	-	-	-	-	-	-	-	-	-	-0.4	-0.43	-0.45	-0.5	-
h	13	4	-	-	-	-	-	-	-	-	-	-	-	-	-	-	-	-	-	-	-	-	-	-0.4	-0.54	-0.59	-0.5	-
g	13	5	-	-	-	-	-	-	-	-	-	-	-	-	-	-	-	-	-	-	-	-	-	1.3	1.18	1.08	1.0	-
h	13	5	-	-	-	-	-	-	-	-	-	-	-	-	-	-	-	-	-	-	-	-	-	-1.0	-1.07	-1.14	-1.2	-
g	13	6	-	-	-	-	-	-	-	-	-	-	-	-	-	-	-	-	-	-	-	-	-	-0.4	-0.37	-0.31	-0.2	-
h	13	6	-	-	-	-	-	-	-	-	-	-	-	-	-	-	-	-	-	-	-	-	-	-0.1	-0.04	-0.07	-0.1	-
g	13	7	-	-	-	-	-	-	-	-	-	-	-	-	-	-	-	-	-	-	-	-	-	0.7	0.75	0.78	0.8	-
h	13	7	-	-	-	-	-	-	-	-	-	-	-	-	-	-	-	-	-	-	-	-	-	0.7	0.63	0.54	0.4	-
g	13	8	-	-	-	-	-	-	-	-	-	-	-	-	-	-	-	-	-	-	-	-	-	-0.4	-0.26	-0.18	-0.1	-
h	13	8	-	-	-	-	-	-	-	-	-	-	-	-	-	-	-	-	-	-	-	-	-	0.3	0.21	0.10	-0.1	-
g	13	9	-	-	-	-	-	-	-	-	-	-	-	-	-	-	-	-	-	-	-	-	-	0.3	0.35	0.38	0.3	-
h	13	9	-	-	-	-	-	-	-	-	-	-	-	-	-	-	-	-	-	-	-	-	-	0.6	0.53	0.49	0.4	-
g	13	10	-	-	-	-	-	-	-	-	-	-	-	-	-	-	-	-	-	-	-	-	-	-0.1	-0.05	0.02	0.1	-
h	13	10	-	-	-	-	-	-	-	-	-	-	-	-	-	-	-	-	-	-	-	-	-	0.3	0.38	0.44	0.5	-

Table 3 12th Generation International Geomagnetic Reference Field *(Continued)*

g	13	11	-	-	-	-	-	-	-	-	-	-	-	-	-	-	-	-	-	-	-	0.4	0.41	0.42	0.5	-
h	13	11	-	-	-	-	-	-	-	-	-	-	-	-	-	-	-	-	-	-	-	-0.2	-0.22	-0.25	-0.3	-
g	13	12	-	-	-	-	-	-	-	-	-	-	-	-	-	-	-	-	-	-	-	0.0	-0.10	-0.26	-0.4	-
h	13	12	-	-	-	-	-	-	-	-	-	-	-	-	-	-	-	-	-	-	-	-0.5	-0.57	-0.53	-0.4	-
g	13	13	-	-	-	-	-	-	-	-	-	-	-	-	-	-	-	-	-	-	-	0.1	-0.18	-0.26	-0.3	-
h	13	13	-	-	-	-	-	-	-	-	-	-	-	-	-	-	-	-	-	-	-	-0.9	-0.82	-0.79	-0.8	-

Here, Schmidt semi-normalized spherical harmonic coefficients are provided. Coefficients for degrees n=1-13 in units of nanotesla are listed for IGRF and definitive DGRF main-field models. Coefficients for degrees n=1-8 in units of nanotesla/year are listed for the predictive secular variation. Undefined coefficients are marked with '-'; these should be set to 0.0 in numerical calculations as is the case in the coefficient files available online.

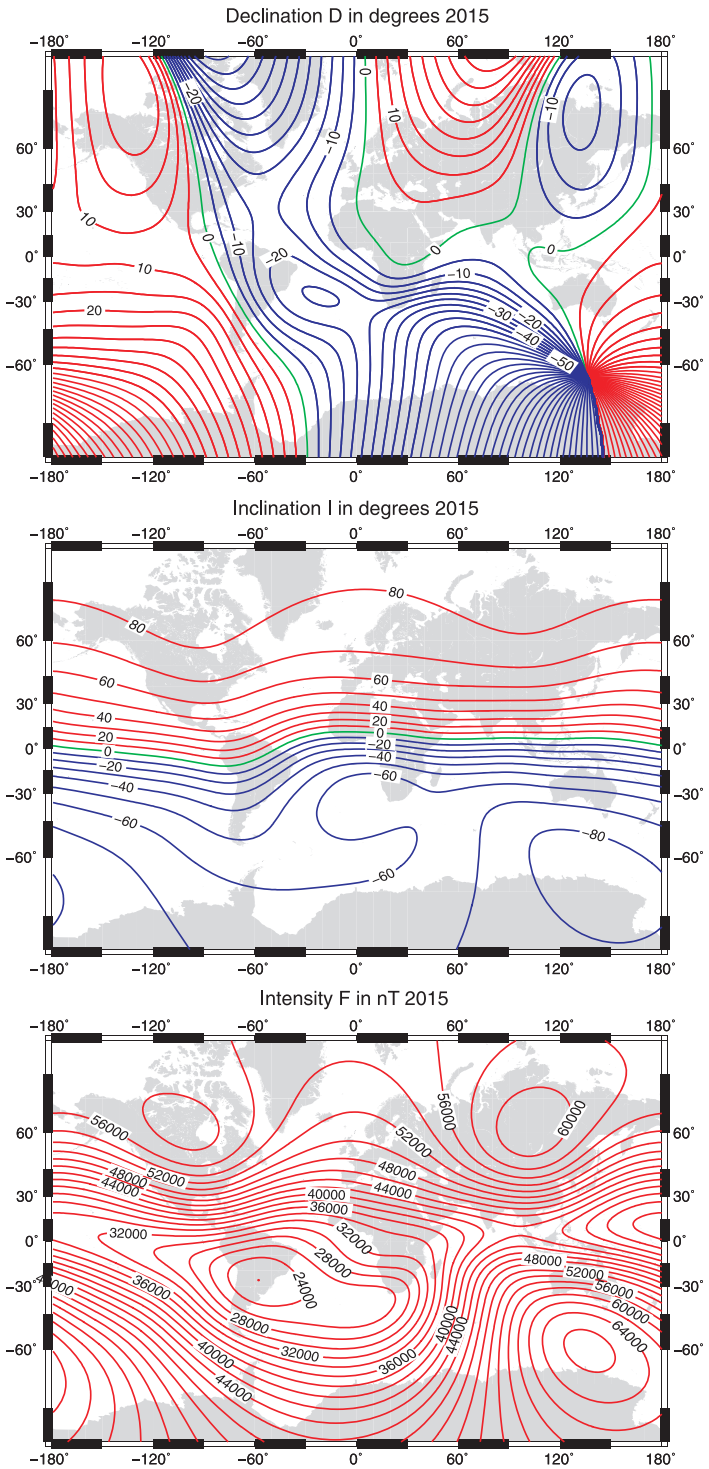

Figure 1 Maps of the magnetic declination D (top, units are degrees), inclination I (middle, units are degrees), and total intensity F (bottom, units are nT) at the Earth's mean radius $r = a$ in 2015; the red dot indicates the minimum intensity. Projection is Mercator.

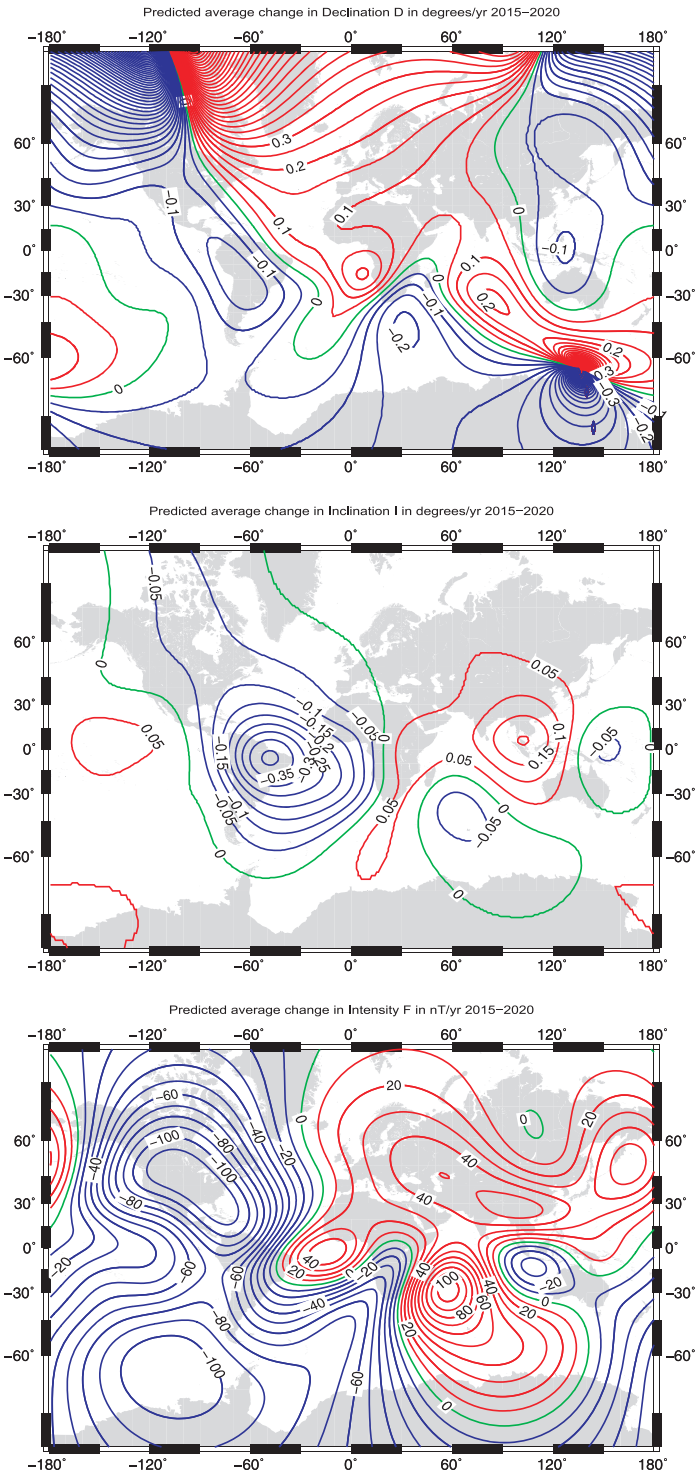

Figure 2 Maps of the predicted rate of change per year in the declination D (top, units are degrees/year), the inclination I (middle, units are degrees/year), and total intensity F (bottom, units are nT/year) at the Earth's mean radius $r = a$ for the interval 2015.0 to 2020.0. Projection is Mercator.

for the MF models and of nT/year for the predictive SV model. The coefficients are also available at http://www.ngdc.noaa.gov/IAGA/vmod/igrf.html, together with software to compute the magnetic field components at times and locations of interest, in both geodetic and geocentric reference frames. IGRF-12 is also available from the World Data Centers listed at the end of this paper.

We display in Figure 1 maps of the declination D, inclination I, and total intensity F in 2015.0 on the Earth's reference sphere ($r = a$) in a Mercator projection that is well suited to navigation. The green lines are the zero contours; in the declination map, the line shows the agonic line where true geographic and magnetic north/south as predicted by the model coincide on the Earth's surface. The general features shown by the maps in 2015 are well known (e.g., Finlay et al. 2010a) and have slowly evolved through the 115 years covered by IGRF-12. In particular, the minimum of magnetic intensity (see Figure 1 bottom), also known as the South Atlantic Anomaly, has continuously drifted westward and decreased since 1900. The point of minimum intensity at the Earth's surface is currently over Southern Paraguay and is expected to cross the political boundary with Argentina during the second half of 2016. Maps of the predictive annual rate of change for D, I, and F between 2015 and 2020 at the Earth's surface are shown in Figure 2. They are consistent with the continuation of the long-established westward drift and deepening of the South Atlantic Anomaly.

The positions of the geomagnetic poles and the magnetic dip poles in the northern and southern hemispheres, tabulated in Table 4, are presented in Figure 3 on the Earth's reference sphere. We recall that the geomagnetic poles are the points of intersection between the tilted axis of a central inclined magnetic dipole and the sphere of radius $a = 6,371.2$ km. Their positions, expressed in the geocentric co-ordinate system, are antipodal and can be

Table 4 Magnetic pole positions since 1900 as determined from IGRF-12 in WGS84 geodetic latitude

	North dip pole		South dip pole		North geomagnetic pole		South geomagnetic pole	
Epoch	Latitude	Longitude	Latitude	Longitude	Latitude	Longitude	Latitude	Longitude
1900.0	70.46	-96.19	-71.72	148.32	78.68	-68.79	-78.68	111.21
1905.0	70.66	-96.48	-71.46	148.55	78.68	-68.75	-78.68	111.25
1910.0	70.79	-96.72	-71.15	148.64	78.66	-68.72	-78.66	111.28
1915.0	71.03	-97.03	-70.80	148.54	78.64	-68.57	-78.64	111.43
1920.0	71.34	-97.39	-70.41	148.20	78.63	-68.38	-78.63	111.62
1925.0	71.79	-98.00	-69.99	147.63	78.62	-68.27	-78.62	111.73
1930.0	72.27	-98.69	-69.52	146.79	78.60	-68.26	-78.60	111.74
1935.0	72.80	-99.34	-69.06	145.77	78.57	-68.36	-78.57	111.64
1940.0	73.30	-99.87	-68.57	144.60	78.55	-68.51	-78.55	111.49
1945.0	73.93	-100.24	-68.15	144.44	78.55	-68.53	-78.55	111.47
1950.0	74.64	-100.86	-67.89	143.55	78.55	-68.85	-78.55	111.15
1955.0	75.18	-101.41	-67.19	141.50	78.54	-69.16	-78.54	110.84
1960.0	75.30	-101.03	-66.70	140.23	78.58	-69.47	-78.58	110.53
1965.0	75.63	-101.34	-66.33	139.53	78.60	-69.85	-78.60	110.15
1970.0	75.88	-100.98	-66.02	139.40	78.66	-70.18	-78.66	109.82
1975.0	76.15	-100.64	-65.74	139.52	78.76	-70.47	-78.76	109.53
1980.0	76.91	-101.68	-65.42	139.34	78.88	-70.76	-78.88	109.24
1985.0	77.40	-102.61	-65.13	139.18	79.04	-70.90	-79.04	109.10
1990.0	78.09	-103.68	-64.91	138.90	79.21	-71.13	-79.21	108.87
1995.0	79.09	-105.42	-64.79	138.76	79.39	-71.42	-79.39	108.58
2000.0	80.97	-109.64	-64.66	138.30	79.61	-71.57	-79.61	108.43
2005.0	83.19	-118.24	-64.55	137.85	79.82	-71.81	-79.82	108.19
2010.0	85.02	-132.84	-64.43	137.32	80.09	-72.21	-80.09	107.78
2015.0	86.29	-160.06	-64.28	136.59	80.37	-72.63	-80.37	107.37
2020.0	86.39	169.80	-64.11	135.76	80.65	-73.17	-80.65	106.83

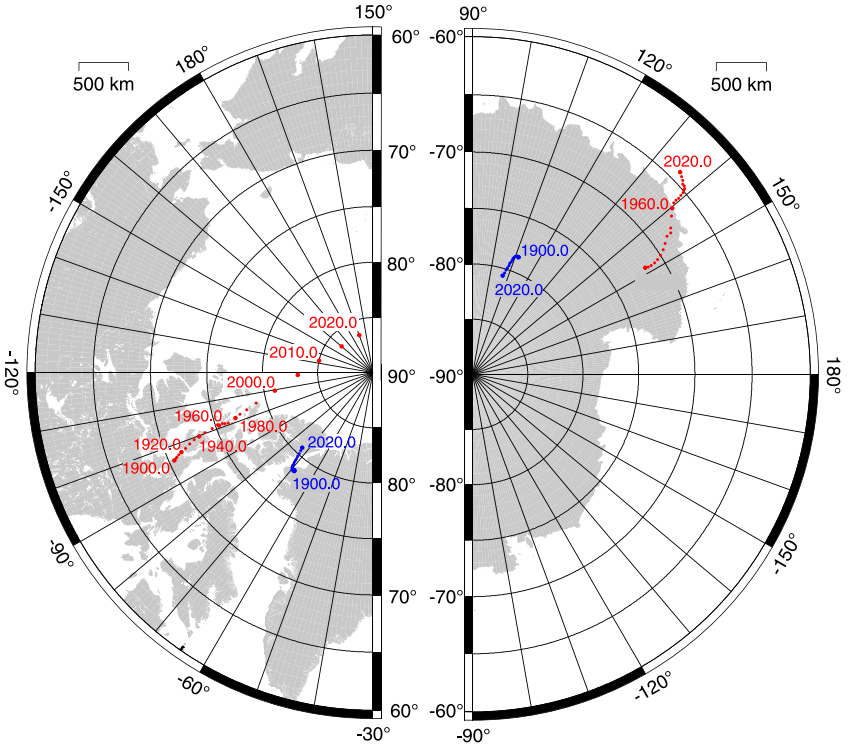

Figure 3 Motion of the magnetic dip pole (red) and geomagnetic pole (blue) since 1900 from IGRF-12 in the northern hemisphere (left) and the southern hemisphere (right). Stereographic projection is employed. The scale bar gives an indication of distance on the WGS84 ellipsoid that is correct along lines of constant longitude and also along the middle lines of latitude shown.

determined from only the three dipole ($n = 1$) Gauss coefficients. The magnetic dip poles are defined as the points on the Earth's surface where the magnetic field inclination, as determined from the entire field model to degree $n = N$, is vertical. They are referred to the north and south magnetic poles and are given in Table 4 for the field as observed in the geodetic WGS84 co-ordinate system. The comparison between the locations of the geomagnetic poles and the dip poles is of interest as, seen in the spherical frame, they would coincide if the Earth's magnetic field was perfectly dipolar. However, this is not the case. The comparison also illustrates the comparatively slower drift in time of the Earth's geomagnetic dipole compared to other contributions of the magnetic field. Interestingly, the movements of the north and south magnetic poles have not been erratic and have constantly moved northward since 1900. The tilt between the geomagnetic and the geographic axes is at present reducing with time; it is about 9.7° in 2015.0 and projected to be 9.4° in 2020. The north magnetic pole appeared to be accelerating rather smoothly over the last century (Figure 4) from about 5 to about 50 km/year with an increased acceleration around 1990 (Chulliat et al. 2010). The peculiar acceleration of the north and south magnetic poles between 1945 and 1955 as calculated by IGRF should be regarded with caution; see Xu (2000) for a discussion. Perhaps the most striking feature of IGRF-12 is that the north magnetic pole appears to have started a phase of deceleration with a velocity of about 53.2 km/year in 2015 and a projected velocity of 42.6 km/year in 2020. Note however that the later estimate relies on the predictive (SV) part of IGRF-12 for epoch 2015.0 to 2020.0 and that retrospective analysis has shown that errors could be significant (e.g., Finlay et al. 2010b). The locations computed from models are also intrinsically approximate due to the limited spatial resolution of the IGRF-12 models. For further details on the limitations of the IGRF for various applications and on difficulties in estimating its accuracy, readers should refer to Lowes (2000) or consult the IGRF 'Health Warning' found at http://www.ngdc.noaa.gov/IAGA/vmod/igrfhw.html.

IGRF-12 online data products

Further general information about the IGRF:
http://www.ngdc.noaa.gov/IAGA/vmod/igrf.html.
The coefficients of IGRF-12 in various file formats:
http://www.ngdc.noaa.gov/IAGA/vmod/igrf12coeffs.txt

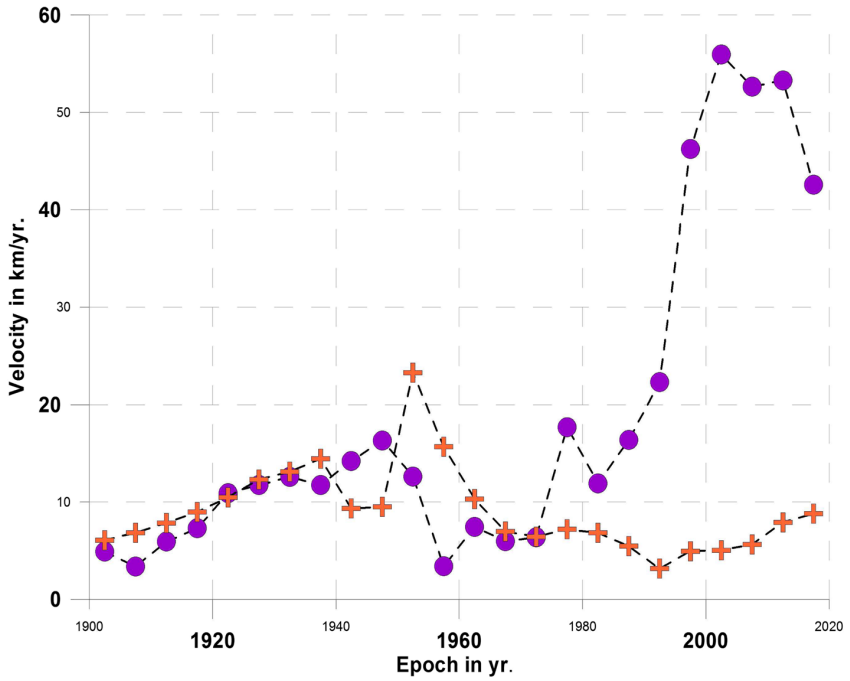

Figure 4 The northward velocity of the geomagnetic dip poles in the northern (purple dots) and southern (orange crosses) hemisphere as estimated by IGRF-12 on the WGS84 spheroid.

Fortran software for synthesizing the field from the coefficients:
http://www.ngdc.noaa.gov/IAGA/vmod/igrf12.f
C software for synthesizing the field from the coefficients (Linux):
http://www.ngdc.noaa.gov/IAGA/vmod/geomag70_linux.tar.gz
C software for synthesizing the field from the coefficients (Windows):
http://www.ngdc.noaa.gov/IAGA/vmod/geomag70_windows.zip
Online computation of field components from the IGRF-12 model:
http://www.ngdc.noaa.gov/geomag-web/?model=igrf
http://www.geomag.bgs.ac.uk/data_service/models_compass/igrf_form.shtml
http://wdc.kugi.kyoto-u.ac.jp/igrf/point/index.html
Archive of legacy versions of the IGRF model:
http://www.ngdc.noaa.gov/IAGA/vmod/igrf_old_models.html

Appendix: World Data Centers

WORLD DATA SERVICE FOR GEOPHYSICS, BOULDER
NOAA National Centers for Environmental Information, NOAA, 325 Broadway, E/GC, Boulder, CO 80305-3328 UNITED STATES OF AMERICA
INTERNET: http://www.ngdc.noaa.gov

WORLD DATA CENTRE FOR GEOMAGNETISM, COPENHAGEN
DTU Space, Diplomvej, Building 327, DK 2800, Kgs. Lynbgy, DENMARK
TEL: +45 4525 9713
FAX: +45 353 62475
EMAIL: cfinlay@space.dtu.dk
INTERNET: http://www.space.dtu.dk/English/Research/Scientific_data_and_models

WORLD DATA CENTRE FOR GEOMAGNETISM, EDINBURGH
British Geological Survey
Murchison House, West Mains Road
Edinburgh, EH9 3LA
UNITED KINGDOM
TEL: +44 131 650 0234
FAX: +44 131 668 4368
EMAIL: wdcgeomag@bgs.ac.uk
INTERNET: http://www.wdc.bgs.ac.uk/

WORLD DATA CENTRE FOR GEOMAGNETISM, KYOTO

Data Analysis Center for Geomagnetism and Space Magnetism
Graduate School of Science, Kyoto University
Kitashirakawa-Oiwake Cho, Sakyo-ku
Kyoto, 606-8502, JAPAN
TEL: +81 75 753 3929
FAX: +81 75 722 7884
EMAIL: iyemori@kugi.kyoto-u.ac.jp
INTERNET: http://wdc.kugi.kyoto-u.ac.jp

WORLD DATA CENTRE FOR GEOMAGNETISM, MUMBAI
Indian Institute of Geomagnetism
Colaba, Mumbai, 400 005, INDIA
TEL: +91 22 215 0293
FAX: +91 22 218 9568
EMAIL: abh@iigs.iigm.res.in
INTERNET: http://iigm.res.in

Competing interests
The authors declare that they have no competing interests.

Authors' contributions
ET and CCF coordinated the work with full support from the IGRF-12 task force members. CDB generated Figure 3 and verified with independent software the values given in Table 4. All authors participated to the construction of magnetic field candidate models referenced in the manuscript. All authors analyzed and discussed the final IGRF-12 model and approved the final version of the manuscript.

Authors' information
ET, CCF, CDB, PA, AD, GH, WK, VL, FJL, SM, NO, VP, and TJS are members of the IGRF-12 task force.

Acknowledgements
The institutes that support magnetic observatories together with INTERMAGNET are thanked for promoting high standards of observatory practice and prompt reporting. The support of the CHAMP mission by the German Aerospace Center (DLR) and the Federal Ministry of Education and Research is gratefully acknowledged. The Ørsted Project was made possible by extensive support from the Danish Government, NASA, ESA, CNES, DARA, and the Thomas B. Thriges Foundation. The authors also acknowledge ESA for providing access to the Swarm L1b data. E. Canet acknowledges the support of ESA through the Support to Science Element (STSE) program. This work was partly funded by the Centre National des Etudes Spatiales (CNES) within the context of the project of the 'Travaux préparatoires et exploitation de la mission Swarm.' W. Kuang and A. Tangborn were funded by NASA and the NSF. This work was partly supported by the French 'Agence Nationale de la Recherche' under the grant ANR-11-BS56-011 and by the Région Pays de Loire, France. I. Wardinski was supported by the DFG through SPP 1488. The IGRF-12 task force finally wishes to express their gratitude to C. Manoj and A. Woods for maintaining the IGRF web pages at NGDC. This is IPGP contribution no. 3625.

Author details
[1]Laboratoire de Planétologie et Géodynamique de Nantes, University of Nantes, UMR 6112 CNRS, 1 chemin de la Houssinière F-44322, Nantes, France. [2]DTU Space, National Space Institute, Technical University of Denmark, Diplomvej 371, Lyngby, Denmark. [3]British Geological Survey, Murchison House, West Mains Road, EH9 3LA, Edinburgh, UK. [4]Cooperative Institute for Research in Environmental Sciences, University of Colorado, 216 UCB Boulder, CO 80309-0216, USA. [5]NOAA National Centers for Environmental Information (NCEI), 325 Broadway, E/GC, Boulder, CO 80305-3328, USA. [6]Institut de Physique du Globe de Paris, Sorbonne Paris Cité, Univ. Paris Diderot, CNRS, 1 rue Jussieu F-75005, Paris, France. [7]University Grenoble Alpes, ISTerre, CNRS, F-38041, Grenoble, France. [8]Université Grenoble Alpes, F-38000, Grenoble, France. [9]CEA, LETI, MINATEC Campus, F-38054, Grenoble, France. [10]Pushkov Institute of Terrestrial Magnetism, Ionosphere and Radio Wave Propagation, IZMIRAN, Kaluzhskoe Hwy 4, Troitsk, Moscow, Russia. [11]ETH Zürich Institut für Geophysik, Earth and Planetary Magnetism Group, Sonneggstrasse 58092 Zürich, Switzerland. [12]Institut de Physique du Globe de Strasbourg, UMR 7516-CNRS, Université de Strasbourg/EOST, Strasbourg, France. [13]Key Laboratory of Earth and Planetary Physics, Institute of Geology and Geophysics, Chinese Academy of Sciences 100029, Beijing, China. [14]Centre National d'Etudes Spatiales, 8 Avenue Edouard Belin, F-31400 Toulouse, France. [15]GFZ German Research Centre for Geosciences, Telegrafenberg, 14473 Potsdam Germany. [16]Planetary Geodynamics Laboratory, NASA GSFC, Greenbelt MD, USA. [17]School of Chemistry, University of Newcastle upon Tyne, NE1 7RU, Newcastle, UK. [18]CNES, Centre National d'Etudes Spatiales, 2 Place Maurice Quentin F-75001, Paris, France. [19]Départment de Géophysique USTHB, University of Algiers, PB 32 El-Alia Bab-Ezzouar, Algiers, Algeria. [20]Joint Center for Earth Systems Technology, UMBC, Baltimore, USA.

Received: 30 January 2015 Accepted: 13 April 2015
Published online: 27 May 2015

References

Alken P, Maus S, Chulliat A, Manoj C (2015) NOAA/NGDC candidate models for the 12th Generation International Geomagnetic Reference Field. Earth Planets Space 2015 67:68. doi:10.1186/s40623-015-0215-1

Barraclough DR (1987) International Geomagnetic Reference Field: the fourth generation. Phys Earth planet Int 48:279–292

Barton CE (1997) International Geomagnetic Reference Field: the seventh generation. J Geomag Geoelect 49:123–148

Chulliat A, Hulot G, Newitt LR (2010) Magnetic flux expulsion from the core as a possible cause of the unusually large acceleration of the north magnetic pole during the 1990s. J Geophys Res. 115, B07101, doi:10.1029/2009JB007143

Finlay CC, Maus S, Beggan CD, Bondar TN, Chambodut A, Chernova TA, Chulliat A, Golovkov VP, Hamilton B, Hamoudi M, Holme R, Hulot G, Kuang W, Langlais B, Lesur V, Lowes FJ, Lühr H, Macmillan S, Mandea M, McLean S, Manoj C, Menvielle M, Michaelis I, Olsen N, Rauberg J, Rother M, Sabaka TJ, Tangborn A, Tøffner-Clausen L, Thébault E, et al. (2010a) International Geomagnetic Reference Field: the eleventh generation. Geophys J Int 183(3):1216–1230. doi:10.1111/j.1365-246X.2010.04804.x.

Finlay CC, Maus S, Beggan CD, Hamoudi M, Lesur V, Lowes FJ, Olsen N, Thébault E (2010b) Evaluation of candidate geomagnetic field models for IGRF-11. Earth Planets Space IGRF Special issue 62(10):787–804

Finlay CC, Olsen N, Tøffner-Clausen L (2015) DTU candidate field models for IGRF-12 and the CHAOS-5 geomagnetic field model. Earth Planets Space, in press

Fournier A, Aubert J, Thébault E (2015) A candidate secular variation model for IGRF-12 based on Swarm data and inverse geodynamo modelling. Earth Planets and Space 67:81. doi:10.1186/s40623-015-0245-8

Gillet N, Barrois O, Finlay CC (2015) Stochastic forecasting of the geomagnetic field from the COV-OBS.x1 geomagnetic field model and candidate models for IGRF-12. Earth, Planets and Space 2015 67:71. doi:10.1186/s40623-015-0225-z

Hamilton B, Ridley VA, Beggan CD, Macmillan S (2015) The BGS magnetic field candidate models for the 12th generation IGRF. Earth, Planets and Space 2015 67:69. doi:10.1186/s40623-015-0227-x

Hamoudi M, Thébault E, Lesur V, Mandea M (2007) GeoForschungsZentrum Anomaly Magnetic MAp (GAMMA): a candidate model for the world digital magnetic anomaly map. Geochem Geophysics Geosystems 8(6)

Hemant K, Thébault E, Mandea M, Ravat D, Maus S (2007) Magnetic anomaly map of the world: merging satellite, airborne, marine and ground-based magnetic data sets. Earth Planet Sci Lett 260(1):56–71

Hulot G, Olsen N, Sabaka TJ (2007) The present field, geomagnetism. In: Schubert G (ed). Treatise on Geophysics, vol 5. Elsevier, Amsterdam. pp 33–75

IAGA Division I Study Group Geomagnetic Reference Fields (1975) International Geomagnetic Reference Field 1975. J Geomag Geoelect 27:437–439

Langel RA, Estes RH (1982) A geomagnetic field spectrum. Geophys Res Lett 9.4:250–253

Langel RA, Barraclough DR, Kerridge DJ, Golovkov VP, Sabaka TJ, Estes RH (1988) Definitive IGRF models for 1945, 1950, 1955, and 1960. J Geomag Geoelect 40:645–702

Langel RA (1992) International Geomagnetic Reference Field: the sixth generation. J Geomag Geoelect 44:679–707
Léger JM, Jager T, Bertrand F, Hulot G, Brocco L, Vigneron P, Lalanne X, Chulliat A, Fratter I (2015) In-flight performances of the absolute scalar magnetometer vector mode on board the Swarm satellites. Earth Planets and Space 57(25 April 2015):67
Lesur V, Rother M, Wardinski I, Schachtschneider R, Hamoudi M, Chambodut A (2015) Parent magnetic field models for the IGRF-12 GFZ-candidates. Earth Planets Space, in press
Lowes FJ (2000) An estimate of the errors of the IGRF/DGRF fields 1945–2000. Earth Planets Space 52(12):1207–1211
Macmillan S, Maus S, Bondar T, Chambodut A, Golovkov V, Holme R, Langlais B, Lesur V, Lowes FJ, Lühr H, Mai W, Mandea M, Olsen N, Rother M, Sabaka TJ, Thomson A, Wardinski I (2003) The 9th-Generation International Geomagnetic Reference Field. Geophys J Int 155:1051–1056
Mandea M, Macmillan S (2000) International Geomagnetic Reference Field - the eighth generation, 2000. Earth Planets Space 52:1119–1124
Maus S, Macmillan S, Chernova T, Choi S, Dater D, Golovkov V, Lesur V, Lowes FJ, Lühr H, Mai W, McLean S, Olsen N, Rother M, Sabaka TJ, Thomson A, Zvereva T (2005) The 10th-generation International Geomagnetic Reference Field. Geophys J Int 161:561–565
Maus S, Sazonova T, Hemant K, Fairhead JD, Ravat D (2007) National geophysical data center candidate for the world digital magnetic anomaly map. Geochem Geophys Geosyst 8(6):Q06017. doi:10.1029/2007GC001643
Neubert T, Mandea M, Hulot G, von Frese R, Primdahl F, Jørgensen JL, Friis-Christensen E, Stauning P, Olsen N, Risbo T (2001) Ørsted satellite captures high-precision geomagnetic field data, EOS. Trans Am. Geophys Un 82:81
Peddie NW (1982) International Geomagnetic Reference Field: the third generation. J Geomagn Geoelect 34:309–326
Reigber C, Lühr H, Schwintzer P (2002) CHAMP mission status. Adv Space Res 30:129–134
Saturnino D, Civet F, Langlais B, Thébault E, Mandea M (2015) Main field and secular variation candidate models for the 12th IGRF generation after 10 months of Swarm measurements, Earth, Planets and Space, in press
Thébault E, Finlay CC, Alken P, Beggan CD, Canet E, Chulliat A, Langlais B, Lesur V, Lowes FJ, Manoj C, Rother M, Schachtschneider R (2015) Evaluation of candidate geomagnetic field models for IGRF-12. Earth Planets Space, in press
Vigneron P, Hulot G, Olsen N, Léger JM, Jager T, Brocco L, Sirol O, Coïsson P, Lalanne X, Chulliat A, Bertrand F, Boness A, Fratter I (2015) A 2015 International Geomagnetic Reference Field (IGRF) candidate model based on Swarm's experimental absolute magnetometer vector mode data. Earth Planets Space, in press
Xu WY (2000) Unusual behaviour of the IGRF during the1945–1955 period. Earth Planets Space 52:1227–1233
Zmuda AJ (1971) The International Geomagnetic Reference Field: introduction. Bull Int Assoc Geomag Aeronomy 28:148–152

Langel RA (1992) International Geomagnetic Reference Field: the sixth generation. J Geomag Geoelect 44:679–707
Léger JM, Jager T, Bertrand F, Hulot G, Brocco L, Vigneron P, Lalanne X, Chulliat A, Fratter I (2015) In-flight performances of the absolute scalar magnetometer vector mode on board the Swarm satellites. Earth Planets and Space 57(25 April 2015):67
Lesur V, Rother M, Wardinski I, Schachtschneider R, Hamoudi M, Chambodut A (2015) Parent magnetic field models for the IGRF-12 GFZ-candidates. Earth Planets Space, in press
Lowes FJ (2000) An estimate of the errors of the IGRF/DGRF fields 1945–2000. Earth Planets Space 52(12):1207–1211
Macmillan S, Maus S, Bondar T, Chambodut A, Golovkov V, Holme R, Langlais B, Lesur V, Lowes FJ, Lühr H, Mai W, Mandea M, Olsen N, Rother M, Sabaka TJ, Thomson A, Wardinski I (2003) The 9th-Generation International Geomagnetic Reference Field. Geophys J Int 155:1051–1056
Mandea M, Macmillan S (2000) International Geomagnetic Reference Field - the eighth generation, 2000. Earth Planets Space 52:1119–1124
Maus S, Macmillan S, Chernova T, Choi S, Dater D, Golovkov V, Lesur V, Lowes FJ, Lühr H, Mai W, McLean S, Olsen N, Rother M, Sabaka TJ, Thomson A, Zvereva T (2005) The 10th-generation International Geomagnetic Reference Field. Geophys J Int 161:561–565
Maus S, Sazonova T, Hemant K, Fairhead JD, Ravat D (2007) National geophysical data center candidate for the world digital magnetic anomaly map. Geochem Geophys Geosyst 8(6):Q06017. doi:10.1029/2007GC001643
Neubert T, Mandea M, Hulot G, von Frese R, Primdahl F, Jørgensen JL, Friis-Christensen E, Stauning P, Olsen N, Risbo T (2001) Ørsted satellite captures high-precision geomagnetic field data, EOS. Trans Am. Geophys Un 82:81
Peddie NW (1982) International Geomagnetic Reference Field: the third generation. J Geomagn Geoelect 34:309–326
Reigber C, Lühr H, Schwintzer P (2002) CHAMP mission status. Adv Space Res 30:129–134
Saturnino D, Civet F, Langlais B, Thébault E, Mandea M (2015) Main field and secular variation candidate models for the 12th IGRF generation after 10 months of Swarm measurements, Earth, Planets and Space, in press
Thébault E, Finlay CC, Alken P, Beggan CD, Canet E, Chulliat A, Langlais B, Lesur V, Lowes FJ, Manoj C, Rother M, Schachtschneider R (2015) Evaluation of candidate geomagnetic field models for IGRF-12. Earth Planets Space, in press
Vigneron P, Hulot G, Olsen N, Léger JM, Jager T, Brocco L, Sirol O, Coïsson P, Lalanne X, Chulliat A, Bertrand F, Boness A, Fratter I (2015) A 2015 International Geomagnetic Reference Field (IGRF) candidate model based on Swarm's experimental absolute magnetometer vector mode data. Earth Planets Space, in press
Xu WY (2000) Unusual behaviour of the IGRF during the1945–1955 period. Earth Planets Space 52:1227–1233
Zmuda AJ (1971) The International Geomagnetic Reference Field: introduction. Bull Int Assoc Geomag Aeronomy 28:148–152

B.2 Electrical conductivity of the Earth's mantle from the first Swarm magnetic field measurements

During my thesis I participated in the work concerning the modelling of the induced electrical currents in the Earth's mantle to infer information on its structure. This work used the first months of the Swarm mission measurements. The resulting paper is reproduced here.

AGU PUBLICATIONS

Geophysical Research Letters

RESEARCH LETTER
10.1002/2015GL063397

Special Section:
ESA's Swarm Mission, One Year in Space

Electrical conductivity of the Earth's mantle from the first Swarm magnetic field measurements

F. Civet[1], E. Thébault[1], O. Verhoeven[1], B. Langlais[1], and D. Saturnino[1]

[1]CNRS, University of Nantes, Laboratoire de Planétologie et de Géodynamique, UMR-6112, Nantes, France

Key Points:
- Eletromagnetic induction from satellite data
- Electrical conductivity of the Earth's mantle
- Temperature gradient of the lower mantle

Correspondence to:
F. Civet,
francois.civet@univ-nantes.fr

Citation:
Civet, F., E. Thébault, O. Verhoeven, B. Langlais, and D. Saturnino (2015), Electrical conductivity of the Earth's mantle from the first Swarm magnetic field measurements, *Geophys. Res. Lett.*, *42*, doi:10.1002/2015GL063397.

Received 18 FEB 2015
Accepted 26 MAR 2015
Accepted article online 2 APR 2015

Abstract We present a 1-D electrical conductivity profile of the Earth's mantle down to 2000 km derived from L1b Swarm satellite magnetic field measurements from November 2013 to September 2014. We first derive a model for the main magnetic field, correct the data for a lithospheric field model, and additionally select the data to reduce the contributions of the ionospheric field. We then model the primary and induced magnetospheric fields for periods between 2 and 256 days and perform a Bayesian inversion to obtain the probability density function for the electrical conductivity as function of depth. The conductivity increases by 3 orders of magnitude in the 400–900 km depth range. Assuming a pyrolitic mantle composition, this profile is interpreted in terms of temperature variations leading to a temperature gradient in the lower mantle that is close to adiabatic.

1. Introduction

On 22 November 2013, the European Space Agency successfully launched the Swarm satellite mission devoted to the study of the Earth's magnetic environment. The Swarm scientific mission consists of three identical satellites carrying vector and scalar magnetometers, two of which (A and C) flying side by side at about 450 km and a third (B) being at about 530 km with a phase shift increasing with time that will allow the constellation to survey all local times during its nominal lifetime. Swarm will thus permit the best ever separation of the internal and external magnetic field sources. This configuration, in particular, opens the possibility to better probe the conductivity of the Earth's mantle [*Kuvshinov et al.*, 2006; *Püthe and Kuvshinov*, 2013a, 2013b; *Velímský*, 2013], which is one of the primary science objectives of the mission [e.g., *Olsen et al.*, 2013]. Electromagnetic (EM) induction studies from space were carried out during the past two decades [*Olsen*, 1999a; *Constable and Constable*, 2004; *Kuvshinov and Olsen*, 2006; *Velímský*, 2010; *Civet and Tarits*, 2013]. They show reasonably good agreement for periods ranging from 1 day to a few months but differ more significantly at the shortest and longest periods. This difficulty arises because some internal and external magnetic field sources overlap in time and in space so that their separation is ambiguous over these time periods [e.g., *Olsen*, 1999b]. For example, the long-term external field variation can hardly be distinguished from the Earth's main field secular variation, and periods of about 1 day are smeared with various effects such as the ionospheric field daily variation [*Tarits and Grammatica*, 2000] or the field induced by ocean tides [*Tyler et al.*, 2003]. A further complication is due to the heterogeneous distribution of the satellite magnetic field measurements in space and especially in time that introduces data gaps [*Civet and Tarits*, 2013]. The common way to circumvent this difficulty is to average the magnetic components over one or several orbits [e.g., *Olsen*, 1999a]. Another approach recently put forward by *Civet and Tarits* [2013, 2014] in the context of the planetary exploration is to fill gaps using a proxy for the variability of the external magnetic field.

Despite these limitations EM induction satellite-based studies generally agree with an electrical conductivity increase with depth from $\simeq 0.01$ S m^{-1} near the surface to $\simeq 10$ S m^{-1} at 2000 km depth. Such conductivity values are supported by laboratory mineral conductivity measurements [e.g., *Xu et al.*, 2000]. However, major mineralogical discontinuities arising in the mantle are not seen by these EM studies without prior information.

Electrical conductivity of mantle minerals depends on internal structure through pressure, temperature, oxygen fugacity, and composition. Composition includes not only the constituent mineral phase but also the chemistry of the phase such as iron content and minor phases such as partial melt and water. Recent laboratory measurements of mineral conductivity (see the reviews of *Yoshino* [2010] and *Karato* [2011]) have identified the sensitivity of the conductivity to all these parameters and therefore allow a precise modeling of the conductivity in terms of internal structure. For example, *Khan and Shankland* [2012] have recently

AGU Geophysical Research Letters 10.1002/2015GL063397

evaluated the water content in the Earth's mantle from Bayesian inversion of electromagnetic induction data recorded at geomagnetic observatories distributed across the globe using laboratory-based conductivity profiles.

In this paper we derive a 1-D electrical conductivity profile from electromagnetic induction theory based on 10 months of Swarm satellite measurements using a Bayesian approach. These profiles are interpreted in terms of temperature variations using laboratory-based electrical conductivity of minerals.

2. Method

The application of the EM induction theory to remote magnetic field measurements can be complex, and we introduce some classical simplifying assumptions (see, for instance, *Kuvshinov*, [2012], for a recent review). First, the low Earth-orbiting Swarm satellites are assumed to fly in source-free regions where the magnetic field $\mathbf{B}$ derives from the potential V through $\mathbf{B} = -\nabla V$. The magnetic potential V in space, being the solution of Laplace's equation, can be expanded in terms of internal and external spherical harmonic (SH) functions. The EM method for probing the mantle requires the contributions of the external magnetic field and of their induced counterparts to be isolated from other fields such as the core and the lithospheric fields. The magnetic field measurements have thus to be corrected for a model describing the static internal magnetic fields and their temporal variations. After these corrections, the magnetic field residuals are expected to contain only the externally inducing and the internally induced parts. Then the major source of external field is assumed to be produced by the ring current in the Earth's magnetosphere for periods longer than 1 day. This source is far enough from the measurements to be considered as large scale and mostly dipolar but close enough to the Earth to further assume that the electromagnetic wave is stationary for these periods. This 1 day lower bound for the period also allows us to mitigate the induction effects from the Earth's ionospheric field that is prominent at shorter periods and smaller spatial wavelengths [e.g., *Friis-Christensen et al.*, 2006; *Olsen et al.*, 2006]. Under these approximations the magnetospheric potential can be written in the space frequency domain as

$$V(\mathbf{r},\omega) = a\sum_{n=1}^{\infty}\sum_{m=-n}^{n}\left[\epsilon_n^m(\omega)\left(\frac{r}{a}\right)^n + \iota_n^m(\omega)\left(\frac{a}{r}\right)^{n+1}\right]P_n^{|m|}(\cos\theta)\,e^{im\phi}, \tag{1}$$

where ω is the angular frequency, a the Earth's reference radius equal to 6371.2 km, and ϵ and ι are the external (inducing) and internal (induced) Gauss coefficients, respectively. $P_n^m(\cos\theta)$ are the associated Schmidt-normalized Legendre function, of degree n and order m, and $\mathbf{r}$ the vector position where r, θ, and ϕ are radius, colatitude, and longitude, respectively. A classical procedure to infer the 1-D electrical conductivity of the mantle is to estimate geomagnetic response functions. These functions are defined as the ratio, in the frequency domain, between different observed electromagnetic components [e.g., *Olsen*, 1999b]. The response function depends only on the degree n, assuming that the Earth's mantle is spherically symmetric. We further consider that the geometry of the inducing source is dominated by the SH degree 1 and order 0 of the ring current. Once external and internal potentials are known for several frequencies, it becomes possible to construct a model in depth of the electrical conductivity in the Earth's interior [e.g., *Schmucker*, 1985]. We use a forward problem that estimates the internal response $\iota^m_{n,\,\mathrm{model}}(\omega)$ of a conductive medium induced by a unitary source. We further use the linearity of the transfer function Q (i.e., $\iota = Q.\epsilon$) to compare $\iota^m_{n,\,\mathrm{model}}(\omega)$ and $\iota^m_{n,\,\mathrm{observed}}(\omega)$ [*Tarits and Mandea*, 2010; *Civet and Tarits*, 2013, 2014]. The algorithm assumes a spherical semi-infinite medium of high electrical conductivity at the core mantle boundary and goes upward through successive conductive layers to estimate the induced response in terms of internal potentials for the considered frequencies ω.

3. Data Selection and Processing

3.1. Selection of the Swarm Measurements

The magnetic field measurements of the three Swarm satellites are considered from 26 November 2013 to 27 September 2014 (ESA L1 product, baseline 03). We select only the latest or the reprocessed Swarm data. We screen their quality flags defined in the Level1b Product Definition Document [*Tøffner-Clausen*, 2013]. We reject all Absolute Scalar Magnetometer (ASM) measurements corresponding to the flag quality code 255 and keep only the Vector Field Magnetometer (VFM) measurements identified as being in nominal mode. We also exclude the measurements made during satellite maneuvers which induce artificial time-varying magnetic fields. We carried out a preliminary comparison between the selected data and a candidate to the eleventh

AGU Geophysical Research Letters 10.1002/2015GL063397

generation of the International Geomagnetic Reference Field model [*Thébault et al.*, 2010]. This allowed us to identify and remove large outliers remaining in the data sets for specific days (25 March, 26 March, 8 April, 11 September, and 12 September).

3.2. Correction for the Main and Lithospheric Fields

We correct the raw vector measurements ($\mathbf{B}_{\text{raw}}$) with a dedicated main field model ($\mathbf{B}_m$) built from a subset of the entire Swarm magnetic measurements. This model is computed using the following approach. We first subsample the data set every 10 s and separate the scalar and vector data into midlatitudes (between −52° and 52° magnetic latitudes) and polar regions (for magnetic latitudes larger than $|52°|$). Vector data in the polar regions are discarded. All scalar and vector data at midlatitudes are selected for 22:00–5:00 local time in order to minimize the contributions from the ionospheric field. In contrast the scalar data are used in the polar regions at all local times in the dark side (Sun at least 2° below the horizon). A further selection is based on the provisional *Dst* (Disturbance storm time) and *ap* (index of the auroral geomagnetic activity). The *Dst* index and its time variation over the three previous hours is requested to be lower than |5| nT, and the *ap* index, which measures the general magnetic activity at the planetary scale, is requested to satisfy $ap \leq 27$ after having met the same requirement over the previous 3 h. All selected data correspond to $Kp \leq 2°$ (*Kp* is a 3 h planetary index of the geomagnetic activity).

The resulting subset of measurements is then inverted in terms of spherical harmonics up to degree 40 for the internal part with a linear secular variation up to degree 13. We coestimate the static external magnetic field up to degree 2 with the degree 1 parameterized by the provisional *Dst* index. The inversion is carried out using a robust iteratively reweighted least squares (IRLS) inversion scheme with Huber weighting to minimize the effect of outliers. This field model $\mathbf{B}_m$ is then used to correct the entire selected vector measurements. The scalar measurements are now no longer considered. Then the lithospheric field model ($\mathbf{B}_l$) of *Lesur et al.* [2010] is used to correct for the lithospheric field at higher spatial resolution, between degrees 41 and 80. This step is important to reduce the leakage of the lithospheric field along the satellite orbits [*Thébault et al.*, 2012]. A visual inspection of the corrected data $\tilde{\mathbf{B}}$ (with $\tilde{\mathbf{B}} = \mathbf{B}_{raw} - \mathbf{B}_m - \mathbf{B}_l$) allows us to identify measurements with remaining suspicious behavior. We identify the measurements that differ by more than 3.5 times the standard deviation of the residual field at midlatitudes. When outliers are identified, the entire day is removed from our database, including in the polar areas. Figure 1 shows that before this processing, measurements from satellites A and C contained aberrant values that need to be filtered out. The ionospheric field and, in particular, the equatorial electrojet in the latitude range [−20°, 20°], can be seen in the right part of Figure 1. Finally, only data for which the Sun is 6° above the horizon are selected. This limit is a good compromise between the global data coverage and the reduction of ionospheric disturbances. One side effect of selecting mostly sunlit data is to introduce gaps in the time series for each satellite data set lasting from a few hours to a few days.

3.3. Computation of the Electrical Response

In the selected and corrected measurements the magnetospheric field is assumed to be dominant over the ionospheric field. This is a simplification considering the complexity of separating ionospheric from magnetospheric parts. Nevertheless, we restrict ourselves to periods larger than 1 day to further reduce the effect of the ionospheric field at shorter periods [*Hutton*, 1972]. For each day we select the residual measurements of the three satellites and estimate the external magnetospheric field and its induced counterpart. We consider all three magnetic components of the magnetic field to better separate the external and the internal contributions.

The inversion is carried out in the geomagnetic dipole coordinate system. All vector data are weighted by $\sin\theta$, in order to account for the higher data density in the polar regions. The parameter estimation relies again on an IRLS algorithm using Huber weighting, and the solution was expanded to SH degree 2 to minimize the spectral leakage effects of smaller spatial scales on the degree 1 parameter. For each day we verify that the inverse problem is well conditioned (small covariance between Gauss coefficients). This guarantees that the separation between internal and external sources is numerically reliable and that the estimated Gauss coefficients are individually meaningful. We exploit this lack of correlation to directly estimate the standard deviation of the Gauss coefficients from the diagonal elements of the covariance matrix. In addition we apply a bootstrap estimation approach to investigate the fluctuation of the parameter estimation. Each day, the internal and external Gauss coefficients are estimated 1000 times from random subsets containing each 50% of the entire data set. The daily standard deviation on each Gauss coefficient estimated by this approach

AGU Geophysical Research Letters 10.1002/2015GL063397

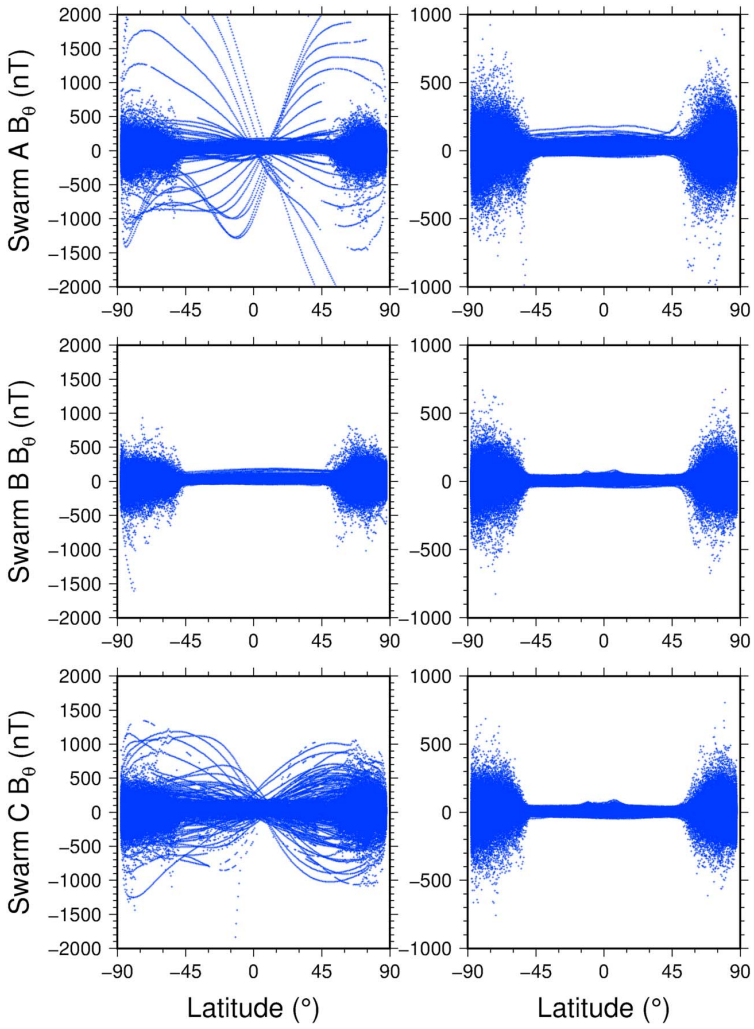

Figure 1. North component of Swarm magnetic field measurements after reduction of the main and lithospheric fields, (left) before and (right) after rejection of outliers (see text for details).

is smaller than the standard deviation estimated via the parameter covariance matrix, confirming that the internal and external coefficients are robustly estimated. Finally, the effect of the mismatch between the ASM magnetic field intensity and the intensity field computed from the VFM magnetometers, which may reach a few nT peak to peak, is analyzed in the time and frequency domains (not shown). We verify that this mismatch does not significantly affect the estimation of the dipole Gauss coefficients for periods exceeding 1 day.

The daily estimations of the internal and external Gauss coefficients are hereafter noted $\tilde{r}_n^m(t)$ and $\tilde{\varepsilon}_n^m(t)$, with $\tilde{\sigma}_i(t)$ and $\tilde{\sigma}_e(t)$ their estimated standard deviation, respectively. Only the degree 1 and order 0 coefficient is used in this study. Nonetheless, we argue that more internal/external field coefficients will be resolved when longer measurement time series are available and when the satellites reach their definitive orbital configuration, thus providing robust magnetospheric field estimations at different local times.

One major advantage of the Swarm mission is that having three satellites flying reduces the longest time gap to 1 day. Five such gaps are found, when comparable studies using a single satellite may have gaps exceeding 15 days [*Civet and Tarits*, 2013]. For the internal and external coefficients of degree 1 and order 0, we fill these temporal gaps with the help of the provisional *Dst* index. The direct comparison between the *Dst* index and

AGU Geophysical Research Letters 10.1002/2015GL063397

the Gauss coefficients is not feasible, but a linear correlation between the Gauss coefficients and the *Dst* index can be assumed [*Langel and Estes*, 1985]. A regression analysis over the available time series leads to

$$\begin{aligned} \tilde{\imath}_1^0(t) &= -2.12 - 0.14\ Dst(t), \\ \tilde{\varepsilon}_1^0(t) &= 12.33 - 0.53\ Dst(t). \end{aligned} \tag{2}$$

These linear relationships are used to convert the mean *Dst* index into $\tilde{\imath}_1^0(t)$ and $\tilde{\varepsilon}_1^0(t)$ for the five missing days, leading to a regular and complete time series over 305 consecutive days; for these five above mentioned days, the standard deviation of the dipole coefficients is set to 0.

The Fourier transform $\tilde{\imath}_1^0(\omega)$ and $\tilde{\varepsilon}_1^0(\omega)$ of the time series and, by linearity, their standard deviation $\tilde{\sigma}_i(\omega)$ and $\tilde{\sigma}_e(\omega)$ are computed. Each time series of 305 days was tapered to zero until the next power of 2 (512 days) in order to avoid spectral leakage and Gibbs effects. This defines a new space of frequencies ω_f. The signal-to-noise ratio for the external potential is 1 – 2 orders of magnitude larger than for the internal potential. From $\tilde{\varepsilon}_1^0(\omega_f)$ we then compute the estimated complex internal induced response $\tilde{\varepsilon}_1^0(\omega)$ for periods ranging between 2 and 256 days assuming that the inducing potential $\tilde{\varepsilon}_1^0(\omega_f)$ is error-free, thus considering in the following only the standard deviation $\tilde{\sigma}_i(\omega)$.

3.4. Estimation of the Vertical Mantle Electrical Conductivity Profile

Since our algorithm computes the internal response from an inducing source and because we can neglect the errors on the inducing source, we impose that conductivity parameters σ should minimize

$$\chi^2 = \sum_{f=1}^{N_f} \left[\log\left(\left| \frac{\tilde{\imath}_1^0(\omega_f) - \imath_1^0(\omega_f)}{\tilde{\sigma}_i(\omega_f)} \right| \right) \right]^2 + \alpha \sum_{l=1}^{L} \log\left(\frac{\sigma_{l+1}}{\sigma_l} \right). \tag{3}$$

where N_f is the number of frequencies used and L is the number of layers. This inverse problem is nonlinear and generally ill-posed, especially when dealing with noisy measurements that are only available for a restricted time period. We designed a Markov chain Monte Carlo (McMC) algorithm to solve equation (3) to circumvent some of the difficulties arising from such a nonlinear ill-posed inverse problem relying on a poorly conditioned inverse matrix. Within the Bayesian framework, the inverse problem consists in estimating marginal probability distributions for the conductivity. It is well known [e.g., *Tarantola*, 1987, chapter 2] that this requires an extensive exploration of the model space. An elegant way to overcome this difficulty is to construct a Markov chain during which model parameters are randomly updated at each iteration. In the McMC algorithm, parameter values decreasing the misfit function have better chance to be reselected at the next iteration than values increasing it. The second term of equation (3) is designed to smooth the conductivity contrasts between two consecutive layers with a damping parameter α. We choose a value of α so that the smoothing constraint does not exceed about 2% of the total cost function on average, i.e., the conductivity estimates are not entirely determined by the smoothing constraint. The posterior marginal probability distribution is explored through a Markov process based upon a Gibbs's sampler of the conductivity values (see, for instance, *Schott et al.* [1999], for a detailed algorithm). We consider mantle conductivity values lying between 10^{-4} and 10^3 S m^{-1} and divide this interval into 50 cells equally spaced in a logarithmic scale. We do not a priori impose the number and thickness of the vertical layers, as *Constable* [1993] highlights the danger of the a priori layered approach that results in oscillatory solutions. Instead, the algorithm arbitrarily starts with four layers of 500 km thickness between the surface and 2000 km depth, and iteratively refines the vertical discretization of the conductivity profile in the following way. After convergence of the Markov chain for the initial problem with four layers, the algorithm identifies the maximum likelihood estimated values of the conductivity for each layer. When the difference of conductivity between two consecutive layers exceeds half an order of magnitude, the algorithm considers that there is a discontinuity. It, therefore, divides the lowermost layer into two thinner layers. The thickness of the upper one of these two is rounded to the nearest 50 km (maximum vertical resolution). As a result, the lower part of the divided layer is always as thick as or thinner than the upper one, and no layer is thinner than 50 km. A new Markov chain inversion is then run for the problem involving this new distribution of layers. This procedure is designed to obtain a conductivity model whose vertical complexity is determined by the data rather than by the a priori model of the mantle stratification. At the end of the iterative process, when no discontinuity is found for layers thicker than 50 km, the algorithm returns the probability density function (pdf) with the maximum likelihood of the electrical conductivity for 14 layers of varying thickness. The vertical resolution is better in the 500 km to 1000 km depth range thus

AGU Geophysical Research Letters 10.1002/2015GL063397

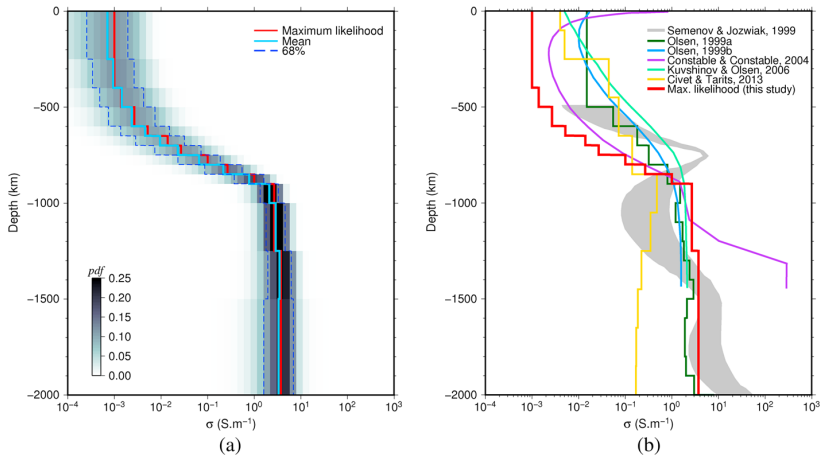

Figure 2. (left) Probability density function (pdf) of electrical conductivity profile obtained from McMC inversion of Swarm L1b data. The maximum likelihood (red) and the mean value (plain blue) with 1 standard deviation error bar (dashed blue) are also represented. (right) Maximum likelihood of the McMC pdf (red) compared to previous studies [*Semenov and Jozwiak*, 1999; *Olsen*, 1999a, 1999b; *Constable and Constable*, 2004; *Kuvshinov and Olsen*, 2006; *Civet and Tarits*, 2013].

showing the depths at which the conductivity values are better constrained by the measurements. The normalized root-mean-square between the observed and the maximum likelihood induced Fourier coefficients after convergence of the McMC is 1.43 and their correlation is 0.90. This gives us confidence that the model is statistically significant.

4. Results and Discussion

We show in Figure 2 the pdf of the electrical conductivity profile derived from the Bayesian inversion of internally induced potentials. The pdf maximum likelihood, its mean, and its associated 1 standard deviation interval, are also displayed, as well as profiles of previous studies. As the pdf is not symmetrically distributed, small discrepancies appear between the mean and the maximum likelihood. In the whole depth range, the one sigma uncertainty is of the order of 0.5 log unit with a somewhat larger uncertainty between 0 and 500 km depth, because we do not consider periods shorter than 2 days.

The pdf of the electrical conductivity profile is characterized by an increase from 0.001 S m^{-1} at 400 km depth to $\simeq$ 1 S m^{-1} at 900 km depth. This 3 orders of magnitude increase may be related to the mineralogical transformations of upper mantle minerals into their lower mantle phases [e.g., *Xu et al.*, 2000]. For depths larger than 900 km, the electrical conductivity shows a small increase from $\simeq$ 1 S m^{-1} at 900 km depth to $\simeq$ 4 S m^{-1} at 2000 km depth. As no mineralogical transformation occurs in this depth range, the small conductivity increase can be directly related to pressure increase and temperature variation. Compared to previous studies by *Semenov and Jozwiak* [1999], *Olsen*, [1999a, 1999b], *Kuvshinov and Olsen* [2006], and *Civet and Tarits* [2013], we observe that our results are characterized by a much smaller conductivity in the upper mantle and the transition zone. For depths larger than 800 km, our results show a very good agreement with the results of *Olsen* [1999a, 1999b] and *Kuvshinov and Olsen* [2006]. Below 1000 km there is a disagreement with the results of *Constable and Constable* [2004], which is possibly due to the misuse of the multitaper approach as pointed by *Kuvshinov and Olsen* [2006].

We tentatively interpret this electrical conductivity profile in terms of temperature variations with depth. We follow the modeling of *Khan and Shankland* [2012] who computes the electrical conductivity of a rock aggregate as the effective medium mean of individual mineral phase conductivity σ_i of the form

$$\sigma_i = \sigma_0^i \exp\left(\frac{-H_i}{kT}\right) \tag{4}$$

where T is temperature and k is Boltzmann constant. The preexponential factor σ_0^i and the activation enthalpy H_i depend on the composition of mineral i and to a lesser extent on pressure and oxygen fugacity. Two

AGU Geophysical Research Letters 10.1002/2015GL063397

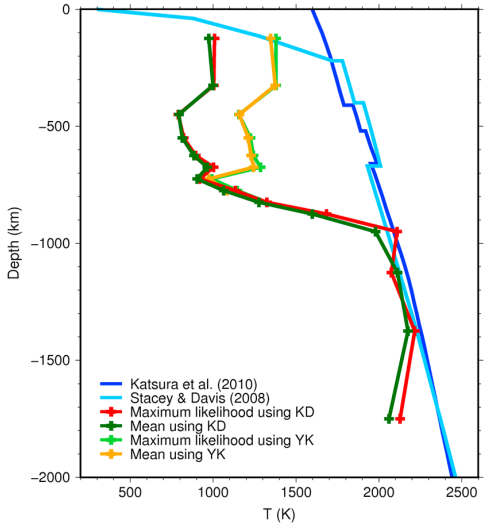

Figure 3. Temperature profiles associated with maximum likelihood and mean conductivity values of Figure 2. Temperature profiles in red and dark green are obtained with the electrical conductivity database of *Karato* [2011] (KD), whereas light green and orange profiles are obtained with the database of *Yoshino* [2010] (YK). Geotherm of *Stacey and Davis* [2008], along with the adiabatic temperature profile of *Katsura et al.* [2010] are shown for comparison.

different databases are used for σ_0^i and H_i parameters: YK (Yoshino, Katsura, and coworkers [*Yoshino*, 2010]) and KD (Karato, Dai, and coworkers [*Karato*, 2011]). The YK database is supplemented with the more recent results of *Zhang et al.* [2012] in order to model the conductivity of hydrous pyroxene along with corrected values for the conductivity of hydrous wadsleyite [*Yoshino and Katsura*, 2012]. These two databases are different for the upper mantle but agree for lower mantle minerals for which the measurements of *Xu et al.* [2000] are used in both cases.

Although oxygen fugacity correction is included in the two databases, assumptions on composition and pressure profile are required in order to interpret conductivity in terms of temperature only. The mantle mineralogy is assumed to be given by a pyrolitic model [*Irifune*, 1987]. The mineralogical transformations are computed at each pressure/temperature conditions according to phase diagrams discussed in *Vacher et al.* [1998] for dry mineralogy. Water content is assumed to be equal to 0.01% in the upper mantle and 0.1% in the mantle transition zone, in agreement with both geochemical analysis of basalts and study of geophysically inferred electrical conductivity of Earth's interior [*Karato*, 2011]. Pressure is assumed to be identical to preliminary reference Earth model [*Dziewonski and Anderson*, 1981] values. These assumptions on composition and pressure allow us to isolate the temperature effect on conductivity and thus to derive a temperature profile from conductivity through standard numerical root search.

We show in Figure 3 the interpretation in terms of temperature variations of the maximum likelihood and mean estimators of electrical conductivity pdf of Figure 2 calculated using the KD and YK mineralogical databases sampled at the center of each layer. Two recent geotherms [*Stacey and Davis*, 2008; *Katsura et al.*, 2010] are also represented. Given the close agreement between the maximum likelihood and the mean electrical conductivity in the upper mantle, the variations of the temperature deduced from these estimators are nearly identical in this depth range for a given model. The choice of the database used to constrain the conductivity of minerals, however, induces large differences in the temperature profile in the upper mantle and the transition zone (Figure 3). This is largely due to the discrepancies that exist between laboratory measurements of hydrous minerals performed by the two research groups.

In the lower mantle both databases are identical and share the modeling of *Xu et al.* [2000] for lower mantle phases. In the 1000–1500 km depth range, the computed temperature profiles are close to the geotherms of *Stacey and Davis* [2008] and *Katsura et al.* [2010] and are characterized by an adiabatic gradient of 0.3 K/km. For depths greater than 1500 km, the mean and maximum likelihood estimators become significantly different, highlighting the decrease in resolution in the pdf at such depths.

Negative temperature gradients are observed in the upper mantle and transition zone. One is found 50 km below the 670 km deep transition zone. High-pressure mineral phases are more conductive than their low-pressure ones, and conductivity increase is expected. As the interpretation of conductivity is done in terms of temperature only, an increase in conductivity smaller than the one predicted by laboratory-based measurements and pyrolitic model is falsely interpreted as a temperature decrease. Instead, it should be interpreted as inaccurate estimate of the depth at which the conductivity increases or as erroneous assumptions on composition of the a priori pyrolitic model or the chosen water content. Two other negative gradients are observed in the uppermost and lowermost parts of the profile where uncertainties on the conductivity

AGU Geophysical Research Letters 10.1002/2015GL063397

model are larger (Figure 2). Joint inversion of Swarm data supplemented with complementary data (such as seismological data) are required to go beyond the simple conductivity to temperature interpretation in order to discriminate between temperature and composition effects.

5. Conclusions

In this study we use magnetic field measurements acquired during the first 10 months of the ESA Swarm mission to estimate the ratio of the externally inducing to the internally induced magnetic field and to derive a 1-D electrical conductivity profile to a depth of 2000 km. We start from the raw L1b Swarm magnetic field measurements of the three satellite vector and scalar magnetometers. We build a model for the main internal magnetic field and its secular variation to highlight the magnetospheric external field and its induced part and then estimate the electrical conductivity in the Earth's mantle. This, we think, warrants a good control of the entire processing scheme that allows detecting electrical conductivity discontinuities. The 1-D conductivity profile is then interpreted in terms of temperature variations, and we obtain a temperature gradient in the lower mantle which is close to an adiabatic one.

We note that these results have previously been obtained by *Khan and Shankland* [2012] from observatory data and relying on thermodynamical modeling to identify the phase transitions. Using less than 1 year of satellite measurements is not sufficient to derive a definitive temperature profile for the Earth's mantle. We, nevertheless, show that the Swarm mission already provides consistent and promising results in the lower mantle and has also the ability to challenge our current view of temperature and composition in the upper mantle and transition zone. This study will be pursued as more Swarm measurements become available. We also have to acknowledge that discrepancies between laboratory measurements of hydrous iron-bearing minerals have to be reconciled too. In order to use the whole information contained in the pdf of the conductivity, a further step will be to perform a Bayesian inversion of the Swarm data directly in terms of temperature, along with composition if complementary data or priors are used [e.g., *Verhoeven et al.*, 2009; *Khan and Shankland*, 2012]. It is also hoped that additional measurements acquired during the next years of the Swarm mission will considerably improve these results. First, the number of available measurements will provide narrower estimates of the electrical conductivity pdf function. Second, longer time periods will allow deeper conductivity estimates. The final orbital configuration will also permit a better estimation of the magnetospheric fields at shorter periods and thus to investigate the conductivity at shallower depths.

Acknowledgments
Swarm Level 1b products are freely available by FTP to ESA-EO registered users (for access details, see https://earth.esa.int/web/guest/swarm/data-access). This work was partly funded by the Centre National des Études Spatiales (CNES) within the context of the project of the "Travaux préparatoires et exploitation de la mission Swarm." We also thank Pascal Tarits for useful discussions. We are grateful to Amir Khan, Alexei Kuvshinov, Christoph Püthe, and an anonymous reviewer for their constructive remarks.

The Editor thanks Amir Khan and an anonymous reviewer for their assistance in evaluating this paper.

References

Civet, F., and P. Tarits (2013), Analysis of magnetic satellite data to infer the mantle electrical conductivity of telluric planets in the solar system, *Planet. Space Sci.*, *84*, 102–111.
Civet, F., and P. Tarits (2014), Electrical conductivity of the mantle of Mars from MGS magnetic observations, *Earth Planets Space*, *66*(1), 85, doi:10.1186/1880-5981-66-85.
Constable, S. (1993), Constraints on mantle electrical conductivity from field and laboratory measurements, *J. Geomagn. Geoelec.*, *45*(9), 707–728.
Constable, S., and C. Constable (2004), Observing geomagnetic induction in magnetic satellite measurements and associated implications for mantle conductivity, *Geochem. Geophys. Geosyst.*, *5*, Q01006, doi:10.1029/2003GC000634.
Dziewonski, A. M., and D. L. Anderson (1981), Preliminary reference Earth model, *Phys. Earth Planet. Inter.*, *25*(4), 297–356.
Friis-Christensen, E., H. Lühr, and G. Hulot (2006), Swarm: A constellation to study the Earth's magnetic field, *Earth Planets Space*, *58*, 351–358.
Hutton, R. (1972), Some problems of electromagnetic induction in the equatorial electrojet region-I magneto-telluric relations, *Geophys. J. R. Astron. Soc.*, *28*(3), 267–284, doi:10.1111/j.1365-246X.1972.tb06128.x.
Irifune, T. (1987), An experimental investigation of the pyroxene-garnet transformation in a pyrolite composition and its bearing on the constitution of the mantle, *Phys. Earth Planet. Int.*, *45*, 324–336, doi:10.1016/0031-9201(87)90040-9.
Karato, S. (2011), Water distribution across the mantle transition zone and its implications for global material circulation, *Earth Planet. Sci. Lett.*, *301*, 413–423, doi:10.1016/j.epsl.2010.11.038.
Katsura, T., A. Yoneda, D. Yamazaki, T. Yoshino, E. Ito, D. Suetsugu, C. Bina, T. Inoue, D. Wiens, and M. Jellinek (2010), Adiabatic temperature profile in the mantle, *Phys. Earth Planet. Inter.*, *183*, 212–218, doi:10.1016/j.pepi.2010.07.001.
Khan, A., and T. Shankland (2012), A geophysical perspective on mantle water content and melting: Inverting electromagnetic sounding data using laboratory-based electrical conductivity profiles, *Earth Planet. Sci. Lett.*, *317*, 27–43, doi:10.1016/j.epsl.2011.11.031.
Kuvshinov, A. (2012), Deep electromagnetic studies from land, sea, and space: Progress status in the past 10 years, *Surv. Geophys.*, *33*, 169–209, doi:10.1007/s10712-011-9118-2.
Kuvshinov, A., and N. Olsen (2006), A global model of mantle conductivity derived from 5 years of CHAMP, Ørsted, and SAC-C magnetic data, *Geophys. Res. Lett.*, *33*, L18301, doi:10.1029/2006GL027083.
Kuvshinov, A., T. Sabaka, and N. Olsen (2006), 3-D electromagnetic induction studies using the Swarm constellation: Mapping conductivity anomalies in the Earth's mantle, *Earth Planets Space*, *58*, 417–427.
Langel, R., and R. Estes (1985), The near-Earth magnetic field at 1980 determined from MAGSAT data, *J. Geophys. Res.*, *90*(B3), 2495–2509, doi:10.1029/JB090iB03p02495.

AGU Geophysical Research Letters 10.1002/2015GL063397

Lesur, V., I. Wardinski, M. Hamoudi, and M. Rother (2010), The second generation of the GFZ Reference Internal Magnetic Model: GRIMM-2, *Earth Planets Space*, *62*, 765–773, doi:10.5047/eps.2010.07.007.
Olsen, N. (1999a), Long-period (30 days–1 year) electromagnetic sounding and the electrical conductivity of the lower mantle beneath Europe, *Geophys. J. Int.*, *138*(1), 179–187, doi:10.1046/j.1365-246x.1999.00854.x.
Olsen, N. (1999b), Induction studies with satellite data, *Surv. Geophys.*, *20*(3), 309–340.
Olsen, N., R. Haagmans, T. J. Sabaka, A. Kuvshinov, S. Maus, M. E. Purucker, M. Rother, V. Lesur, and M. Mandea (2006), The Swarm end-to-end mission simulator study: A demonstration of separating the various contributions to Earth's magnetic field using synthetic data, *Earth Planets Space*, *58*, 359–370.
Olsen, N., et al. (2013), The Swarm Satellite Constellation Application and Research Facility (SCARF) and Swarm data products, *Earth Planets Space*, *65*, 1189–1200, doi:10.5047/eps.2013.07.001.
Püthe, C., and A. Kuvshinov (2013a), Determination of the 1-D distribution of electrical conductivity in Earth's mantle from Swarm satellite data, *Earth Planets Space*, *65*, 1233–1237, doi:10.5047/eps.2013.07.007.
Püthe, C., and A. Kuvshinov (2013b), Determination of the 3-D distribution of electrical conductivity in Earth's mantle from Swarm satellite data: Frequency domain approach based on inversion of induced coefficients, *Earth Planets Space*, *65*(11), 1247–1256, doi:10.5047/eps.2013.09.004.
Schmucker, U. (1985), *Magnetic and Electric Fields Due to Electromagnetic Induction by External Sources, Landolt-Börnstein New-Ser.*, 100–125, vol. 5/2b, Springer, Berlin.
Schott, J. -J., M. Roussignol, M. Menvielle, and F. Nomenjahanary (1999), Bayesian inversion with Markov chains-II. The one-dimensional DC multilayer case, *Geophys. J. Int.*, *138*, 769–783, doi:10.1046/j.1365-246X.1999.00905.x.
Semenov, V., and W. Jozwiak (1999), Model of the geoelectrical structure of the mid and lower mantle in the Europe-Asia region, *Geophy. J. Int.*, *138*(2), 549–552, doi:10.1046/j.1365-246X.1999.00888.x.
Stacey, F., and P. Davis (2008), *Physics of the Earth*, 4th ed., 548 pp., Cambridge Univ. Press, Cambridge, U. K.
Tarantola, A. (1987), *Inverse Problem Theory. Methods for Data Fitting and Model Parameter Estimation*, Elsevier, Amsterdam.
Tarits, P., and N. Grammatica (2000), Electromagnetic induction effects by the solar quiet magnetic field at satellite altitude, *Geophys. Res. Lett.*, *27*, 4009–4012, doi:10.1029/1999GL011249.
Tarits, P., and M. Mandea (2010), The heterogeneous electrical conductivity structure of the lower mantle, *Phys. Earth Planet. Inter.*, *183*, 115–125, doi:10.1016/j.pepi.2010.08.002.
Thébault, E., A. Chulliat, S. Maus, G. Hulot, B. Langlais, A. Chambodut, and M. Menvielle (2010), IGRF candidate models at times of rapid changes in core field acceleration, *Earth Planets Space*, *62*, 753–763, doi:10.5047/eps.2010.05.004.
Thébault, E., F. Vervelidou, V. Lesur, and M. Hamoudi (2012), The satellite along-track analysis in planetary magnetism, *Geophys. J. Int.*, *188*(3), 891–907, doi:10.1111/j.1365-246X.2011.05281.x.
Tøffner-Clausen, L. (2013), Swarm level 1b product definition. SW-RS-DSC-SY-0007, Issue 5.15. [Available at https://earth.esa.int/documents/10174/1514862/Swarm_L1b_Product_Definition.]
Tyler, R. H., S. Maus, and H. Lühr (2003), Satellite observations of magnetic fields due to ocean tidal flow, *Science*, *299*(5604), 239–241.
Vacher, P., A. Mocquet, and C. Sotin (1998), Computation of seismic profiles from mineral physics: The importance of the non-olivine components for explaining the 660 km depth discontinuity, *Phys. Earth Planet. Inter.*, *106*, 275–298, doi:10.1016/S0031-9201(98)00076-4.
Velímský, J. (2010), Electrical conductivity in the lower mantle: Constraints from CHAMP satellite data by time-domain EM induction modelling, *Phys. Earth Planet. Inter.*, *180*, 111–117, doi:10.1016/j.pepi.2010.02.007.
Velímský, J. (2013), Determination of three-dimensional distribution of electrical conductivity in the Earth's mantle from Swarm satellite data: Time-domain approach, *Earth Planets Space*, *65*, 1239–1246, doi:10.5047/eps.2013.08.001.
Verhoeven, O., A. Mocquet, P. Vacher, A. Rivoldini, M. Menvielle, P. -A. Arrial, G. Choblet, P. Tarits, V. Dehant, and T. Van Hoolst (2009), Constraints on thermal state and composition of the Earth's lower mantle from electromagnetic impedances and seismic data, *J. Geophys. Res.*, *114*, B03302, doi:10.1029/2008JB005678.
Xu, Y., T. Shankland, and B. Poe (2000), Laboratory-based electrical conductivity in the Earth's mantle, *J. Geophys. Res.*, *105*(B12), 27,865–27,875, doi:200010.1029/2000JB900299.
Yoshino, T. (2010), Laboratory electrical conductivity measurement of mantle minerals, *Surv. Geophys.*, *31*, 163–206, doi:10.1007/s10712-009-9084-0.
Yoshino, T., and T. Katsura (2012), Erratum to: Re-evaluation of electrical conductivity of anhydrous and hydrous wadsleyite [Earth Planet. Sci. Lett. 337–338 (1) (2012) 56–67], *Earth Planet. Sci. Lett.*, *357*, 422–422, doi:10.1016/j.epsl.2012.10.020.
Zhang, B., T. Yoshino, X. Wu, T. Matsuzaki, S. Shan, and T. Katsura (2012), Electrical conductivity of enstatite as a function of water content: Implications for the electrical structure in the upper mantle, *Earth Planet. Sci. Lett.*, *357–358*(1), 11–20.

Appendix C

VO-ESD_1 and VO-ESD_6 models residuals

Here are showed the residuals for models VO-ESD_1 and VO-ESD_6. The residual of each VO-ESD_1 model corresponds to the difference between the model and the corresponding VO-ESD value at the same period. In contrary, for the VO-ESD_6 models each value corresponds to the residuals during the six periods over a $5^o \times 2.5^o$ surface for vector and $10^o \times 2.5^o$ surface for scalar components.

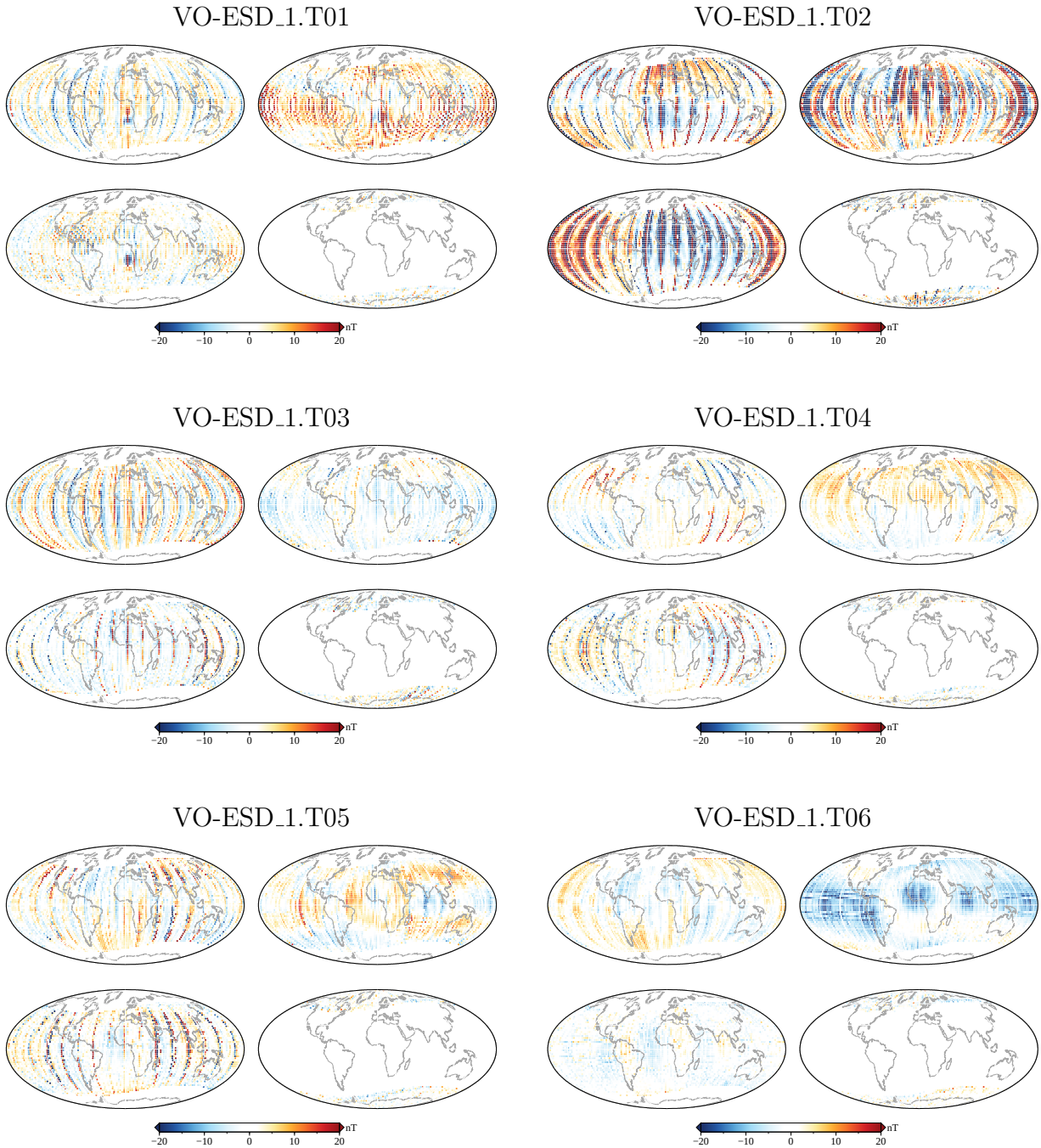

Figure C.1: Residuals between the VO-ESD time series used as input data and corresponding 1-period VO-ESD_1 model. For each model and from (*top left*) to (*bottom right*), X, Y, Z, and F, respectively.

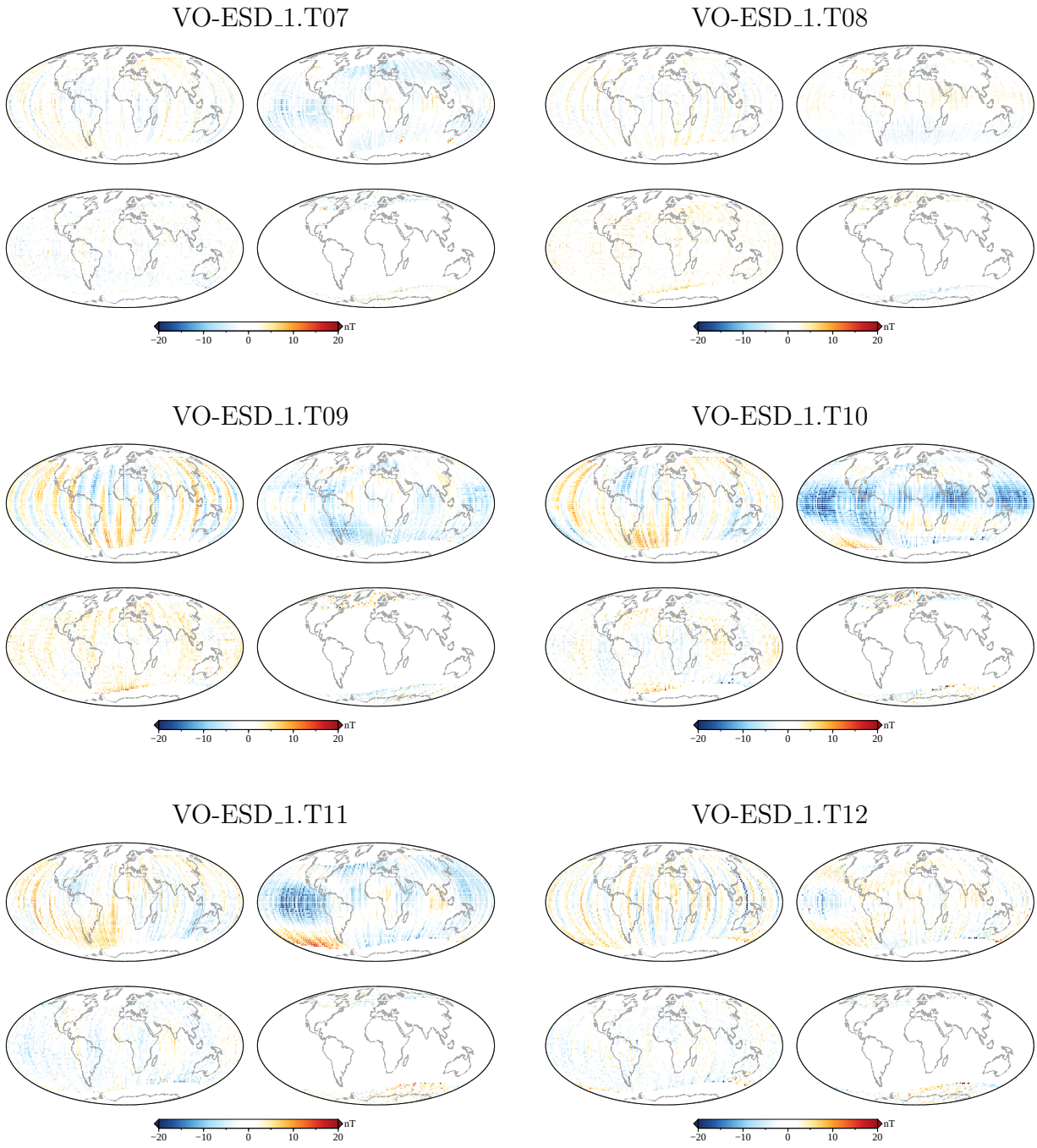

Figure C.1: (cont.)

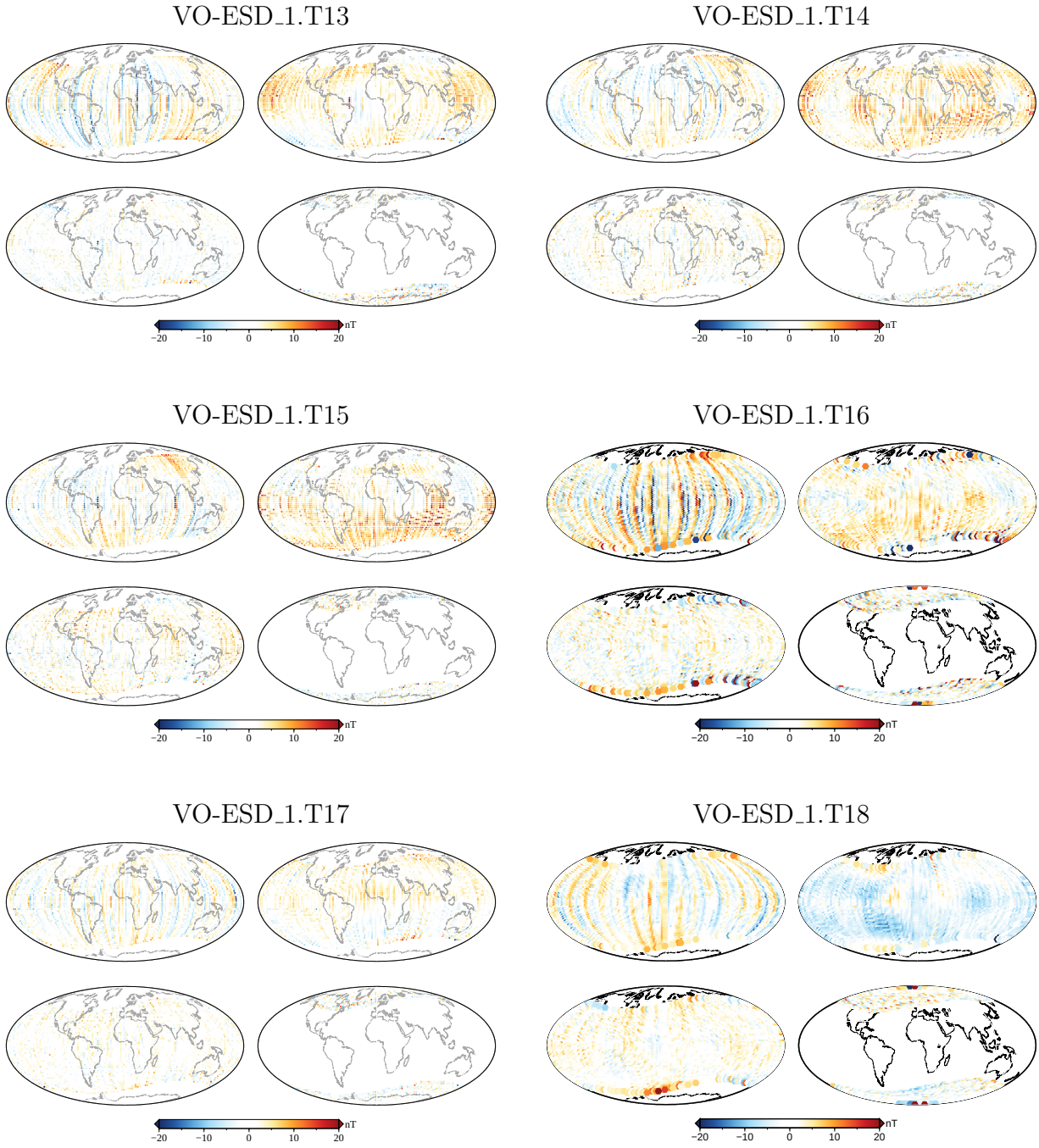

Figure C.1: (cont.)

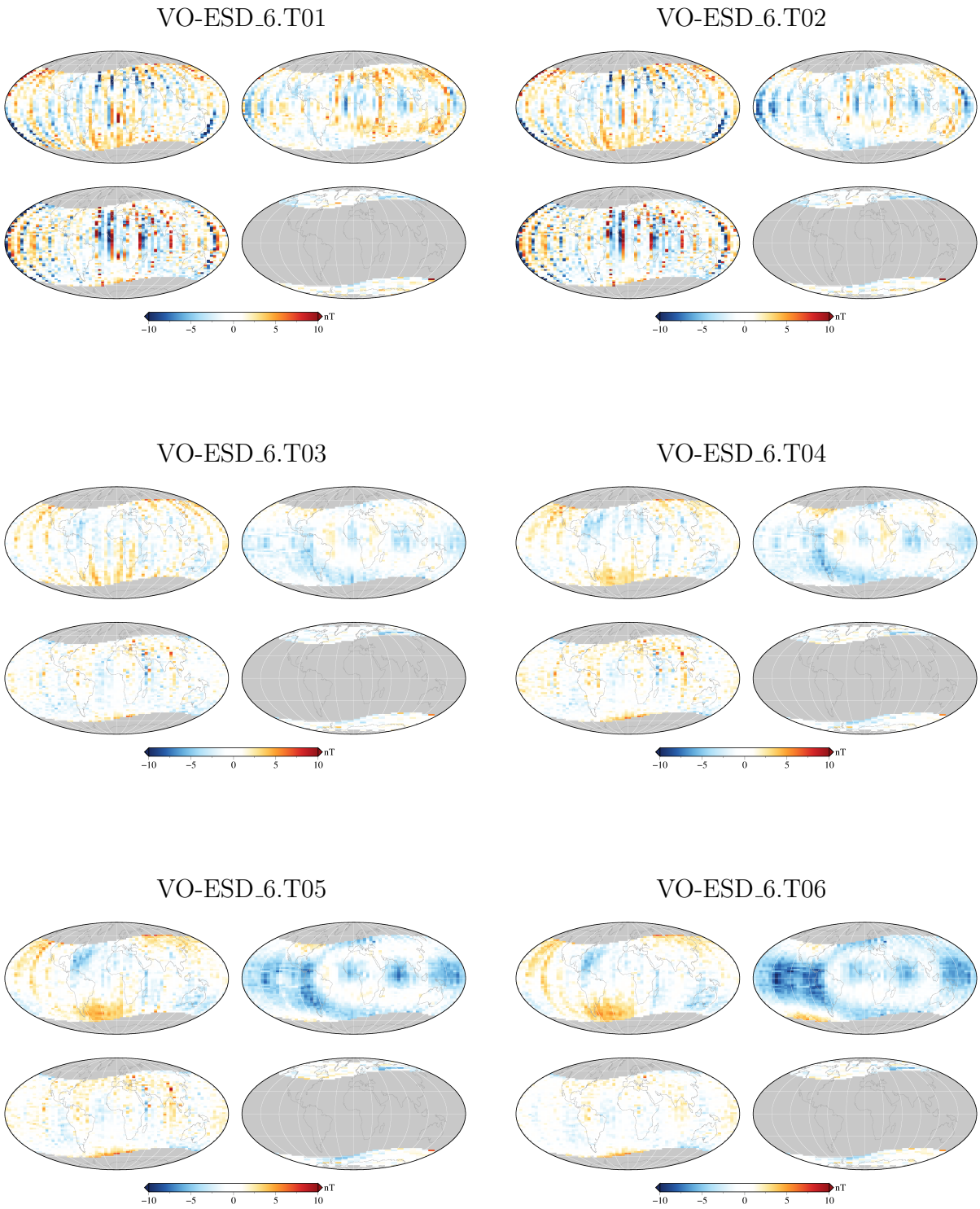

Figure C.2: Residuals between the VO-ESD time series used as input data and the VO-ESD_6 models. Each value corresponds to the mean of the residuals during the six periods over a $5^o \times 2.5^o$ surface for vector and $10^o \times 2.5^o$ surface for scalar components. For each model and from (*top left*) to (*bottom right*), X, Y, Z, and F, respectively.

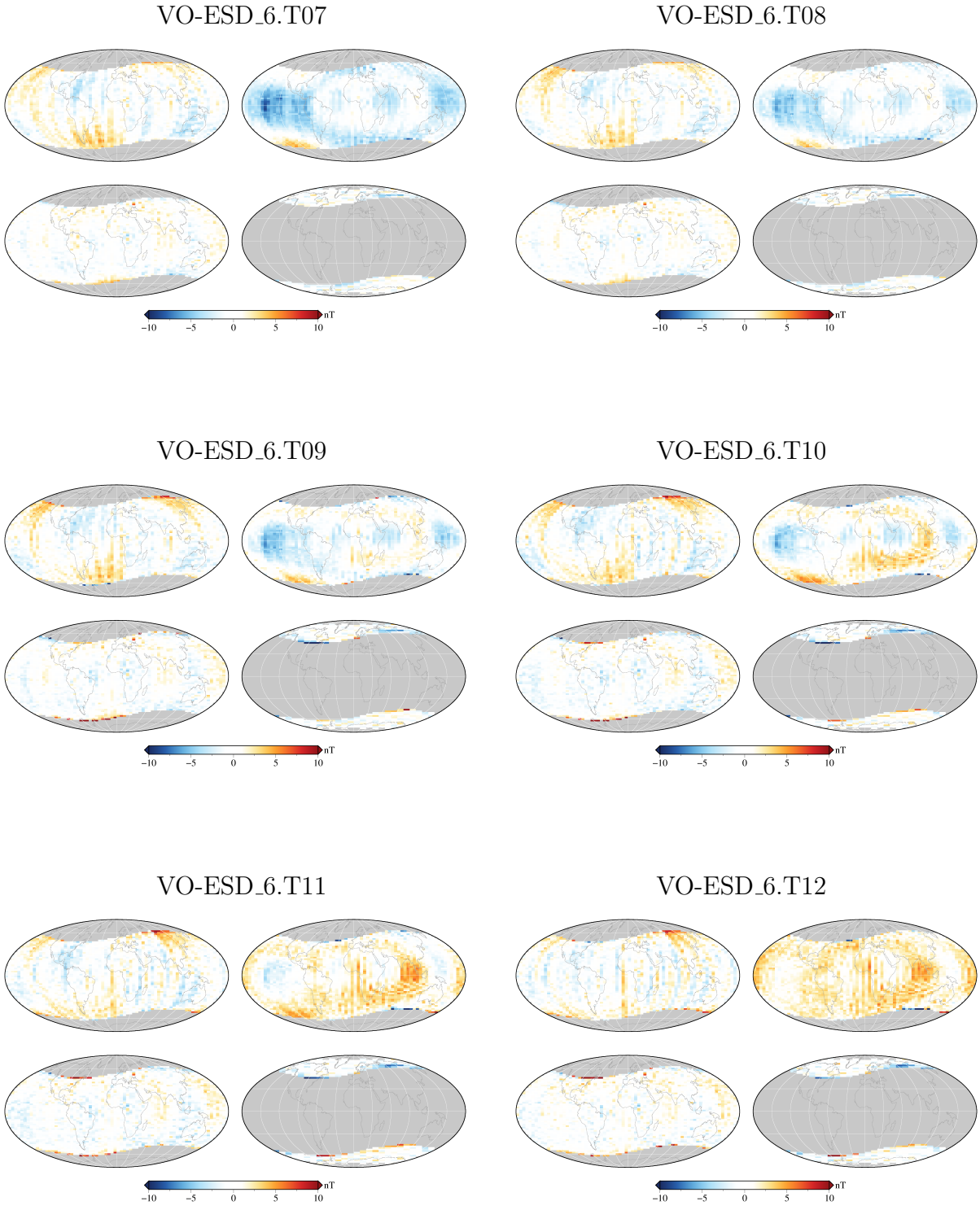

Figure C.2: (cont.)

VO-ESD_6.T13

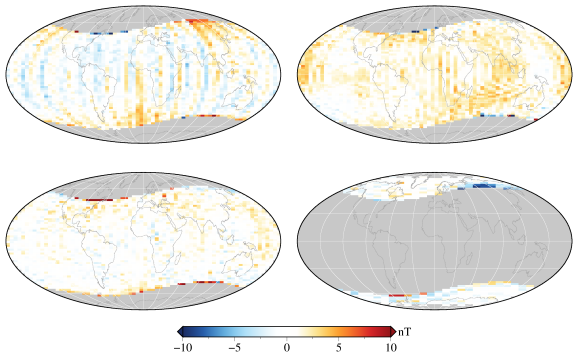

Figure C.2: (cont.)

Bibliography

Achache, J., Y. Cohen, and G. Unal (1991), "The French program of circumterrestrial magnetic surveys using stratospheric balloons." *Eos, Transactions American Geophysical Union*, 72, 97–101.

Alberto, P., O. Oliveira, and M. A. Pais (2004), "On the non-uniqueness of main geomagnetic field determined by surface intensity measurements: the Backus problem." *Geophys. J. Int.*, 159.

Alexandrescu, M., V. Courtillot, and J-L. Le Mouël (1997), "High-resolution secular variation of the geomagnetic field in western Europe over the last 4 centuries: Comparison and integration of historical data from Paris and London." *Journal of Geophysical Research: Solid Earth (1978–2012)*, 102, 20245–20258.

Alexandrescu, M., C. H. Duyen, and J-L. Le Mouël (1994), "Geographical distribution of magnetic observatories and field modelling." *Journal of geomagnetism and geoelectricity*, 46, 891–901.

Alexandrescu, M., D. Gibert, G. Hulot, J-L. Le Mouël, and G. Saracco (1995), "Detection of geomagnetic jerks using wavelet analysis." *J. geophys. Res*, 100, 12557–12572.

Alken, P., S. Maus, A. Chulliat, and C. Manoj (2015), "NOAA/NGDC candidate models for the 12th generation International Geomagnetic Reference Field." *Earth, Planets and Space*, 67, 1–9.

Amit, H. and P. Olson (2008), "Geomagnetic dipole tilt changes induced by core flow." *Physics of the Earth and Planetary Interiors*, 166, 226–238.

Aubert, J., C. C. Finlay, and A. Fournier (2013), "Bottom-up control of geomagnetic secular variation by the earth's inner core." *Nature*, 502, 219–223.

Backus, G. (1970), "Non-uniqueness of the external geomagnetic field determined by surface intensity measurements." *J. Geophys. Res.*, 75, 6337 6341.

Backus, G., R. Parker, and C. Constable (1996), *Foundations of Geomagnetism*. Cambridge University Press, Cambridge, UK.

Barraclough, D. R. (1987), "International geomagnetic reference field: the fourth generation." *Physics of the Earth and Planetary Interiors*, 48, 279–292.

Barton, C. E. (1997), "International geomagnetic reference field: The seventh generation." *Journal of geomagnetism and geoelectricity*, 49, 123–148.

Baumjohann, W. and R. Nakamura (2007), "Magnetospheric contribution to the terrestrial magnetic field." In *Treatise on Geophysics* (M. Kono, ed.), volume 5, Geomagnetism, 77–92, Elsevier, Amsterdam, The Netherlands.

Beggan, CD, KA Whaler, and S Macmillan (2009), "Biased residuals of core flow models from satellite-derived virtual observatories ." *Geophysical Journal International*, 177, 463–475.

Bloxham, J. and A. Jackson (1992), "Time-dependent mapping of the magnetic field at the core mantle boundary." *J. Geophys. Res.*, 97, 19537–19563.

Bloxham, J., S. Zatman, and M. Dumberry (2002), "The origin of geomagnetic jerks." *Nature*, 420, 65–68.

Box, G. E. P. and G. M. Jenkins (1976), *Time Series Analysis: Forecasting and Control*. Holden-Day.

Cain, J. C. (2007), "POGO (OGO-2, -4, and -6 spacecraft)." In *Enc. Geomag. Paleomag.* (D Gubbins and E Herrero-Bervera, eds.), 407–408, Springer, Netherlands.

Cain, J. C. and R. E. Sweeney (1973), "The POGO data." *Journal of Atmospheric and Terrestrial Physics*, 35, 1231–1247.

Cain, J. C., Z. Wang, C. Kluth, and D. R. Schmitz (1989), "Derivation of a geomagnetic model to n = 63." *Geophys. Jour.*, 97, 431–441.

Canet, E., A. Fournier, and D. Jault (2009), "Forward and adjoint quasi-geostrophic models of the geomagnetic secular variation." *J. Geophys. Res.*, 114.

Chambodut, A., I. Panet, M. Mandea, M. Diament, M. Holschneider, and O. Jamet (2005), "Wavelet frames: an alternative to spherical harmonic representation of potential fields." *Geophys. J. Int.*, 163.

Chapman, S. and J. Bartels (1940), *Geomagnetism*, volume 1 of *The International series of monographs on physics*. Clarendon Press.

Christensen, U. and J. Wicht (2007), "Numerical dynamo simulations." In *Treatise on Geophysics* (P. Olson, ed.), volume 8, Core Dynamics, 254–282, Elsevier, Amsterdam, The Netherlands.

Christensen, U. R., J. Aubert, and G. Hulot (2010), "Conditions for Earth-like geodynamo models." *Earth Planet. Sci. Lett.*, 296, 487–496.

Civet, F, E Thébault, O Verhoeven, B Langlais, and D Saturnino (2015), "Electrical conductivity of the earth's mantle from the first swarm magnetic field measurements." *Geophysical Research Letters*.

Cohen, Y., M. Alexandrescu, G. Hulot, and J. L. Le Mouël (1997), "Candidate models for the 1995 revision of igrf, a worldwide evaluation based on observatory monthly means." *Journal of geomagnetism and geoelectricity*, 49, 279–290.

Constable, C. G. (1988), "Parameter estimation in non-gaussian noise." *Geophysical Journal International*, 94, 131–142.

Courtillot, V, J Ducruix, and JL Le Mouël (1978), "Sur une accélération récente de la variation séculaire du champ magnétique terrestre." *CR Acad. Sci. D*, 287, 1095–1098.

Courtillot, V. and J-L. Le Mouël (2007), "The study of earth's magnetism (1269–1950): A foundation by peregrinus and subsequent development of geomagnetism and paleomagnetism." *Reviews of Geophysics*, 45.

Covington, J. (1993), "Improvement of equivalent source inversion technique with a more symmetric dipole distribution model." *Physics of the earth and planetary interiors*, 76, 199–208.

Cox, A., R. Doell, and B. Dalrymple (1963), "Geomagnetic polarity epochs and Pleistocene geochronometry." *Nature*, 198, 1049–1051.

Davidson, P.A. (2001), *An Introduction to Magnetohydrodynamics*. Cambridge Texts in Applied Mathematics, Cambridge University Press.

De Boor, C. (2001), *A practical guide to splines; rev. ed.* Applied mathematical sciences, Springer, Berlin, URL `https://cds.cern.ch/record/1428148`.

Dolginov, Sh. Sh., L. N. Zhuzgov, N. V. Pushkov, and L. O. Tyurmina (1962), "Some results

of measurements of the constant geomagnetic field above the ussr from the third artificial earth satellite." *Geomagnetism and Aeronomy*, 2, 877.

Dyment, J. and J. Arkani-Hamed (1998), "Equivalent source magnetic dipoles revisited." *Geophysical research letters*, 25, 2003–2006.

Dziewonski, A.M. and D.L. Anderson (1981), "Preliminary reference earth model." *Phys. Earth Planet. Int.*, 25, 297–356.

Finlay, C. C. and A. Jackson (2003), "Equatorially dominated magnetic field change at the surface of Earth's core." *Science*, 300, 2084–2086.

Finlay, C. C., S. Maus, C. D. Beggan, M. Hamoudi, F. J. Lowes, N. Olsen, and E. Thébault (2010), "Evaluation of candidate geomagnetic field models for IGRF-11." *Earth Planets Space*, 62, 787–804.

Finlay, C. C., S Maus, CD Beggan, TN Bondar, A Chambodut, TA Chernova, A Chulliat, VP Golovkov, B Hamilton, M Hamoudi, et al. (2010), "International geomagnetic reference field: the eleventh generation." *Geophysical Journal International*, 183, 1216–1230.

Finlay, C. C., N. Olsen, and L. Tøffner-Clausen (2015), "DTU candidate field models for IGRF-12 and the CHAOS-5 geomagnetic field model." *Earth, Planets and Space*, 67, 114.

Fournier, A., J. Aubert, and E. Thébault (2015), "A candidate secular variation model for IGRF-12 based on Swarm data and inverse geodynamo modelling." *Earth, Planets and Space*, 67, 81.

Fournier, A., C. Eymin, and T. Alboussière (2007), "A case for variational geomagnetic data assimilation: Insights from a one-dimensional, nonlinear, and sparsely observed mhd system." *Nonlin. Proc. Geophy*, 14.

Fournier, A., G. Hulot, D. Jault, W. Kuang, A. Tangborn, N. Gillet, E. Canet, J. Aubert, and F. Lhuillier (2010), "An Introduction to Data Assimilation and Predictability in Geomagnetism." *Space Sci. Rev.*, 155, 247–291.

Friis-Christensen, E., H. Lühr, and G. Hulot (2006), "Swarm: A constellation to study the Earth's magnetic field." *Earth Planets Space*, 58, 351–358.

Gauss, C. F. (1839), "Allgemaine theorie des erdmagnetismus." *Resultate*, 3, 47 pp.

Gee, J. S. and D. V. Kent (2007), "Source of oceanic magnetic anomalies and the geomagnetic

polarity time scale." In *Treatise on Geophysics* (M. Kono, ed.), volume 5, Geomagnetism, 455–507, Elsevier, Amsterdam, The Netherlands.

Gillet, N., O. Barrois, and C. C. Finlay (2015), "Stochastic forecasting of the geomagnetic field from the cov-obs. x1 geomagnetic field model, and candidate models for igrf-12." *Earth, Planets and Space*, 67, 71.

Gillet, N., D. Jault, C. C. Finlay, and N. Olsen (2013), "Stochastic modeling of the earth's magnetic field: inversion for covariances over the observatory era." *Geochemistry, Geophysics, Geosystems*, 14, 766–786.

Gillet, N., V. Lesur, and N. Olsen (2010), "Geomagnetic Core Field Secular Variation Models." *Space Sci. Rev.*, 155, 129–145.

Girdler, R. W., P.T. Taylor, and J. J. Frawley (1992), "A possible impact origin for the Bangui magnetic anomaly (Central Africa)." *Tectonophysics*, 212, 45–58.

Glatzmaier, G. A. and P. H Roberts (1995), "A three-dimensional self-consistent computer simulation of a geomagnetic field reversal." *Nature*, 337.

Haines, G. V. (1985), "Spherical cap harmonic analysis." *J. Geophys. Res.*, 90, 2583–2591.

Hamilton, B., V. A. Ridley, C. D. Beggan, and S. Macmillan (2015), "The BGS magnetic field candidate models for the 12th generation IGRF." *Earth, Planets and Space*, 67, 1–15.

Heelis, R.A. (2004), "Electrodynamics in the low and middle latitude ionosphere: A tutorial." *Journal of Atmospheric and Solar-Terrestrial Physics*, 66, 825–838.

Heirtzler, J. R. (2002), "The future of the South Atlantic anomaly and implications for radiation damage in space." *J. Atm. Sol. Terr. Phys.*, 64.

Holme, R (2007), "Large-scale flow in the core." In *Treatise on Geophysics*, volume 8, Core Dynamics, 107–130, Elsevier Amsterdam.

Holschneider, M., A. Chambodut, and M. Mandea (2003), "From global to regional analysis of the magnetic field on the sphere using wavelet frames." *Physics of the Earth and Planetary Interiors*, 135, 107–124.

Hulot, G., C. Eymin, B. Langlais, M. Mandea, and N. Olsen (2002), "Small-scale structure of the geodynamo inferred from Ørsted and Magsat satellite data." *Nature*, 416, 620–623.

Jackson, A. (2003), "Intense equatorial flux spots on the surface of the Earth's core." *Nature*, 424, 760–763.

Jackson, A. and C. C. Finlay (2007), "Geomagnetic secular variation and its applications." In *Treatise on Geophysics* (G. Schubert, ed.), volume 5, Geomagnetism, 147–193, Elsevier, Amsterdam, The Netherlands.

Jackson, A., A. R. T. Jonkers, and M. R. Walker (2000), "Four centuries of geomagnetic secular variation from historical records." *Phil. Trans. R. Soc. London*, 358, 957–990.

Jankowski, J. and C. Sucksdorff (1996), *Guide for Magnetic Measurements and Observatory Practice*. Int. Assoc. Geomag. Aeronomy, Warsaw.

Kelley, M. C. (2009), *The Earth's Ionosphere: Plasma Physics & Electrodynamics*, volume 96. Academic press.

Kerridge, D. (2007), "IAGA, International Association of Geomagnetism and Aeronomy." In *Enc. Geomag. Paleomag.* (D Gubbins and E Herrero-Bervera, eds.), 828–829, Springer, Netherlands.

Kono, M. (2007), "Geomagnetism in perspective." In *Treatise on Geophysics* (G. Schubert, ed.), volume 5, Geomagnetism, 1 – 31, Elsevier, Amsterdam, The Netherlands.

Korte, M., C. Constable, F. Donadini, and R. Holme (2011), "Reconstructing the Holocene geomagnetic field." *Earth and Planetary Science Letters*, 312, 497 – 505, URL `http://www.sciencedirect.com/science/article/pii/S0012821X11006261`.

Korte, M., A. Genevey, C. G. Constable, U. Frank, and E. Schnepp (2005), "Continuous geomagnetic field models for the past 7 millennia: 1. A new global data compilation." *Geochemistry, Geophysics, Geosystems*, 6.

Korte, M., M. Mandea, H.-J. Linthe, A. Hemshorn, P. Kotzé, and E. Ricaldi (2009), "New geomagnetic field observations in the South Atlantic Anomaly region." *Ann. Geophys*, 52, 65–82.

Kotzé, P. B., M. Mandea, and M. Korte (2007), "Modelling the southern African geomagnetic field secular variation using ground survey data for 2005." *South African Journal of Geology*, 110, 187–192.

Kuvshinov, A. and N. Olsen (2005), "3-D modelling of the magnetic fields due to ocean tidal flow." In *Earth Observation with CHAMP: Results from Three Years in Orbit* (C. Reigber, H. Lühr, P. Schwintzer, and J. Wickert, eds.), 359–365, Springer, Berlin.

Kuvshinov, A. and N. Olsen (2006), "A global model of mantle conductivity derived from 5 years of CHAMP, Ørsted, and SAC-C magnetic data." *Geophys. Res. Lett.*, 33.

Langel, R. A. (1987), *Geomagnetism, Vol. 1, Jacobs, J. A., Ed.*, chapter 4 - The Main Field, 249–512. Academic Press.

Langel, R. A. (1992), "International geomagnetic reference field." *Journal of geomagnetism and geoelectricity*, 44, 679–707.

Langel, R. A., R. T. Baldwin, and A. W. Green (1995), "Toward an improved distribution of magnetic observatories for modeling of the main geomagnetic field and its temporal change." *Journal of geomagnetism and geoelectricity*, 47, 475–508.

Langel, R. A., D. R. Barraclough, D. J. Kerridge, V. P. Golovkov, T. J. Sabaka, and R. H. Estes (1988a), "Definitive igrf models for 1945, 1950, 1955, and 1960." *Journal of geomagnetism and geoelectricity*, 40, 645–702.

Langel, R. A. and R. H. Estes (1982), "A geomagnetic field spectrum." *Geophys. Res. Lett.*, 9, 250–253.

Langel, R. A. and R. H. Estes (1985), "The near-Earth magnetic field at 1980 determined from MAGSAT data." *J. Geophys. Res.*, 90, 2495 2509.

Langel, R. A., R. H. Estes, and G. D. Mead (1982), "Some new methods in geomagnetic field modeling applied to the 1960-1980 epoch." *J. Geomag. Geoelectr.*, 34, 327–349.

Langel, R. A. and W. J. Hinze (1998), *The Magnetic Field of the Earth's Lithosphere*. Cambridge University Press, Cambridge, UK.

Langel, R. A., D. J. Kerridge, D. R. Arraclough, and S. R. C. Malin (1986), "Geomagnetic temporal change: 1903-1982, A spline representation." *Journal of geomagnetism and geoelectricity*, 38, 573–597.

Langel, R. A., J. R. Ridgway, M. Sugiura, and K. Maezawa (1988b), "The geomagnetic field at 1982 from DE-2 and other magnetic field data." *Journal of geomagnetism and geoelectricity*, 40, 1103–1127.

Langlais, B., H. Larnier, H. Amit, E. Thébault, and A. Mocquet (2014), "A new model for the (geo)magnetic power spectrum, with application to planetary dynamo radii." *Earth Planet. Sci. Lett.*, 401.

Langlais, B. and M. Mandea (2000), "An IGRF candidate main geomagnetic field model for epoch 2000 and a secular variation model for 2000-2005." *Earth Planets Space*, 52, 1137–1148.

Langlais, B., M. Mandea, and P. Ultré-Guérard (2003), "High-resolution magnetic field modeling: application to MAGSAT and Ørsted data." *Phys. Earth Planet. Int.*, 135, 77–91.

Langlais, B. and M. E. Purucker (2007), "A polar magnetic paleopole associated with Apollinaris Patera." *Planet. Spa. Sci.*, 55.

Langlais, B., M. E. Purucker, and M. Mandea (2004), "Crustal magnetic field of Mars." *J. Geophys. Res.*, 109.

Le Huy, M., M. Alexandrescu, G. Hulot, and J-L. Le Mouël (1998), "On the characteristics of successive geomagnetic jerks." *Earth, planets and space*, 50, 723–732.

Léger, J.-M., T. Jager, F. Bertrand, G. Hulot, L. Brocco, P. Vigneron, X. Lalanne, A. Chulliat, and I. Fratter (2015), "In-flight performance of the Absolute Scalar Magnetometer vector mode on board the Swarm satellites." *Earth, Planets and Space*, 67, 57.

Lesur, V. (2006), "Introducing localized constraints in global geomagnetic field modelling." *Earth Planets Space*, 58, 477–483.

Lesur, V., S. Macmillan, and A. Thomson (2005), "A magnetic field model with daily variations of the magnetospheric field and its induced counterpart in 2001." *Geophysical Journal International*, 160, 79–88.

Lesur, V., N. Olsen, and W. P. Thomson (2011), *Geomagnetic Observations and Models*, volume 5, chapter Geomagnetic Core Field Models in the Satellite Era. IAGA Special Sopron Book Series.

Lesur, V., M. Rother, I. Wardinski, R. Schachtschneider, M. Hamoudi, and A. Chambodut (2015), "Parent magnetic field models for the IGRF-12 GFZ-candidates." *Earth, Planets and Space*, 67, 1–15.

Lesur, V., I. Wardinski, M. Hamoudi, and M. Rother (2010), "The second generation of the GFZ Reference Internal Magnetic Model: GRIMM-2." *Earth Planets Space*, 62.

Lesur, V., I. Wardinski, M. Rother, and M. Mandea (2008), "GRIMM: the GFZ Reference Internal Magnetic Model based on vector satellite and observatory data." *Geophys. J. Int.*, 173.

Liu, D., A. Tangborn, and W. Kuang (2007), "Observing system simulation experiments in geomagnetic data assimilation." *J. Geophys. Res.*, 112.

Lowes, F. J. (1966), "Mean square values on the sphere of spherical harmonic vector fields." *J. Geophys. Res.*, 71, 2179.

Lowes, F. J. (1974), "Spatial power spectrum of the main geomagnetic field and extrapolation to the core." *Geophys. J. R. Astr. Soc.*, 36, 717–730.

Lowes, F. J., T. Bondar, V. P. Golovkov, B. Langlais, S. MacMillan, and M. Mandea (2000), "Evaluation of the candidate Main Field model for IGRF 2000 derived from preliminary Ørsted data." *Earth Planets Space*, 52, 1183–1186.

Lühr, H., S. Maus, M. Rother, and D. Cooke (2002), "First in-situ observation of night-time F-region currents with the CHAMP satellite." *Geophysical research letters*, 29, 127–1.

Macmillan, S., S. Maus, T. Bondar, A. Chambodut, V. Golovkov, R. Holme, B. Langlais, V. Lesur, F. Lowes, H. Lühr, W. Mai, M. Mandea, N. Olsen, M. Rother, T. Sabaka, A. Thomson, and I. Wardinski (2003), "The 9th-Generation International Geomagnetic Reference Field." *Geophys. J. Int.*, 155.

Macmillan, S. and N. Olsen (2013), "Observatory data and the Swarm mission." *Earth, Planets and Space*, 65, 1355–1362.

Malin, S. R. C. and B. M. Hodder (1982), "Was the 1970 geomagnetic jerk of internal or external origin?" *Nature*.

Mandea, M., R. Holme, A. Pais, K. Pinheiro, A. Jackson, and G. Verbanac (2010), "Geomagnetic jerks: rapid core field variations and core dynamics." *Space science reviews*, 155, 147–175.

Mandea, M. and S. Macmillan (2000), "International geomagnetic reference field the eighth generation." *Earth, planets and space*, 52, 1119–1124.

Mandea, M. and P. Mayaud (2004), "Guillaume Le Nautonier, un précurseur dans l'histoire du géomagnétisme." *Revue d'histoire des sciences*, 57, 161–173.

Mandea, M. and N. Olsen (2006), "A new approach to directly determine the secular variation from magnetic satellite observations." *Geophys. Res. Lett.*, 33.

Matzka, J., A. Chulliat, M. Mandea, C. C. Finlay, and E. Qamili (2010), "Geomagnetic observations for main field studies: from ground to space." *Space Sci. Rev.*, 155.

Mauersberger, P. (1956), "Das mittel der energiedichte des geomagnetischen hauptfeldes an der erdoberfläche und seine säkulare änderung." *Gerlands Beitr. Geophys*, 65, 207–215.

Maus, S. (2007), "CHAMP." In *Enc. Geomag. Paleomag.* (D Gubbins and E Herrero-Bervera, eds.), 59–60, Springer, Netherlands.

Maus, S. (2010a), "An ellipsoidal harmonic representation of earth's lithospheric magnetic field to degree and order 720." *Geochemistry, Geophysics, Geosystems*, 11.

Maus, S. (2010b), "Magnetic field model MF7." `http://http://www.geomag.us/models/MF7.html`.

Maus, S., U. Barckhausen, H. Berkenbosch, N. Bournas, J. Brozena, V. Childers, F. Dostaler, J. D. Fairhead, C. Finn, R. R. B. von Frese, C. Gaina, S. Golynsky, R. Kucks, H. Lühr, P. Milligan, S. Mogren, R. D. Müller, O. Olesen, M. Pilkington, R. Saltus, B. Schreckenberger, E. Thébault, and F. Caratori Tontini (2009), " EMAG2: A 2 arc min resolution Earth Magnetic Anomaly Grid compiled from satellite, airborne, and marine magnetic measurements." *Geochem., Geophys., Geosyst.*, 10.

Maus, S. and H. Lühr (2006), "A gravity-driven electric current in the Earth's ionosphere identified in CHAMP satellite magnetic measurements." *Geophys. Res. Lett.*, 33.

Maus, S., H. Lühr, G. Balasis, M. Rother, and M. Mandea (2005), "Introducing POMME, the POtsdam Magnetic Model of the Earth." In *Earth Observation with CHAMP: Results from Three Years in Orbit* (C. Reigber, H. Lühr, P. Schwintzer, and J. Wickert, eds.), 293–298, Springer, Berlin.

Maus, S., H. Lühr, M. Rother, K. Hemant, G. Balasis, P. Ritter, and C. Stolle (2007), "Fifth-generation lithospheric magnetic field model from CHAMP satellite measurements." *Geochem., Geophys., Geosyst.*, 8.

Maus, S., S. MacMillan, T. Chernova, S. Choi, D. Dater, V. Golovkov, V. Lesur, F. Lowes, H. Lühr, W. Mai, et al. (2005), "The 10th-generation international geomagnetic reference field." *Geophysical Journal International*, 161, 561–565.

Maus, S., S. MacMillan, F. Lowes, and T. Bondar (2005a), "Evaluation of candidate geomagnetic field models for the 10th generation of IGRF." *Earth Planets Space*, 57, 1173–1181.

Maus, S., S. McLean, D. Dater, H. Lühr, M. Rother, W. Mai, and S. Choi (2005b),

"NGDC/GFZ candidate models for the 10th generation International Geomagnetic Reference Field." *Earth Planets Space*, 57, 1151–1156.

Maus, S., M. Rother, R. Holme, H. Lühr, N. Olsen, and V. Haak (2002), "First scalar magnetic anomaly map from CHAMP satellite data indicates weak lithospheric field." *Geophys. Res. Lett.*, 29.

Maus, S., M. Rother, C. Stolle, W. Mai, S. Choi, H. Lühr, D. Cooke, and C. Roth (2006), "Third generation of the Potsdam Magnetic Model of the Earth (POMME)." *Geochem., Geophys., Geosyst.*, 7.

Mayaud, P. N. (1980), *Derivation, meaning and use of geomagnetic indices*. AGU Geophys. Monographs; no. 22, Washington, D. C.

Mayer, C. and T. Maier (2006), "Separating inner and outer Earth's magnetic field from CHAMP satellite measurements by means of vector scaling functions and wavelet." *Geophys. J. Int.*, 167.

Mayhew, M. A. (1979), "Inversion of satellite magnetic anomaly data." *Journal of Geophysics Zeitschrift Geophysik*, 45, 119–128.

Mayhew, M. A. and R. H. Estes (1983), "Equivalent source modeling of the core magnetic field using Magsat data." *J. Geomag. Geoelectr.*, 35, 119–130.

Mayhew, M. A., B. D. Johnson, and R. A. Langel (1980), "An equivalent source model of the satellite-altitude magnetic anomaly field over Australia." *Earth Planet. Sci. Lett.*, 51, 189–198.

Menvielle, M., T. Iyemori, A. Marcahudon, and M. Nosé (2011), *Geomagnetic Observations and Models*, volume 5, chapter Geomagnetic Indices, 229–264. IAGA Special Sopron Book Series.

Merrill, R. T., W. McElhinny, and P. L. McFadden (1998), *The Magnetic Field of the Earth: Paleomagnetism, the Core, and the Deep Mantle*. Acad. Press.

Mitchell, A. C. (1932), "Chapters in the history of terrestrial magnetism, I, On the directive property of a magnet in the Earth's field and the origin of nautical compass ." *Journal of Geophysical Research*, 37, 105–146.

Mochizuki, E., Y. Yokoyama, I. Shimizu, and Y. Hamano (1997), "Spherical harmonic analysis

in terms of unevenly distributed observation points and its applications to geomagnetic data." *Journal of geomagnetism and geoelectricity*, 49, 1013–1033.

Neubert, T. and F. Christiansen (2003), "Small-scale, field-aligned currents at the top-side ionosphere." *Geophysical research letters*, 30.

Neubert, T., M. Mandea, G. Hulot, R. von Frese, F. Primdahl, J. L. Jørgensen, E. Friis-Christensen, P. Stauning, N. Olsen, and T. Risbo (2001), "Ørsted satellite captures high-precision geomagnetic field data." *Eos, Transactions American Geophysical Union*, 82, 81–88.

O'Brien, M. S. and R. L. Parker (1994), "Regularized geomagnetic field modelling using monopoles." *Geophys. J. Int.*, 118, 566–578.

Oliveira, J. S., B. Langlais, M. A. Pais, and H. Amit (2015), "A modified equivalent source dipole method to model partially distributed magnetic field measurements, with application to mercury." *Journal of Geophysical Research: Planets*.

Olsen, N. (1997), "Ionospheric F-region currents at middle and low latitudes estimated from Magsat data." *Journal of Geophysical Research: Space Physics (1978–2012)*, 102, 4563–4576.

Olsen, N. (1999), "Induction studies with satellite data." *Surveys in Geophysics*, 20, 309–340.

Olsen, N. (2002), "A model of the geomagnetic field and its secular variation for epoch 2000 estimated from Ørsted data." *Geophys. J. Int.*, 149.

Olsen, N., E. Friis-Christensen, R. Floberghagen, P. Alken, C. D. Beggan, A. Chulliat, E. Doornbos, J.T. da Encarnacao, B. Hamilton, G. Hulot, J. van den IJssel, A. Kuvshinov, V. Lesur, H. Luehr, S. Macmillan, S. Maus, M. Noja, P.E.H. Olsen, J. Park, G. Plank, C. Puethe, J. Rauberg, P. Ritter, M. Rother, T.J. Sabaka, R. Schachtschneider, O. Sirol, C. Stolle, E. Thébault, A.W.P. Thomson, L. Toffner-Clausen, J. Velimsky, P. Vigneron, and P.N. Visser (2013), "The Swarm Satellite Constellation Application and Research Facility (SCARF) and Swarm data products." *Earth Planets Space*, 65.

Olsen, N., R. Haagmans, T. J. Sabaka, A. Kuvshinov, S. Maus, M. E. Purucker, M. Rother, V. Lesur, and M. Mandea (2006a), "The Swarm End-to-End mission simulator study: A demonstration of separating the various contributions to Earth's magnetic field using synthetic data." *Earth Planets Space*, 58, 359–370.

Olsen, N., R. Holme, G. Hulot, T. Sabaka, T. Neubert, L. Tøffner-Clausen, F. Primdahl,

J. Jørgensen, J.-M. Leger, D. Barraclough, J. Bloxham, J. Cain, C. Constable, V. Golovkov, A. Jackson, P. Kotze, B. Langlais, S. Macmillan, M. Mandea, J. Merayo, L. Newitt, M. Purucker, T. Risbo, M. Stampe, A. Thomson, and C. Voorhies (2000), "Ørsted initial field model." *Geophys. Res. Lett.*, 27, 3607–3610.

Olsen, N., G. Hulot, V. Lesur, C. C. Finlay, C. Beggan, A. Chulliat, T. J. Sabaka, R. Floberghagen, E. Friis-Christensen, R. Haagmans, et al. (2015), "The Swarm Initial Field Model for the 2014 geomagnetic field." *Geophysical Research Letters*, 42, 1092–1098.

Olsen, N., G. Hulot, and T. J. Sabaka (2007), "The present field." In *Treatise on Geophysics* (M. Kono, ed.), volume 5, Geomagnetism, 33–75, Elsevier, Amsterdam, The Netherlands.

Olsen, N., G. Hulot, and T. J. Sabaka (2010), "Measuring the Earth's Magnetic Field from Space: Concepts of Past, Present and Future Missions." *Space Sci. Rev.*, 155, 65–93.

Olsen, N., F. Lowes, and T. J. Sabaka (2005a), "Ionospheric and induced field leakage in geomagnetic field models, and derivation of candidate models for DGRF 1995 and DGRF 2000." *Earth, planets and space*, 57, 1191–1196.

Olsen, N., H. Lühr, C. C. Finlay, T. J. Sabaka, I. Michaelis, J. Rauberg, and L. Tøffner-Clausen (2014), "The CHAOS-4 geomagnetic field model." *Geophysical Journal International*, 197, 815–827.

Olsen, N., H. Lühr, T. J. Sabaka, M. Mandea, M. Rother, L. Tøffner-Clausen, and S. Choi (2006b), "CHAOS-a model of the Earth's magnetic field derived from CHAMP, Ørsted, and SAC-C magnetic satellite data." *Geophys. J. Int.*, 166.

Olsen, N. and M. Mandea (2007), "Investigation of a secular variation impulse using satellite data: The 2003 geomagnetic jerk." *Earth Planet. Sci. Lett.*, 255.

Olsen, N., M. Mandea, T. J. Sabaka, and L. Tøffner-Clausen (2009), "CHAOS-2-a geomagnetic field model derived from one decade of continuous satellite data." *Geophys. J. Int.*

Olsen, N., T. J. Sabaka, and F. Lowes (2005b), "New parameterization of external and induced fields in geomagnetic field modeling, and a candidate model for IGRF 2005." *Earth Planets Space*, 57, 1141–1149.

Olsen, N. and C. Stolle (2012), "Satellite geomagnetism." *Annual Review of Earth and Planetary Sciences*, 40, 441–465.

Olsen, N., L. Tøffner-Clausen, T. J. Sabaka, P. Brauer, J. M. G. Merayo, J. L. Jørgensen, J.-M.

Léger, O. V. Nielsen, F. Primdahl, and T. Risbo (2003), "Calibration of the Ørsted vector magnetometer." *Earth Planets Space*, 55, 11–18.

Olsen, Nils, Gauthier Hulot, and Terence J Sabaka (2010), "Sources of the geomagnetic field and the modern data that enabletheir investigation." In *Handbook of geomathematics*, 105–124, Springer.

Olson, P. and H. Amit (2006), "Changes in earth's dipole." *Naturwissenschaften*, 93, 519–542.

Peddie, N. W. (1982), "International geomagnetic reference field: The third generation." *Journal of geomagnetism and geoelectricity*, 34, 309–326.

Peltier, A. and A. Chulliat (2010), "On the feasibility of promptly producing quasi-definitive magnetic observatory data." *Earth Planets Space*, 62.

Pinheiro, K. and A. Jackson (2008), "Can a 1-D mantle electrical conductivity model generate magnetic jerk differential time delays?" *Geophys. J. Int.*, 173.

Poirier, Jean-Paul (2000), *Introduction to the Physics of the Earth's Interior*. Cambridge University Press.

Press, W. H., S. A. Teukolsky, W. T. Vetterling, and B. P. Flannery (1992), *Numerical Recipes in C (2nd Ed.): The Art of Scientific Computing*. Cambridge University Press, New York.

Purucker, M. E. (2004), "Annihilators at Mars: are there alternative but reasonable magnetization distributions in the Martian crust that explain the MGS magnetic field observations." In *Eos, Jt. Assem. Suppl.*, volume 85. Abstract P33A-01.

Purucker, M. E. (2007), "MAGSAT." In *Enc. Geomag. Paleomag.* (D. Gubbins and E. Herrero-Bervera, eds.), 673–674, Springer, Netherlands.

Purucker, M. E., B. Langlais, N. Olsen, G. Hulot, and M. Mandea (2002), "The southern edge of cratonic North America: Evidence from new satellite magnetometer observations." *Geophys. Res. Lett.*, 29.

Purucker, M. E., D. Ravat, H. Frey, C. Voorhies, T. Sabaka, and M. H. Acuña (2000), "An altitude-normalized magnetic map of Mars and its interpretation." *Geophys. Res. Lett.*, 27.

Purucker, M. E., T. J. Sabaka, and R. A. Langel (1996), "Conjugate gradient analysis: A new tool for studying satellite magnetic data sets." *Geophysical research letters*, 23, 507–510.

Reay, S. J., D. C. Herzog, S. Alex, E. P. Kharin, S. McLean, M. Nosé, and N. A. Sergeyeva

(2011), *Geomagnetic Observations and Models*, volume 5, chapter Magnetic Observatory Data and Metadata: Types and Availability, 162–194. IAGA Special Sopron Book Series.

Regan, R. D., J. C. Cain, and W. M. Davis (1975), "A Global magnetic anomaly map." *J. Geophys. Res.*, 80, 794–802.

Ridley, Victoria and Susan Macmillan (2014), "Validation of Swarm satellite magnetic data using observatory measurements." Poster presented at 3rd Swarm Meeting, June 19–20, Copenhagen, Denmark.

Roberts, P. H. and S. Scott (1965), "On analysis of the secular variation." *Journal of geomagnetism and geoelectricity*, 17, 137–151.

Runcorn, S. K. (1975), "On the interpretation of Lunar magnetism." *Phys. Earth Planet. Int.*, 10, 327–335.

Sabaka, T. J. and R. T. Baldwin (1993), "Modeling the Sq magnetic field from POGO and MAGSAT satellite and contemporaneous hourly observatory data, Phase 1." Technical report, Contract Rep. HSTX/G&G- 9302, Hughes STX Corp. for NASA/GSFC Contract NASS- 31760.

Sabaka, T. J., N. Olsen, and R. A. Langel (2002), "A comprehensive model of the quiet-time, near-Earth magnetic field: phase 3." *Geophys. J. Int.*, 151.

Sabaka, T. J., N. Olsen, and M. E. Purucker (2004), "Extending comprehensive models of the Earth's magnetic field with Ørsted and CHAMP data." *Geophysical Journal International*, 159, 521–547.

Sabaka, T. J., N. Olsen, R. H. Tyler, and A. Kuvshinov (2015), "CM5, a pre-Swarm comprehensive geomagnetic field model derived from over 12 yr of CHAMP, Ørsted, SAC-C and observatory data." *Geophysical Journal International*, 200, 1596–1626.

Sabaka, T. J., L. Tøffner-Clausen, and N. Olsen (2013), "Use of the comprehensive inversion method for swarm satellite data analysis." *Earth, Planets and Space*, 65, 1201–1222.

Saturnino, D., B. Langlais, F. Civet, E. Thébault, and M. Mandea (2015), "Main field and secular variation candidate models for the 12th IGRF generation after 10 months of Swarm measurements." *Earth, Planets and Space*, 67, 96.

Schott, J. J. and E. Thébault (2011), *Geomagnetic Observations and Models*, volume 5, chapter

Modelling the earth's magnetic field from global to regional scales, 229–264. IAGA Special Sopron Book Series.

Shewchuk, J. R. (1994), "An introduction to the conjugate gradient method without the agonizing pain." Technical report, Pittsburgh, PA, USA.

Shure, L., R. L. Parker, and G. E. Backus (1982), "Harmonic splines for geomagnetic modelling." *Phys. Earth Planet. Int.*, 28, 215–229.

Stolle, C., H. Lühr, M. Rother, and G. Balasis (2006), "Magnetic signatures of equatorial spread F as observed by the CHAMP satellite." *J. Geophys. Res.*, 111.

Storey, L. R. O. (1953), "An investigation of whistling atmospherics." *Philosophical Transactions of the Royal Society of London A: Mathematical, Physical and Engineering Sciences*, 246, 113–141.

Tarduno, J. A., M. K. Watkeys, T. N. Huffman, R. D. Cottrell, E. .G. Blackman, A. Wendt, C. A Scribner, and C. L. Wagner (2015), "Antiquity of the south atlantic anomaly and evidence for top-down control on the geodynamo." *Nature communications*, 6.

Taylor, R. (1841), *Scientific Memoirs, Selected from the Transactions of Foreign Academies of Science and Learned Societies, and from Foreign Journals*. Number 2 in Scientific Memoirs, R. and J. E. Taylor.

Thébault, E., C. C. Finlay, P. Alken, C. Beggan, E. Canet, A. Chulliat, B. Langlais, V. Lesur, F. Lowes, C. Manoj, M. Rother, and R. Schachtschneider (2015a), "Evaluation of candidate geomagnetic field models for igrf-12." *Earth, Planets and Space*, 67, 112.

Thébault, E., C. C. Finlay, C. D. Beggan, P. Alken, J. Aubert, O. Barrois, F. Bertrand, T. Bondar, A. Boness, L. Brocco, E. Canet, A. Chambodut, A. Chulliat, P. Coïsson, F. Civet, A. Du, A. Fournier, I. Fratter, N. Gillet, B. Hamilton, M. Hamoudi, G. Hulot, T. Jager, M. Korte, W. Kuang, X. Lalanne, B. Langlais, J.-M. Léger, V. Lesur, F. J. Lowes, S. Macmillan, . Mandea, C. Manoj, S. Maus, N. Olsen, V. Petrov, M. Rother, T. J. Sabaka, D. Saturnino, R. Schachtschneider, O. Sirol, A. Tangborn, V. Taylor, A. Thomson, L. Tøffner-Clausen, P. Vigneron, I. Wardinski, and T. Zvereva (2015b), "International Geomagnetic Reference Field: the 12th generation." *Earth Planets Space*, 67, 79.

Thébault, E., M. Purucker, K. A. Whaler, B. Langlais, and T. J. Sabaka (2010), "The Magnetic Field of the Earth's Lithosphere." *Space Sci. Rev.*, 155.

Thébault, E., J. J. Schott, and M. Mandea (2006), "Revised Spherical Cap Harmonic Analysis (R-SCHA): Validation and Properties." *J. Geophys. Res.*, 111.

Thomson, A. W. P. and V. Lesur (2007), "An improved geomagnetic data selection algorithm for global geomagnetic field modelling." *Geophysical Journal International*, 169, 951–963.

Tøffner-Clausen, L. (2013), "Swarm Level 1b Product Definition, SW-RS-DSC-SY-0007, Issue 5.15." `https://earth.esa.int/documents/10174/1514862/Swarm_L1b_Product_Definition`.

Tøffner-Clausen, L. (2015), "Swarm Corrected Mag-L Preliminary Data Release Notes."

Torta, J. M., F. J. Pavón-Carrasco, S. Marsal, and C. C. Finlay (2015), "Evidence for a new geomagnetic jerk in 2014." *Geophysical Research Letters*.

Turner, G. M., J. Rasson, and C. Reeves (2007), "Observation and measurement techniques." In *Treatise on Geophysics* (M. Kono, ed.), volume 5, Geomagnetism, 94–143, Elsevier, Amsterdam, The Netherlands.

Tyler, R. H., S. Maus, and H. Lühr (2003), "Satellite observations of magnetic fields due to ocean tidal flow." *Science*, 299, 239–241.

Ultré-Guérard, P., D. Jault, M. Alexandrescu, and J. Achache (1998), "Improving geomagnetic field models for the period 1980-1999 using Ørsted data." *Earth Planets Space*, 50, 635–640.

Van der Sluis, A. and H. A. Van der Vorst (1987), "Numerical solution of large, sparse linear algebraic systems arising from tomographic problems." In *Seismic tomography*, 49–83, Springer.

van Sabben, Da (1966), "Magnetospheric currents, associated with the ns asymmetry of sq." *J. Atmos. Terrest. Phys.*, 28.

Vestine, E. H., W. L. Sibley, J. W. Kern, and J. L. Carlstedt (1963), "Integral and spherical-harmonic analysis of the geomagnetic field for 1955.0, Part 2." *J. Geomag. Geoelectr.*, 15, 73–89.

Vogt, P. R. and O. E. Avery (1974), "Detailed magnetic surveys in the northeast atlantic and labrador sea." *Journal of Geophysical Research*, 79, 363–389, URL `http://dx.doi.org/10.1029/JB079i002p00363`.

Wardinski, I. and R. Holme (2006), "A time-dependent model of the earth's magnetic field

and its secular variation for the period 1980–2000." *Journal of Geophysical Research: Solid Earth*, 111, URL http://dx.doi.org/10.1029/2006JB004401. B12101.

Wardinski, I. and V. Lesur (2012), "An extended version of the C3FM geomagnetic field model: application of a continuous frozen-flux constraint." *Geophysical Journal International*, 189, 1409–1429, URL http://gji.oxfordjournals.org/content/189/3/1409.abstract.

Wessel, Paul, Walter H. F. Smith, Remko Scharroo, Joaquim Luis, and Florian Wobbe (2013), "Generic mapping tools: Improved version released." *Eos, Transactions American Geophysical Union*, 94, 409–410, URL http://dx.doi.org/10.1002/2013EO450001.

Whaler, K. A. and C. D. Beggan (2015), "Derivation and use of core surface flows for forecasting secular variation." *Journal of Geophysical Research: Solid Earth*, 120, 1400–1414, URL http://dx.doi.org/10.1002/2014JB011697. 2014JB011697.

Zmuda, A. (1971), "The international geomagnetic reference field 1965.0: introduction." *Bull. Int. Assoc. Geomagn. Aeron.*, 28, 148–152.

l'université nantes angers le mans
PÔLE DE RECHERCHE ET D'ENSEIGNEMENT SUPÉRIEUR

UNIVERSITÉ DE NANTES

Thèse de Doctorat

Diana SATURNINO

Describing temporal variations of the geomagnetic field using a modified virtual observatory scheme: application to Swarm measurements

Une méthode d'observatoires virtuels pour décrire les variations temporelles du champ géomagnétique et application aux mesures de la mission Swarm.

Abstract

A description of the temporal variations of the main geomagnetic field (i.e., the secular variation, or SV) is crucial to the understanding of core dynamo generation. It is known with high accuracy at observatory locations, which are globally unevenly located, hampering the determination of a global pattern of these variations. Satellites have allowed global surveys of the field and its SV. Their data has been used by global spherical harmonic models using data selection criteria to reduce external contributions. SV small spatial scales may not be well described by these models, and can show significant errors compared to ground measurements. This study attempts to extract temporal variation time series from satellite measurements as it is done at observatory locations. We follow a Virtual Observatories (VO) approach, defining a global mesh of VOs at satellite altitude. We apply an Equivalent Source Dipole (ESD) technique. For each VO and a given time interval all measurements are reduced to a unique location, leading to time series similar to those available at the ground. Synthetic data is first used to validate the approach. We then apply our scheme to Swarm mission measurements. We locally compare the VO-ESD derived time series to ground observations and to satellite-based model predictions. The approach is able to describe field's time variations at local scales. The global mesh of VO time series is used to derive global spherical harmonic models. For a simple parametrization the model well describes the trend of the magnetic field both at satellite altitude and at the surface. Nevertheless more complex modelling can be made to properly profit of VO-ESD time series.

Key Words

Earth's magnetic field, modelling, inversion, satellite measurements, data analysis, Swarm mission, virtual observatories, IGRF model.

Résumé

La description des variations temporelles du champ géomagnétique (variation séculaire ou SV) est cruciale pour la compréhension de la dynamo. La SV est connue avec une grande précision dans les observatoires magnétiques, qui ont une répartition spatiale inégale. Les satellites donnent des observations globales du champ et de sa SV. Leurs données sont utilisées par les modèles globaux en harmoniques sphériques. Les petites échelles spatiales de la SV décrites par ces modèles peuvent montrer des erreurs par rapport aux mesures des observatoires. Dans cette étude je tente d'extraire des séries temporelles avec des mesures satellitaires comme dans les observatoires. L'approche des observatoires virtuels (VO) est suivie. Un maillage global de volumes à l'altitude du satellite est défini. Pour cela, la technique des Equivalent Source Dipoles (ESD) est appliquée. Pour chaque VO et intervalle de temps donné, toutes les mesures sont réduites à un endroit unique, menant à des séries temporelles similaires à celles disponibles dans les observatoires à la surface. *L'approche est validée avec des donnes synthétiques et puis* appliquée aux mesures de la mission Swarm. Les séries temporelles VO-ESD sont comparées à celles à la surface et aux prédictions par un modèle. L'approche décrit correctement les variations temporelles du champ à l'échelle locale. Un maillage global de VO est construit et utilisé pour obtenir des modèles globaux. Les modèles sont capables de décrire l'évolution du champ magnétique à la fois à l'altitude du satellite et à la surface. Toutefois des modélisations plus complexes pourront être faites pour profiter des séries temporelles VO-ESD.

Mots clefs

Champ magnétique terrestre, modélisation, inversion, analyse de mesures, mesures satellitaires, Mission Swarm, observatoires virtuels, sources dipolaires équivalentes, modèle IGRF.